SURFACE ACOUSTIC WAVE ANALOGUE MATCHED FILTER REALISATION AND APPLICATIONS IN DIGITAL SPREAD SPECTRUM COMMUNICATIONS

A thesis submitted to the Faculty of Science of the University of Edinburgh, for the degree of Doctor of Philosophy

by

B J DARBY, BSc

Electrical Engineering Department

May 1974

EDINBURGEN EX BIBL UNIV.

ABSTRACT

SURFACE ACOUSTIC WAVE ANALOGUE MATCHED FILTER REALISATION AND APPLICATIONS IN DIGITAL SPREAD SPECTRUM COMMUNICATIONS

The design of the surface acoustic wave (SAW) analogue matched filter (AMF) and the SAW non-linear convolver are examined. High performance devices are demonstrated. Potential applications are identified in burst mode transmission of data employing characteristic frequency and time domain encoded signals as address waveforms. Simple prototype modulator-demodulator configurations and their evaluation are described.

First, the fundamentals of the Rayleigh surface wave mode transduction and propagation on piezoelectric single crystal substrates are described. Key device realisations and important applications are tabulated.

Next, the basic features of spread spectrum communications are reviewed covering: the important cross-correlation demodulation process, highlighting the differences between active correlator and matched filter receivers; current link implementations; and the system characteristics emphasising multiple access considerations.

This leads to a comparison of SAW and microelectronic matched filters, namely: the SAW fixed and programmable AMF; the SAW non-linear convolvers; the microelectronic (ME) charge-transfer AMF; and the ME digital matched filter. The SAW AMF is identified as exhibiting distinct advantages over the other realisations: passive, asynchronous analogue operation at IF with large dynamic range, simple hardware and relatively low cost.

Next, the design of SAW AMF is examined and a novel dual-tap geometry described for significant performance improvements. Experimental results are given to illustrate 'second-order' distortion producing mechanisms and their reduction. Preliminary experiments on the degenerate SAW non-linear convolver are presented to demonstrate device performance and operation in correlating periodic pseudonoise signals.

Then, the incorporation of SAW AMF in novel modem configurations employing random access discrete address spread spectrum transmissions with on-off keyed and multiple alternative signaling is discussed. Finally, prototype modem configurations are demonstrated and their performance evaluated. Emphasis rests on the high performance achieved and the design flexibility offered by SAW.

It is considered that the original work contained in this Thesis is mainly comprised firstly by those sections describing AMF design for spurious signal cancellation and the non-linear convolver experiments; and secondly, by those sections delineating the incorporation of AMF in, and detailed evaluation of, spread spectrum modems.

ACKNOWLEDGMENT

The author would like to express his gratitude to Professor J H Collins for his expert supervision and provision of excellent research facilities. Also, to Professor W E J Farvis for his arrangement of entry to the postgraduate course and continued interest in this work.

I would also like to express my appreciation to various members of staff for helpful discussions, particularly Dr J M Owens, Mr P M Grant and Dr D P Morgan. Thanks are due to Messers R D Lambert and R R Halstead for fabrication of a large number of specialised devices.

I would like to thank Miss Irene Black for her special care and expertise in typing the manuscript. Finally, many thanks to my wife, Sue, for her tremendous encouragement and for drawing most of the figures.

CONTENTS

Please note that Figures and Photographs are interleaved within text.

	Page No
TITLE PAGE	*(i)*
ABSTRACT	*(ii)*
ACKNOWLEDGMENTS	*(iv)*
CONTENTS	*(v)*
CHAPTER 1 INTRODUCTION TO THESIS	1
1.1 Aims and Outline of Thesis	1
1.2 Basic SAW Device Considerations	4
CHAPTER 2 INTRODUCTION TO DIGITAL SPREAD SPECTRUM COMMUNICATIONS	14
2.1 Introduction	14
2.2 Operating Principles of the General Spread Spectrum Link	15
2.3 Basic Spread Spectrum Modulation Techniques	18
2.3.1 General classifications	18
2.3.2 Generation and correlation properties of pseudo-noise sequences	20
2.3.3 Continuous direct sequence spread spectrum	25
2.3.4 Frequency-hopping spread spectrum	27
2.3.5 Time-hopping spread spectrum	28
2.4 Matched Filter and Correlator Receivers; Enhancement of Signal-to-Noise Ratio	29
2.5 Spread Spectrum System Characteristics ..	35

Page No

2.5.1 Multiple access and spectrum utilisation .. 35

2.5.2 Jamming resistance 41

2.5.3 Multipath resolution; protection against signal fading 41

2.5.4 Range measurement 42

2.6 Summary 43

CHAPTER 3 A COMPARISON OF ANALOGUE AND DIGITAL MATCHED FILTERS 45

3.1 Introduction 45

3.2 Fixed Coded Surface Acoustic Wave Analogue Matched Filter 47

3.2.1 Current performance data 47

3.2.2 Fabrication and complexity 50

3.2.3 Necessary peripheral hardware 51

3.2.4 Cost analysis 51

3.3 Programmable Surface Acoustic Wave Analogue Matched Filter 51

3.3.1 Current performance data 51

3.3.2 Fabrication and complexity 53

3.3.3 Necessary peripheral hardware 54

3.3.4 Cost analysis 54

3.4 Surface Acoustic Wave Non-Linear Convolvers .. 54

3.4.1 Current performance data 54

3.4.2 Fabrication and complexity 59

3.4.3 Necessary peripheral hardware 60

3.4.4 Cost analysis 60

3.5 Charge-Transfer Analogue Matched Filters .. 61

3.5.1 Current performance data 61

3.5.2 Fabrication and complexity 64

3.5.3 Necessary peripheral hardware 65

3.5.4 Cost analysis 65

Page No

3.6 Digital Matched Filters 65

3.6.1 Current performance data 65

3.6.2 Fabrication and complexity 68

3.6.3 Necessary peripheral hardware 68

3.6.4 Cost analysis 68

3.7 Summary of Comparison Data 68

CHAPTER 4 THE REALISATION AND EVALUATION OF SAW MATCHED FILTERS FOR BIPHASE SIGNALS 72

4.1 Introduction 72

4.2 SAW Biphase Coded Analogue Matched Filter Design and Analysis 74

4.2.1 First-order design considerations 75

4.2.2 Characterisation of first order AMF designs 93

4.2.3 Analysis of acoustic wave impedance mismatch 105

4.2.4 Performance of second-order AMF designs .. 109

4.2.5 Summary on AMF design 112

4.3 SAW Non-Linear Convolver Experiments 114

4.3.1 Basic phenomenological convolver theory .. 114

4.3.2 Degenerate convolver experiments 119

CHAPTER 5 POTENTIAL APPLICATIONS OF SAW AMF IN SPREAD SPECTRUM COMMUNICATIONS MODEMS 123

5.1 Introduction 123

5.2 Bandspread OOK Signaling 124

5.2.1 Adaptive threshold receiver concept incorporating SAW AMF 127

5.2.2 OOK modems for multiple access discrete address systems 129

Page No

5.3 Spread Spectrum Multiple-Alternative Signaling 133

5.3.1 Binary modems incorporating coded SAW AMF .. 137

5.4 Summary 138

CHAPTER 6 EXPERIMENTAL SPREAD SPECTRUM MODEMS INCORPORATING BINARY PHASE CODED SAW AMF 139

6.1 Introduction 139

6.2 Spread Spectrum OOK Modem Evaluation 140

6.3 Experimental Binary FSK Spread Spectrum Modem 145

6.4 OOK Modem for Random Access, Discrete Address Communications 150

6.5 Summary 153

CHAPTER 7 FINAL REMARKS 154

REFERENCES 156

APPENDIX *(Consisting of four published papers)*

I

II

III

IV

CHAPTER 1

INTRODUCTION TO THESIS

1.1 AIMS AND OUTLINE OF THESIS

Recently acoustic surface wave modes comprising Rayleigh, Love and Stoneley waves[1-3] and their hybrids[4,5] have received considerable attention for their potential in realising a wide range of signal processing devices[6.7]. Most effort has been focussed on developing Rayleigh wave components because efficient reciprocal broad-band transduction[8,9] and low loss propagation is simply achieved on free surfaces of readily available piezoelectric substrates.

A crucial stage in Rayleigh wave technology has now been reached with devices passing from a research to an engineering development and fully specified prototype phase. This transition has been accomplished sucessfully with two applications which received early emphasis, namely: the pulse expansion-compression filter pairs for high resolution chirp radar[10]; and the complex frequency filter for colour television[7,11]. In parallel with this evolution recognition of the important features of microminiaturisation, accurately designable and reproducible high performance and high yield with projected low costs attracted further interest and rapid growth of other device applications followed, notably in spread spectrum communications.

The aims of this Thesis are twofold; firstly to examine the design and performance of surface acoustic wave (SAW) analogue matched filters (AMF) and the SAW non-linear convolver for processing binary phase-shift keyed (PSK) signals; and secondly, to identify potential applications for these devices in digital spread spectrum communications equipments. In addressing these aims the layout of the Thesis is as follows:

Firstly, Section 1.2 deals primarily with the fundamentals of SAW technology, briefly delineating the important features of the interdigital transducer and Rayleigh wave propagation on anisotropic single crystal substrates, and concludes by tabulating several current devices and their potential applications.

Next, Chapter 2 introduces the basic spread spectrum communications link and discusses the factors influencing the choice of spread spectrum modulation and techniques for data transfer. The requirement for correlation detection implicit in recovering transmitted data from the spread spectrum signal is examined. The fundamental differences between the active correlator and matched filter in signal processing are highlighted.

A comparison between surface wave and competing microelectronic matched filter realisations is made in Chapter 3. The devices studied are: the SAW AMF; SAW non-linear convolver; the digital matched filter and the family of tapped charge-transfer analogue shift registers. The key advantages of the SAW AMF and non-linear convolvers are illustrated in comparisons of predicted parameter bounds, present day performances, fabrication complexity, peripheral hardware required and relative cost. The information is presented mainly in tabular form.

Having established the advantages and disadvantages of SAW matched filter implementations, Chapter 4 examines their design and evaluation. This begins with a consideration of fixed coded AMF design emphasising the *major* causes of distortion inherent with simple transducer geometries. A significant reduction of spurious SAW signals arising from periodic mismatch of wave impedance and a close to theoretical response is demonstrated with the use of a novel

coded transducer configuration[12]. Following this, the basic theory of operation and preliminary experimental work carried out on the SAW non-linear convolver[13,14] are described illustrating its use for processing repetitive biphase waveforms.

In Chapter 5 potential applications of SAW AMFs as *primary* signal processors in digital spread spectrum communications are presented. First, the influence of matched filter predetection processing on communications link error rate performance for both non-coherent on-off keyed (OOK) and multiple-alternative (M-ary) signaling techniques are reviewed. Next, the incorporation of SAW AMFs in novel modulator-demodulator (modem) configurations for high performance spread spectrum multiple-access systems employing these basic signaling techniques is illustrated. Emphasis is given to the key advantages offered by SAW; namely: a reduction in hardware complexity for the rapid synthesis and detection of frequency and time encoded pulse patterns; and the possibility of fully asynchronous modem operation.

Chapter 6 describes firstly the evaluation of "back-to-back" modem configurations for simple noncoherent OOK signaling[15] and orthogonal binary frequency-shift keyed signaling[15]. The error rate performances are described for signals corrupted by bandlimited white noise and cochannel interference and are shown to fit the theory discussed in Chapter 5. The Chapter concludes with a description of the error rate performance of a two signature random access, discrete address modem employing noncoherent OOK signaling and a hard-decision receiver logic[15]. This modem illustrates the encoding complexity, the simple hardware obtained and the near theoretical performance achieved with SAW AMFs.

Chapter 7 concludes the Thesis with a brief discussion of outstanding problems both from a device design and applications standpoint.

An appendix comprises a section of published papers.

1.2 BASIC SAW DEVICE CONSIDERATIONS

This section concentrates on the important properties of Rayleigh wave (hereafter referred to as surface acoustic wave (SAW)) transduction and propagation on piezoelectric substrates which are necessary as background information to Chapters 3, 4. Specific design problems relating to analogue matched filter implementation and performance are covered in Chapter 4. A number of general review articles have appeared on surface waves and their applications notably those by White[16], Kino and Matthews[7], Morgan[17] and Collins and Hagon[18].

Surface acoustic waves propagate on the free surface of solids with velocities approximately 10^5 times slower than electromagnetic waves in free space, are non dispersive and, for frequencies <2 GHz, exhibit an attenuation per wavelength, on certain crystalline substrates, lower than for electromagnetic waves[9,16]. The wave amplitude decays as a function of penetration depth[19] with most energy confined to within approximately one acoustic wavelength of the surface[19]. For piezoelectric solids, the mechanical motion is accompanied by an in phase electric field whose magnitude is related to the strain by the piezoelectric equations of state[16]. The piezoelectric effect stores energy which produces an effective stiffening of the material elastic constants and produces a commensurate increase in wave velocity compared with a purely elastic wave[16].

Efficient transduction of SAW is achieved with the interdigital electrode array, devised by White and Voltmer[8], which couples directly to the electric fields associated with the wave motion. Interdigital transducers (IDT) consist of N pairs of interleaved metal electrodes, Figure 1.1, formed on a flat polished surface of a piezoelectric substrate using photolithographic and metal deposition

processes developed for planar integrated circuit fabrication. Reliable, low resistance connections are made to the pattern by thermal compression bonding techniques. An applied voltage impulse causes, through the piezoelectric effect, an instantaneous strain pattern with periodicity, λ, equal to the local periodicity of the structure and with a spatial extent equal to the electrode overlap, W (Figure 1.1). Two contradirected, traveling surface waves are generated having a time varying spatial pattern which closely resembles the pattern of the IDT electrodes. The similarity between IDT structure and the canonical form of a transversal filter has been pointed out by Squire et al[20]. This fact is applied in Chapter 4, where constant periodicity and unapodized (constant W) IDTs are employed. For this basic IDT, which is shown in Figure 1.2, maximum coupling to surface wave energy occurs when the applied voltage alternates with frequency, f_o, given by

$$f_o = v_s/\lambda_o \qquad \ldots 1.1$$

where v_s is the surface wave velocity. This condition is referred to as acoustic synchronism as SAW contributions from each electrode pair add coherently.

The factors affecting IDT performance are primarily:

(1) The piezoelectric crystal and its orientation, which determine:

- the SAW phase and group velocities and the angle, termed the power flow angle[21] (ϕ) between them;

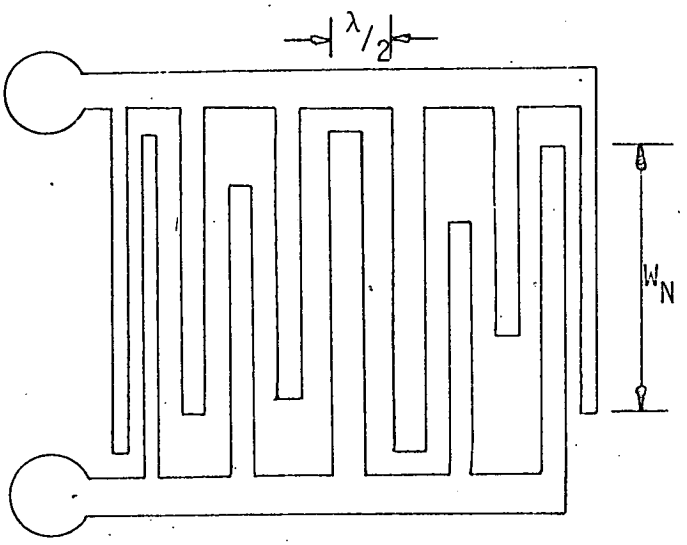

FIGURE 1.1 GENERAL FORM OF SAW IDT WITH VARYING PERIODICITY AND ELECTRODE OVERLAP

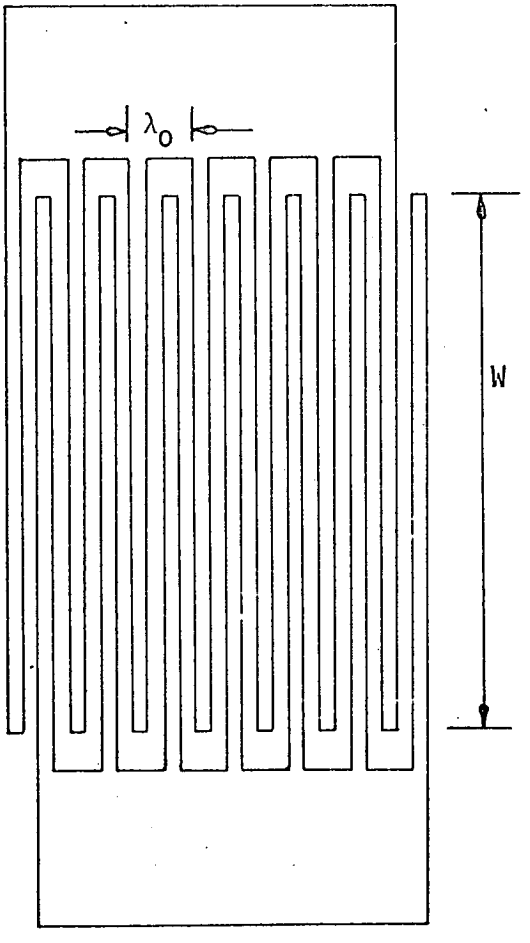

FIGURE 1.2 BASIC CONSTANT PERIODICITY, UNAPODISED SAW IDT

- the type of wave (SAW, bulk[22]) coupled piezoelectrically and the strength of coupling;
- the array capacitance through substrate permittivity and piezoelectric coupling and;
- the optimum efficiency - bandwidth product and corresponding number of electrode pairs[9] required.

(2) The interdigital array dimensions and electrode material -

- the electrode spatial periodicity determines the instantaneous acoustic synchronism frequency (equation 1.1);
- the array electrode geometrical pattern determines its frequency transfer function[20,23] and directional properties;
- determine the total array capacitance which increases linearly with aperture and the number of electrodes;
- the acoustic aperture and substrate material determine the acoustic radiation conductance[9], and;
- the electrode material causes resistive losses, its thickness/density causes dispersion[24] and its mass and electrical shorting effect lead to acoustic wave impedance discontinuities which give rise to scattering to bulk modes and spurious SAW[12,25] signals (see Chapter 4).

(3) Electrical networks connected to the IDT affect:

- the frequency response and coupling efficiency[9,26] and;
- the amplitude and phase of regenerated SAW signals[9].

Smith et al[9] have described equivalent circuit models, applied to each periodic section of an IDT, which are based on the 3-port Mason[9] circuit for bulk wave transducers. The overall IDT response in terms of its 3-port scattering parameters is obtained by evaluating the admittance matrix for (N-1) sections having acoustic ports cascaded and electric ports in

parallel. Two circuit models were proposed which relate to the relative magnitudes of the perpendicular(max for crossed field model) and parallel (max for in-line model) electric field components associated with the wave. Of these, the crossed field model is currently accepted as being the most accurate. This has been established by the measurement of acoustic reflection loss as a function of electric load and comparing this with theory from the two models[27] for both quartz and lithium niobate substrates.

The transducer equivalent circuit derived from the crossed field model, for periodic unapodized electrodes, is shown in Figure 1.3, where the acoustic radiation conductance $Ga(\omega)$ and $Ba(\omega)$, which are a Hilbert transform pair[23], are given by[9]:

$$Ga(\omega) = 2Go \tan(\theta/4).\ \sin(N\theta/2) \qquad \ldots 1.2$$

$$Ba(\omega) = Go \tan(\theta/4)\left[4N + \tan(\theta/4).\ \sin N\theta\right] \qquad \ldots 1.3$$

where,

$$Go = \frac{\omega_o C_s k^2}{2\pi} \qquad \ldots 1.4$$

and, ω_0 is the synchronous radian frequency, C_s the capacitance per section, k^2 the effective electromechanical coupling constant[9], and $\theta = 2\pi\omega/\omega_0$.

At acoustic synchronism, Ga has a peak value given by:

$$\hat{Ga} = 8N^2k^2f_oC_s \qquad \ldots 1.5$$

and the *acoustic* susceptance, Ba, is zero. The total susceptance, B, being determined by the transducer capacitance C_T,(NC_s).

For frequencies near acoustic synchronism[9], the fundamental SAW excitation frequency, equations 1.2 and 1.3 are approximated by:

$$Ba(\omega) = \frac{\hat{Ga}}{2x^2}\ .\ (\sin 2x + 2x) \qquad \ldots 1.7$$

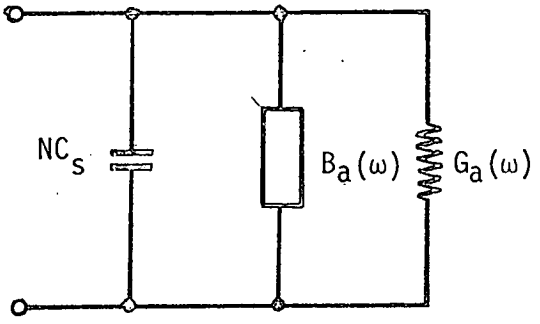

FIGURE 1.3 EQUIVALENT CIRCUIT FOR N PERIOD IDT DERIVED FROM THE CROSSED-FIELD MODEL

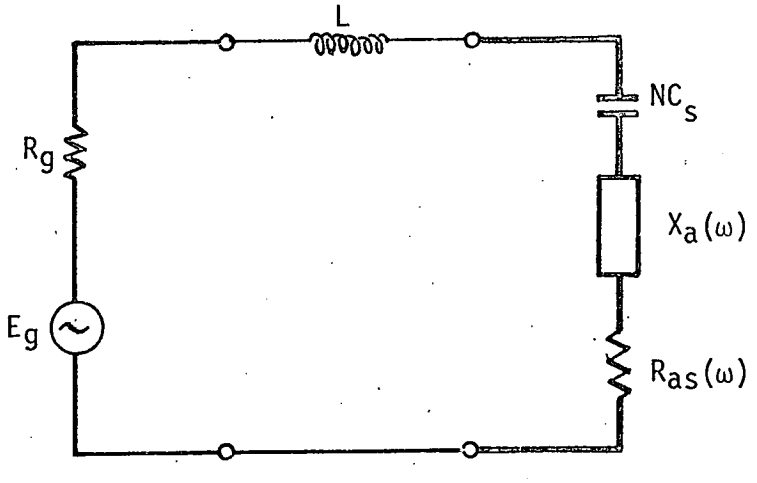

FIGURE 1.4 SERIES TUNED CONFIGURATION

where $x = N\pi(\omega-\omega_0)/\omega_0$.

The bandwidth for efficient SAW excitation is limited by the zeros in radiation conductance, conversely poles of conversion loss, occurring at frequencies, f_∞ given by:

$$f_\infty = f_0 \pm \frac{f_0}{N} \qquad \ldots 1.8$$

The transducer conversion loss at f_0 is minimised by using an inductor to provide a conjugate match. The series tuned configuration is shown in Figure 1.4, where the equivalent series components are obtained by transformation of Figure 1.3:

$$\hat{R}_{as} = \frac{\hat{G}a}{\hat{G}a^2 + B^2} \sim \frac{\hat{G}a}{B^2} \qquad \ldots 1.9$$

since B>Ga usually, similarly the series reactance at f_0,

$$X \sim B^{-1} \qquad \ldots 1.10$$

Thus, using equations 1.5, 1.9; gives

$$\hat{R}_{as} = \frac{2k^2}{\pi^2 f_0 C_s} \qquad \ldots 1.11$$

Equation 1.11 suggests that $\hat{R}_{as}$ is independent of the number of interdigital periods. This holds in practice for a wide range of N[23]. In addition, $\hat{R}_{as}$ is proportional to W^{-1}, since C_s is proportional to W, which allows the series radiation resistance to be matched to the generator series resistance, Rg, through correct choice of acoustic aperture*. The maximum fractional bandwidth (B_{opt}), associated with minimum phase dispersion across the band, and conversion loss at fo, for *series* tuning is obtained when[9]:

---

* FOOTNOTE Parallel tuning could be employed. However to match the commonly used 50 Ω and 75 Ω generator impedances impracticably large values of W result; eg $\hat{G}a$ = 0.02 mho when W ≃50 cm, with f_0 = 100 MHz and N = 25 on (ST,X) quartz. Whereas, for series tuning W ~1.3 mm.

$$B_{opt} = \sqrt{\frac{4k^2}{\pi}} = \frac{1}{N_{opt}} \qquad \ldots 1.12$$

Table 1.1 lists the values of B_{opt}, N_{opt} for the materials currently preferred for AMF applications, also included are the material parameters v_s, k^2 and C_s and the value of W' required to match in to 50 Ω. A comprehensive list may be found in reference 21.

TABLE 1.1 TRANSDUCER DESIGN PARAMETERS

MATERIAL	v_s (km sec^{-1})	k^2	B_{opt} %	N_{opt}	C_s ($pF.mm^{-1}$)	W'
YZ lithium niobate	3.488	.049	22	4.5	0.5	108
ZX lithium niobate	3.798	.052	25	4	0.5	110
[111], [011] $Bi_{12}GeO_{20}$	1.69	.014	13.5	7.5	0.38	90
Y, X Quartz	3.159	.0022	5.3	19	0.055	53
ST,X Quartz	3.1576	.0017	4	25	0.055	41

$W' = \frac{W}{\lambda_o}$ for matching a 50 Ω generator or load resistance.

The minimum conversion loss at synchronism for the simple IDT shown in Figure 1.2 is 3 dB due to bidirectional launching of surface waves. Hence, for two identical colinear transducers forming a simple delay line, the minimum theoretical insertion loss is 6 dB since,[9,28] by reciprocity, the receiving transducer can only deliver one half of the incident SAW power to the load. The remainder of the power is reradiated equally in two opposite directions. This reradiation of power constitutes a spurious acoustic signal. In simple delay lines this appears, having been reflected off the input transducer, as a triple-transit signal[28] which can be reduced by mismatching both transducers or by designing unidirectional IDTs.[28,29] For complex receiving interdigital arrays,

(eg in pulse compression filters, and multiply tapped delay lines), the reradiated SAW signal is sensed by the receiving array on the *second transit*. Here, the ratio of regenerated power to power in the load is usually decreased by mismatching the output transducer (see Chapter 4).

In practice, the 6 dB minimum insertion loss (0 dB for unidirectional transducers) for a delay line is never obtained. Firstly, there are two loss mechanisms in transduction due to (1) losses in the tuning inductor, and (2) losses in the parasitic resistance of the IDT metal electrodes.[28] Secondly, several loss mechanisms occur in propagation[21]:

(1) Propagation loss due to phonon interactions which has an approximately f^2 dependence, and air loading which adds a linear term with frequency. Empirical expressions have been given by Slobodnik.[21] These predict losses of the order of 0.066 dB/μS and 0.028 dB/μS for Y,X quartz and Y,Z lithium niobate at 100 MHz, while the corresponding losses at 1 GHz are 2.6 dB/μS and ~1 dB/μS respectively.

(2) Beam steering losses arise through noncolinearity of SAW phase and group velocity vectors causing a receiving IDT to be partially illuminated by the acoustic beam. The loss is a function of substrate material, its basic orientation and the misalignment (θ) to the pure mode axis (specific directions where $\phi = 0$). The degree of beam steering resulting from a given misalignment is determined from the slope of the power-flow angle ($\partial\phi/\partial\theta$). For materials exhibiting perfect parabolic velocity surfaces[21] the extent of beam steering is *estimated* from simple analytic functions; for example the delay B(μS) for 3 dB beam steering loss is given by[21]

$$B = \frac{[1 - (2)^{-\frac{1}{2}}]\ W'}{f \tan\theta \left|\frac{\partial\phi}{\partial\theta}\right|} \quad (\mu S) \qquad \ldots 1.13$$

where $W' = \frac{W}{\lambda}$, f is the frequency in MHz. As an example, B = 470 μS for W' = 100, f = 100 MHz on (ST,X) quartz where[21] $\frac{\partial\phi}{\partial\theta} = 0.378$ and assuming $\theta = 0.1^{o}$.

(3) Diffraction results in a changing acoustic beam profile and eventual beam spreading. The slope of the power-flow angle is again used to estimate the extent of beam spreading. Diffraction may be retarded or increased in relation to diffraction for isotropic media[30,31], this depends on the value of $\partial\phi/\partial\theta$. A choice of crystal orientation allows an exchange between beam steering and diffraction losses[21,31].

The near and far field diffraction regions are clearly defined by the loss curves given by Bristol[27] and Szabo and Slobodnik[31]. For wavelength normalised propagation distances Z' (Z' = Z/λ), the diffraction loss remains under 3 dB for (Z'/W') less than ~30 for quartz substrates. The 3 dB diffraction loss delay C (μS) is given by[21,31]:

$$C = \frac{1.769\ W'}{(1 + \partial\phi/\partial\theta)f} \qquad \ldots 1.14$$

where f is in MHz. A value of 128 μS is obtained for C on (ST,X) quartz assuming the same parameters as in the beam steering example. The influence of diffraction on AMF design is indicated in Chapter 4.

(4) Non-linear effects are observed with high acoustic powers causing generation of second harmonic traveling waves[32] thus depleting power at the fundamental frequency. In quartz, the basic non-linear mechanism is a lattice anharmonicity expressed by the third-order elastic constants[33]. The nature of the non-linear mechanism in lithium niobate is not fully understood. In addition to a purely elastic non-linearity there is the possibility of a non-linear photo-elastic or electro-optic effect, due to the strong piezo-electric coupling, having an interaction of the form

$$D = KS^2 \qquad \ldots 1.15$$

where S is the acoustic strain amplitude and D is the electric displacement. The effect is observed both with bulk mode[16] and surface mode propagation. The latter provides the stronger interaction because of the higher power density obtained with SAW. Lean et al[32] report changes in attenuation of SAW, at 200 MHz on Y,Z lithium niobate, from <1 dB cm^{-1} at 21 dBm launched acoustic power, to ~6 dB cm^{-1} at 33 dBm acoustic power. It is this large non-linear effect rather than surface breakdown phenomena which may impose a limitation on the input power level for linear delay line applications.

Real-time convolution and correlation has been obtained through the non-linear interaction between contra-flowing acoustic signals[34]. Chapter 4 describes preliminary experiments[13,14] using this effect.

(5) The excitation of bulk modes by synchronous scattering from IDTs results in depletion of power from the incident SAW beam. The problem is acute for wideband and large arrays; important aspects of this problem are discussed in Chapter 4.

In summary, propagation attenuation and air loading is a major propagation loss mechanism at microwave frequencies but reduces to <0.1 dB/μS for most single crystals at 200 MHz. Beam steering and diffraction are negligible sources of loss at frequencies below ~200 MHz unless long delays are considered. Further, trade offs between these two mechanisms may be achieved through choice of substrate orientation and using wider acoustic apertures. At high acoustic power levels non-linear effects cause additional loss which increases with centre frequency and in situations where narrow acoustic beams are produced, eg guiding[35], due to enhanced power densities.

The important design constraints imposed by the first-order temperature coefficient of delay are analysed for their effect on phase coded analogue matched filter realisation and performance in Chapter 4.

Finally, some of the key devices and applications[6] realised with SAW technology are listed in Table 1.2.

TABLE 1.2 KEY SAW DEVICES AND POTENTIAL APPLICATIONS

SAW DEVICE	POTENTIAL APPLICATIONS	ADVANTAGES	PROBLEM AREAS/DISADVANTAGES
DELAY LINE[6]	DELAY EQUALISATION IN SPACE DIVERSITY DIGITAL LINKS, RECIRCULATING INTEGRATORS, BLOCK ORIENTED RANDOM ACCESS MEMORIES,	HIGH IF OPERATION IN-BUILT FREQUENCY FILTERING, FIXED GROUP DELAY EQUALISATION, HIGH BIT RATES, HIGH STORAGE CAPACITY.	INSERTION LOSS, TEMPERATURE STABLE SUBSTRATES RESULT IN MARGINAL BANDWIDTHS, HIGH COST PER STORED BIT.
FREQUENCY FILTER[6]	IF FILTER, SATELLITE CHANNEL MULTIPLEXING FILTERS	NO ADJUSTMENTS, LIGHT WEIGHT, FIXED GROUP DELAY	INSERTION LOSS,
OSCILLATOR[6]	SPACE QUALIFIED LOCAL OSCILLATOR DRIVE; ANALOGUE COMMUNICATIONS MODULATOR; MEDICAL TELEMETRY	HIGH OPERATING FUNDAMENTAL, CAPABLE OF WIDE % DEVIATION, HIGH SHORT TERM STABILITY, RUGGED	LONG TERM STABILITY POOR WITH PRESENT TECHNIQUES
DISCRIMINATOR[6]	ANALOGUE COMMUNICATIONS DEMODULATOR, AUTOMATIC FREQUENCY CONTROL	HIGH OPERATING IF, MINIMAL ADJUSTMENT	OPERATING BANDWIDTH AND LINEARITY UNPROVEN
BIT MATCHED FILTER[6]	DIGITAL IF PROCESSOR,	OPTIMISES SIGNAL-TO-NOISE, HIGH IF, WIDEBAND, ANALOGUE AND PASSIVE	GAIN REQUIRED
BIPHASE-CODED MATCHED FILTER[6,12]	IF SPREAD SPECTRUM MODULATION-DEMODULATION; SMALL RADAR	PASSIVE; ANALOGUE; ASYNCHRONOUS; HIGH PERFORMANCE; WIDE RANGE OF BANDWIDTH AND TIME DELAY POSSIBLE	PROGRAMMABILITY LIMITED; TIME-BANDWIDTH PRODUCT <2000,
CHIRP FILTER[10]	PULSE COMPRESSION RADAR; SECURE ALTIMETRY; ELECTRONICALLY VARIABLE DELAY	<35 dB TIME SIDELOBES ACHIEVABLE; TIME-BANDWIDTH PRODUCTS TYPICALLY 100-500 AND 5000 DEMONSTRATED	FIXED CODED
CONVOLVER[13, 14,17,34]	RADAR; SPREAD SPECTRUM SIGNALING; FOURIER ANALYSIS; TIME COMPRESSION, EXPANSION AND INVERSION	LARGE DEGREE OF PROGRAMMABILITY; LARGE TIME-BANDWIDTH 500-1000 TYPICAL;	LOW EFFICIENCY FOR ACOUSTIC CONVOLVER; FABRICATION DIFFICULT FOR SEMICONDUCTOR AND DIODE CONVOLVERS; ADDITIONAL HARDWARE REQUIRED FOR ASYNCHRONOUS OPERATION; TIME COMPRESSED OUTPUT.
PSEUDO-NOISE GENERATOR[6]	ACCEPTANCE TESTING OF DIGITAL LINKS; SPREAD SPECTRUM MODULATOR	DIRECT PSK MODULATION AT IF; HIGH CHIP RATE; LONG SEQUENCES; LOW POWER	FIXED CHIP RATE AND LIMITED CODE SELECTION.

CHAPTER 2

INTRODUCTION TO DIGITAL SPREAD SPECTRUM COMMUNICATIONS

2.1 INTRODUCTION

This Chapter introduces basic digital spread spectrum communication techniques and considers the inherent interrelation of the system characteristics obtained with the category of wideband modulation employed.

First, the operation of the general spread spectrum link is described, covering principles of wideband modulation and receiver implementation. Next, the three commonly used wideband modulation techniques; namely: (1) direct pseudo-noise (PN); (2) frequency-hopping (FH); and (3) time-hopping; are discussed. Then, the two possible receiver implementations, comprising the matched filter and active correlator, are compared in their ability to perform the key demodulation process necessary for data recovery.

Advantages of matched filter signal processing emerge for certain applications and these are examined in the remainder of this Thesis.

Finally, the characteristics required of a communications system are examined and the performance of spread spectrum techniques discussed in providing selective enhancement of:

> Cochannel multiple access; channel utilisation; low detectability by unauthorised receivers; jamming immunity; multipath resolution; and range and velocity measurement.

Discussions will be limited to the factors influencing the transmission of digital signals which enable efficient processing of various types of traffic; voice, data in fixed and variable format and automatic telemetry. Suitable accessing procedures allow the differing rates and channel occupancy of large numbers of subscribers to be accommodated in a single system. Further advantages include: the capability of signal regeneration; error detection and correction; the possibility of encryptic encoding; compatibility with terminal equipments such as digital computers and teleprinters; and the feasibility of high speed complex processors due to a continuing development of cheap and reliable integrated circuits. These latter factors are of growing importance as the volume of transmitted *data* is increasing and should supercede voice transmission in many important situations - eg, automatic inertial navigation reporting for air-traffic control (ATC)[36].

2.2 OPERATING PRINCIPLES OF THE GENERAL SPREAD SPECTRUM LINK

Primarily, spread spectrum modulation provides the capability of low error rate communication in the presence of high cochannel interference levels.[37,38] This is achieved by transmitting a signal derived by modulating the data with a characteristic signal possessing a bandwidth typically >1000 times the data rate. At the receiver, data is recovered at low input signal-to-noise ratios (typically -5 dB to -30 dB) through cross-correlation with a replica of the wideband signal employed at the transmitter. During normal link operation, the predetection correlation process results in an enhancement of signal-to-noise ratio (processing gain) which allows achievement of a minimum

detection error rate concomitant with the signaling method used, see Chapters 5, 6.

The general digital spread spectrum link assumes the form shown in Figure 2.1. Input baseband data, at rate R baud, digitally phase (PSK) or frequency (FSK) modulates an intermediate frequency (IF) carrier producing a constant amplitude bandpass signal[38]. This data signal, $D_1(t)$, is then multiplied by the distinct wideband modulation, $C_1(t)$, in the spread spectrum modulator. The information is thus spread over the total bandwidth, $B_s (\gg R)$, of the characteristic signal, $C_1(t)$.

After upconversion, the wideband signal ($D_1(t)\ C_1(t)$) is transmitted and subsequently appears at the receiver input linearly superimposed with other cochannel transmissions, jamming signals and thermal noise. The received signal plus interference is processed at a suitable IF by the correlator whose function is represented schematically by the spread spectrum demodulator and integrating filter. Multiplication of the received signal by an exact, time synchronised, replica of the wideband modulation is carried out in the spread spectrum demodulator. The output of the demodulator stage contains the terms shown in Table 2.1.

The integrator completes the implementation of the correlation function. Detection of the high correlation value obtained with zero time lag of the reference determines the necessary synchronisation between transmitter and receiver. To avoid false synchronisation the autocorrelation function of the modulation ideally exhibits a well defined peak and zero secondary peaks at non zero reference time lags. This type of two-level autocorrelation

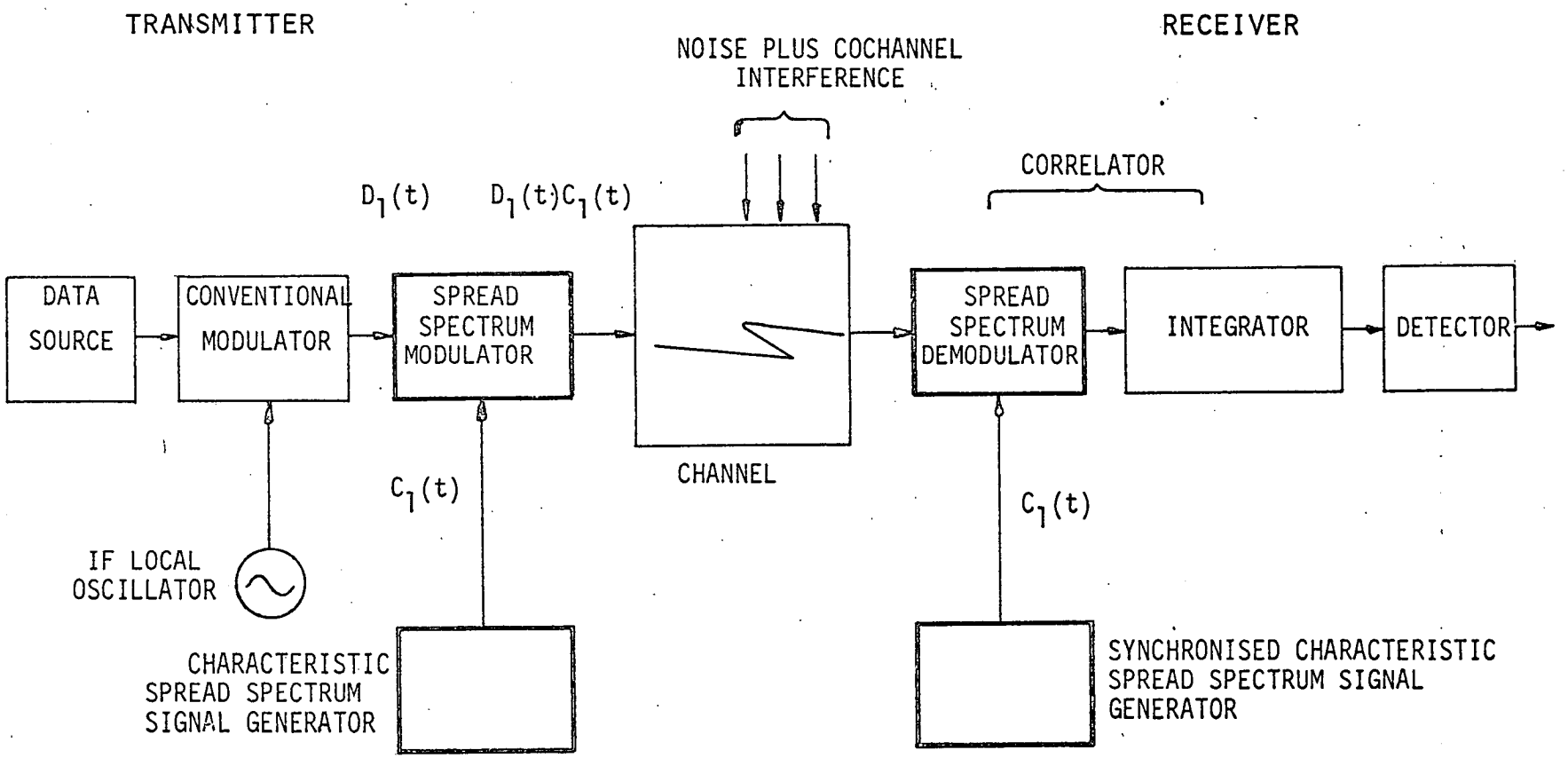

FIGURE 2.1 GENERAL FORM OF DIGITAL SPREAD SPECTRUM LINK

TABLE 2.1 SIGNAL AND INTERFERING COMPONENTS ARISING FROM SPREAD SPECTRUM DEMODULATION

Signal	*Origin*
$C_1^2(t)\ D_1(t)$	required signal component
+	
$C_1(t)\ C_2(t)\ D_2(t)$	components of mutually interfering signals using the same network
+	
+	
$C_1(t)\ C_k(t)\ D_k(t)$	
+	
$C_1(t)\ J(t)$	component of jamming signal, J(t)
+	
$C_1(t)\ C_1(t-T_m)\ D_1(t-T_m)$	multipath component with delay T_m
+	
$C_1(t)\ N(t)$	thermal noise component

function is characteristic of a stochastic process as for example, displayed by stationary white noise, and is approximated with certain deterministic pseudo-random signals (see Section 2.3).

Conventional phase or frequency demodulation, required to reconstruct the baseband signal, is usually incorporated with the correlator as illustrated in the next Section. At the end of the integration period ($T = {}^1/R$), the sampled value of the first term in Table 2.1 represents the data signal, $D_1(t)$ since the data is of constant polarity over the bit time, T. The final stage in the link is the decision on bit polarity taken on this sample in accordance with the signaling method used (see Chapter 5).

The integrals of all cross-product terms, shown in Table 2.1, are ideally zero, in which case each receiver would be able to reconstruct its own data signal and discriminate against all others. In practice it is difficult to achieve the complete signal orthogonality implied by zero integrals of the cross-products. The approach generally adopted is to select $\{C_k(t)\}$ with bounded crosscorrelation values for all time displacements[39].

In principle, the correlation process outlined above can be performed either with a "correlator" or a "matched filter" receiver[40,41]; identical peak output signal-to-noise ratios (SNR) result at the sampling instant, $(t = T)$. The enhancement of SNR, sketched in Figure 2.2, obtained at the sampling instant, or processing gain (G_p), is maximum[41] for stationary bandlimited white noise equal to $2B_sT$. Other interference conditions have been examined by Mayher[42] and are discussed further in Section 2.4. The choice between correlator and matched filter receivers is governed to some degree by the required processing gain which is potentially greater, in practical implementation, for the correlator[38]. However, many other factors are involved relating to the spread spectrum signal format, the role of the link and the achievement of high message rates; these are examined in Sections 2.3 and 2.4.

2.3 BASIC SPREAD SPECTRUM MODULATION TECHNIQUES

2.3.1 General Classifications

The first classification applicable to wideband modulation signals concerns their derivation. Two basic methods exist:

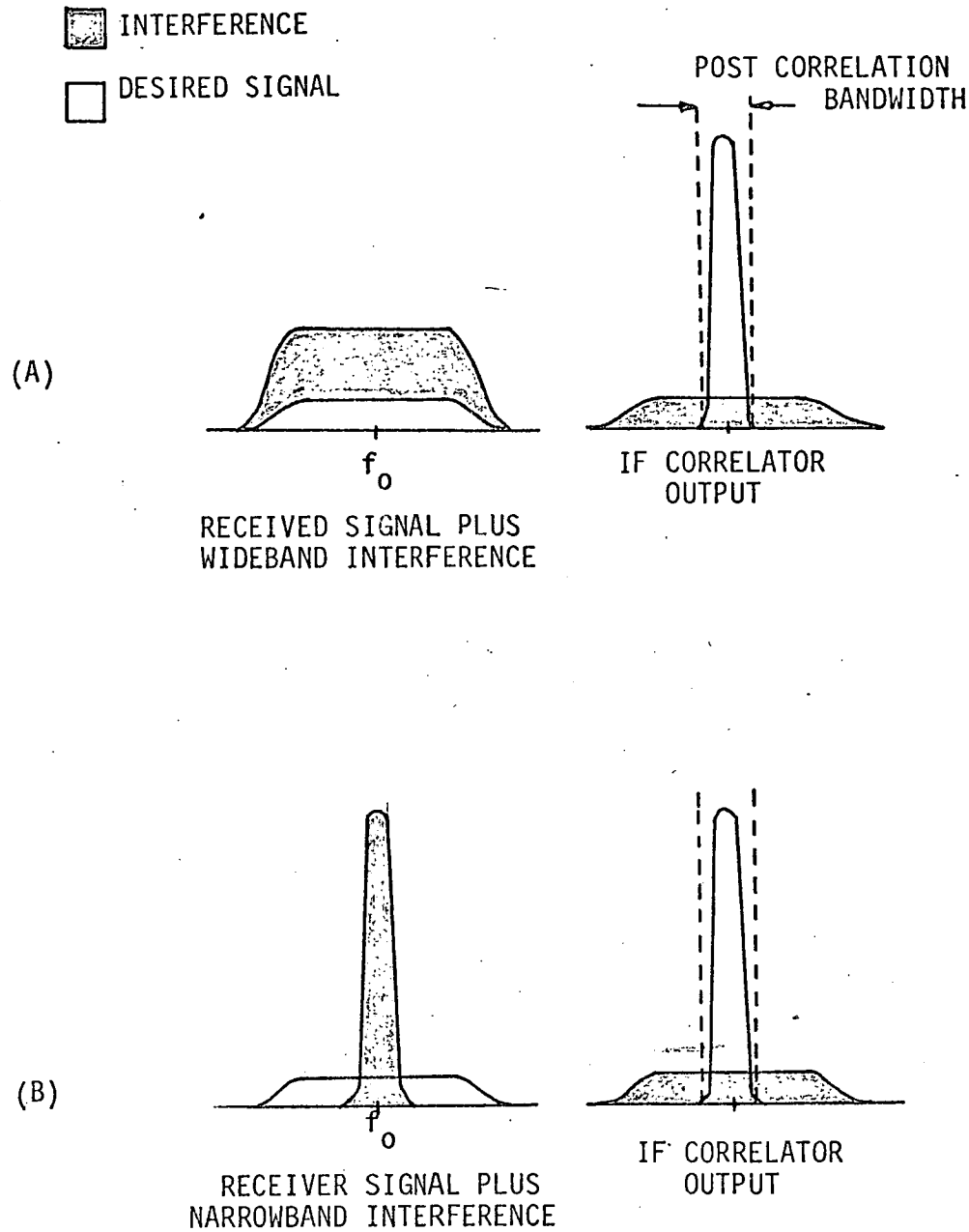

FIGURE 2.2 FREQUENCY-DOMAIN ILLUSTRATION OF WIDEBAND (A) AND NARROWBAND (B) INTERFERENCE REJECTION THROUGH CROSSCORRELATION

(1) Direct modulation - in which a characteristic waveform and the data signal are multiplied directly. The resulting signal has a bandwidth and spectrum envelope essentially determined by the modulating characteristic waveform.

(2) Indirect modulation - here, a characteristic waveform, usually a binary sequence, is used either: (i) to select randomly a carrier frequency on which data is continuously transmitted until the control sequence selects a different carrier; or (ii) to control the times of transmission, on a fixed carrier frequency. Type (i) is a general statement of frequency-hopping in which the total signal bandwidth, B_s and the control sequence (hopping) rate are essentially independent and the spectrum is usually flat. Type (ii) describes time-hopping spread spectrum which has a bandwidth determined by the modulation rate during the 'on' period. Time hopping is usually used in conjunction with other spread spectrum techniques.

Specific combinations of these basic modulation techniques result in systems possessing special characteristics; for example, coding in both frequency and time domains allows random access to a large number of potential users[43] by assigning addresses comprised of specific pulse patterns. This random access, discrete address technique is discussed fully in Chapters 5, 6.

The waveforms used in both the direct and indirect techniques ideally exhibit the two-level autocorrelation function alluded to in Section 2.2. Maximal length pseudo-noise (PN) sequences[37,38] exhibit periodic autocorrelation functions approaching the ideal, while being simple to generate and potentially providing signals with large time-bandwidth products (TBs). Hence, for these reasons PN sequences have been commonly used. Other waveforms have been employed in pulsed mode direct spread spectrum links, these include the binary Barker[44,45] and Turyn[46] waveforms and the linear fm (chirp)[45,47,48] signal. Reference will be made to these in later sections.

2.3.2 Generation and Correlation Properties of Pseudo-Noise Sequences

Binary waveforms are conveniently produced by the well known shift-register generation technique[45,49,50]. The generator comprises a clocked digital delay line implemented with cascaded binary storage elements connected to a logic feedback circuit which determines the input to the first stage. By suitable choice of register length (n), the feedback function $f(x_1, x_2, \ldots, x_n)$ and the initial state of the register: $x_1, x_2, \ldots, x_n$, *any binary sequence* may be produced.

The linear maximal length sequences (m-sequences), produced by a feedback function comprising *only* modulo-2 addition of specified shift-register stages, exhibit the desired two-level autocorrelation function, shown in Figure 2.3. The m-sequence has the longest period (L) possible for the register length employed. This longest period L, is given by:

$$L = 2^n - 1 \qquad \ldots 2.1$$

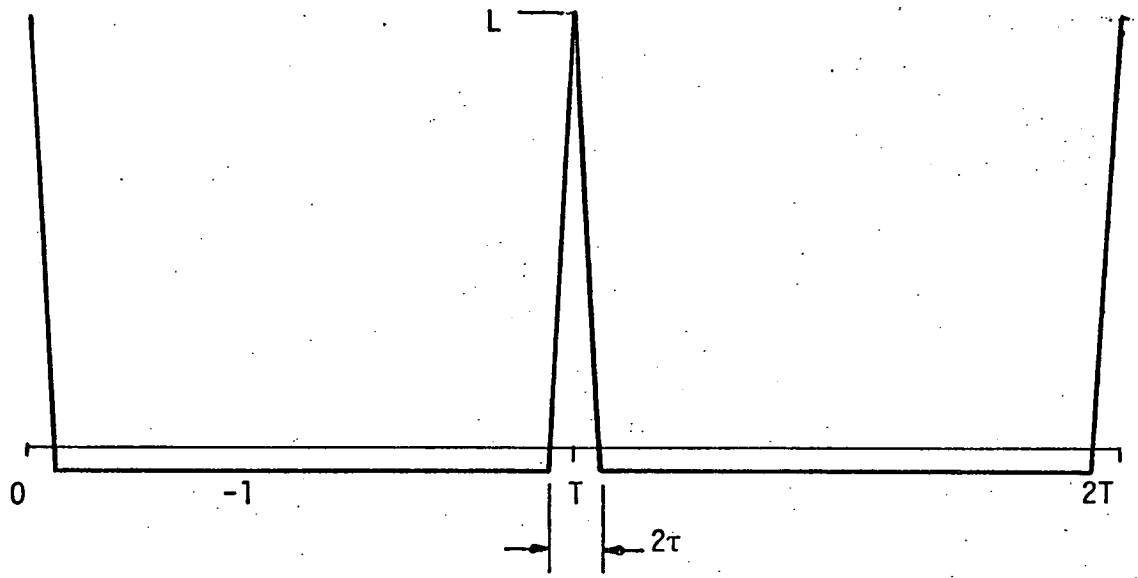

FIGURE 2.3 M-SEQUENCE PERIODIC AUTOCORRELATION FUNCTION

The sequence repeats after L digits. The all 'zero' state of the register is not allowed as the logic becomes 'locked' and sequence generation does not occur.

The feedback functions required for m-sequence generation are listed by Peterson[50] for n up to 34. Feedback functions are expressed in polynomial form from which corresponding feedback connections are readily determined.

The power spectrum of an m-sequence is obtained by calculating the Fourier Transform of the autocorrelation function; via the Wiener-Khinchine[51] theorem. The important characteristics of the spectrum are:

- due to the periodicity, a line spectrum is obtained with frequencies at multiples of $(L\tau)^{-1}$, where τ is the duration of a code chip;

as the total power in the spectrum is constant,

- the power associated with each spectral line is inversely proportional to the sequence period ($L\tau$);
- the spectral envelope is proportional to $\text{sinc}(\omega\tau|2)$, thus the signal bandwidth (B_s) is determined by the chip rate ($^1/\tau$) and not by the length of the waveform;
- the power at zero frequency is proportional to L^{-2}.

The mutual crosscorrelation performance of sets of *periodic* m-sequences is difficult to predict. However, the following general points serve as a guide:

- for m-sequence pairs with relatively prime lengths the cross-correlation is small and constant for all relative displacements[37,49];
- for equal length m-sequences with L values having small factors, high crosscorrelation values are usually exhibited between some of the possible sequence pairs[37,39]. Conversely, it is found that for prime L; the cross-correlation peaks are generally low. In most cases, sequence lengths L having factors p, have cross-correlation peaks $\sim Lp^{-1}$ occuring at p distinct cyclic shifts of the two codes.

Gold[39] has studied the properties of non-maximal length sequences generated by shift register with feedback logic derived by multiplying together the primitive [50] characteristic polynomials

of degree n corresponding to an m-sequence pair with maximum cross-correlation χ_{12} defined by:

$$\chi_{12} \leqslant \begin{cases} 2^{(n+1)/2} + 1 & \text{odd n} \\ 2^{(n+2)/2} + 1 & \text{even n and n not a multiple of 4} \end{cases} \quad \ldots 2.2$$

The product polynomial determines the feedback function for generation of $2^n + 1$ distinct sequences each of length $2^n - 1$, with the cross-correlation function of any pair bounded according to equation 2.2. As an example, Gold[39] gives the characteristic polynomial of a 14 stage generator which produced 129 different linear sequences of length 127 (n = 7) having $\chi_{jk} < 17$; equation 2.2, odd n. The cost incurred is that the periodic autocorrelation function is no longer two-valued, but is also bounded by the same inequality. This can result in operational difficulties in achieving synchronisation acquisition.

The *aperiodic* autocorrelation function of any binary sequence is characterised by a time-sidelobe pattern having a mirror symmetry about the peak. The heights of the time-sidelobes are determined by the code structure, Boehmer[52] has found binary codes of <100 chips with low time sidelobes ($\sim 0.6\sqrt{L}$) for radar applications. However, the communication requirement is usually for a large set of codes with good autocorrelation and low mutual cross-correlation properties. The results of some extensive computer searches[53] are briefly discussed below. An example of the aperiodic autocorrelation function of a 127 chip m-sequence is shown in Figure 2.4.

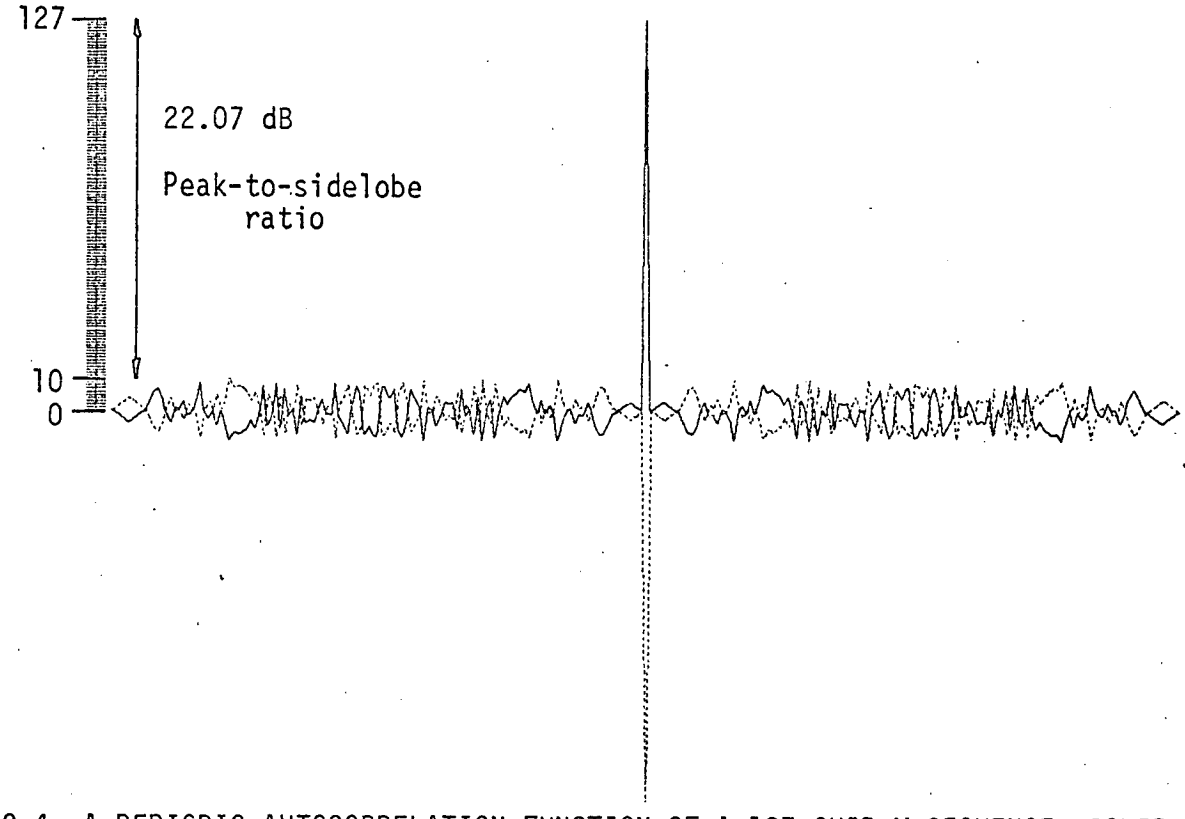

FIGURE 2.4 A PERIODIC AUTOCORRELATION FUNCTION OF A 127 CHIP M-SEQUENCE: SOLID CURVE. THE SOLID PLUS BROKEN CURVES ILLUSTRATE THE rf ENVELOPE PRIOR TO DEMODULATION

As an extension to Gold's computations, TRW[53] discovered a "parent" m-sequence of length 8191 (n = 13) with sixteen disjoint subsequences of 511 chips and a maximum aperiodic cross-correlation between any pair of 47. The number of sequences can be increased from 16 to 19 with the same cross-correlation bound. This is achieved by choosing the initial state of each subsequence so that the tail of one sub-sequence and the beginning of the next overlap by 40 chips. The proposed application was a range differencing surveillance system for ATC[36] over the continental United States. The large number of unique codes required (~¼ million) were obtained through various code, pulse rate and pulse position combinations. SAW matched filters were proposed to implement the prototype receiver.

An important consideration when designing uncoordinated code-division multiple-access systems with pulsed transmissions is that the auto-to-cross correlation ratio is approximately equal to the processing gain[43], both expressed in decibels. This indicates an approximate limit to the communication capacity obtainable (see Section 2.5) without increasing the size of code directories; for example, by the use of coded time-frequency patterns[43,54].

The choice of sequence length generally depends on two requirements:

(1). For a given code clock rate the number of spectral lines encompassed by the receiver IF bandwidth will be directly proportional to the sequence length. The greater the spectral line density, the more "noise-like" interfering signals will appear.

(2) The average time required to achieve synchronisation is proportional to the code length for "serial search" synchronisations[55,56] when a prior knowledge of the time uncertainty of the receiver code generator is not available. The rate of search is effectively determined by the processing gain and the local oscillator frequency uncertainty[38,57]. Synchronisation acquisition-time reduction methods using surface wave analogue matched filters have been described by Hunsinger[56] and the principles involved are briefly discussed below.

2.3.3 Continuous Direct Sequence Spread Spectrum

Direct PN bandspreading systems are commonly used for military satellite communications[37,38,56], a simplified modem block diagram is shown in Figure 2.5 together with a waveform diagram. The digital data signal and the clock synchronised, high chip-rate spreading code are conveniently combined at baseband by modulo-2 addition. Typical parameters are: data rate 2.4 K baud, and a bandwidth expansion factor of 2000. The spreading code length being of the order of 2047 (n = 11) to 16383 (n = 14). The resulting continuous digital signal biphase modulates a carrier at IF. This is followed by up-conversion and transmission.

The receiver must know the transmitter characteristic PN sequence, its phase and clock rate, the carrier frequency and carrier phase, before correct spread spectrum demodulation can be performed. Once synchronisation has been acquired a delay-lock code tracking loop[57] maintains receiver code synchronisation.

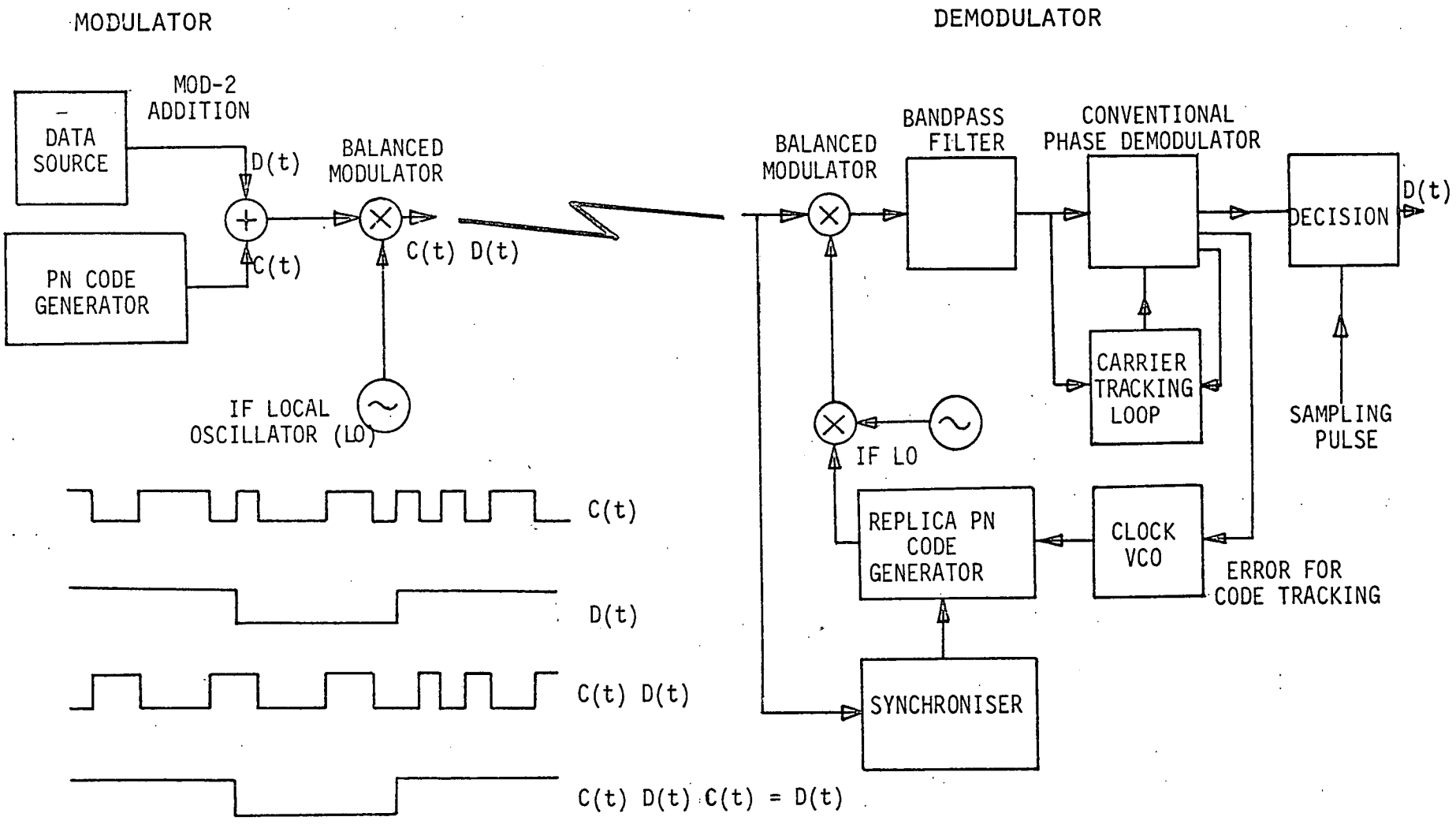

FIGURE 2.5 ESSENTIALS OF A DIRECT PN MODEM

Bandpass correlator techniques are commonly employed for spread spectrum demodulation[55]. The combination of large (30-40 dB) processing gain and signal bandwidth (3-10 MHz) are not at present conveniently achieved by most matched filter technologies in a single device, see Chapter 3.

A carrier-tracking loop[38], implemented with a Costas[38] or a squaring[38] circuit, provides the coherent IF reference carrier for conventional coherent demodulation[57]. The output is sampled at time T and binary decisions are made on bit polarity.

The post bandpass correlation processing in the receiver is thus identical with that for simple phase-shift keyed (PSK) modulation which achieves the optimum error rate performance for binary signaling[57].

A fundamental problem in link operation is centred on the rapid acquisition of the initial receiver synchronisation. With serial search techniques[38,56], the acquisition time required is proportional to the product of the receiver time uncertainty and processing gain (TBs). Typical search periods are of the order of 2 seconds[55].

Synchronisers incorporating SAW analogue matched filters (AMF) with TB_S ~127 have resulted in acquisition time reductions of two orders of magnitude[55]. The AMF detects a suitably chosen subsequence of the long PN signature generated at the transmitter. Recognition of this subsequence provides a time reference for the receiver generator. With short ($\lesssim$1000 chip) PN spreading codes, or when synchronisation preambles are transmitted, the AMF can be fixed coded. When the use of preambles is excluded, or primarily when the PN code duration is necessarily long[55,56], a programmable AMF is set to detect a subsequence in advance of the known time

uncertainty. Here a highly stable clock and some prior knowledge of propagation delay is desirable. Reliable synchronisation decisions require ~15 dB output signal-to-noise ratios; this necessitates AMF processing gains of >25 dB (TB_s>300) and some form of automatic gain control (see Chapter 5) for current link applications[37].

2.3.4 Frequency-Hopping Spread Spectrum

In frequency-hopping (FH) systems[38] the available bandwidth is divided into a number of contiguous subchannels. Bandspreading is achieved by transmitting successive pulses of length $T(=1/R)$ on carrier frequencies determined by a digital frequency synthesiser controlled by PN sequence and the data bit polarity, Figure 2.6. The resulting wideband signal consists of a sequence of orthogonal binary frequency-shift keyed (FSK) pulses pseudo-randomly hopped over the signal bandwidth, B_s.

At the receiver, an identical digital frequency synthesiser is synchronised to the transmitter and used as the reference for spread spectrum demodulation. The resulting output is a reconstructed binary FSK signal from which a baseband signal is obtained usually by making "greatest of" decisions on the sampled envelope demodulated output of two bit matched filters[56,57], see Chapters 5, 6. Noncoherent FSK signaling exhibits higher bit error rates than coherent PSK signaling but is more easily implemented in terms of receiver hardware. Multiple-FSK signaling is also possible, with an attendant reduction in bit error rate[56,57], by using k data bits to select one of 2^k "tones" which are effectively spread spectrum modulated as before. In this case the optimum receiver comprises a bank of 2^k bit matched filters and a "greatest-of" decoder[57].

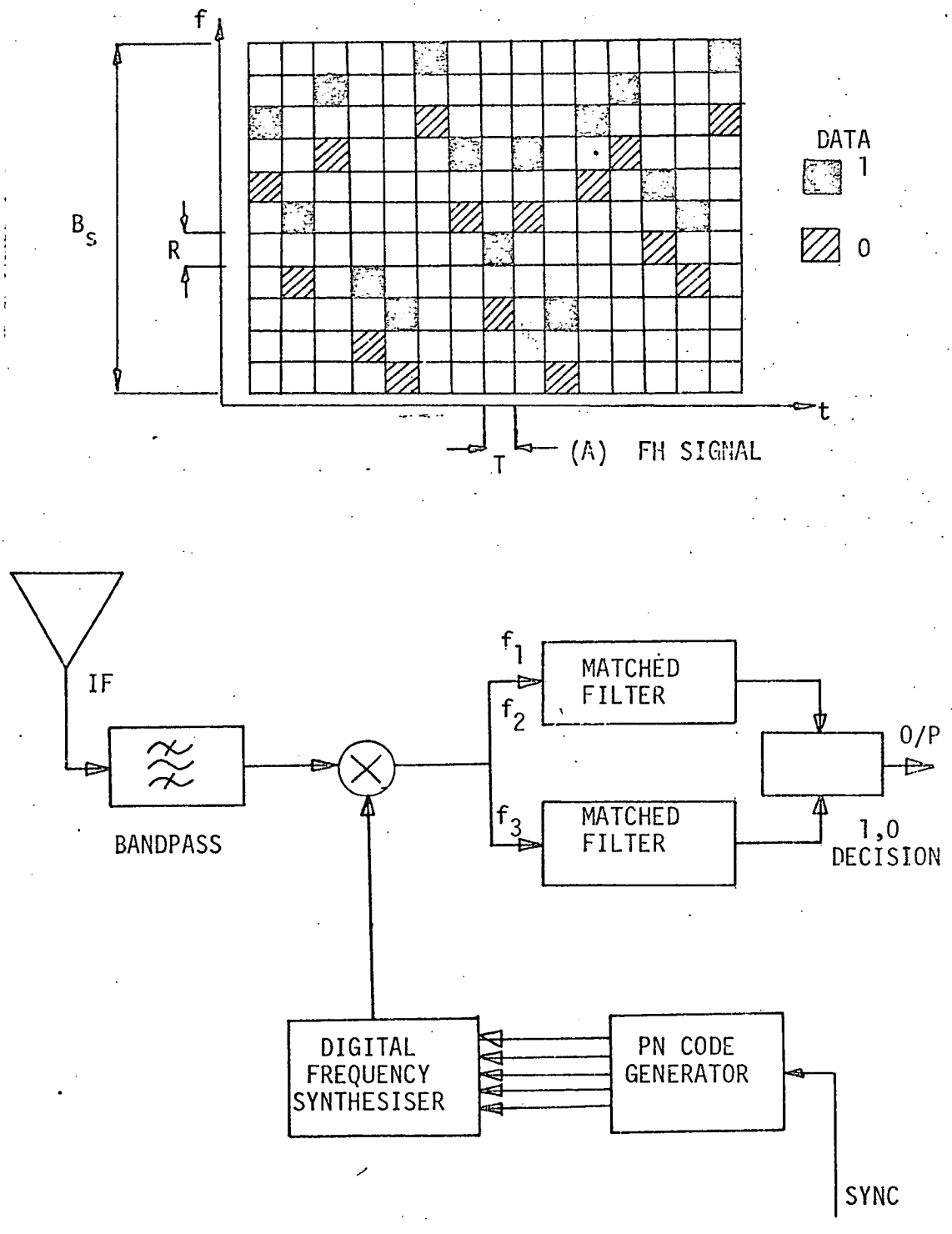

FIGURE 2.6 ILLUSTRATION OF FH SIGNAL (A) AND BASIS OF BINARY FSK-FH RECEIVER (B)

Two advantages of FH over direct PN modulation emerge:

(1) the total rf bandwidth (B_s) is essentially independent of the PN code clock rate and is controlled by selecting the number and size of frequency hops; and

(2) a much lower accuracy of PN code synchronisation[38,56] is required to achieve synchronisation, for PN links the necessary accuracy is proportional to $^1/B_s$ while for FH links it is only $^1/R$.

Conversely, this latter property results in a lower accuracy for FH in navigation applications since the pulse duration is much greater than $^1/B_s$.

Other basic configurations including a possible configuration for coherent FH are discussed by Cahn[38]. Improvements in FH system design are possible, notably the increased time resolution available, by using SAW AMFs in both spread spectrum modulator and demodulator[58]. Some aspects of the use of SAW devices in frequency agile transmissions are outlined in Chapter 5.

2.3.5 Time-Hopping Spread Spectrum

Time-hopping (TH) modulation[38] is usually employed in conjunction with other spread spectrum techniques. Basically, short high power pulses are transmitted in time-slots determined by a PN code. Data bits are stored for high speed transmission during the burst. The receiver functions by the input to the demodulator with a synchronised replica PN sequence. This low activity factor transmission enables multiple access through pseudo-random gating of the interference and partially overcomes the dynamic range limitation of direct PN techniques when used with a geographically dispersed net.

A time-hopping modem block diagram is given in Figure 2.7.

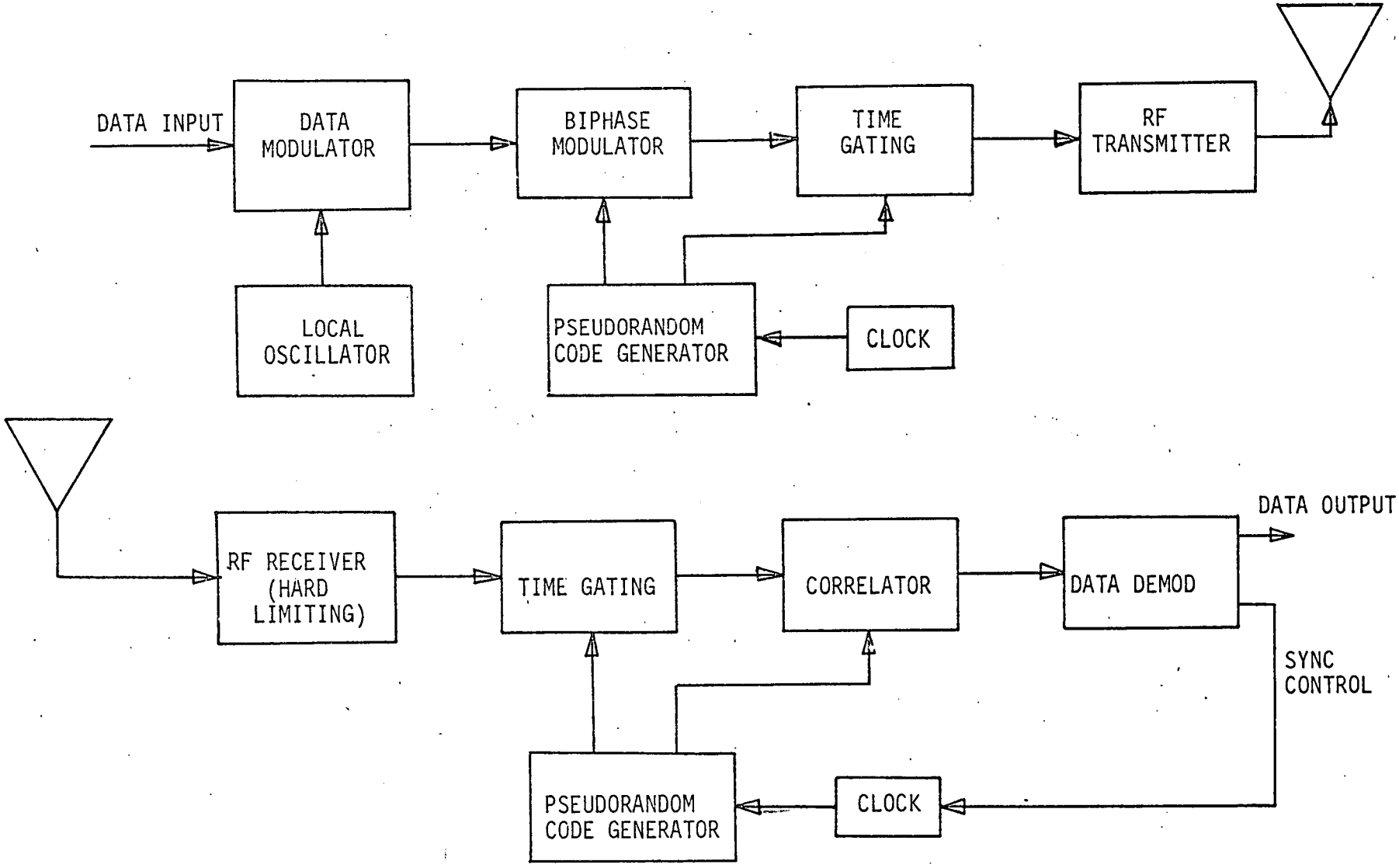

FIGURE 2.7 ESSENTIALS OF PN/TH SPREAD SPECTRUM SYSTEM

2.4 MATCHED FILTER AND CORRELATOR RECEIVERS; ENCHANCEMENT OF SIGNAL-TO-NOISE RATIO

The relationship of signal-to-noise ratio (SNR) to message "intelligibility" is distinct for analogue and digital signaling. In analogue systems, the SNR effectively determines the *fidelity* of the demodulated message waveform. However, for a digital link *demodulation fidelity* is unimportant, the factor determining final message *quality* is the *decision error probability* per bit. Where additive Gaussian noise constitutes the primary interference, the error probability decreases monotonically as the input SNR increases. Thus, the primary objective of digital signal predetection processing is to enhance the SNR and, in achieving this, signal fidelity is lost.

Two basic signal processing devices exist; namely the matched filter and active correlator; in theory[57,59] both are optimum although the link requirements may predicate the choice of either one.

The principles of matched filtering are well established and have been reviewed in many texts; for example see Turin[41], Raemer[59], Lange[51]. For the specific case of signals corrupted by *white, stationary* noise maximum instantaneous output SNR is obtained at time $t = T_o$ for a linear filter[41] characterised by an impulse response, h(t):

$$h(t) \triangleq ks\ (T_o - t) \qquad \ldots 2.3$$

where k is a gain constant, and $T_o \geq T$, the signal duration, to satisfy causality. Thus, the impulse response is a delayed and time reversed replica of the matched signal, s(t).

The equivalent frequency domain definition follows:

$$H(j\omega) \triangleq kS^*(j\omega)\ \exp(-j\omega T_o) \qquad \ldots 2.4$$

where $S^*(j\omega)$ is the complex conjugate of the Fourier Transform of $S(t)$, and $H(j\omega)$ is the matched filter frequency transfer function, see Chapter 4. Thus, apart from the amplitude factor and phase shift term ($k\ \exp(-j\omega T_o)$), the transfer function is given by the complex conjugate of the matched signal spectrum.

The filter response, $v(t)$ to $s(t)$ is given by the convolution integral:

$$v(t) = \int_{-\infty}^{\infty} s(\tau)\ h(t-\tau)\ d\tau \qquad \ldots 2.5$$

Now, $h(t) = 0$ for $0>t>T_o$ is a condition of physical realisability, and using equation 2.3, the convolution integral becomes:

$$v(t) = k \int_{o}^{t} s(\tau)\ s(T_o-t+\tau)\ d\tau \qquad \ldots 2.6$$

which is the *delayed autocorrelation function* of $s(t)$. The output, $v(t)$, has a maximum value at time $t = T_o$:

$$v(T_o) = k \int_{o}^{T_o} s(\tau)\ s(\tau)\ d\tau. \qquad \propto E \qquad \ldots 2.7$$

where E is the total signal energy[41,59].

This last result, equation 2.7, leads to alternative and more generally realisable methods of implementing matched filter operation. Equation 2.7 results from the correlation integral:

$$\chi_{sr}(\tau) = \int_{-\infty}^{\infty} s(t).\ r(t+\tau)\ dt \qquad \ldots 2.8$$

when the signal waveform $s(t)$ and reference waveform $r(t)$ are identical, each of duration T_o, and the delay variable, $\tau = 0$. Then,

$$\chi_{sr}(0) = \int_0^{T_o} s(t)\, s(t)\, dt \qquad \ldots 2.9$$

Note, however that for the matched filter, the autocorrelation function is produced as a real-time function, and not expressed in the delay (τ) coordinate, equation 2.8.

The integrand in equation 2.8 is recognised as a signal resulting from a mixing operation and the remainder of the operation is simply a bandpass integration $(0,T_o)$ centred at frequency f_o where

$$f_o = f_s \pm f_r \qquad \ldots 2.10$$

and f_s, f_r are the signal and reference carrier frequencies.

Generally, f_o is a convenient system IF and conventional demodulation is achieved in a separate operation. The final process common to both the matched filter and correlator consists of sampling at time T_o and performing a decision according to the signaling technique employed[57].

Figure 2.8 illustrates the equivalence of matched filtering and correlation. Figure 2.9 compares the waveforms produced by both the matched filter and correlator for a variety of signals completely known apriori. Often, in practice the correlator output is dumped[57] after sampling, this allows a zero-threshold device to discriminate data 1, 0. Table 2.2 summarises the differences in implementation of the two processors for coherent PN spread spectrum signals.

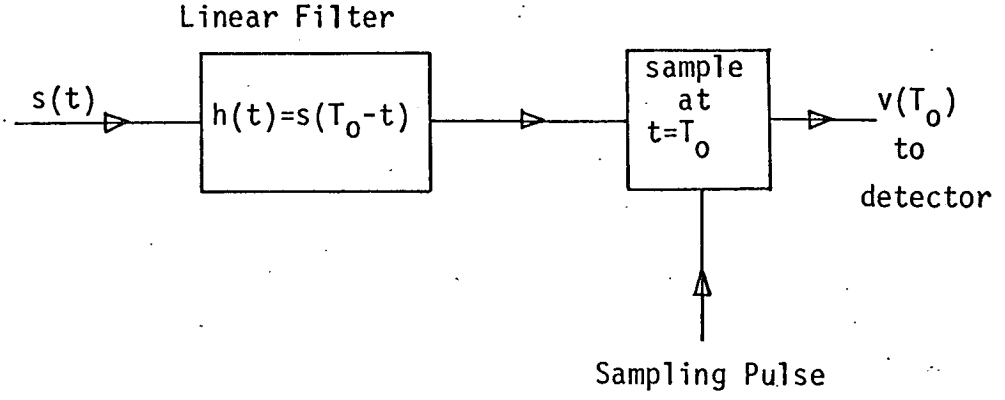

(A) Linear matched filter

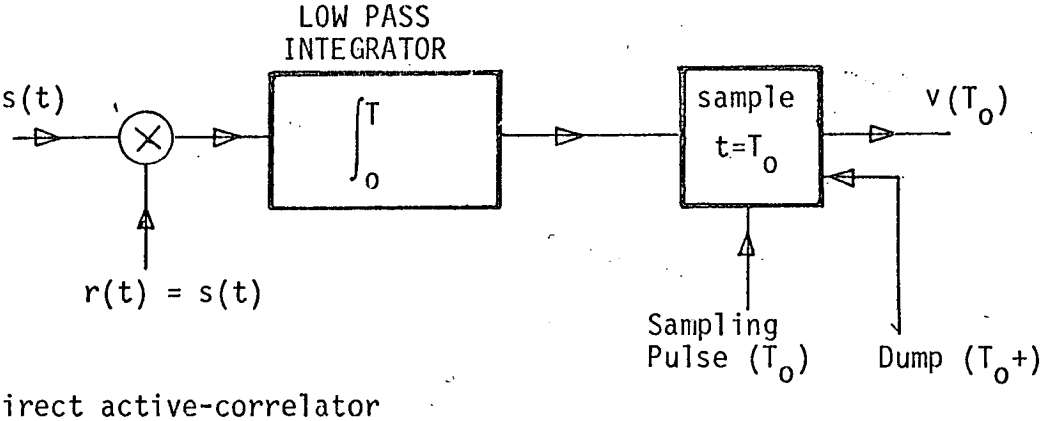

(B) Direct active-correlator

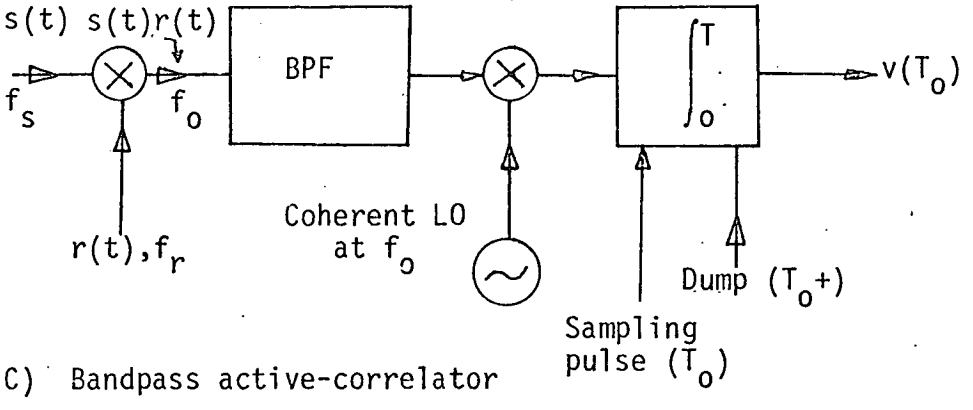

(C) Bandpass active-correlator

FIGURE 2.8 ILLUSTRATION OF THE EQUIVALENCE OF THE LINEAR MATCHED FILTER (A) THE DIRECT (B) AND BANDPASS (C) ACTIVE CORRELATORS

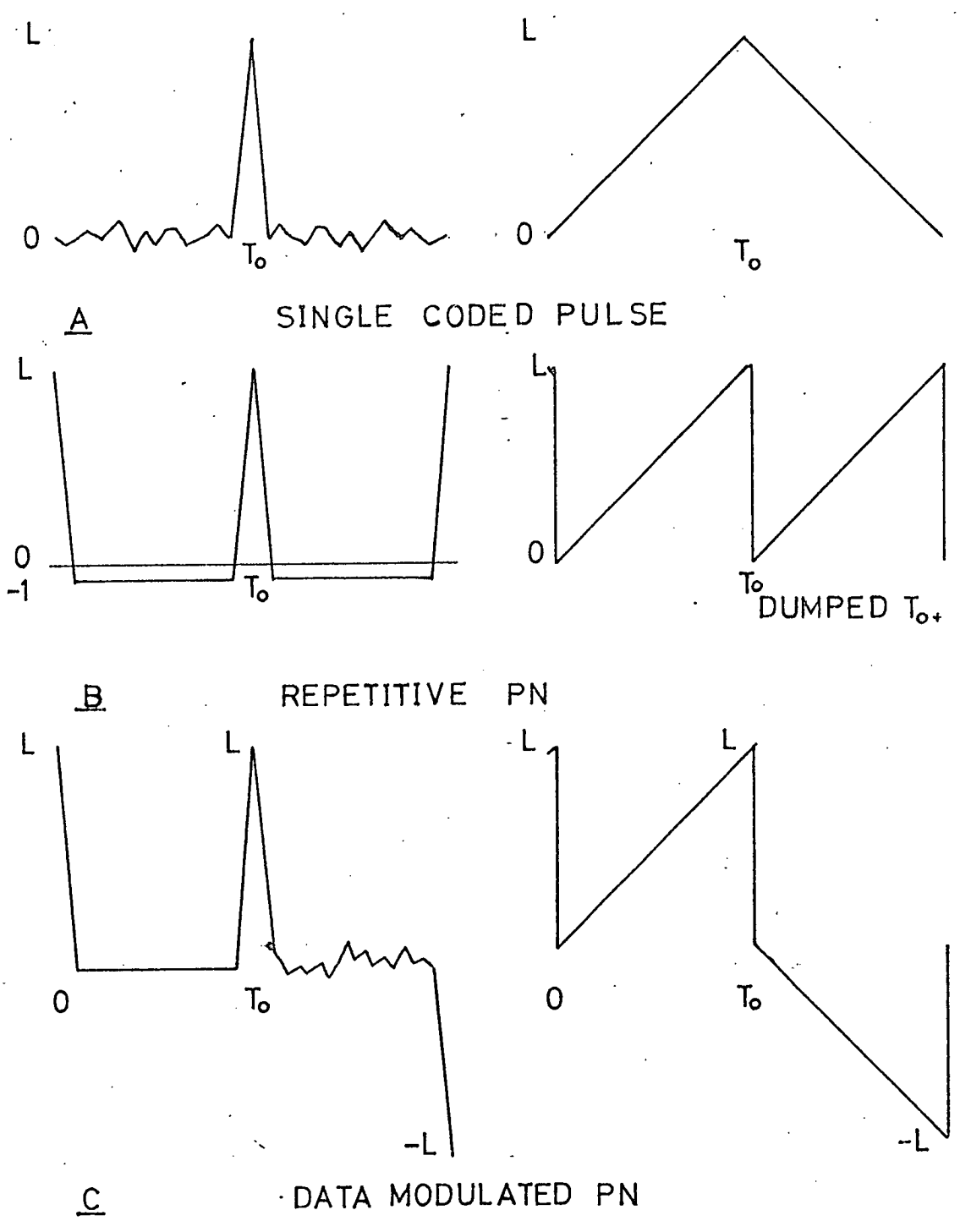

FIGURE 2.9 COMPARISON OF AMF AND CORRELATOR O/P FOR SIGNALS KNOWN APRIORI

TABLE 2.2 COMPARISON OF MATCHED FILTER AND CORRELATOR OPERATION FOR DIRECT PN LINKS

	SINGLE MATCHED FILTER	CORRELATOR
Device Implementation	Linear Transversal Filter $h(t) = s(T_o - t)$	Multiplier plus integrator
Reference signal	Static	Synchronous
Levels of synchronisation required for coherent processing	•Coherent reference carrier •Chip timing * •Data bit timing	•Coherent ref carrier •Chip timing •PN code phase •Data bit timing
Current TB_s limit (B_s=3-10 MHz)	~1000†, ≲500 typical limited by achievable delay (Chapter 3)	$\gtrsim 10^4$ achievable, practical limitation on accuracy only[38].

* Not required in SAW AMF, Chapters 3, 4

† SAW AMF, Chapter 3

Note: With matched filtering the data bit duration, $T = nL/B_s$, $n = 1,2,3,..$ for correlators usually $T<L/B_s$

For most spread spectrum multiple access systems with approximately equal power signals at the receiver, the "noise" is quasi-stationary and approximately white[42]. In addition, Mayher[42] has shown that for signals with large TB_s, Gaussian output statistics can be assumed for a linear matched filter receiver (or correlator). These assumptions are important in practice since: the matched filters take a simple form, being synthesised according to equations 2.3, 2.4; prewhitening filters[40,41,59] which are not optimum for all conditions, are not required; and error probability calculations are well known for Gaussian noise statistics[57].

The *maximum* output SNR (ρ_o) is given (see Raemer[59], p177, and Turin[41]) by:

$$\rho_o = \frac{2E}{N_o} \qquad \ldots 2.11$$

where, N_o is the double sided input noise spectral density (assumed constant white). Thus ρ_o depends only on the *total* signal energy E, and not on the signal duration, waveform or bandwidth.

One further basic result relates the peak output signal-to-noise power ratio to the average input signal-to-noise power ratio, ρ_i:

$$\rho_o = \frac{2E}{N_o} = 2B_sT\rho_i \qquad \ldots 2.12$$

where B_s is the signal bandwidth, hence

$$\rho_i = \frac{E}{B_sN_oT} \qquad \ldots 2.13$$

The factor B_sT is recognised as the bandwidth expansion factor of Section 2.2. For *fixed* signal energy and signals corrupted by *white* noise there is *no processing gain advantage* in bandspreading. Any increase in B_s is compensated for by an equal decrease in ρ_i. However, an increase in the resolvability of signals in a channel suffering multipath transmission is obtained and, in radar applications target spatial resolution is achieved. Similarly, increasing T with fixed E, lowers ρ_i by the same ratio.

Full processing gain is achievable if the interference is *bandlimited* white noise with *fixed* total power spread over the signal bandwidth, B_s. As B_s is increased, ρ_i *increases* since the interference power spectral density decreases until the total thermal noise power becomes comparable with the total interference power;

compare with equation 2.23. In systems without overall relative power control it is generally difficult to determine ρ_i precisely, due to differences in received power from widely distributed transmitters.

Two general cases of relative interference to signal bandwidths, B_I, B_s respectively, were investigated by Mayher[42]; giving the effective processing gains for coherent and noncoherent reception, Ga, G_i' respectively, as:

$$1.\ B_s \geqslant B_I,\ G_p \doteq 2G_p' = \frac{2B_sT}{\text{sinc}^2(x)} \qquad \ldots 2.14$$

where $x = \frac{\Delta\omega}{2B_s}$ is the radian frequency difference between desired signal and interfering signal carriers.

$$2.\ B_s < B_I,\ G_p \doteq 2G_p' = \frac{2B_IT}{\text{sinc}^2(y)} \qquad \ldots 2.15$$

where

$$y = \frac{\Delta\omega}{2B_I}$$

Two important points emerge:

(a) from equation 2.14, $\Delta\omega$ effectively determines G_p indicating the potential usefulness of frequency hopping techniques.

(b) where $B_s < B_I$, (2.15) the effective processing gain increases in direct proportion to B_I for fixed total interference power because the interference spectral density decreases. This points to the possibility of coexistence between wide and narrow band transmissions, allowing a situation where spread spectrum modulation might be used, for example, as an emergency signaling technique without disrupting the narrow band transmissions. These factors are discussed in the next section.

2.5 SPREAD SPECTRUM SYSTEM CHARACTERISTICS

Spread spectrum techniques provide the potential capability of:

Cochannel multiple-access, by employing non-correlated wideband signals; some degree of jamming immunity; a selective calling capability by assignment of characteristic signals; and through the large signal bandwidths employed: an accurate navigation facility for mobile operation; and some degree of multipath tolerance.

2.5.1 Multiple Access and Spectrum Utilisation

Spread spectrum techniques use available bandwidth and time in a cooperative manner overcoming many of the problems associated with frequency division multiple access (FDMA) and time division multiple access (TDMA) in providing reliable links for large numbers of *uncoordinated* simultaneous users.

FDMA techniques have been widely used because of the low equipment costs involved. Several Air-Traffic Control (ATC) subsystems[36] employ FDMA, examples being the Instrument Landing System (ILS), Distance Measuring Equipment (DME) and the newer Microwave Landing System (MLS).

In implementation, the channel is subdivided into nonoverlapping, narrow frequency bands. These narrow bands are assigned to avoid line-of-sight interference; when ground stations are in close proximity and to avoid excessive dynamic variations in channel loading.

One of the biggest problems of FDMA is the cross-talk level encountered when the channel has a nonlinear amplitude characteristic (eg a hardlimiting satellite repeater[60]). Intermodulation products are produced and a careful choice of a frequency plan[61] is necessary to avoid them. This frequency plan results in considerably more bandwidth being required than for a linear channel.

TDMA provides multiple access of many subscribers without causing mutual interference. This is achieved by constraining each subscriber to transmit in allocated time slots thus eliminating signal overlap at intended receivers. Computer-determined channel assignments can minimize idle channel time. However, signal identification by time of arrival measurement suffers from uncertainties in transmission delay time and the predominant problems encountered are:

(1) extra channel time is required to ensure TDMA channel allocations;

(2) excess hardware is required to participate in a structured TDMA net, and;

(3) long delays are encountered in accessing the channel.

One of the advantages of spread spectrum multiple access (SSMA) systems is the identification of transmitters (or receivers) by their characteristic signatures (or receiver addresses). The number of potential multiple access discrete address[43,54] (MADA) system users is dictated by the available number of uniquely identifiable signatures. The choice of signature format is dependent on the operational requirements of the system. For example, code division multiple access systems which allocate a different PN spreading code to each user are not directly suitable for mobile communications[43,56].

Combinations of weak signals from distant transmitters and strong signals from close-in users can easily prevent reliable communication as the link dynamic range (typically 30 dB) is easily exceeded[43]. However, if repeating stations (eg satellites) are used, code division multiple access is achieved by equalising signal powers at each receiver through control of each transmitter up-link (ground-satellite link) power. The total multiple access system data rate can be estimated for satellite communication by modifying an expression for practical channel capacity derived by Costas[62] and making use of the spectrum utilization arguments used both by Costas[62] and Kepcke[63].

The basic expression derived from an examination of practical M-ary transmissions can be written:

$$R = \frac{B_s}{\rho_o} \cdot \frac{S_D}{N} \qquad \ldots 2.16$$

where R is the practical channel capacity in bits/sec, B_s equals the signal and total channel bandwidth, S_D is the received (desired) signal power, N is the total noise plus interference at the input, ρ_o is the effective signal-to-noise ratio at the output of a matched filter receiver with non-coherent detection; where $\rho_o \gtrsim 15$ dB for error rates $\lesssim 10^{-5}$, with binary FSK signaling.

The fraction of the satellite power which comprises the desired signal power (S_D) is given by

$$S_D = S(S_U/S_T)\mu \qquad \ldots 2.17.$$

where S is the effective received power, S_T the total power at the satellite receiver, S_U the uplink power per ground station, μ is the loss factor due to hard limiting, $0.25 \leq \mu \leq 1$. The ratio of S_T to S_U following Kepcke[63] is given by:

$$S_T/S_U = 1 + \alpha(K-1) + (2B_s N_u/S_u) \qquad \ldots 2.18$$

where α = "activity factor", K = total number of stations, $2B_s N_u$ = satellite receiver noise power with N_u equal to the satellite receiver noise power density (Watts/Hz). The total noise power at the ground receiver is

$$N = 2B_s N_o + S(1-(S_u/S_T)\mu) \qquad \ldots 2.19$$

This is comprised of ground receiver self noise of density N_o (Watts/Hz) and clutter (other users) plus satellite receiver noise.

Thus, the signal to noise ratio at the input to the matched filter is

$$\frac{S_D}{N} = \frac{S(S_u/S_T)\,\mu}{2B_s N_o + S[1-(S_U/S_T)\mu]} \qquad \ldots 2.20$$

Substitution into equation 2.4 yields

$$R = \frac{B_s}{\rho_o} \cdot \frac{S(S_u/S_T)}{2B_s N_o + S[1-(S_u/S_T)]} \qquad \ldots 2.21$$

with (S_u/S_T) given by equation 2.18. Now, in a practical situation the assumption that sufficient power is available from the ground terminal transmitters to effectively saturate the satellite TWTs is valid. Thus, the ratio (S_u/N_u) is large. Further, the number of users, K, is also large with the result that $\alpha K > 1$. With these assumptions equation 2.18 becomes

$$S_T/S_u = \alpha K \qquad \ldots 2.22$$

and therefore, the practical channel capacity equation reduces finally to

$$R = \frac{B_s}{\rho_o} \cdot \frac{S_\mu}{\alpha K(2B_s N_o + S)} \qquad \ldots 2.23$$

Equation 2.22 shows that if the rf bandwidth is increased a "thermal noise" limited regime is encountered where the total clutter power becomes comparable with the receiver noise power. In this region, with control of uplink power levels, code division multiple access systems perform well. However, if $2B_s N_o$ is less than S, the clutter dominates. In this situation, coordinated ie, (TDMA or FDMA) systems perform more optimally than direct PN spread spectrum systems. However, broad band systems can offer a greater channel capacity if the "activity factor", α is small[62] this leads to systems using PN time hopping and frequency hopping[38] and combinations of the two techniques. Also, some experimental evidence exists for the possibility of transmitting both SSMA and a small number of FDMA signals over a satellite link[60] power balancing is required, but further development could prove important both for system flexibility and optimum channel utilisation.

In frequency hopping, interference from unwanted signals is produced when a frequency component of the "de-hopped" unwanted signal falls in the receiver IF passband[38]. Two situations can give rise to this:

(1) when the receiver code introduces a frequency shift coinciding with a frequency shift in the unwanted signal.

The frequency of occurrence is a measure of the correlation between the PN codes determining hops.

(2) when the channel amplitude characteristic is nonlinear giving rise to intermodulation products as in the FDMA situation.

These problems could be reduced by applying a direct PN modulation to each frequency hop at the expense of increased bandwidth. Here, each transmission is characterised by two identifying codes:

(1) the frequency-hop code, and

(2) the (short) PN code impressed on each carrier.

Matched filter[41] detection could be usefully employed to detect the short PN code and, with surface acoustic wave devices, it would be economically favourable in terms of power consumption and equipment complexity to duplicate this matched filter in each channel as discussed by Collins and Grant[64] and implemented by Burke[58].

An important MADA technique uses specific pulse patterns in time and frequency to allow random access by allocating a unique pattern to each receiver[43,54]. This pattern constitutes the receiver address, rather than precede the message as with standard multiplexed signals. The whole address pattern can, for example, be pulse position modulated or delta modulated for voice transmissions[43] while data transmission can be achieved by M-ary signaling techniques[65] (see Chapter 5). In this case, a receiver is allocated M quasi-orthogonal addresses corresponding to 2^k data bit combinations, taking k-bits at a time. Matched filters prove optimum in decoding the address data and modulation. Implementations of modems for random access, discrete address (RADA) links are described in Chapter 5 and evaluation of OOK RADA in Chapter 6.

2.5.2 Jamming Resistance

In order to jam a communication link effectively, the interfering signal must have a power per unit bandwidth comparable to that of the desired signal. Jam resistance may, to some extent, be provided by "brute force" techniques, such as maximising the effective radiated power, and restricting antenna coverage. However, it can be shown in analogy with eqn 2.22, that spread spectrum transmissions place the jammer at a power disadvantage equal to the receiver processing gain if arbitrary jamming signals are used. The processes of jamming and anti-jamming are limited only by the complexity and expense of the equipments involved.

2.5.3 Multipath Resolution; Protection Against Signal Fading

Frequency selective fading occurs[57] when signals are received from two or more transmission paths simultaneously. This is known as multipath or multimode propagation. These paths may arise due to:

the multiple reflections of skywaves at HF for long distance transmissions, tropospheric scatter at VHF and UHF and also aircraft echoes and reflections from surrounding objects (eg buildings) at UHF and above.

Typical multipath spreads for tropospheric scatter at UHF are 100 ns to 500 ns at ranges below approximately 200 mi, and up to about 5 μs at 500 mi range. Fading rates may be typically 1 per second for tropospheric scatter rising to approximately 50 per second for aircraft echoes.

The effect of multipath may be regarded as producing troughs and peaks in the channel frequency response a typical separation between selective fading troughs being 2 MHz for medium ranges and 200 kHz for longer ranges. Thus, if narrow band signals are used, they may fall

into a fading trough when a severe loss in signal-to-noise (20-30 dB) can occur for significant fractions of one second. Three important diversity techniques[66] offer protection against high error rates:

(1) space diversity, using directional antennas,

(2) frequency diversity, transmitting on two or more frequencies simultaneously, and

(3) time diversity, ie essentially message repetition.

Spread spectrum modulation possesses inherent frequency diversity.[38] If the signal spectrum is sufficiently wide that several fading troughs are spanned, some components of the signal will cancel and others reinforce. Thus, the signal is not entirely destroyed and the delayed signals are independently resolvable, with little mutual interference. The wider the signal bandwidth the smaller the resolvable time delay becomes.

As well as giving rise to fading, multipath propagation also imposes a limitation on the maximum keying rate. If data signals are transmitted contiguously in time, the pulse duration must be greater than the channel time-spread. If this is not the case, severe inter-symbol interference may occur.

2.5.4 Range Measurement

Range measurements find application in navigation[38,48] and in providing power control information for satellite communications. Direct PN modulation is an attractive technique, as signal arrival times can be measured to a small fraction of a chip duration, and multipath discrimination, multiple access and interference resistance are also obtained. Applications include both:

(1) passive navigation[36], where the differences in time of arrival of signals from four time-synchronised transmitters (eg on board satellites) enable accurate calculation of position: latitude, longitude and altitude and;

(2) active navigation where transponding beacons are employed and the user compares the relative code phase shifts in his receiver.

With a repetitive signal this is accomplished by serial search techniques. Velocity information is obtained by measuring the carrier tracking loop deviation (Doppler shift) from a reference oscillator.

2.6 SUMMARY

In most applications a "hybrid" spread spectrum signal processing system would prove optimum, amalgamating the appropriate advantages of the three main classifications:

PN: Accurate time-of-arrival measurement
Multipath tolerance by discrimination
Maximum processing gain

FH: Low speed PN code generator
Rapid acquisition of synchronisation
Multiple access by orthogonal frequency slots
Multipath tolerance by frequency diversity

TH: Multiple access by non-overlapping time slots
High bandwidth efficiency of TDMA available
Pulsed transmitter operation

The need to acquire synchronisation is the biggest disadvantage of present equipments, especially for data transmission where speed is often a prime requirement. Significant reductions in acquisition time

can be achieved with programmable matched filters. However, matched filters should find extensive applications as primary processors in systems employing short rf pulses, eg, FH, TH and RADA. Here, fully asynchronous operation proves invaluable for high rate transmission, at the expense of a signal-to-noise degradation due to the use of noncoherent detection. Also important is the waveform synthesis capability of matched filters - the impulse response is a time reversed replica of the matched signal; which can be used to generate a variety of complex waveforms. Currently, the most attractive candidate for this application is the surface acoustic wave device technology which offers passive, chip and rf asynchronous operation. Surface wave matched filters are compared with the competing microelectronic implementations in the next Chapter.

CHAPTER 3

A COMPARISON OF ANALOGUE AND DIGITAL MATCHED FILTERS

3.1 INTRODUCTION

Two basic technologies are capable of synthesising matched filters with parameters suitable for real-time processing of biphase spread spectrum signals. These technologies have produced the following devices: the SAW analogue matched filter (AMF), in both fixed coded and programmable forms; the SAW non-linear convolvers; the microelectronic analogue charge-transfer matched filters, (CTMF); and the microelectronic digital matched filter (DMF).

These devices have strictly complementary performances and the optimum implementation depends on a number of system related factors. To provide a common basis for comparison the following operating characteristics are assumed:

- received signals are down-converted to IF prior to matched filter processing;
- the matched filter operation is asynchronous;
- the device processes the whole waveform - video integration is excluded; and,
- signals are output in real-time.

Each device is analysed in turn, Sections 3.2 to 3.6, emphasis being given to the following key factors:

- current device performance data;
- fabrication and complexity;
- peripheral electronics involved in meeting the assumed link characteristics;
- a cost *estimate* for a device capable of processing a biphase coded waveform 127 chips long with a 10 MHz bandwidth.

The cost analysis assumes manufacture of ~100 off and includes materials, photomasks, processing and test. It is assumed that research and development costs are not involved. Programmability is *not emphasised* in the operation of the link however, the degree of programmability offered is noted. For this analysis the programmable AMF is regarded as being distinct from the fixed coded device in that parameter limitations derive from separate constraints. Operating principles are not documented in detail.

The final section (3.7) summarises the device comparison in three tables and a chart. Two tables give (1) a merit rating and (2) present day achievable parameters; the third table contrasts forecasted performances and the chart illustrates the key B_s, TB_s bounds. The performance forecast is based on a requirement for "acceptable" reliability and yield for fabrication standards *typical* of present-day microelectronic processing, eg electron beam resist exposure is excluded.

3.2 FIXED CODED SURFACE ACOUSTIC WAVE ANALOGUE MATCHED FILTER

3.2.1 Current Performance Data

The fidelity of SAW AMF response is determined *chiefly* by three perturbing mechanisms each giving rise to coherent spurious acoustic signals:

- multiple reflected SAW signals due to acoustic wave impedance mismatch[12,16,25,67,68] (Chapters 1, 4);
- reradiated bidirectional SAW signals due to electro-acoustic regeneration[12,16,25,67,68] (Chapters 1, 4); and,
- bulk mode conversion[67,68] by synchronous scattering from taps.

The two spurious SAW signals are sensed by taps in the array giving rise to unwanted outputs. Bulk mode generation depletes power from the surface wave producing a 'roll-off' in the impulse response.

Three different 'second-order' geometrical design approaches, illustrated in Figure 3.1, have resulted in *partial* suppression of spurious levels:

(1) the split electrode plus 'fill-in' array[27,68];

(2) the dual-tap geometry[12]; and

(3) the angled tap array geometry[69,70].

A qualitative comparison of the effect of these three geometries is given in Table 3.1; a detailed comparison of (1), (2) is presented in Chapter 4. Also included is one further technique, reported by LaRosa et al[71], which employs multi-layer metalisation to reduce wave impedance mismatch. A spurious level suppression of ~50% was claimed for a Cr-Cu-Au structure on (ST,X) quartz. A combination of these techniques may prove necessary in achieving particular performance specifications.

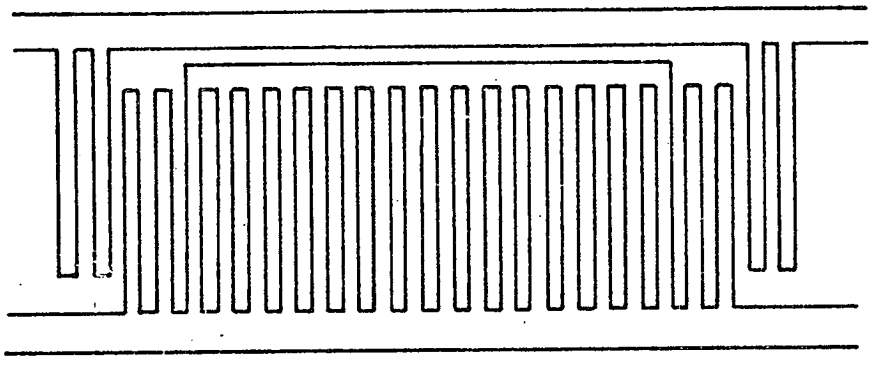

(A) SPLIT-ELECTRODE PLUS DUMMY ARRAY

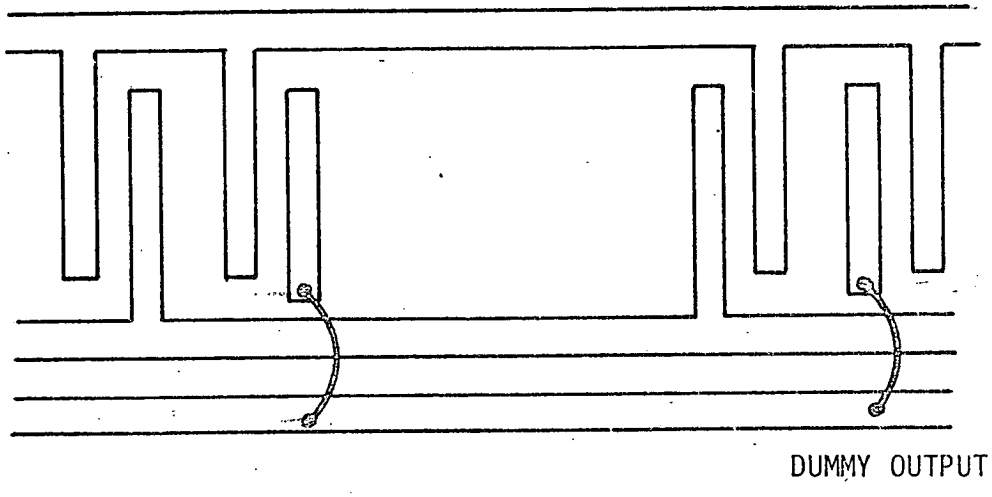

(B) DUAL-TAP ARRAY

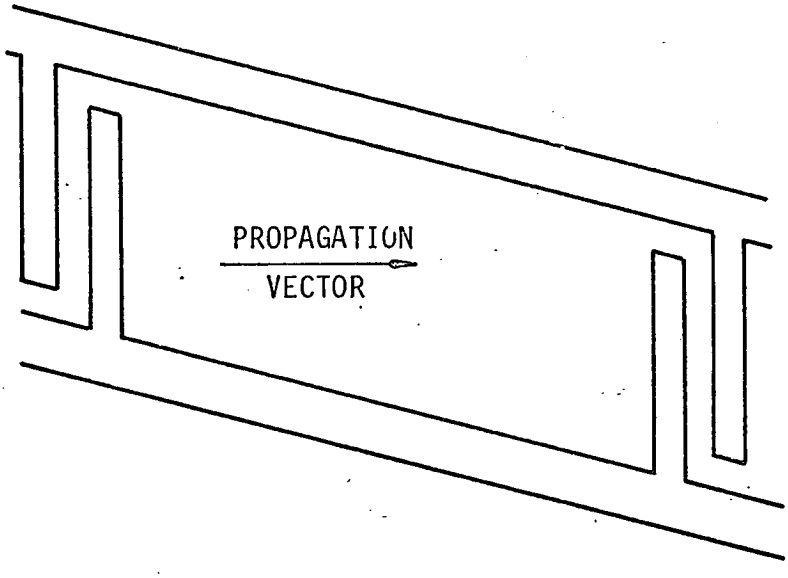

(C) INCLINED ARRAY

FIGURE 3.1 COMPARISON OF SECOND ORDER AMF GEOMETRIES

TECHNIQUE	MECHANISMS PRODUCING SPURIOUS SIGNALS			DISADVANTAGES
	wave impedance mismatch	electroacoustic regeneration	bulk mode generation	
Split-electrode geometry	Theoretically complete cancellation	No effect *	Occurs out of band, at 2X original frequency	Higher photolith resolution required for given bandwidth
Dual-tap array	Large cancellation	Large cancellation	Increased	Higher interconnect complexity
Angled tap array	Spurious not detected	Spurious not detected	Low roll-off impulse response	Potentially higher insertion loss. Larger area required.
Multi-layer metallisation	Reduced by 50%	No effect *	Reduced	Increased fabrication complexity

* Reduced by lowering output load resistance - increases insertion loss

TABLE 3.1 COMPARISON OF AMF DESIGN TECHNIQUES FOR SPURIOUS SIGNAL REDUCTION

CONSTRUCTION AND SUBSTRATE	B_s (MHz)	f_o (MHz)	TB_s	PERFORMANCE			REFERENCE
				δ(P/S) (dB)	Spurious level (dB)	CW IL (dB)	
Split-electrode lithium niobate (ST,X) quartz	5 10	30 120	127 127	~1 ~0.5	<-30 <-30	25 40	68
Dual-tap (ST,X) quartz	5 5 10	127 127 118	13 31 127	~1 <1 ~2	-30 <-30 <-30	55* 55) ~60)	12 Chapter 4
Angled tap array (ST,X) quartz Lithium niobate	76.8 50	12.8 200	127 127	<1 ~2	<-25 --	65 --	69 70
Multi-layer metal (ST,X) quartz	10	60	1010	~2	--	110†	71,74

Key: B_s, bandwidth; f_o, centre frequency; TB_s, time-bandwidth product equals no of taps; δ(P/S), peak-to-max sidelobe degradation; CW IL, insertion loss to CW signal at f_o; *, IL to one tap; †, unmatched.

TABLE 3.2 PERFORMANCE DATA FOR RECENT AMF DESIGNS

Typical fractional 3 dB bandwidths, with <1 dB passband ripple, <10 nsec group delay variation and input IDT conversion loss 6-8 dB, are ~40% on lithium niobate[26], ~9% on (ST,X) quartz[72], ~12% on (Y,X) quartz[72] and estimated as ~25% on bismuth germanium oxide.

Yields obtainable with conventional photolithography limit the maximum practicable synchronous frequency on quartz and lithium niobate for large area arrays of *split-electrode* taps to ≲250 MHz. On bismuth germanium oxide the corresponding limit is ~130 MHz. With the other array configurations this limit is approximately doubled. Allowable diffraction losses[31] and required time-bandwidth products determine the low frequency limit of ~20 MHz.

Maximum delays obtainable for a single array on *one crystal surface* are approximately 80 μsec for quartz and lithium niobate, and 150 μsec for bismuth germanium oxide; with readily available crystals now ~25 cm long[73]. An AMF with 102 μsec delay on (ST,X) quartz was obtained by Vasile and LaRosa[74] using a 'wrap-around' geometry.

The dynamic range of an SAW AMF receiver is determined by the onset of nonlinear effects at high acoustic power levels (~20 dBm) and by IF amplifier noise figures, (~2 dB). With an insertion loss to the correlation peak typically 20 dB, the dynamic range is approximately 90 dB before demodulation.

Degradations in performance as a function of temperature change (ΔT) have been computed by Carr et al[46]. For example, a 3 dB degradation in peak-sidelobe ratio is obtained for $\Delta T \simeq 4°C$ on lithium niobate and $\Delta T \approx 100°C$ on (ST,X) quartz assuming $B_S T = 127$ and *seven wavelengths* between taps at 70 MHz, (see Chapter 4).

Table 3.2 gives performance data for recently reported designs using the improved configurations outlined in Figure 3.1 and Table 3.1.

3.2.2 Fabrication and Complexity

Processing techniques developed from those used in integrated circuit (IC) manufacture enable high yield fabrication of a large range of current AMF designs. Key limitations arise in photomask production, substrate growth and preparation and photolithographic reproduction.

A photo-master is composed at final size using the step and repeat technique. Currently, this process is capable of ~1 μm line-widths over a 6 mm square field with placement accuracies typically ~0.1 μm and 0.25 μm for laser interferometer and Moire fringe counting equipments respectively. Phase coding may be incorporated in the mask design using one of several simple techniques, see Chapter 4.

Large (~25 cm), optically homogeneous and accurately aligned (±0.1°) single crystals are available in the commonly used substrate materials[73]. Optical quality polishing (~0.12 μm centre line average surface finish) is a long procedure requiring supervision by skilled personnel.

Thin (1000-3000 Å) uniform metal films are readily obtained by various vacuum deposition techniques. Conventional 'contact' photo-lithography and chemical etching allows production of electrode widths down to ~3 μm over areas up to ~7 cm square with good yield. Lift-off techniques[75] are capable of obtaining electrode widths as low as ~1 μm and when used in conjunction with conformable masks *high yield*, high resolution and large area coverage have been demonstrated[75].

3.2.3 Necessary Peripheral Hardware

The necessary peripheral hardware comprises:

- A two section wideband input matching network designed for minimum insertion loss with low group delay variation.
- A noncoherent demodulator at the AMF output to present video signals to subsequent decision circuitry.

3.2.4 Cost Analysis

A simple cost analysis prices a preprogrammed AMF with 127 taps operating at 10 MHz chip rate at approximately £150.

3.3 PROGRAMMABLE SURFACE ACOUSTIC WAVE ANALOGUE MATCHED FILTER

3.3.1 Current Performance Data

The extent of SAW AMF programmability achieved by current techniques is limited to the selection of biphase waveforms having equal bandwidths (B_s) and TB_s products. In general, AMF recoding is accomplished by switching the connections from each tap to the rf summing busses. The polarity of individual taps is determined by the state of corresponding stages of an adjacent serial code store, Figure 3.2.

A number of tap and switching circuit configurations have been suggested, as described in a recent review by Staples and Claiborne[76]. To date, the most advanced programmable AMF designs have resulted from hybrid fabrication techniques using either diode-ring phase switches or single-pole single-throw (SPST) configurations to select tap phase, Figure 3.3.

EDINBURGEN EX BIBL UNIV.

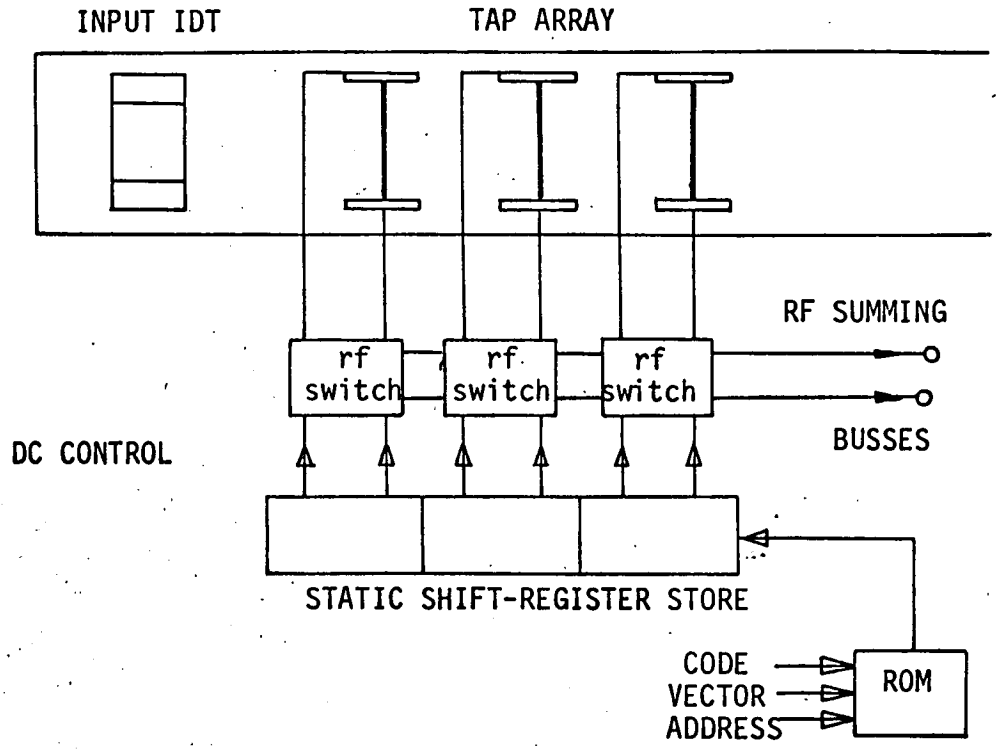

FIGURE 3.2 ESSENTIAL FEATURES OF PROGRAMMABLE AMF

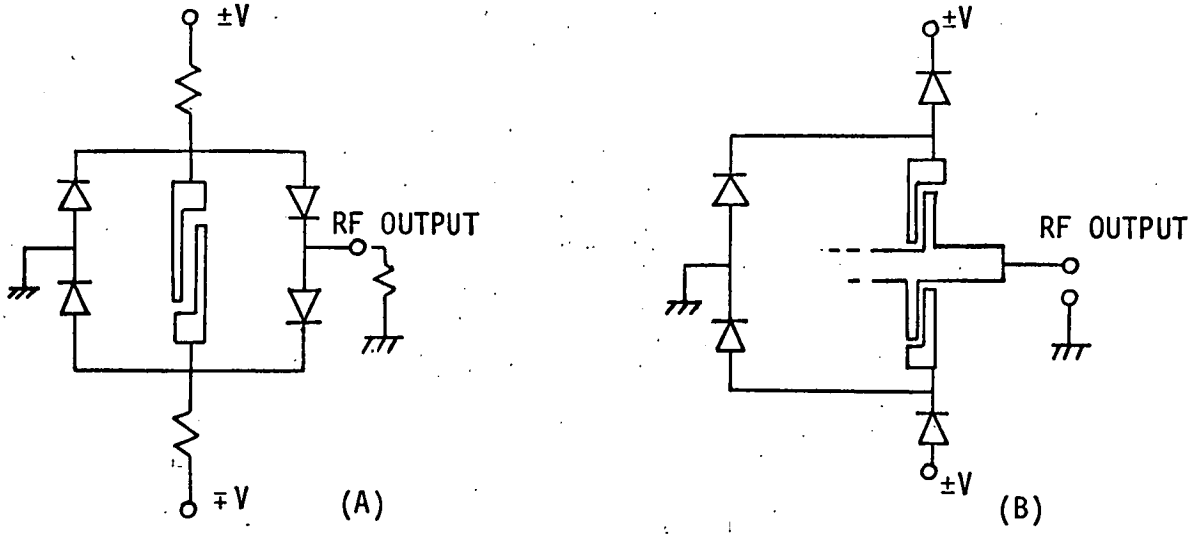

FIGURE 3.3 (A) QUAD-DIODE PHASE SWITCH APPLIED TO A SINGLE IDT TAP, AND (B) DIODE ARRANGEMENT FOR SPST ON-OFF SWITCHING OF A SINGLE TWO-IDT TAP

The performance of programmable AMFs is determined: firstly, by the factors influencing the fidelity of the fixed coded device; and secondly, by the rf switch performance. In principle, the methods described in Section 3.2.1 for reducing spurious levels apply equally to the SAW component of the programmable device. Switch performance depends mainly on the circuit configuration and the parameters of the diodes used. A key design parameter is the ratio of diode reverse-bias junction capacitance (C_D) to tap capacitance (C_T) which effectively determines the shunt loss of the diode ring circuit and the isolation of the SPST switch[76]. With tap capacitances typically 0.3 pF a diode capacitance $\lesssim$0.05 pF is required[76,77] for low shunt losses ($\lesssim$3 dB) and high isolation (>20 dB) for AMFs with TB_s ~150. The ratio C_D/C_T becomes increasingly important as TB_s increases.

Hagon et al[77] have reported a hybrid structure comprising a 128 tap AMF fabricated on (ST,X) quartz adjacent to 8 silicon-on-sapphire (SOS) 16 stage p-channel MOS shift registers with parallel buffer stores controlling low capacitance (~0.02 pF) SOS diode-ring switches. The major objection to this type of arrangement is the requirement for a large number of stitch bonds carrying rf signals. An improved method of fabrication, taking high performance SAW programmable AMFs nearer total integration, was recently reported by the same team[78]. The device comprised a 63 tap AMF on an aluminium nitride film grown on sapphire and integrated with SOS diode ring switches and rf summing busses. The SOS programming circuits were arranged as before and the bond wires between code store and switches carried *only bias currents and not rf*. Table 3.3 gives parameters and performance details of these two devices. Also included are

details of a hybrid-thin film pin-diode SPST switching circuit and (ST,X) quartz SAW tapped delay line[79].

TABLE 3.3 PROGRAMMABLE AMF COMPARISON

CONSTRUCTION	B_s (MHz)	TB_s	δ(P/S) (dB)	CW IL (dB)	POWER* CONSUMPTION (mW)		REF
					SWITCH	STORE	
Hybrid: (ST,X) quartz, SOS	10	128	<-2	67	<1	~8	77
Hybrid: AℓN, SOS	20	63	--	--	<1	~8	78
Hybrid: (ST,X) quartz, pin thin film, TTL	10	31	-4	74	0.75	~10	79

Key: *, per tap

3.3.2 Fabrication and Complexity

Hybrid construction represents the only means *presently* available for realising large TB_s product ($\lesssim$200) programmable AMFs. Integrated or thin film techniques are mandatory in achieving low capacitance diode circuits compatible in size with tap spacings to avoid large fan-out. Hagon et al[78] demonstrated the feasibility of integrating SAW AMF and diode switches with a *high development cost* aluminium nitride and silicon on sapphire process. This device also featured an 8 die SOS MOSFET code store designed to align with the switching circuits and resulting in short stitch bonds between substrates. In comparison, Lambert et al[79] reported a 31 tap AMF on (ST,X) quartz abutting with SPST 0.05 pF beam lead diode, and thin film resistor switching networks on glass, fanning out on printed circuit board to a TTL serial code storage register.

The need for reliable wire bonds between multiple substrates and state of the art integrated SOS circuit design limits bandwidths to below ~30 MHz and TB_s products to below ~200.

3.3.3 Necessary Peripheral Hardware

An external code generator is required to update the device shift-register store. The remaining hardware, with the exception of a power supply, is identical to that detailed in Section 3.2.

3.3.4 Cost Analysis

The works cost of a programmable AMF is estimated at £2000 for both hybrid SOS IC and thin film approaches when produced in small quantities[79].

3.4 SURFACE ACOUSTIC WAVE NON-LINEAR CONVOLVERS

3.4.1 Current Performance Data

Parametric interactions between contra-directed, colinear surface acoustic waves have been used to obtain the convolution[34,80] of signal [s(t)] and reference [r(t)] waveforms at rf. The device behaves as a linear filter with an impulse response determined by r(t). Matched filtering is achieved by arranging r(t) to be a time reversed[13,14] replica of s(t), equation 2.3. However, the output signal obtained differs from the true correlation function in compressing the time scale[80] by a factor of 2. Further, the convolver is not inherently asynchronous since complete correlation is obtained only when the signal and reference acoustic waveforms are launched in time-slots which allow total overlap. Morgan et al[81] have demonstrated a technique for obtaining asynchronous operation which involves a 50% duty cycle pulsed reference signal and an output gating signal. The penalty incurred is a reduction in the *maximum signal duration* to *one half of the propagation delay under the parametric port* (T_p). This requirement

limits the maximum TB_s product obtainable with any convolver configuration. In addition extra circuitry is required to recover real-time information.

Three different non-linear phenomena based on: substrate non-linearity[80]; semiconductor charge carrier - rf field interactions[34]; and junction diode *I-V* characteristics[79,82] have resulted in devices *potentially capable* of high fidelity matched filtering of *large* TB_s (>500) signals. For a wide range of input power levels a bilinear relationship is exhibited between the output power (P_o) and the two input powers (P_s, P_r). The *external* bilinear coefficient (C_E) is an important parameter in device assessment[34]. An *internal* bilinear coefficient (C_I) allows comparison between the various parametric interactions employed[34]. The bilinear coefficients are:

$$C_E = \ell.C_I \triangleq \ell.P_o(P_{ar}.P_{as})^{-1} \qquad \ldots 3.1$$

where ℓ is a loss factor and P_{ar}, P_{as} are the *acoustic* reference and signal powers; usually measured in mW and conveniently expressed in dBm.

The acoustic convolver, described by Luukkala and Kino[80], employs a weak parametric interaction described *empirically* by the fundamental constitutive equations characterising third order non-linear piezoelectric dielectrics[83]. Several substrate materials have been compared[84] with the conclusion that lithium niobate ($LiNbO_3$) offers the best combination of coupling strength and achievable time-bandwidth product.

Two modes of operation[80] are possible with this nonlinear effect:

(1) Degenerate, (see Chapter 4); where the received signal s(t) and the reference r(t) are on the same carrier frequency, ω_o.

Over the interaction region, a stationary (zero wavenumber) electric field is produced at frequency $2\omega_0$. This parametric signal is spatially invariant at the correlation instant and is conveniently sensed by uniform electrodes deposited directly on the upper and lower crystal surfaces. Figure 3.4 shows the essential features of the device geometry. Other signals at $2\omega_0$ are spatially periodic and are eliminated by the integrating effect of the output electrode.

(2) Non degenerate; where s(t) and r(t) are on carriers at ω_1 and ω_2. The parametric signal at $[\omega_1 + \omega_2]$ is sensed by an interdigital structure with a periodicity given by $2\pi \ v_s / |\omega_1 - \omega_2|$, where v_s is the SAW propagation velocity. Both frequency filtering and the spatial filtering action of the output electrode select the desired signal. Figure 3.5 illustrates the configuration.

The basic degenerate acoustic convolver is inefficient with a typical C_E value of -95 dBm for lithium niobate. Thus, with maximum P_s and P_r values of ~27 dBm, the dynamic range is typically 50 dB when a 20 MHz bandwidth amplifier is used at the output.

Spurious signals arise from three main effects:

- transduction of travelling wave second harmonic signals at the *edges* of the plate, produced by the medium nonlinearity; [16,32,34]
- the convolution of second transit signals produced by reflections from opposing input ports; and,
- launching bulk waves in the thickness direction.

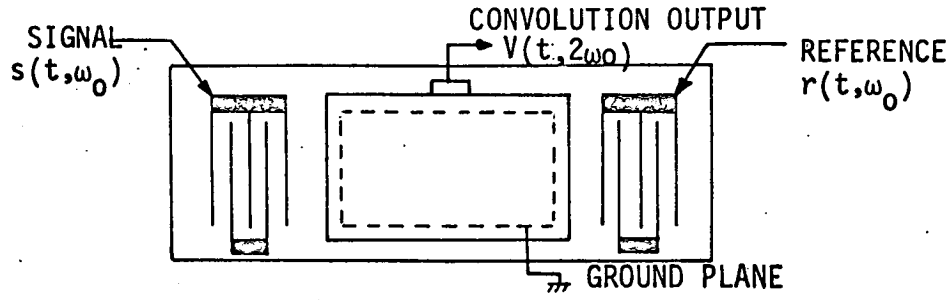

FIGURE 3.4 SAW DEGENERATE CONVOLVER CONFIGURATION

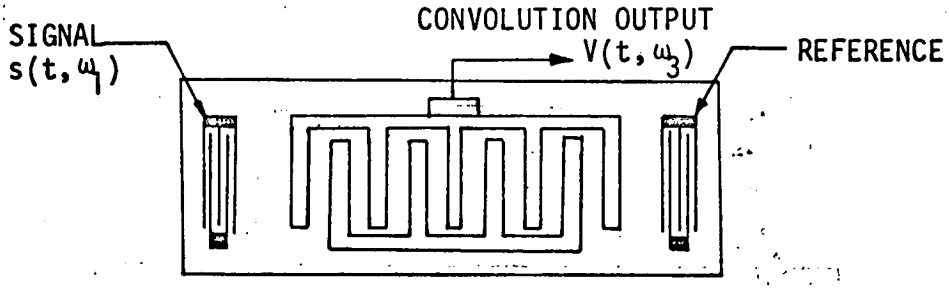

FIGURE 3.5 NONDEGENERATE ($\omega_1 \neq \omega_2$) SAW CONVOLVER

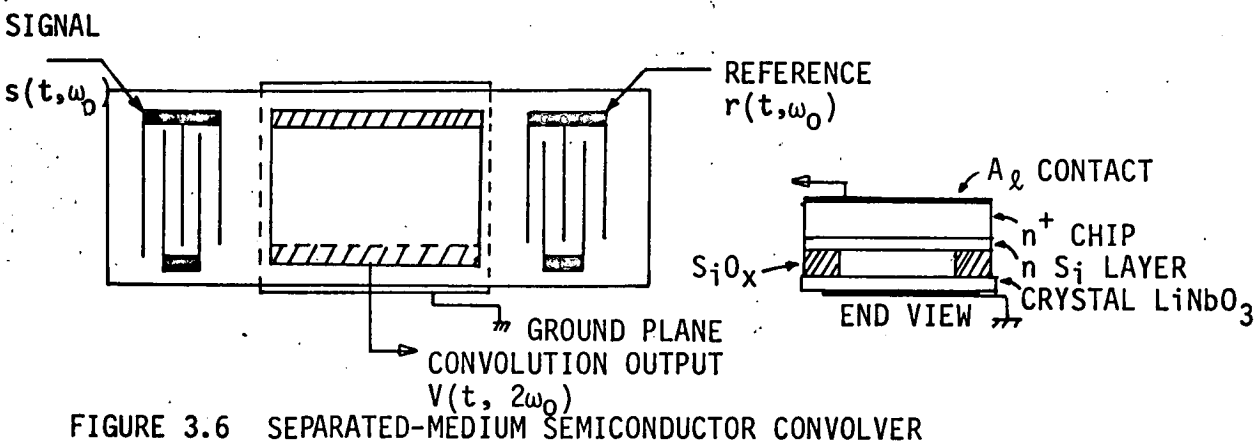

FIGURE 3.6 SEPARATED-MEDIUM SEMICONDUCTOR CONVOLVER

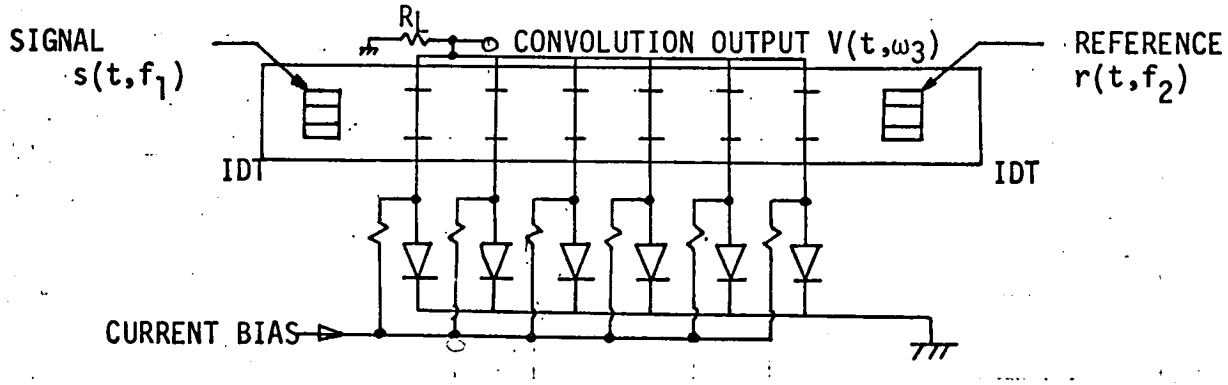

FIGURE 3.7 NONDEGENERATE DIODE CONVOLVER ARRANGEMENT

Reduction of the first type of spurious to <-35 dB is readily achieved[85] by inclining the plate edge from normal incidence, or by indenting the edge of the plate; both techniques are designed to achieve phase cancellation across the spurious wavefront. The second spurious mechanism can be suppressed using multi-strip unidirectional transducer arrangements[86] which result in IDT's with low acoustic reflection coefficients. Finally, the bulk mode signals can be scattered by using a wedge-shaped crystal or by cutting grooves in the lower surface[85].

The non-degenerate convolver is more efficient, C_E increased by ~14 dB, since the interdigital structure senses the parametric signal at the surface where the interaction occurs. Further, the output spurious levels due to second harmonic travelling waves are designed to fall outside the output bandwidth and reflected signal levels are low since the input IDTs are synchronous at different frequencies. However, one reported[34] problem with the non-degenerate structure is bulk mode conversion at the parametric electrode. This coupling has been reduced by separating the crystal surface and electrode structure with a thin (2000 Å) silicon dioxide layer[34]. Values of C_E equal to -81 dBm and C_I of -66 dBm have been demonstrated[34] with a tuned output.

Other non-linear mechanisms have resulted in increased parametric efficiencies. In particular, *significant* improvements have been obtained by employing:

(1) the nonlinear response of a homogeneous semiconductor[34] layer coupled to the rf fields associated with SAW motion; and

(2) the nonlinear current-voltage characteristics of junction diodes connected to delay line taps[79,82].

In the first configuration a uniformly doped semiconductor is placed in close proximity to the surface of a piezoelectric, Figure 3.6. Lithium niobate and bismuth germanium oxide are suitable substrate materials since the strong electromechanical coupling and high relative permittivities minimise losses[34]. With transverse field interactions[34], which give minimal SAW attenuation, the semiconductor behaves essentially as a distributed varactor and has yielded ~30 - 40 dB improvements in C_E compared with the basic device.

The non-degenerate diode convolver of Reeder and Gilden[82] comprises a tapped delay line which samples the linearly superimposed, contra-flowing signal and reference. Each tap is connected to a common load, through a forward biased diode, Figure 3.7, which squares the signal sample. The resulting rf load current contains components at $2\omega_1$, $2\omega_2$, $(\omega_1 + \omega_2)$, $(\omega_1 - \omega_2)$ and ω_1, ω_2. Non-degenerate operation is essential *with the circuit arrangement shown* because it enables filtering of the input harmonics. The taps are positioned so that $\Delta t|f_2 - f_1|$ is a non zero integer[82], where Δt is the tap-tap delay, and f_1 and f_2 are the input carrier frequencies. The effects of the tap sampling are twofold: firstly, the output waveform is subject to distortion[82,88]; and secondly, the maximum bandwidth is limited by the physical size of the diode circuitry. This latter restriction will eventually lead to monolithic fabrication techniques in common with the programmable AMF, Section 3.3.

Typical present-day performance data, comparing the various convolver arrangements discussed, is given in Table 3.4. The principle advantages and disadvantages of convolvers are summarised over:

TABLE 3.4 REPORTED PERFORMANCE DATA FOR CURRENT SAW CONVOLVERS

CONVOLVER TYPE	B_s (MHz)	T_p (μs)	TB_s*	C_E (dBm)	DYNAMIC RANGE (dB)	SPURIOUS (dB)	REF
Acoustic Degenerate ($LiNbO_3$)	20 20	6 4.5	60 45	-95	~50†	-40	34 85
Non degenerate ($LiNbO_3$)	30	6	90	-81	~64†	--	34
Separated semi-conductor $Si/LiNbO_3$	~20 65	~5 9	50 ~290	-64 -62	~84† ~70	-- --	34 87
Diode	10 1.4	3 16.8	15 12	-41 -40	~80 70 #	~-40 -40	85 88

* For asynchronous operation, † calculated for 27 dBm input powers, # saturates for P_s, P_r ≃20 dBm

ADVANTAGES

- High degree of programmability
- Potentially large bandwidth (~100 MHz) and large TB_s (>3000, *not* Diode type)
- Not significantly affected by temperature effects or SAW propagation attenuation

DISADVANTAGES

- Insertion loss inherently higher than AMF
- An input reference waveform is required
- Complex peripheral circuitry required for asynchronous operation
- Asynchronous operation halves the potential TB_s product

3.4.2 Fabrication and Complexity

The basic degenerate acoustic device has a simple structure, so that mask making and photolithogrpahy are relatively straightforward. Since only two IDTs with fine resolutions are required a slightly higher centre frequency may be obtained for the same yield. The non-degenerate convolver requires an SiO_x layer[34,88] hence device fabrication is more difficult for large T_p.

The semiconductor convolver either requires deposition of SiO_x spacers[34,88] or ion beam etching of small supports in the crystal surface[87] and a means of ensuring mechanical rigidity. Further, the task of producing long narrow strips of semiconductor is not trivial. The semiconductor surface is subject to contamination and the structure is sensitive to thermal shock. It is difficult to achieve stable, reproducible results for $T_p > 10$ μs.

The diode convolver is limited by the closest tap spacing achievable and the circuit yield, as for the programmable AMF, but is however a much simpler sircuit. A bandwidth of 30 MHz is currently feasible with ~200 taps.

3.4.3 Necessary Peripheral Hardware

- High power (~1 watt) input amplifiers with ~40% bandwidths.
- Input and output bandpass filters to remove harmonics and to increase the rejection of direct leakage from input ports.
- Reference waveform generator.
- For asynchronous operation a repetitive unity mark-space ratio reference and an output gate[81]. Real-time processing requires a time-expander[85].

3.4.4 Cost Analysis

The cost of the SAW component is estimated to be in the region of £70 using lithium niobate or bismuth germanium oxide. This is the basic cost of the acoustic convolver. The separated semiconductor configuration is expected to cost an additional £50 and the diode convolver, with hybrid Schottky diodes, a further £180. Peripheral electronics for asynchronous operation, real-time recovery, amplifiers, reference generator and filtering is expected to add £250 to the overall cost.

3.5 CHARGE-TRANSFER ANALOGUE MATCHED FILTERS

3.5.1 Current Performance Data

Two basic techniques exist for implementing *analogue* shift registers for time sampled baseband signals; namely, the bucket-brigade device[90] (BBD) and the charge coupled device[91] (CCD).

A BBD stage consists of a transistor (FET or bipolar) switch having an enhanced Miller capacitance, on which signal samples are stored. These samples are periodically shifted from one capacitor to the next by clocking the transistor switch. In the simplest arrangement, Figure 3.8a, two phase clock pulses are required and alternate stages, half-bit stores, contain a signal sample. Tapping is achieved through conventional circuit techniques[92], Figure 3.8b.

The second member of the charge-transfer family, the CCD, operates by storing minority carriers in the inversion regions under an array of biased metal-insulator-semiconductor capacitors. The signal sample, which is proportional to the stored charge, is moved through the array by translating the inversion regions to adjacent electrodes using multiphase clocks, Figure 3.9. Charge packets are usually injected into the device using a reverse-biased p-n junction diode which provides a supply of minority carriers and a gate electrode which controls the flow of carriers to the register.

Tapping has been achieved by sensing the charge flow to one set of clock electrodes. Binary coding is accomplished by simultaneously driving the '1' and '-1' coded clock electrodes independently, then the difference between the total charges flowing to the binary coded electrodes is a measure of the correlation between the shifted signal

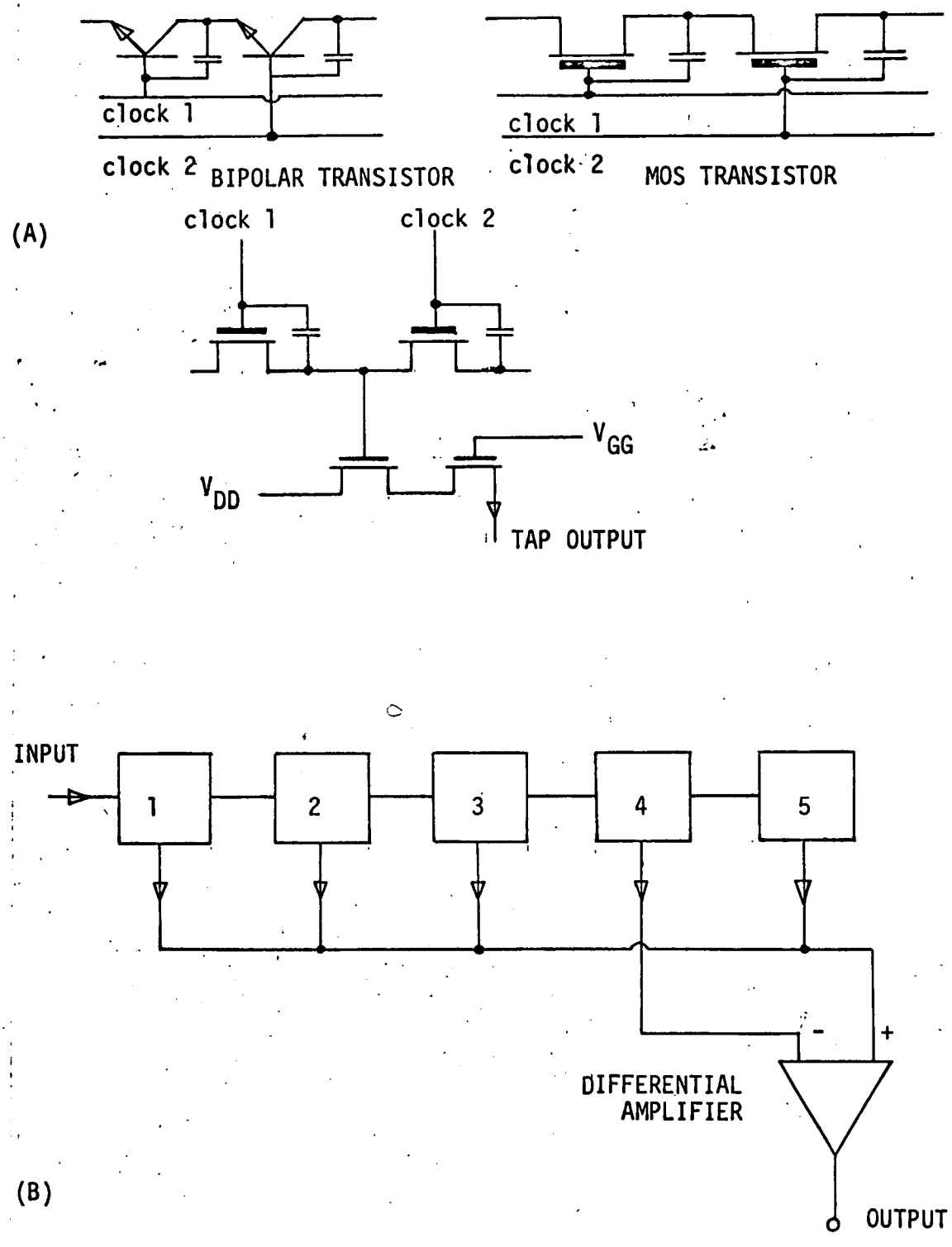

FIGURE 3.8 (A) BUCKET BRIGADE REGISTER STAGES. (B) TAPPING ARRANGEMENT AND CODING TO MATCH THE 5 CHIP BARKER CODE

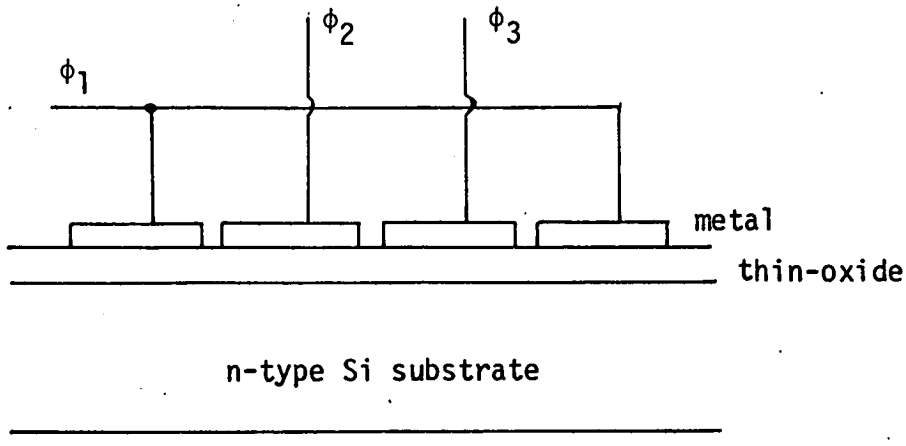

A BASIC THREE PHASE P-CHANNEL METAL GATE CCD

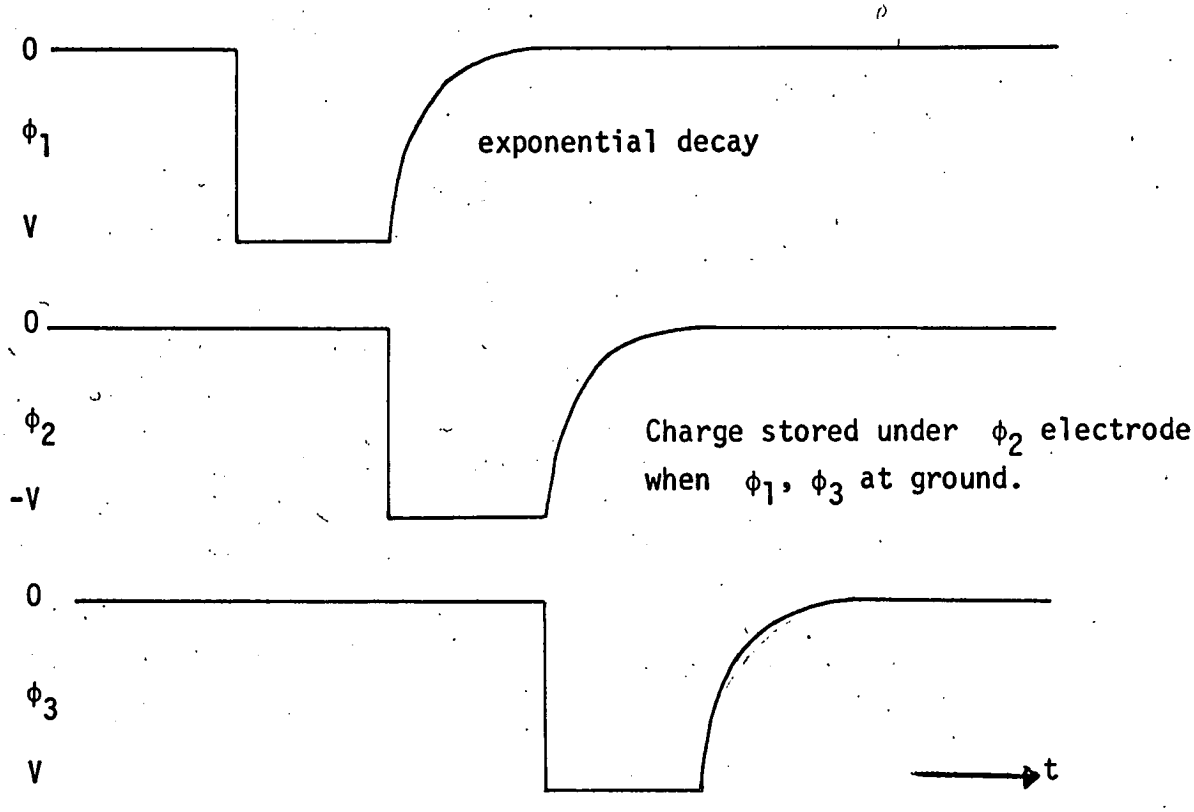

B CLOCK WAVEFORMS,

FIGURE 3.9 BASIC THREE PHASE CCD REGISTER STAGE (A) AND NECESSARY CLOCK WAVEFORMS (B)

and tap coding[93]. This measurement of *charge* flow is made difficult by stray capacitances and may limit this tapping technique to clock rates $\lesssim$50 MHz.

The charge transfer efficiency is a key parameter in any charge transfer device since it determines the maximum number of stages which can be cascaded. Charge transfer inefficiency, ε, is defined as the fraction of signal charge remaining at each transfer. The overall transfer inefficiency product $N\varepsilon$, where N is the number of transfers, must be $\lesssim$0.3 for tolerable signal decay[94]. BBD's have generally exhibited inferior values of ε. In CCD's there are two main sources of transfer inefficiency:

(1) at high clock frequencies, the charge transit time is determined predominantly by diffusion which is responsible for transferring the last small amount of charge.

(2) in surface channel CCD's surface state trapping times are comparable with required transfer times thus, release of charge occurs in later time slots.

The value of ε governs the spurious level[95] and hence determines the dynamic range which is not currently limited by thermal carrier generation. For a three phase device ε is typically 10^{-4} which gives approximately 40 dB dynamic range. The value of ε can be minimised by the following techniques:

- using 'fat zero' operation[95,96] in which a background charge is continuously passed through the array to saturate the surface trapping sites;

- employing long transfer electrodes with narrow gaps[95,96];
- use (100) rather than (111) orientation to reduce Qss levels and increase substrate resistivity ~40-60 Ω-cm;
- adopt the buried channel configuration[96], which has produced $\varepsilon \simeq 10^{-7}$; and,
- by optimising the clock waveforms - a fast rise and slow fall time assists charge transfer.

The use of tapped charge-transfer shift registers for *baseband* AMFs has resulted in the devices detailed in Table 3.5.

TABLE 3.5 COMPARISON OF PRESENT-DAY CTMF PERFORMANCE

DEVICE	CLOCK RATE† (MHz)	T.B_s #	PEAK/SIDELOBE DEGRADATION (dB)	ε	REF
BBD (2 phase)	0.01	13(B)	12.7	2×10^{-2}	92
CCD (3 phase)	0.01-5	13(B)	0.5	10^{-3}	93
CCD (3 phase)	0.001-5	100	--	$\sim10^{-3}$-10^{-4}	94

Key: B, Barker code; † clock rates of ≳100 MHz have been demonstrated for untapped buried channel CCD's shift registers; # register lengths of ~500 have been demonstrated.

Some of the advantages and disadvantages of current CTMFs can be summarised as follows:

ADVANTAGES	*DISADVANTAGES*
• variable clock rate	• multiphase clocks required
• silicon technology, hence wide range of established IC techniques available	• requires demodulation to baseband
• some peripheral circuitry may be integrated with the CTD	• not inherently asynchronous
• baseband processors, which may have bearing on system interfaces, eg computer executive control	• analogue baseband processing is prone to distortion from inter-modulation products
• programmability possible[94]	• sampling action can present other problems, eg aliasing effects
• very low power dissipation in shift register, although clock generators may consume several hundred mW	

3.5.2 Fabrication and Complexity

CCD's are only achievable in integrated circuit form whereas the BBD may be constructed with discrete components. The CCD stage is capable of much greater packing density than the BBD since diffused p-n junctions are not required. For this reason and because of their potentially superior performance, CCDs are emphasised. Large CCD arrays have been fabricated for imaging applications one three phase device consisting of 106 registers each 128 stages long[96]. The design of three phase registers presents topological problems in addressing each set of electrodes. Diffused cross-unders limit device speed by increasing overall capacitance. To overcome these problems two level metallisation structures are now being fabricated[96]. Two phase operation has been achieved by creating the necessary field asymmetry for unidirectional charge transfer through ion implantation doping of a fraction of the substrate under each electrode[96]. In all these structures a channel stopping diffusion prevents transversal charge leakage.

Buried[96] channel structures achieved by ion implantation or diffusion eliminate surface charge trapping and allow high clock rates.

3.5.3 Necessary Peripheral Hardware

For asynchronous operation, a prior knowledge of carrier phase is avoided by employing a quadrature demodulator which produces inphase (I) and quadrature (Q) components. Each component is then processed by two CTMF's which are clocked in phase quadrature to avoid problems with phase locking a local oscillator. This well known arrangement,[94] shown in Figure 3.10, is common to all asynchronous baseband processors. The inphase and quadrature components are squared and summed to reconstruct the video signal for further processing.

Other peripheral hardware includes multiphase clock generators and differential charge amplifiers.

3.5.4 Cost Analysis

An integrated circuit with 4 CCD tapped registers for asynchronous processing of a 127 chip sequence with a chip rate of 10 MHz is within the capability of the technology and would be priced at approximately £50. The peripheral hardware is not complex and should be available for ~£25.

3.6 DIGITAL MATCHED FILTERS

3.6.1 Current Performance Data

The simplest asynchronous DMF configuration[97] is shown in, Figure 3.11 and comprises; a quadrature demodulator, samplers, hard-limiter and four binary parallel correlators[97] with recombination circuitry. Each phase detector produces a bipolar video signal corrupted by noise and interference. Since the binary parallel correlators

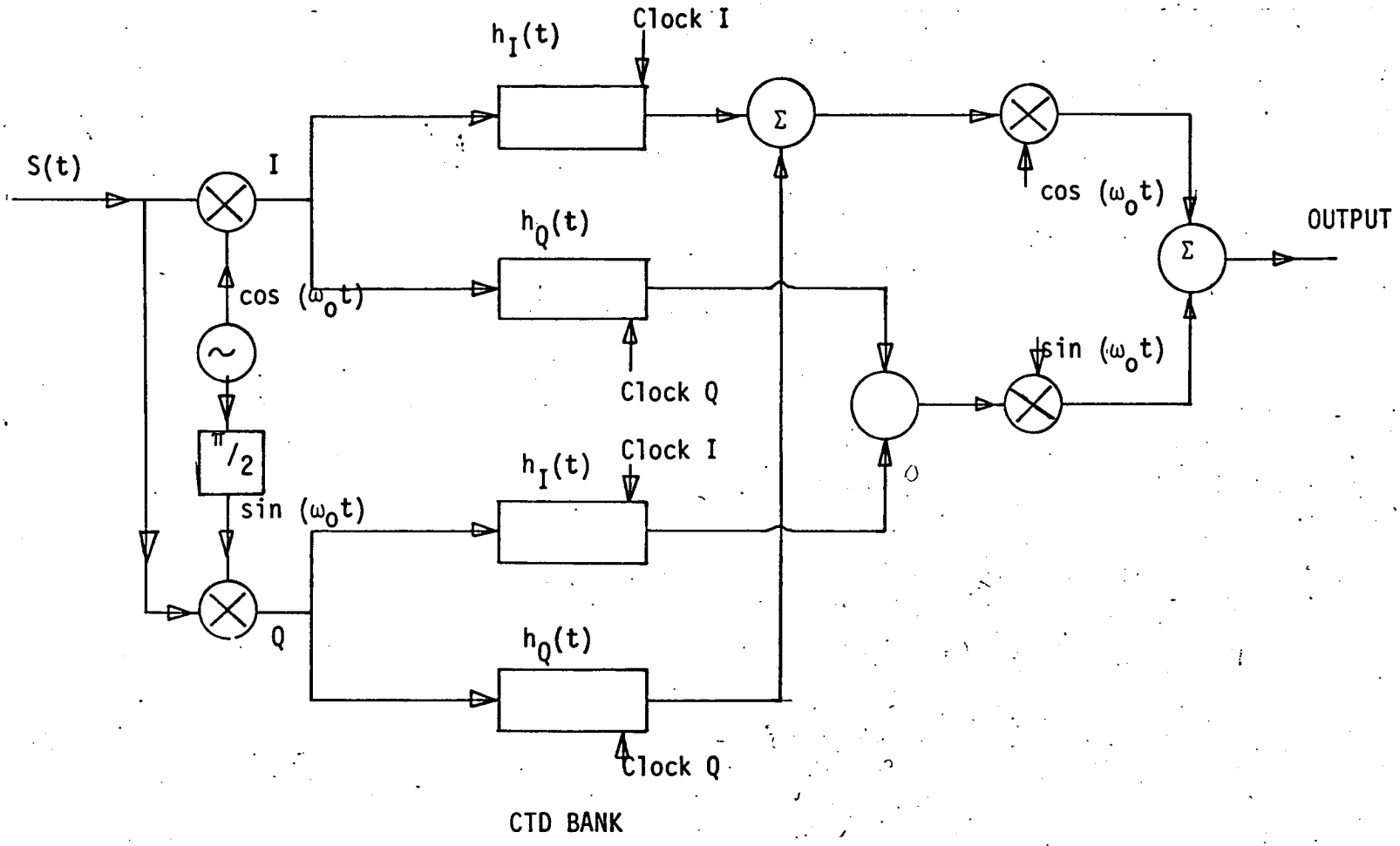

FIGURE 3.10 ASYNCHRONOUS BASEBAND CTD MATCHED FILTER

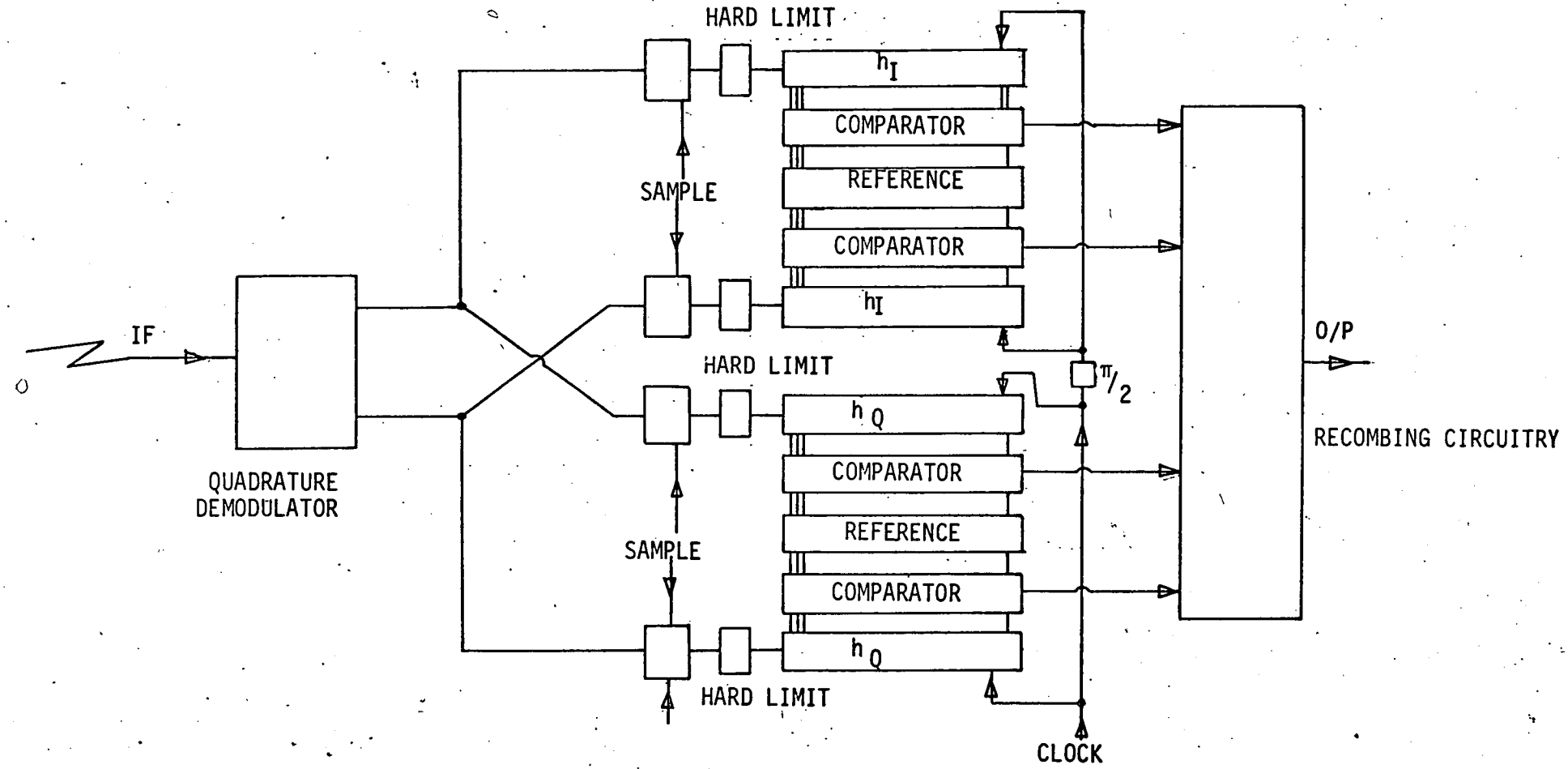

FIGURE 3.11 FULLY ASYNCHRONOUS DMF CONFIGURATION WITH TWO LEVELS OF QUANTISATION

are implemented with tapped binary shift registers it is necessary simply to hard limit the sampled video signals to obtain two levels of quantisation. The baseband signal from the quantisation stage is clocked into the tapped digital delay lines, operating in clock phase quadrature, for correlation with a reference signal held in a quasi-static register. The digital comparator outputs from each correlator are either summed using an operational amplifier to produce an analogue signal, or alternatively the number of agreements minus the number of disagreements counted for digital processing. Finally, a squaring and summation process recombines the sine and cosine components of the video signal.

If the noise statistics are Gaussian with zero mean, then compared with an analogue processor, the loss in SNR is only 2 dB. However, complete loss of correlation can occur whenever the noise or interference (eg cochannel user or jammer) captures the hardlimiters. Complete correlation loss is circumvented by adding a noise-like dither to the video signal prior to limiting. Cahn[38] has described a minimax strategy which results in a 4.8 dB loss in SNR under all conditions. The dynamic range of a binary correlator[97] is limited to 10 $\log_{10}(L)$, (dB), where L is the register length.

The dynamic range can be improved, the sensitivity to capture diminished and the loss in SNR reduced in principle by multilevel quantisation when a further 6 dB in dynamic range is added for each level. However, the complexity of the processor is increased substantially and the cost and power consumption undergo exponential increases. Figure 3.12, shows the general form of a DMF employing M-level quantisation[94]. Typically M = 8 would produce a 50 dB dynamic range.

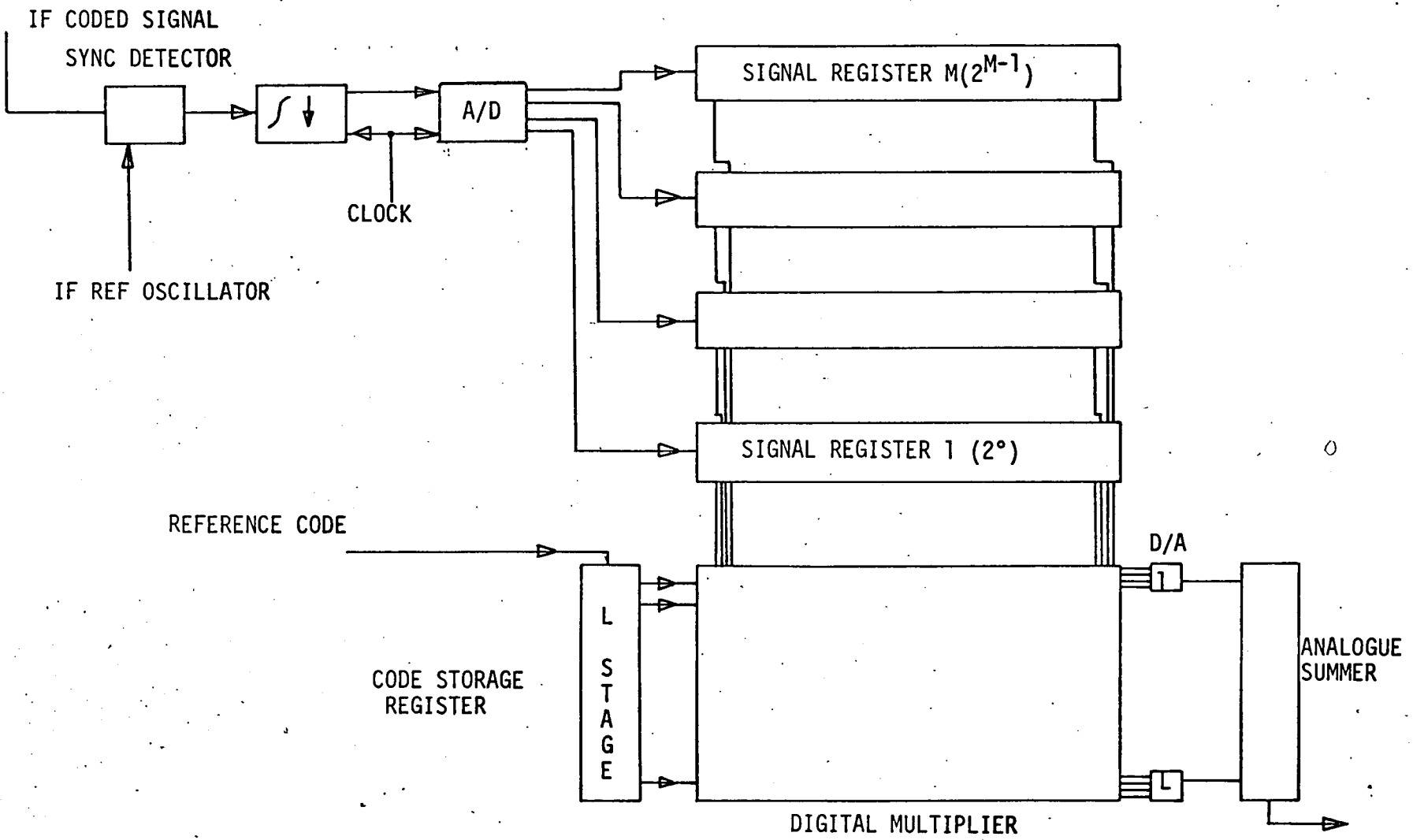

FIGURE 3.12 SIMPLIFIED MULTI-LEVEL BINARY DMF

Shift registers can be implemented in MOS, TTL or ECL families to give clock rates up to 250 MHz with register lengths in excess of 1000 (at the lower clock rates) obtained by cascading LSI packages. The logic families are complementary in that MOS is the slowest but gives the greatest packing densities, ECL has the highest speed and largest power consumption with TTL falling in between; offering reasonable packing densities and medium speeds and power consumption.

Analogue to digital conversion can be achieved at clock rates up to 50 MHz using discrete components and consuming several watts of power.

DMFs have been reported using[94] MSI and discrete packages[97,98] with both binary and multilevel quantisation. Table 3.6 summarises the available data. Some advantages and disadvantages of DMFs are summarised below:

ADVANTAGES

- the digital tapped delay line is highly adaptive, featuring continuously variable clocks and switchable length and tap coding
- the digital format has good noise immunity
- large TB_s products achievable
- interfaces with computer

DISADVANTAGES

- high reliabilities are required
- high power consumption
- complex hardware, large physical size and weight
- requires careful setting up at high clock rates to avoid propagation delay problems

TABLE 3.6 REPORTED DMF PARAMETERS

QUANTISATION LEVELS	REGISTER LENGTH	CLOCK RATE (MHz)	POWER (W)	APPLICATION	REF
2	127	5	--	RADA COMMUNICATION	98
2	63	2.5	--	--	99
2	127	10	*	ASYNCHRONOUS RADAR	97
2	64†	20	--	--	38
8	100	--	40*	--	94

Key: *, TTL; †, cascadable

3.6.2 Fabrication and Complexity

Current state of the art integrated circuit processing should be capable of producing one binary parallel correlator comprising signal and reference registers 127 stages long, comparators and summing amplifiers on one die. The preferred technology would be p-channel MOS possibly with poly-silicon gate electrodes for their slight speed advantage and, more importantly, the inherent extra interconnection complexity. The estimated semiconductor die size would be 250 thou x 250 thou; each register stage being approximately 12 thou x 12 thou. It is anticipated that such a device could operate at 15 MHz clock rate with a power consumption estimated as 1 Watt.

3.6.3 Necessary Peripheral Hardware

A programmable DMF requires code selection elements identical to those used with a programmable AMF, but they are also implemented in microelectronic technology. In addition a stable clock generator is also required.

3.6.4 Cost Analysis

Estimated works cost for a custom designed LSI *binary* DMF, with 10 MHz clock rate and 128 chip sequences, is £50.

3.7 SUMMARY OF COMPARISON DATA

The brief discussions on analogue and digital matched filters, given in Sections 3.2 through 3.6, are summarised here in three tables designed to permit direct comparison between techniques. Table 3.7 gives a merit rating for each approach; Table 3.8 compares the *achievable* current performance data; and finally Table 3.9 predicts parameter bounds for each device, here *simultaneous* achievement of each bound is *not implied*.

The indications from current performances are that the matched filter techniques studied are complementary, each approach possessing its own special merits and shortcomings. The final choice must depend on the specific application

For *near-future* designs, the likely bounds of the key B_s and TB_s parameters, shown in Figure 3.13, indicate different potential applications for each device. Bounds were established firstly by constraining fabrication to *current state-of-art* techniques with an attendant yield included, and secondly by demanding *high fidelity* responses. Thus, tentitively, SAW devices are expected to find *main* applications in high speed data links employing short ($\lesssim$1000 chip) spreading codes; with CTMF and DMF applications tending toward applications where low data rates are necessary, eg deep space telemetry, sonar and post detection radar signal processing.

For many applications, power consumption and weight are often critical factors in final selection. The fixed coded SAW AMF emerges as the one device achieving most of the desired parameters.

	FIXED AMF	PROG AMF	CONVOLVER	DMF	BBSR/CCD
Time-bandwidth	good	fair	very good	excellent	excellent
Bandwidth	medium	low	best	medium	good
Dynamic range	best	very good	very good	poor	good
Variable chip rate	no	no	yes	yes	yes
Temperature dependence	low	medium	minimal	minimal	minimal
Failure	graceful	serious?	serious?	catastrophic	catastrophic
Power consumption	zero	medium	medium	very high	low
Peripherals	simple	modest	complex	modest	modest
Fabrication	simple	medium	very simple	complex	medium
Cost	low	high	medium	medium	very low

TABLE 3.7 MERIT RATING BASED ON CURRENT KNOWLEDGE

	FIXED AMF (QUARTZ)	PROG AMF	PLATE CONVOLVER	DMF	BBSR/CCD
Centre frequency (MHz)	100	120	100	baseband processor	baseband processor
Sequence length (μs)	25	12.7	20	25	10
Chip rate (MHz)	10	10	20	10	10
Time-bandwidth	255	127	400	255	100
Dynamic range in compression (dB)	80	75	55	40	50
Spurious level (-dB)	<30	<25	40	40	40
CW insertion loss (dB)	45	50	75	N/A	N/A

TABLE 3.8 ACHIEVABLE PRESENT-DAY PERFORMANCES OF MATCHED FILTERS

	FIXED AMF	PROG AMF	CONVOLVER	DMF	BBSR/CCD
Centre frequency (MHz)	500	250	500	baseband processor	baseband processor
Sequence length (μs)	80	80	40	arbitrary	arbitrary
Chip rate (MHz)	120	20	200	200	300
Time-bandwidth	2,000	256	8,000	10,000	10,000
Dynamic range in compression (dB)	80	75	65	70	60
Level of spurious responses (dB)	45	40	45	70	60
CW insertion loss (dB)	35	40	35	N/A	N/A

TABLE 3.9 FORECASTED PERFORMANCE GIVING MAXIMUM EXPECTED VALUES OF INDIVIDUAL MATCHED FILTER PARAMETERS

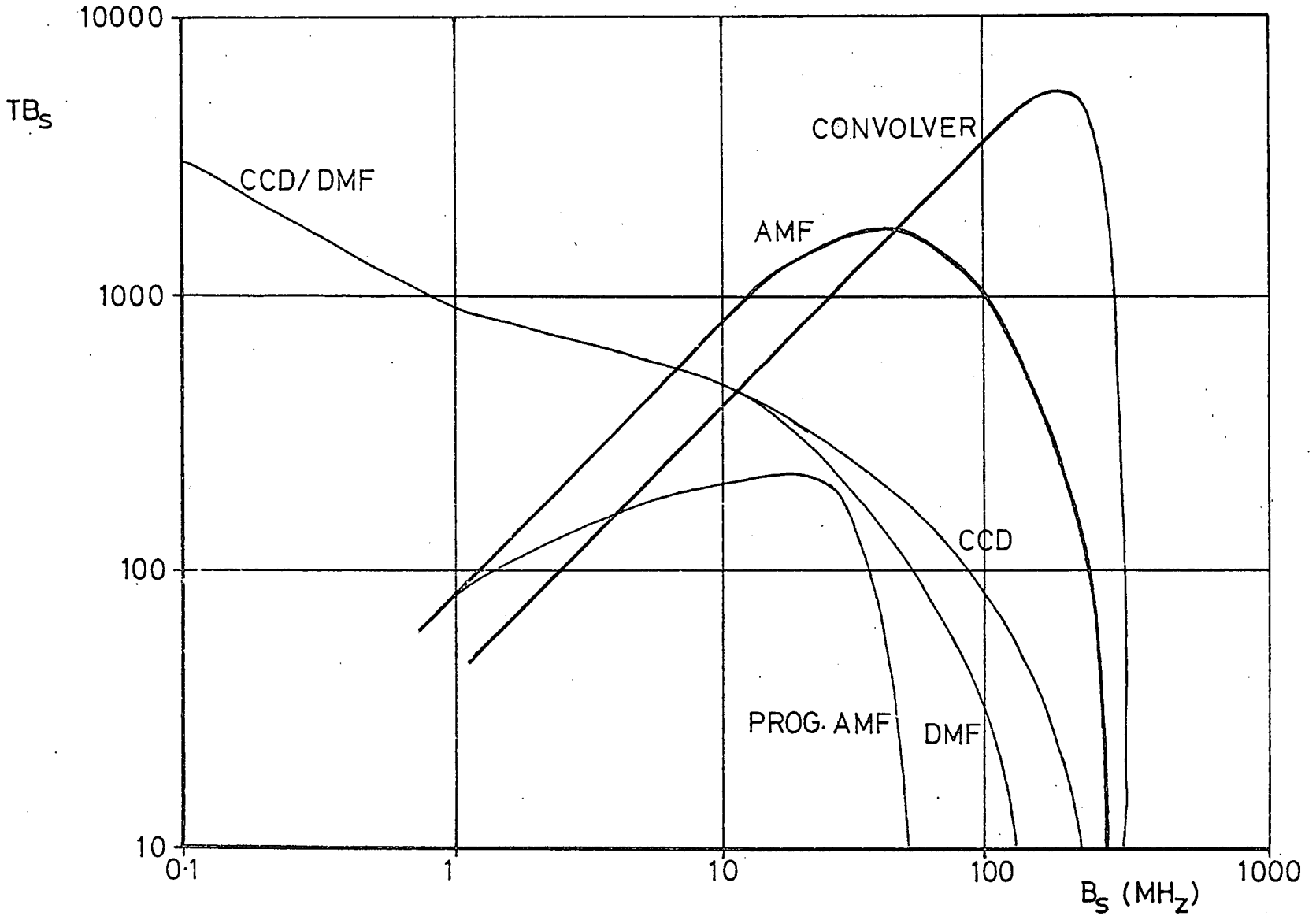

FIGURE 3·13 PREDICTED B_S-TB_S BOUNDS

CHAPTER 4

THE REALISATION AND EVALUATION OF SAW MATCHED FILTERS FOR BIPHASE SIGNALS

4.1 INTRODUCTION

Surface acoustic wave analogue matched filters (AMF) for modest time-bandwidth product ($\lesssim$100) biphase modulated IF signals have been approximated with 'first-order' transversal filter designs. These simple tapped delay line configurations exhibit responses which are distorted by several perturbing mechanisms. Specifically, the major factors producing degradations are:

- a departure from the desired geometry, due to damage caused in device fabrication or imperfections in the photo-master;
- electromagnetic leakage from input to output, resulting in coherent interference with the detected SAW signal;
- bandlimiting, because of IDT design or the characteristics of the electrical matching networks;
- multiple, coherent spurious acoustic signals, generated by the interaction of incident SAW signals with the phase coded transducer array; and,
- SAW propagation effects comprising temperature coefficients of delay, diffraction, beam steering, dispersion and propagation losses, (Chapter 1).

The above factors, which are studied in Section 4.2, all produce degradations in the autocorrelation function (ACF) peak-to-sidelobe ratios and perturb the ideal mirror symmetry about the correlation peak, see Figures 2.3, 2.4. Hence, the severity of distortion contributed by each factor can be assessed, for a given AMF specification, by measuring these degradations. Identification of the major deleterous effects can be accomplished through measurement of impulse response and frequency domain transfer functions. Specific examples are given to illustrate each factor with comparisons made between ideal responses calculated from a simple model and measurement.

With simple designs attempts to reduce insertion loss by increased coupling, or to extend the matched signal TB_s product by simply increasing the number of delay line taps, have been frustrated through the generation of spurious acoustic signals. This factor has been the *chief* cause of distortion; therefore emphasis has been given to their analysis and to finding a means of suppression. The aim being to achieve high fidelity responses *without the penalty of increased insertion loss.* Specific design examples incorporating either a novel dual tap or split-finger geometry have resulted in high performance AMF (<2 dB degradations) matched to biphase signals with TB_s products up to 127. Comparisons are drawn between these two second order designs and combinations of the techniques given in Chapter 3 are suggested for meeting difficult specifications.

The second section (Section 4.3) of this Chapter discusses briefly the basic phenomenological theory for the non-linear acoustic convolver and then gives details of an initial experiment demonstrating *correlation* with a degenerate structure. Here, two independently

generated *periodic* 31 chip PN waveforms were employed as the signal and reference biphase modulating 64 MHz carriers at 7.5 MHz. The experiment highlighted several problems associated with detecting signals employing the acoustic convolver; namely:

- inefficient parametric interaction;
- simple configurations exhibit high level acoustic spurious;
- good electromagnetic isolation is required between ports;
- high quality filters are necessary to reduce harmonic signals generated by mixers and power amplifiers; and,
- the relative timing between signal and reference is important.

Good agreement exists between the bilinear coefficient C_I, obtained with this experiment and values reported in the literature.

4.2 SAW BIPHASE CODED ANALOGUE MATCHED FILTER DESIGN AND ANALYSIS

This section comprises four main parts containing:

(1) AMF design information covering: the basic, ideal geometry; a first-order model; basic material considerations; the temperature sensitivity of AMF; the important trade-off of tap array conversion-loss and regeneration level; and, a discussion on wideband matching to the input IDT.

(2) Specific examples illustrating typical performances of first-order AMF designs and the time and frequency domain evaluation techniques employed.

(3) An analysis of, and designs to suppress, SAW spurious due to acoustic wave impedance mismatch.

(4) Finally, results are presented on second order designs which demonstrate the significant improvements in performance obtained using either a dual-tap[12] or a split-electrode geometry[63].

4.2.1 First-Order Design Considerations

Derivation of the basic AMF geometry

As stated in Chapter 2, Section 2.4 *optimum* predetection processing[41] of signals accompanied by Gaussian, stationary, white noise is achieved by filtering with a linear network with impulse response, h(t) given by; equation 2.3:

$$h(t) \triangleq ks(T_o - t) \qquad \ldots 4.1$$

k is a real constant and T_o is a delay term necessary to satisfy causality. Thus, $T_o \geq L\tau$ where τ is the chip duration and L is the binary sequence length.[45] The phase modulated signal s(t) can be described in the time domain by:

$$s(t) = \sum_{\ell=1}^{L} \exp j\phi_\ell \cdot \text{rect}[t-\tau(\ell-1)] \exp j\omega_o t \qquad \ldots 4.2$$

where ϕ_ℓ is the phase modulation of the ℓ^{th} chip, ω_o is the angular frequency of the carrier and rect(t) is a gating function of width τ:

$$\text{rect}(t) \triangleq \begin{cases} 1, & 0 \leq t \leq \tau \\ 0, & |t| > \tau \end{cases} \quad \ldots 4.3$$

Equation 4.2 can be rearranged as:

$$s(t) = \text{rect}(t) \exp j\omega_0 t * \sum_{\ell=1}^{L} \exp j\phi_\ell \cdot \delta[t-\tau(\ell-1)] \ldots 4.4$$

where * denotes the convolution operator, and $\delta[t-\tau(\ell-1)]$ is the Dirac delta-function. It is well known that any finite bandwidth signal can be represented by a sequence of samples spaced at time intervals corresponding to the reciprocal of the bandwidth[20,57]. The original signal being recovered from the sampled signal by appropriate linear filtering[20,57]. Equation 4.4 indicates this operation where the biphase coding is represented by the summation of L bipolar δ functions, with temporal spacing τ. The necessary reconstruction filtering being achieved by the convolution of this sample sequence with the rf gating function; rect(t) exp $j\omega_0 t$.

The AMF time domain specification given by equations 4.1, 4.4 enable the synthesis of a linear transversal filter[20]; which effectively stores signal samples on an array of taps spatially sampling a lossless nondispersive delay line

Figure 4.1 shows the canonical form of a transversal filter. The tap outputs are weighted and summed according to equation 4.4. On impulsing the filter, reconstruction of the signal from the sample sequence is achieved by a bandpass filter at the input (or output).

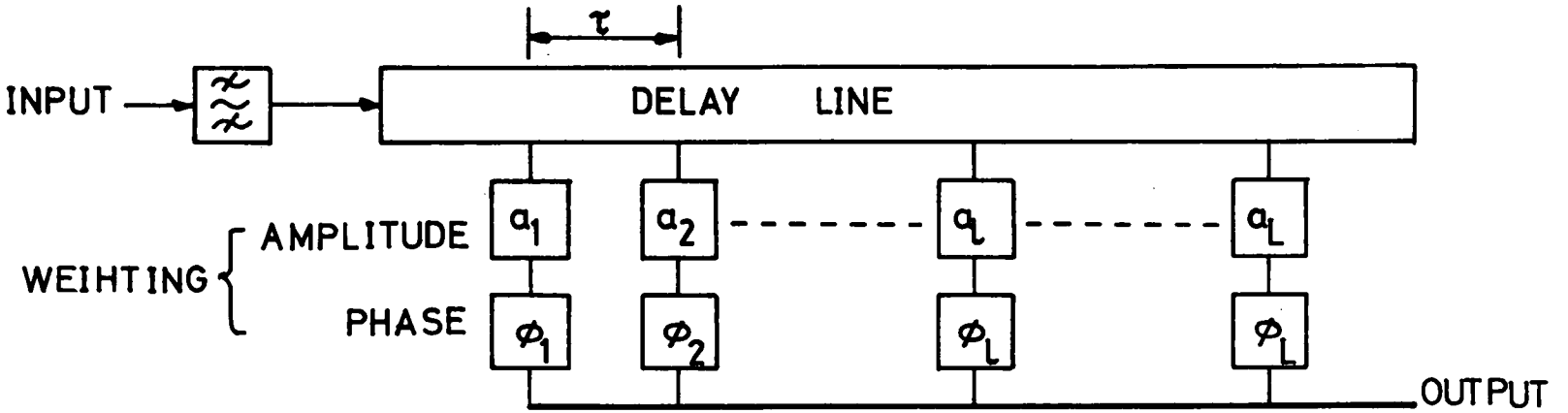

FIGURE 4.1 CANONICAL FORM OF TRANSVERSAL FILTER

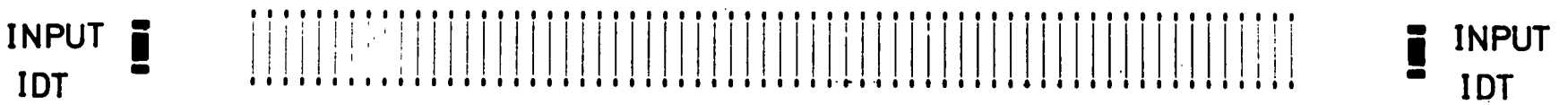

COLINEAR TAP ARRAY

FIGURE 4.2 BASIC SAW AMF GEOMETRY

The feasibility of implementing AMF with an SAW tapped delay line has been demonstrated by various investigators, see Chapter 3, Section 3.2. The basic form, shown in Figure 4.2 consists of a tightly coupled input transducer and a colinear array of wideband weakly coupled transducers tapping the propagating SAW signal[20]. The form shown was employed in early designs; each tap being wire bonded individually to rf sum bars with the connection polarity determined by the chip phase. Thus, enabling use of the same photomask for a variety of biphase codes. Later, coding was introduced at the step and repeat stage of mask making to give pre-programmed AMF. This results in reduced stray capacity, and therefore lower insertion loss; and a physically smaller, more reliable structure by eliminating discrete stitch bonds from each tap and the external interconnect. Also, each mask was made with an input transducer at both ends of the tap array to allow examination of the transmission characteristics of the array, and for generation of either s(t) or s(-t) by impulsing the appropriate IDT.

The desired h(t) is realised when the convolution of the impulse responses of the input IDT and its matching network, $h_i(t)$, and each tap, $h_\ell(t)$, is

$$h_i(t) * h_\ell(t) = \text{rect}(t) \exp j\omega_o t \qquad \ldots 4.5$$

This is approximated if the following three conditions are met:

(1) $h_i(t)$ is matched to the chip; that is $h_i(t)$ is a rectangular rf pulse containing N cycles of carrier where:

$$N = f_o/B_s \qquad \ldots 4.6$$

(2) $h_\ell(t)$ approaches a delta-function;

(3) the taps do not perturb the acoustic wave.

Condition (1) is met for simple designs with an unapodised input transducer having 2N+1 periodic electrodes, where N is given by equation 4.6. Designs with large fractional bandwidths ($>B_{opt}$, Chapter 1) require modification of the input IDT geometry, see a later subsection. The second requirement is approximated when $N \gg M$, where M is the number of synchronous periods on each tap. The design trade-off involves an exchange of loss for low distortion. Finally, condition (3) requires further consideration of both tap array geometry and output load either for high coupling (k^2) substrates such as $LiNbO_3$ or $Bi_{12}GeO_{20}$ or for large TBs product designs. In both cases high levels of spurious acoustic signals are encountered which result in large distortion.

Simple AMF model

Tancrell and Holland[100] have described an elementary model which exhibits the dominant interrelation between transducer geometry and the experimentally determined frequency-domain response function. Although this simple model does not predict insertion loss or spurious signal levels, which can be calculated separately, its usefulness lies in predicting *ideal* frequency domain responses of arbitrary transducer structures. Its accuracy is sufficient for simple geometries on quartz to enable valuable information to be gained on the relative magnitudes of *geometrically* related distortional effects. These geometrical factors comprise: gross defects, appearing during fabrication; *systematic* step and repeat errors; and an "incorrect" choice of N and M, equation 4.5. The "second order" AMF designs exhibit frequency domain transfer functions $H(j\omega)$ which *closely follow* the responses predicted by the Tancrell and Holland impulse model.

The assumptions made for the impulse model can be summarised as follows:

- the piezoelectric coupling is weak - electroacoustic regeneration and depletion of power from the SAW beam are ignored;
- the driving term for the acoustic displacement can be represented by a δ-function source situated at the edges of each electrode;
- the acoustic radiation is uniform along the length of an electrode - diffraction and beam steering are neglected; and,
- the metallised sections do not perturb the wave - reflection of SAW and scattering to bulk modes due to acoustic wave impedance discontinuities, attenuation and dispersion are neglected.

Using the impulse model, the transfer function, $H(j\omega)$, of any tapped delay line with unapodised transducers is given by:

$$H(j\omega) = \sum_{q=1}^{Q} I(q) \exp[jZ_i(q)\omega v_s^{-1}] \sum_{p=1}^{P} T(p) \exp[-jZ_t(p)\omega v_s^{-1}] \quad \ldots 4.7$$

where the first summation term describes (by vector addition) the envelope of the wave radiated from the input transducer in the positive Z-direction. The input IDT has a total of $Q(=4N)$ δ-function sources positioned at regular intervals $Z_i(q)$; $q=1, 2, \ldots Q$. The second summation term describes the response of the tap array, having $P(=4ML)$ sources placed at $Z_t(p)$. The coefficients $I(q)$ and $T(p)$ are complex with magnitude and phase determined by the *electric field gradient* at each electrode edge.

Specifically, for conventional ($\lambda_o/4$) electrodes with constant periodicity the magnitudes of I(q) and T(p) are all equal while the signs alternate in pairs, ie I(1), I(2) are positive; I(3), I(4) are negative; I(5), I(6) are positive, etc. Examination of equation 4.7 shows that it is related to the discrete Fourier transform of s(t) described by equation 4.4.

A computer programme was written to evaluate H(jω), equation 4.7. The input data specifies the synchronous wavelength (λ_o); the SAW propagation velocity (v_s); the parameters N and M; and the tap array phase coding. From this data the arrays I(q), T(p) and $Z_i(q)$, $Z_t(p)$ are first computed. Then the two complex summation terms are evaluated at each specified frequency step over the desired range. Also incorporated in the programme as a subroutine was a standard inverse fast Fourier transform (IFFT) algorithm used to process the calculated H(jω) values. In particular computing the IFFT of:

(1) H(jω), yields h(t);

(2) H(jω) . H*(jω), simulates the conjugate pair performance, see Section 4.2.2 and Chapters 2, 5, 6, where one AMF is used to generate a deterministic waveform and its conjugate is used to detect that waveform; and,

(3) H(jω) S(jω), yields the ideal AMF response to any specified signal S(jω).

Specific examples of the programme use are given in Section 4.2.2.

Factors governing the choice of substrate material

A number of piezoelectric substrate materials have been characterised for SAW devices. These have been extensively reviewed in the literature, especially by Slobodnik[21], and Schulz[101]. Among these, there are currently three *commercially* available single crystal materials suitable for AMF designs operating at VHF; namely: bismuth germanium oxide; lithium niobate; and quartz. Each material has widely differing basic characteristics which may be altered over limited ranges by choosing different crystal cuts and orientations. The ultimate choice of substrate is inextricably linked to the AMF specification which will define operating frequency, bandwidth and delay, and give limits on performance and cost.

In general, to facilitate material comparisons the following major parameters are considered:

- *propagation attenuation and air loading:* see Chapter 1, Section 1.1, which is not negligible at high frequencies ($\gtrsim$300 MHz) or for long delays (>20 μs) at lower frequencies (~100 MHz);
- *beam steering loss:* except for propagation along a direction where the SAW velocity is at an extremum, the acoustic power flow is not colinear with the phase velocity - for long delays accurate alignment to the required propagation direction is necessary, equation 1.13;
- *diffraction loss:* most materials do not exhibit isotropic SAW velocity in the plane of propagation hence simple diffraction theory is inapplicable[31], the near field of the acoustic beam may be extended[30] or foreshortened - in the latter case long delays may be achieved with a wide acoustic beam, however this affects the transducer conversion loss and level of regenerated spurious;

- *coupling efficiency* (k^2): influences IDT conversion loss, obtainable fractional bandwidths and spurious signal levels, all of these points are examined in later subsections;
- *propagation velocity and velocity anisotropy*[20]: very long delays will require a material with relatively low velocity to minimise the acoustic path length, however low velocity results in higher photolithographic resolutions for the same f_o, while the velocity anisotropy will place limits on the required orientation and alignment tolerances to limit frequency and phase mismatch; and
- *temperature coefficients of velocity and delay:* thermal stability and insertion loss have generally been traded-off[46, 101] and materials selected on this criterion alone - phase coded AMF sensitivity to temperature variation is a function of the code, the fractional bandwidth and the code length and is simply calculated from the ambiguity function, see the following subsection.

All design work and evaluations of AMF for this Thesis have been conducted with (ST,X) quartz substrates. This material has the advantage that for propagation along the X-axis, both the surface wave velocity is near, and its temperature dependence is at, an extremum. The higher order coefficients yield an average variation of 2×10^{-6}/°C from -25°C to +75°C. The principle disadvantage is its low coupling coefficient ($k^2 \sim 0.0017$) which yields optimum fractional bandwidths of ~4.5%. To offset this, the reflection loss is correspondingly high. The other major disadvantage is that little beam focusing is realised so that the beam spreads as in isotropic media.

Later subsections examine AMF performance specifications and attempt to relate these back to material parameters. First order design approaches generally ignore propagation attenuation, attempt to circumvent beam steering and diffraction losses, operate with close to optimum fractional bandwidth and employ substrates with low temperature coefficients. Second order designs attempt to remove these restrictions.

Temperature stability of SAW AMF

A significant potential application of SAW AMF lies in the ability to synthesis rapidly and to detect a complex time-frequency encoded pulse[15] pattern for MADA communications[43,54], see Chapter 2, Section 2.5 and Chapters 5,6. However if the AMF in the modulator and demodulator are at different temperatures both thermal expansion and the temperature dependence of SAW velocity produce a mismatch and thus performance degradations. Carr et al[46] have studied temperature effects on performance emphasising degradations in peak-to-sidelobe ratios obtained on code compression. With bit synchronous communication, however, the most important degradation is the loss in peak amplitude producing an attendant increase in *bit error rate*, (Chapter 5).

The correlation peak occurs at the origin of the ambiguity function which may be readily calculated from the general cross correlation function, $\chi(t, f)$. At the origin:

$$\chi(0, \psi_0) = \sum_{\ell=1}^{L} \exp -j(\ell-1)\psi_0 \qquad \ldots 4.8$$

where, $\psi_0 = 2\pi f_0 \tau$ $\qquad \ldots 4.9$

and L is the number of taps, f_0 is the synchronous carrier frequency and τ is the intertap delay.

Now, the intertap delay τ is given by:

$$\tau = d/v_s \qquad \ldots 4.10$$

where d is the tap-tap spacing and v_s is the SAW propagation velocity. If the temperature of the substrate varies then both the acoustic path length and acoustic velocity may be expected to change. In general, the delay time as a function of temperature (T) may be expanded in a Taylor series. However, it has been shown experimentally that the linear coefficients dominate[101]. Thus, the first order coefficient of delay is given by

$$\frac{1}{\tau}\frac{\Delta\tau}{\Delta T} = \frac{1}{d}\frac{\Delta d}{\Delta T} - \frac{1}{v_s}\frac{\Delta v_s}{\Delta T} \qquad \ldots 4.11$$

Hence, equation may be expressed as:

$$\frac{1}{\tau}\frac{\Delta\tau}{\Delta T} = \alpha - \nu \qquad \ldots 4.12$$

where α is the linear expansion coefficient and ν is the first-order temperature coefficient of velocity. From equations 4.9 and 4.11

$$\Delta\psi = 2\pi f_o\, \tau(\alpha-\nu)\, \Delta T \qquad \ldots 4.13$$

and the ambiguity function $|\chi(0,\Delta\psi)|$ may be expressed as

$$|\chi(0,\Delta\psi)| = \frac{\sin(L\Delta\psi/2)}{\sin\,(\Delta\psi/2)} \qquad \ldots 4.14$$

where $\Delta\psi$ may be written, from equation 4.13, as

$$\Delta\psi = 2\pi\ N\ (\alpha-\nu)\ \Delta T \qquad \ldots 4.15$$

here, N is the number of rf cycles per chip ($=f_o\tau$).

The first null in the correlation peak occurs when

$$\Delta\psi = 2\pi/L$$

which corresponds to a small fractional change in bit period.

The values of $\Delta\psi$ at which the correlation peak falls by 3 dB are given by:

$$\Delta\psi_{3dB} = \pm\pi/L \qquad \ldots 4.16$$

This amplitude change corresponds, for most signaling techniques, to a significant increase in bit error rate[57,59] and is thus a convenient value to adopt for design comparison. The temperature change ΔT required to produce this 3 dB amplitude change is:

$$\Delta T_{3dB} = \frac{1}{2LN(\alpha-\nu)} \qquad \ldots 4.17$$

It can be concluded immediately that for any given substrate and desired code length, the *larger the fractional bandwidth* (N^{-1}) possible the more temperature stable the device. For example, on this basis a design operating at B_{opt} on (Y,Z) lithium niobate with N~4 and $(\alpha-\nu)$ ~9×10^{-5} is *not significantly more temperature sensitive* than an equal length device on (Y,X) quartz where N~20 and $(\alpha-\nu)$ ~-22×10^{-6}. The trade-off in this situation would be one of loss versus reflected signal levels and of substrate cost.

Tap array conversion loss and regenerated spurious

The relationship between the phase coded tap array scattering and transmission parameters and electrical load can be accurately predicted using the basic one-dimensional Mason equivalent network model adapted by Smith et al[9] for SAW IDTs. The basic model does not include losses due to beam spreading, scattering to bulk modes and the level of SAW spurious due to wave impedance mismatch.

Figure 4.3 shows the equivalent circuit of a single electrode section for the Mason models[9]. Two extreme models were proposed,

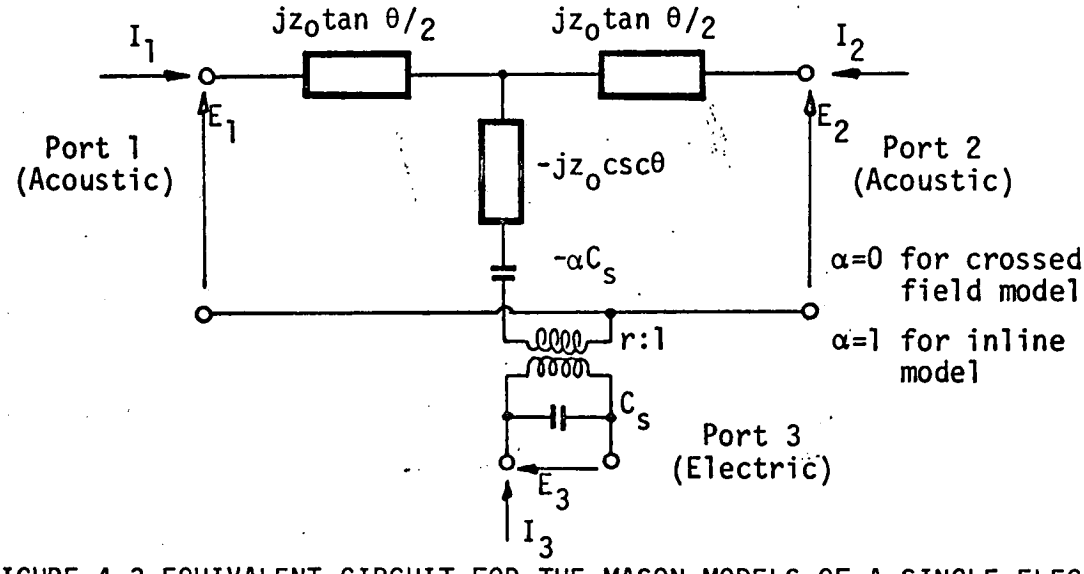

FIGURE 4.3 EQUIVALENT CIRCUIT FOR THE MASON MODELS OF A SINGLE ELECTRODE SECTION

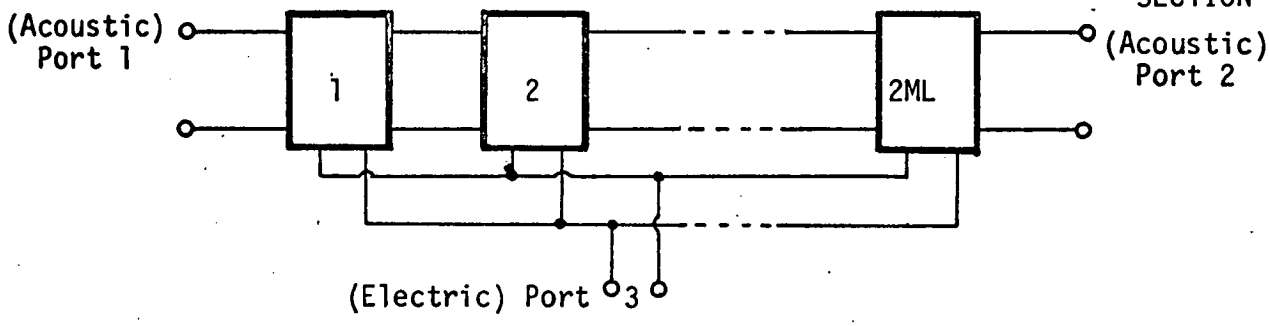

FIGURE 4.4 EQUIVALENT CIRCUIT FOR THE PHASE CODED ARRAY OBTAINED BY CASCADING SINGLE ELECTRODE SECTIONS

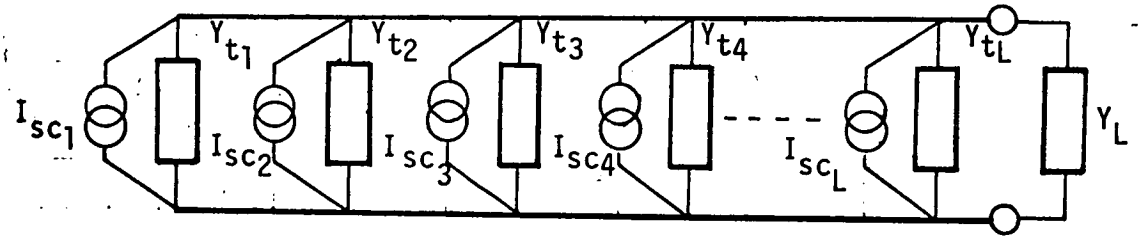

FIGURE 4.5 EQUIVALENT CIRCUIT OF THE TAP ARRAY ELECTRIC PORT

of these the crossed-field representation has demonstrated[27] an accurate fit to experimental data for both quartz and lithium niobate substrates. By cascading sections Figure 4.4 the equivalent 3-port circuit for the phase coded tap array may be characterised in terms of an equivalent, normalised admittance matrix, [Y]. From [Y] the corresponding intrinsic scattering matrix [S] can be calculated[102,103]:

$$[S] = [I-Y]\ [I+Y]^{-1} \qquad \ldots 4.18$$

where [I] is the identity matrix. For a reciprocal, lossless n-port network [S] is unitary, scattering coefficients become interrelated and rapid power-balance checks are possible.

Two key parameters required for computation of array conversion loss and reflection loss are calculated using the scattering[9] matrix:

- p_{11}, the fraction of incident *acoustic power* reflected at port 1, and,
- p_{31}, the fraction of incident *acoustic power* coupled to the electrical load, Y_L at port 3.

Gerard[103] has given general expressions for the power transfer coefficients of an unapodised IDT with port 2 terminated in G_0 and port 3 terminated in Y_L. for frequencies near synchronism. In device evaluation, the important loss parameters are conveniently measured at synchronism when the coefficients p_{ij} become:

$$p_{11} = \frac{1}{D(Y_n)} \qquad \ldots 4.19$$

and,

$$p_{31} = \frac{2Gn}{D(Y_n)} \qquad \ldots 4.20$$

where

$$Yn = Gn + jBn = \frac{G_L}{\hat{G}_a} + \frac{j\omega_o C_T}{\hat{G}a},$$

and

$$D(Yn)_{\omega_o} = 1 + 2Gn + |Yn|^2, \text{ assuming that } Y_L \text{ is real } (= G_L).$$

Thus,

$$p_{11} = \frac{1}{(1+Gn)^2 + Bn^2} \qquad \ldots 4.21$$

and, for bidirectional launching of SAW

$$p_{31} = \frac{2Gn}{(1+Gn)^2 + Bn^2} \qquad \ldots 4.22$$

and the appropriate loss factors, L_{ij}, are:

$$L_{ij} \triangleq -10 \log_{10} (p_{ij}) \qquad \ldots 4.23$$

The quantities, $\hat{G}_a$ and C_T for the coded array are conveniently found by examination of the equivalent circuit of the electrical port shown in Figure 4.5. It is assumed that the coded array consists of L geometrically identical, colinear taps connected to a resistive load R_L. The voltage appearing across the load (V_L) for synchronous CW operation is found by applying Millman's theorem[102]:

$$V_L = \frac{I_{sc} \sum_{\ell=1}^{L} a_\ell}{\sum_{\ell=1}^{L} Y_{t_\ell} + G_L} \qquad \ldots 4.24$$

where Y_{t_ℓ} is the synchronous equivalent admittance for the ℓ^{th} tap derived from the crossed-field model, I_{sc} is the short circuit current available from each tap and $a_\ell (= 1)$ represents the biphase coding of the ℓ^{th} tap.

Now, expressing Y_t in terms of a parallel equivalent circuit, as shown in Figure 1.3, results in

$$\sum_{\ell=1}^{L} Y_{t\ell} = LY_t = L\hat{G}a_t + jLB_t \qquad \ldots 4.25$$

Thus, the *array* radiation conductance ($\hat{G}_a$) and the *total array* susceptance (B) are

$$\begin{aligned} \hat{G}_a &= L\hat{G}a_t \\ B &= LB_t \end{aligned} \qquad \ldots 4.26$$

Equation 4.25 and Figure 4.5 illustrate how each tap is loaded by (L-1) taps acting as shunt parasitic elements and by the external resistive load, R_L.

Following Smith et al[9] a radiation 'Q' (Qr) and a load 'Q' (Q_L) may be defined:

$$Q_r = \omega_o C_T / \hat{G}_a$$

and,

$$Q_L = \omega_o C_T / G_L \qquad \ldots 4.27$$

where C_T is the *total* array capacitance (LC_t) and $\hat{G}_a$, by analogy with equation 1.5, may be represented by:

$$\hat{G}_a = \frac{4k^2}{\pi}\ \omega_o\ C_s\ N_E^2 \qquad \ldots 4.28$$

where N_E is an equivalent number of interdigital periods determined by the array phase coding. Thus, in general:

$$N_E = M \sum_{\ell=1}^{L} a_\ell \qquad \ldots 4.29$$

where M is the number of periods on each tap. Therefore, Q_r may be expressed from equations 4.27, 4.28, 4.29 in the form:

$$Q_r = \frac{\pi L}{4k^2 M \left(\Sigma a_\ell\right)^2} \qquad \ldots 4.30$$

For an uncoded IDT equation 4.30 reduces to the well known expression for Q_r, given by Smith et al, where $N_E = ML$. In general Q_r is a measure of the substrate coupling and degree of coherence of the coded transducer at f_o, an equivalent expression for dispersive arrays has been given by Hartmann[23]. For m-sequence coded taps, the code balance property (Chapter 2, Section 2.3.2) results in:

$$\sum_{\ell-1}^{L} a_\ell = +1$$

for any value of L, thus Q_r can be extremely high. For example, with $L = 127$ and $M = 2$; $Q_r \sim 3 \times 10^4$ on (ST,X) quartz and $Q_r \sim 10^3$on lithium niobate, while Q_L can take on a wide range of values determined by C_T and R_L.

Using equations 4.21, 4.22, 4.27 the reflection loss and conversion loss factors for synchronous CW operation may be expressed in terms of Q_r and Q_L:

$$L_{11} = -10 \log_{10} \left[\frac{Q_L^2}{(Q_r+Q_L)^2 + Q_r^2 Q_L^2} \right] \qquad \ldots 4.31$$

and,

$$L_{31} = -10 \log_{10} \left[\frac{2Q_L Q_r}{(Q_r+Q_L)^2 + Q_r^2 Q_L^2} \right] \qquad \ldots 4.32$$

The value of Q_L which minimises conversion loss is

$$Q_L^2 = Q_r^2/(1+Q_r^2) \qquad \ldots 4.33$$

Thus, $Q_L \sim 1$ for $Q>10$. However, minimum conversion loss is not the only important design criterion; a vital requirement is the suppression of regenerated spurious. Equations 4.31 and 4.32 specify the fundamental interrelation of conversion loss and regeneration. As specific examples, Figures 4.6 and 4.7 illustrate the relationship between L_{11}, L_{31} and Q_L as a function of Q_r. To obtain the Q_r values, equation 4.30, the following parameters were assumed: $M=3$; $k^2=0.0017$ for (ST,X) quartz, Figure 4.6 and $M=1$, $k^2=0.049$ for lithium niobate, Figure 4.7; further, the following biphase codes were used in the calculation:

(1) the 13 chip Barker code, $\left(\sum_{\ell=1}^{L} a_\ell = 5\right)$

(2) the 15 chip m-sequence,
(3) a 31 chip m-sequence,
(4) a 127 chip m-sequence.

$\Bigg\}$ $\sum_{\ell=1}^{L} a_\ell = 1$

These curves show the significant increase in regenerated spurious signal levels obtained with lithium niobate for values of Q_L typically encountered.

Two further sources of conversion loss can be incorporated into the above theory:

(1) Loss due to shunt stray capacitance, C', at the output. Thus,

$$Y_L = G_L + j\omega_o C' \qquad \ldots 4.34$$

which has the effect of increasing B_n in equations 4.21 and 4.22. Hence, both p_{11} and p_{31} are reduced by the same proportion.

(2) Loss due to partial illumination of the receiving IDT acoustic aperture. Assuming colinear propagation, this occurs when the tap array aperture W_T and the input IDT aperture W_I differ. Waldron[104] has shown that the IDT power transfer coefficients are multiplied by the factor α:

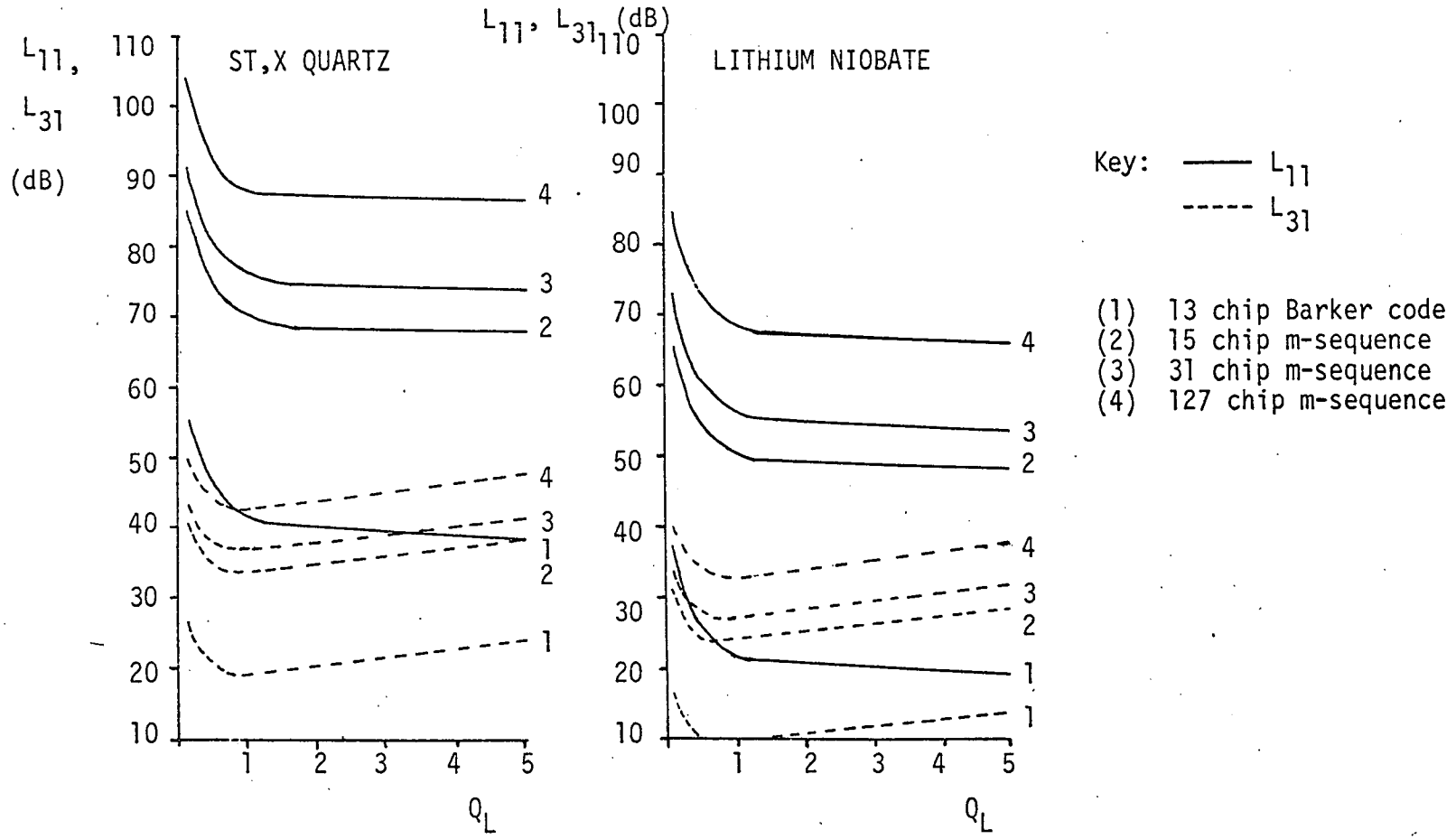

FIGURES 4.6, 4.7 L_{11} AND L_{31} VERSUS Q_L FOR ST,X QUARTZ AND LITHIUM NIOBATE SUBSTRATES RESPECTIVELY AS A FUNCTION OF TAP CODING

$$\alpha = 1 - \beta \qquad \ldots 4.35$$

where, $\beta \leq 1$ is given by

$$\beta = \begin{cases} W_I/W_T, & \text{for } W_I < W_T \\ W_T/W_I, & \text{for } W_T < W_I \end{cases} \qquad \ldots 4.36$$

This loss effect depends on the AMF *geometry only* and thus relates to efficiency and *not* to any fundamental SAW device or material parameter.

Input IDT matching for wideband operation

The synchronous conversion loss of an IDT is minimised under conditions of conjugate impedance matching. Referring to Figure 1.4, this is obtained when:

$$R_g = \hat{R}_{as}$$

and,

$$j\,\omega_o L = 1/j\omega_o C_s N$$

where $C_s N$ is the IDT static capacitive reactance. However, this arrangement can only provide low loss over the optimum fractional bandwidth (B_{opt}), equation 1.12, determined solely by the material electromechanical coupling constant, k^2. It is essential to achieve low conversion loss over bandwidths $>B_{opt}$ thus maintaining a low f_o in order to ease the design problem areas:

(1) fabrication, Chapter 3, Section 3.2;

(2) temperature sensitivity, equation 4.17; and

(3) beam steering and diffraction loss, equations 1.13, 1.14.

The achievement of large fractional bandwidth for low IDT conversion loss has been demonstrated by employing multi-element impedance matching networks[9,26,72,105,106]. In general an asymmetrical network comprised of pure reactances can be designed to give a purely resistive image impedance.

Any output load can be modified by the network so that the input impedance matches R_g at a given frequency. A well characterised impedance matching network, for series resonated loads, comprises cascaded series resonators coupled by K-inverter circuits[106], Figure 4.8, which progressively transform the load (tuned transducer) impedance to match the generator at the input terminals. Almost constant coupling to the series radiation resistance, R_{as}, is obtained by reflecting a controlled amount of the incident power throughout the desired passband.[26,106] The frequency dependent nature of R_{as} requires that the IDT intrinsic acoustic bandwidth $\sim f_o/N$ be increased to ensure minimal variation of radiation resistance over the passband. For this case, the normalised network element values are well tabulated[106] for various amplitude and phase ripple bounds. Also increasing W, thus reducing R_{as}, results in increased fractional bandwidths. The penalty incurred is a corresponding increase in minimum conversion loss.

Usually, the number of variables is sufficiently great that an optimising[26] or an interactive[72] computer programme is essential. Fractional bandwidths of ~9% with <0.5 dB amplitude ripple have been achieved with (ST,X) quartz substrates, see Section 4.2.2, with a two section network employing high Q elements. Less than ~4 dB additional midband conversion loss was obtained. Smith et al[28] have reported 40% bandwidths on lithium niobate using the J-invertor circuit[106] which gave 6.8 dB midband loss and a virtually flat passband. The number of network sections required is not usually more than two for many applications. In most cases the additional complexity and cost are outweighed by the commensurate improvement in performance obtained.[28,72,105]

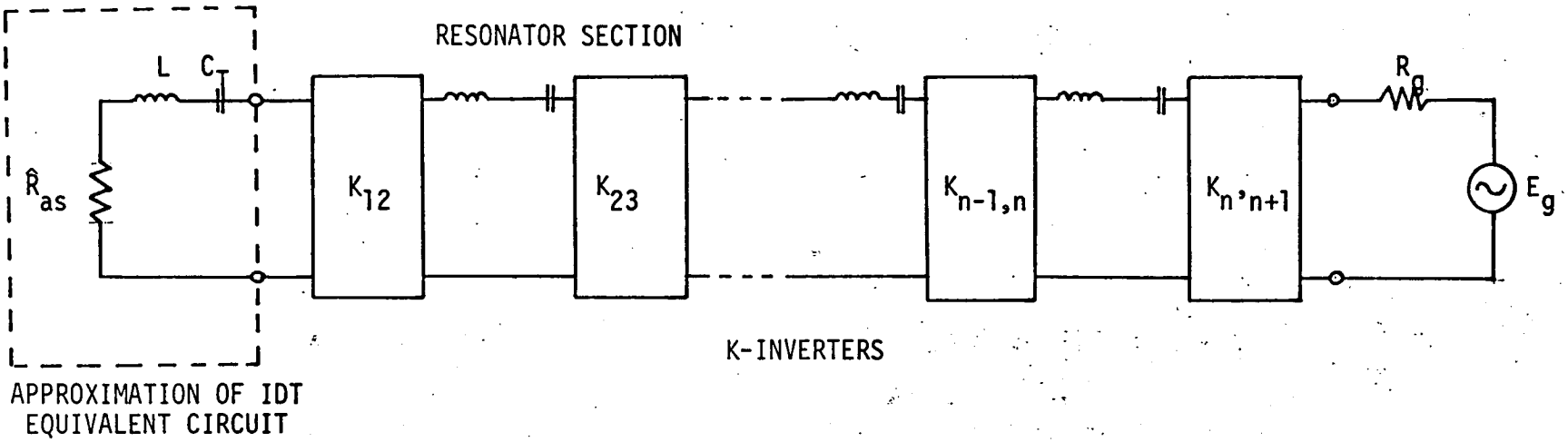

FIGURE 4.8 BAND-PASS COUPLED-RESONATOR MATCHING NETWORK FOR SERIES-RESONATED IDT

4.2.2 Characterisation of First Order AMF Designs

A number of time and frequency domain measurement procedures can be employed to enable the isolation and evaluation of the major distortional effects listed in Section 4.1. The evaluation techniques comprise measurement of: impulse response; autocorrelation response, for both periodic and aperiodic signals; and frequency transfer functions. The important evaluation of AMF processing gain is described in Chapter 6, where error rates are measured for OOK signals in Gaussian bandlimited white noise.

Most of the results given below were obtained for an AMF geometry, shown in Figure 4.2, designed for (ST,X) quartz with the following parameters:

- velocity of propagation, v_s (km sec^{-1}) = 3.1576
- acoustic wavelength at synchronism, λ_o(μm) = 24.8
- synchronous frequency, f_o (MHz) = 127.3
- number of interdigital periods on input transducer, N = 25
- input IDT aperture, W_I' (wavelengths) = 40
- number of interdigital periods per tap, M = 3
- tap aperture, W_T' (wavelengths) = 80
- intertap spacing, d (μm) = $N\lambda_o$ = 620
- number of available taps, L = 65

These parameters approximate the requirements stipulated by equation 4.5 and for this initial design were arrived at through:

(1) specifying a ~5 MHz PN chip rate (=B_s);

(2) the chip rate fixes the intertap spacing, d; mask making constraints result in a 620 μm tap step and repeat interval for (ST,X) quartz, whence B_s = 5.09 MHz;

(3) to simplify input IDT matching; firstly, f_o was chosen to make B_s(%) close to optimum (equation 1.12), and secondly for minimum conversion loss $\hat{R}_{as} \simeq 50\Omega$ (equation 1.11);

(4) *available data* gave $B_{opt} \sim 4\%$ (see Table 1.1) thus, N = 25 and the wavelength - normalised aperture, $W' \sim 40$;

(5) the number of interdigital periods on each tap were chosen for minimal bandlimiting consistent with an acceptable CW conversion loss, $L_{31}<50$ dB and low regeneration $L_{11}>80$ dB, the tap apertures were made wider than the input to counteract beam steering loss on which little reliable data was available.

This mask was one of a set forming a contiguous frequency filter bank (with synchronous frequencies at 127.3, 132.4, 137.5 and 142.6 MHz) designed specifically for FH (Chapters 2, 5) spread spectrum. The performances obtained throughout the set of designs and from device to device varied only slightly (<0.5dB) Results for the lowest frequency design are emphasised because the initial dual-tap[12] AMF was centred at this frequency for direct comparison.

Time domain measurements - AMF impulse and pulse response

The impulse response of an AMF is defined by equation 4.1. To simulate an impulse, a pulse of width less than or equal to one half cycle at the synchronous frequency must be employed. On impulsing, the input IDT generates a bidirectional SAW signal consisting of an rf pulse nominally N cycles long with acoustic wavelength equal to the instantaneous periodicity of the interdigital geometry; nominally λ_o. Imperfections in the launching IDT including geometrical errors present on the photomask and those introduced during device manufacture are reproduced in the acoustic signal. The acoustic pulse propagates along the crystal surface and is sensed by the receiving tap array. The time domain output is given by the convolution of the acoustic signal and the array impulse response.

Figure 4.9A shows the circuit schematic used to observe the impulse response of the SAW AMF. The impulse generator provides a sufficiently short (<5 nS) 5 volt amplitude pulse for use with $f_o \lesssim 200$ MHz when terminated in 50 Ω. The pulse repetition rate is adjusted to include all spurious signals in the pulse period. The amplifiers are selected for their flat gain and phase characteristics and low noise figure. Finally, the use of a wideband oscilloscope allows observation of the VHF output signals.

Direct measurement of insertion loss to one tap can be made by substituting an rf pulse, on a carrier at f_o, for the impulse. Pulses up to N cycles long may be used; wider pulses result in distortion since more than one tap contributes to the output. (This effect also occurs when an input signal is distorted by band-limiting). Figure 4.9B shows the measurement system. The signal from the mixer is split into two equal power pulses by a 3-way pad; one pulse goes to the device and the other through variable attenuators to one channel of the oscilloscope. This signal is used as a reference. The device output is amplified and fed into the other channel of the oscilloscope. It is then possible to compare the amplitudes of all tap output signals by varying the attenuator in the reference channel. Calibration is achieved by replacing the device under test with a variable attenuator adjusted so that the input pulse gives deflection on the oscilloscope equal to that of the reference pulse.

Figure 4.10 shows the impulse responses of two AMF produced from the first-order mask design, described above, by wire bonding to an external rf interconnect pattern. Trace A was obtained from an AMF biphase coded with the 13 chip Barker sequence, trace B shows phase reversals, and trace C corresponds to an AMF coded with a 31 chip

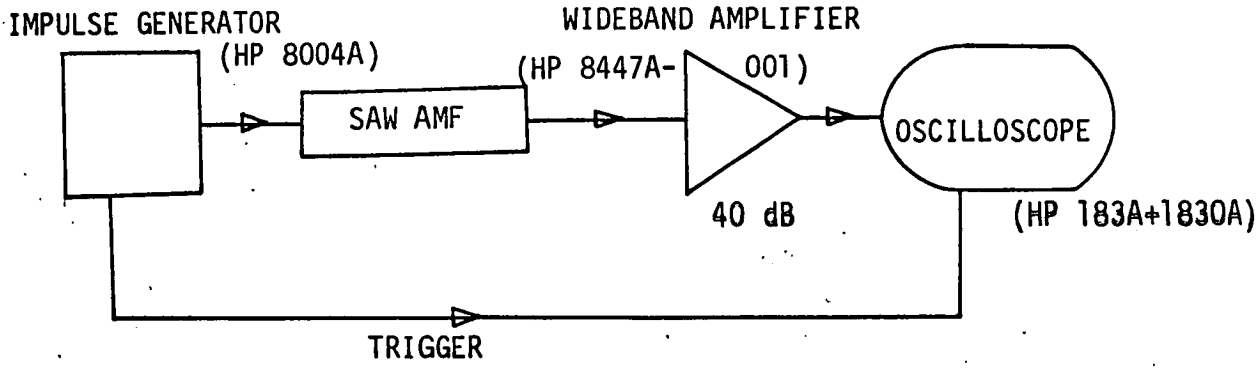

FIGURE 4.9A IMPULSE TESTING

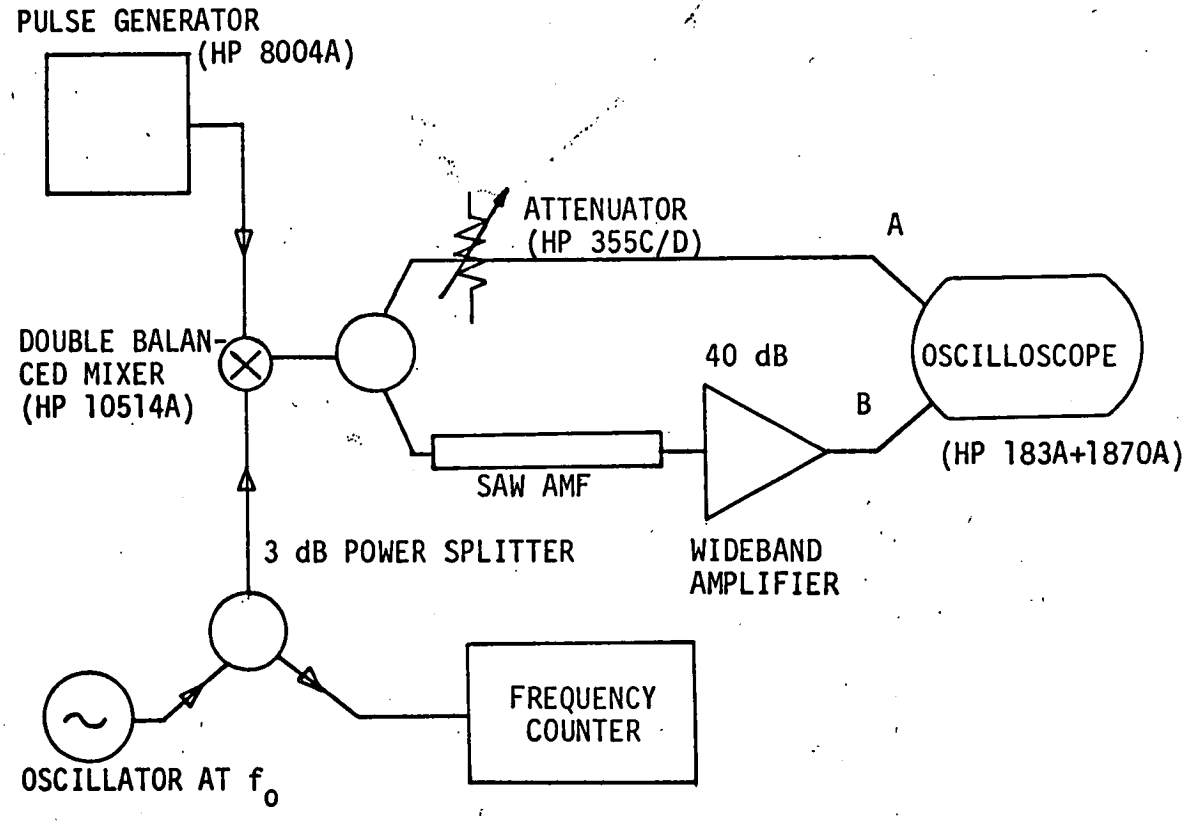

FIGURE 4.9B PULSE TESTING

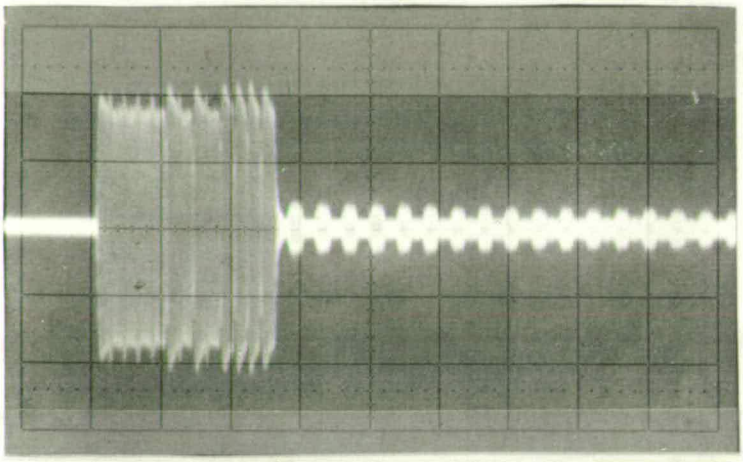

TRACE A: 13 CHIP BARKER CODED AMF; 1.μs/div

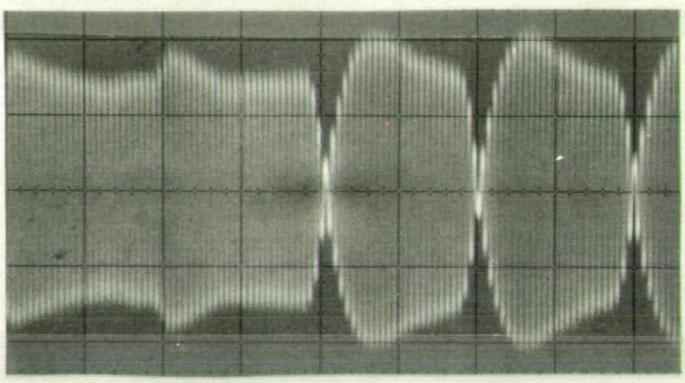

TRACE B: DETAILS OF PHASE REVERSALS; 100ns/div

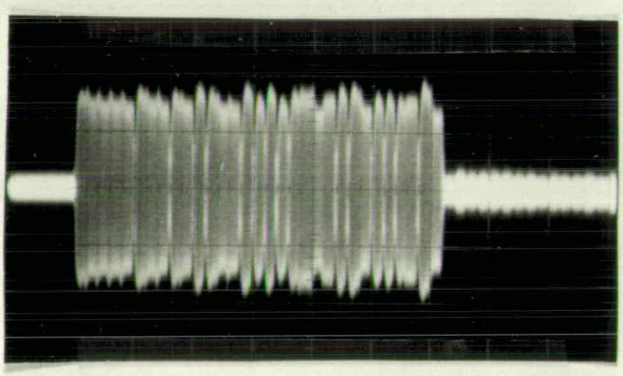

TRACE C: 31 CHIP M-SEQUENCE CODED AMF; 1.μs/div

FIGURE 4.10 IMPULSE RESPONSES OF FIRST ORDER AMF

m-sequence. Both devices clearly exhibit distortional effects.

For the Barker coded device, trace A, a number of well defined spurious acoustic signals having constant widths (~200 nS) and periodicity (~400 nS) extend ≳8 μs beyond the desired phase modulated pulse. The maximum level of these spurious pulses is -17 dB relative to the phase coded output. For the 31 chip m-sequence coded AMF, a different sequence of spurious pulses is obtained having a measured maximum relative level of -20 dB.

Of the distortional mechanisms listed in Section 4.1 only those giving rise to multiple reflections can produce the spurious signals shown. These mechanisms comprise (1) electroacoustic regeneration and (2) acoustic wave impedance mismatch. Figure 4.11 illustrates the production of spurious SAW signals through multiple reflections within the tap array. For clarity the spurious pulse sequences generated by the primary and secondary reflections are drawn separately. Three important points emerge from this simple illustration:

(1) The spurious pulse duration ~τ (ignoring convolutional effects occuring with each tap) and the delay between each primary or secondary spurious ~2τ;

(2) The output signal is comprised of the convolution of the incident pulse with tap array *plus* the convolution of coherent spurious pulses with the tap array: thus the output spurious pattern depends on the specific tap coding; for codes with large imbalance of 0,π chips higher spurious levels should be expected than for "random" codes;

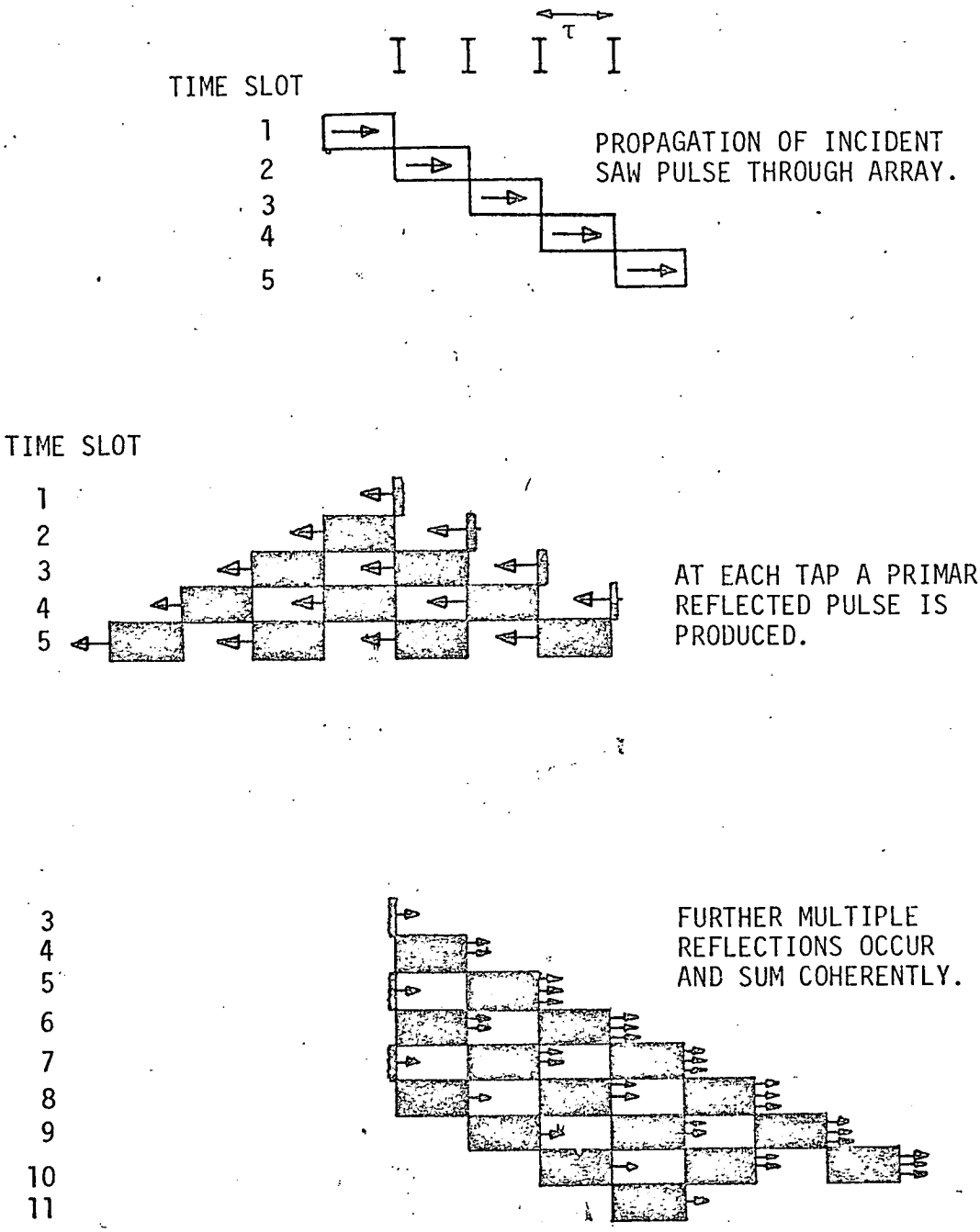

FIGURE 4.11 PICTORIAL REPRESENTATION OF SPURIOUS SAW SIGNAL PRODUCTION

(3) Spurious signals can perturb the amplitude of the phase coded waveform through vector addition of the incident pulse and spurious.

The relative levels of phase coded output and spurious remained constant over a wide range of Q_L obtained by varying R_L and stray capacitance values. Further, the regenerated CW reflection losses computed for both AMF, equations 4.31, 4.34 and 4.35 with C'~ 5 pF, due to the interconnect and $\beta = 0.5$ are >45 dB and >60 dB for the Barker coded device and m-sequence coded device respectively. These facts make acoustic wave impedance mismatch the likely perturbing mechanism[67,68]; see Section 4.2.3, 4.2.4.

For both AMF structures described, a mean insertion loss to one tap of ~55 dB was obtained. With m-sequence biphase coded AMF the mean tap insertion loss should correspond to the CW loss due to the randomness of this class of code. However, the Barker code employed has a theoretical gain of 14 dB for a synchronous CW input over the mean tap insertion loss due to the imbalance (9:4) of $0, \pi$ phase chips. Thus, the CW loss is predicted to be ~41 dB from this measurement. This figure is in good agreement with theory and experiment, see a later sub section.

Time-domain measurement - AMF response to the matched coded waveform

The autocorrelation function (ACF) of any binary waveform depends on the code structure and the mode employed; ie aperiodic or periodic. Aperiodic mode signals may be generated "passively", by impulsing an AMF or "actively" with microelectronic components.

(1) Passive Generation; Expansion-Compression Loop Performance:

The signal is generated by applying either an impulse or an rf pulse of N cycles duration to the AMF input. After suitable amplification, the signal is fed into the device (A*) under test which is arranged to be conjugate, equation 4.1 to the device used for signal generation. The resulting output is displayed on an oscilloscope. Figure 4.12 shows the measurement set up. The following measurements are made:

(1) insertion loss from the generated coded signal to the peak of the compressed output, by substituting attenuator Y for AMF A*;

(2) peak-to-sidelobe ratios, by comparison with a reference signal through attenuator X;

(3) spurious signal level;

(4) base width of autocorrelation peak.

These yield: (1) the compression gain achieved, theoretically equal to 20 $\log_{10}$ [L]; (2) information on the sidelobe pattern for comparison with theory; and, from (4) an indication of the severity of bandlimiting since the basewidth of the ACF peak ideally equals 2τ.

Figure 4.13 shows typical results obtained for the loop (expansion-compression pair in passive generation) performance of the 13 chip Barker coded AMF, trace A and the 31 chip m-sequence coded AMF, trace B. Theoretical ACF responses are given for comparison. The measurements gave the following information:

- both devices achieved near theoretical (<1 dB degradation) compression gain;
- the Barker coded loop produced a peak-to-*maximum* sidelobe ratio of 20 dB ±0.2 dB with a peak-to-spurious ratio of 22 dB ±0.2 dB;

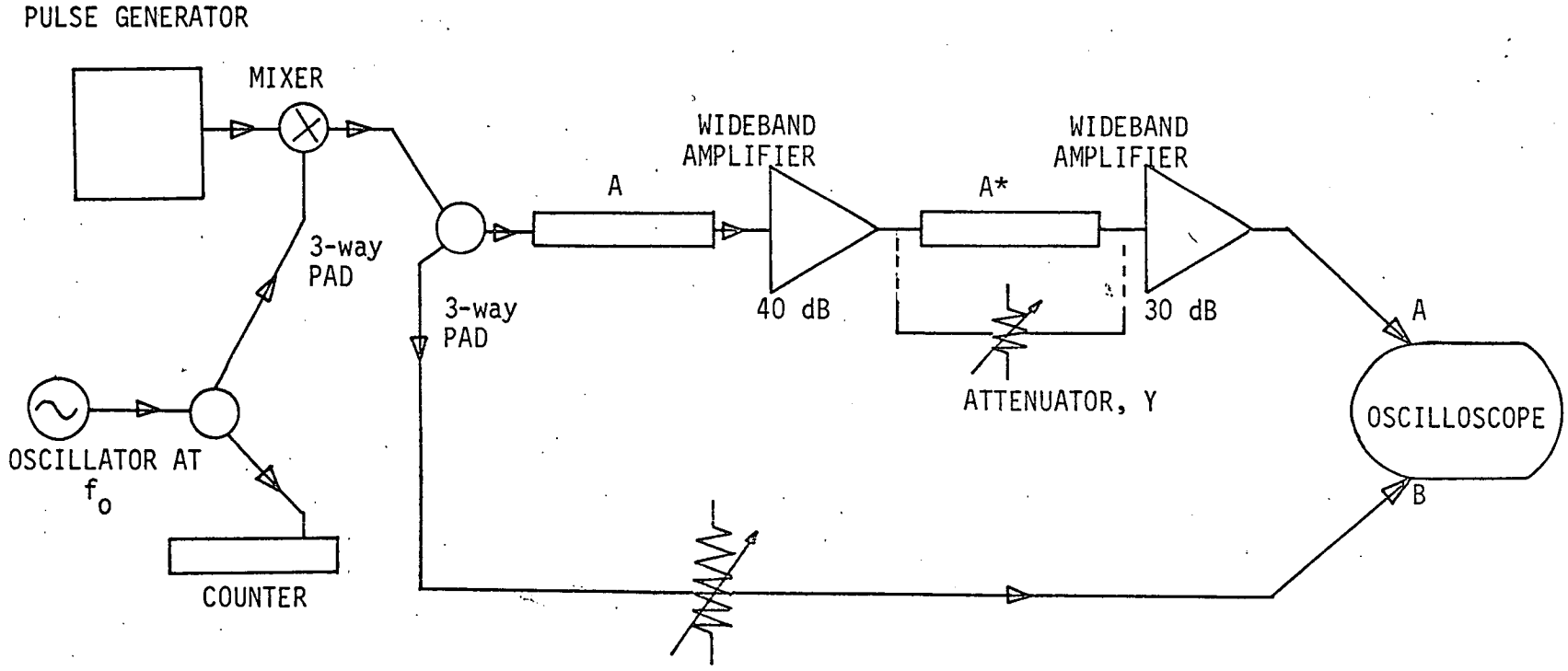

FIGURE 4.12 APERIODIC AUTOCORRELATION MEASUREMENT, EXPANSION/COMPRESSION LOOP

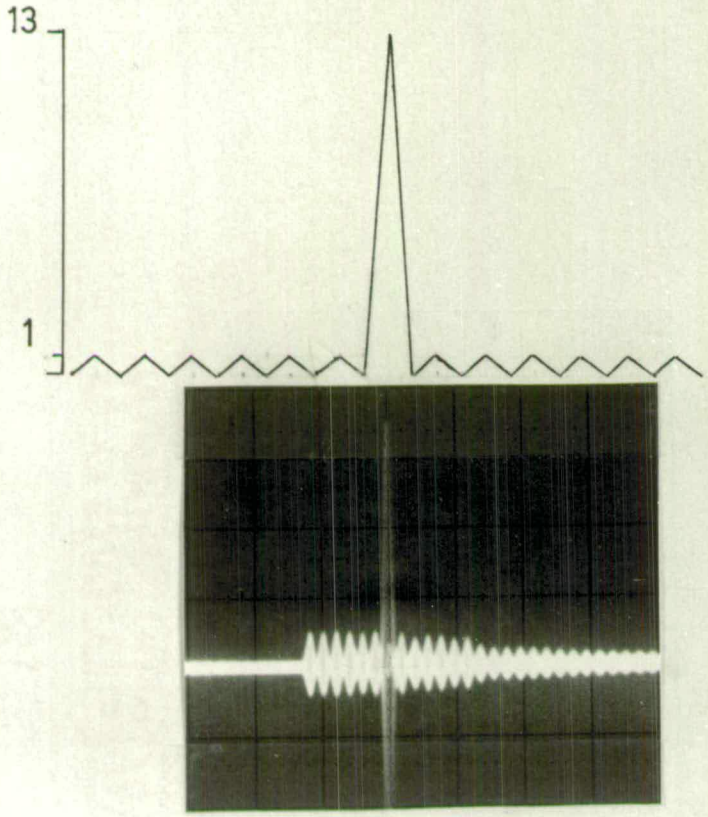

A 13 CHIP BARKER CODED AMF 2μs/div

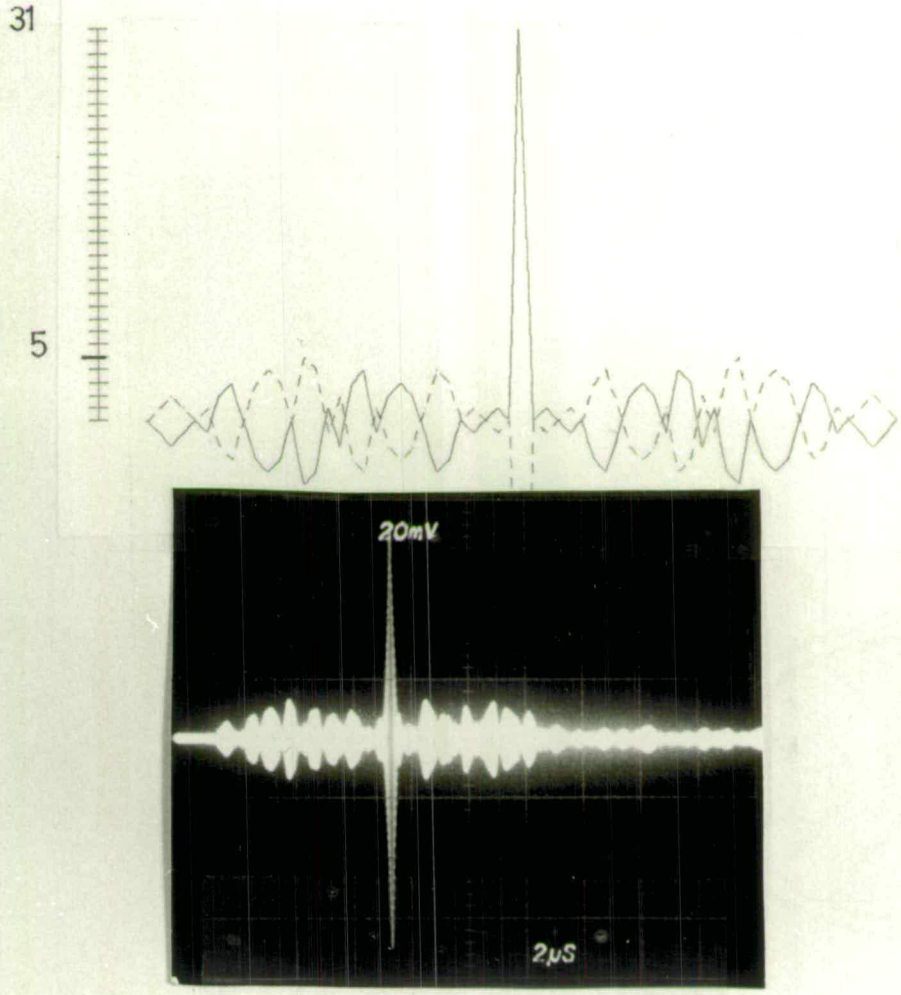

B 31 CHIP M-SEQUENCE CODED AMF

FIGURE 4.13 FIRST-ORDER AMF LOOP PERFORMANCES

- the m-sequence coded loop exhibited a peak-to-*maximum* sidelobe ratio of 16 dB ±0.2 dB and a peak-to-spurious ratio of 25 dB ±0.5 dB;
- the basewidth of the ACF peak ~405 nS compared with 390 nS in theory for both loops hence bandlimiting was occuring.

Although, both loops exhibited close to theoretical compression gains and peak-to-maximum sidelobe ratios, the sidelobe patterns did not closely follow theory.

(2) Active Generation:

A block diagram of the circuitry used to generate biphase modulated aperiodic signals is shown in Figure 4.14. The variable divide by N emitter-coupled logic counter generates a clock at the desired chip rate in synchronisation with the carrier. The clocked sequence generator drives a double-balanced modulator which phase reverses the output when the baseband signal changes level. A trigger pulse generated at the beginning of each code period is used to derive a synchronous gating pulse which drives the other double-balanced modulator. This switches the rf signal on at the beginning and off at the end of the desired phase-coded waveform. The required duty cycle is achieved with appropriate counter circuitry.

Advantages of the active generation method for testing AMF are:

- greater control over the accuracy of the signal is achieved;
- higher signal-to-noise ratios are possible, this allows easier measurement of low-level spurious;

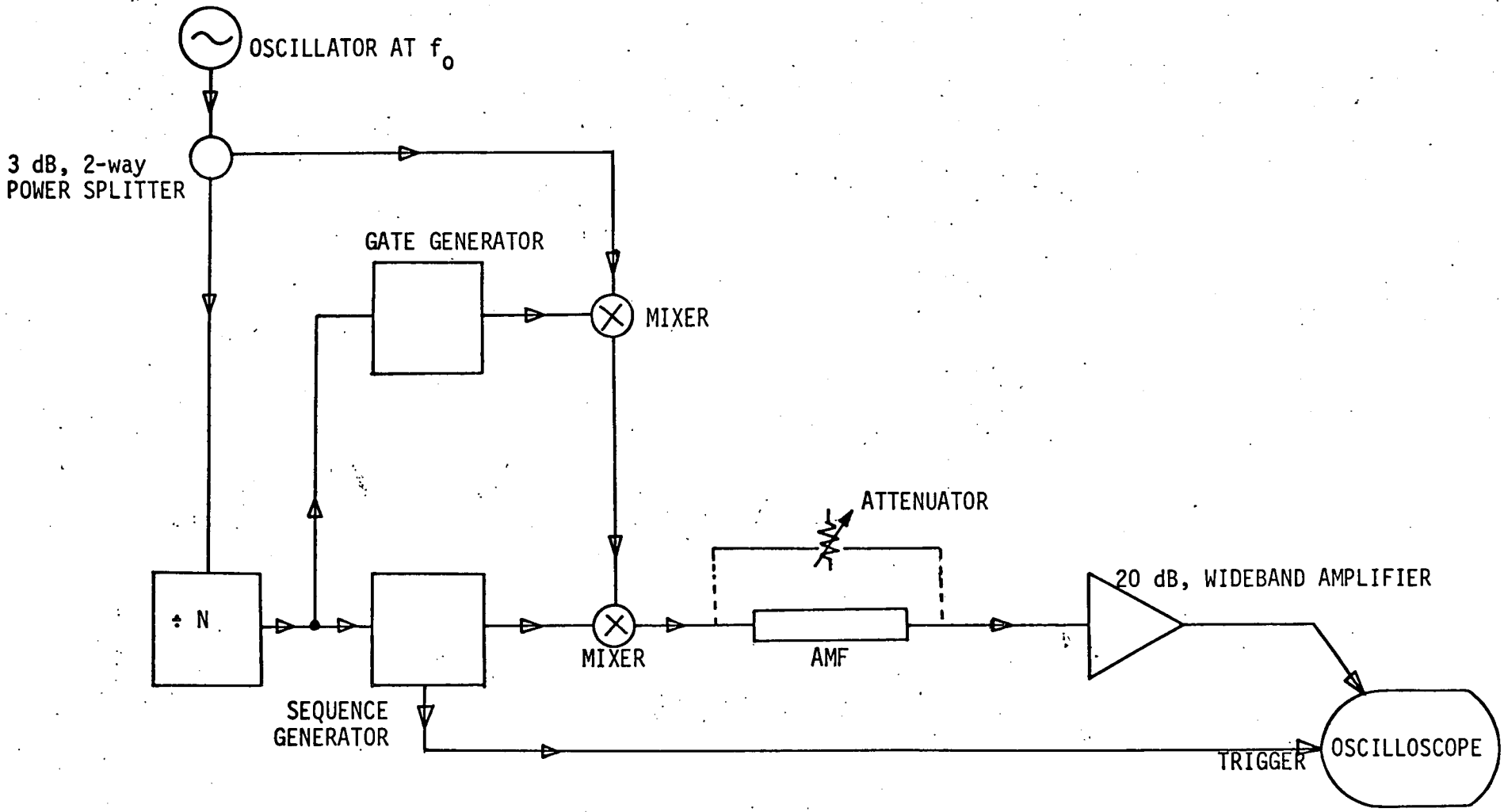

FIGURE 4.14 APERIODIC AUTOCORRELATION MEASUREMENT: ACTIVE GENERATION

- the response to Doppler shifted and adjacent channel signals, see Chapters 5, 6, may be readily ascertained.

An evaluation of the Doppler performance of the 31 chip m-sequence AMF was carried out and the following results were obtained:

(1) the first nulls of the ACF peak theoretically occur for a a frequency offset, Δf given by, from equation 4.8

$$\Delta f = \pm \frac{f_o}{NL}$$

thus, $\Delta f = \pm 164$ kHz

agreement to within ~2 kHz was achieved.

(2) close agreement (<1 kHz difference) was found between experiment and the computed results of Carr et al[46] for the offset in frequency ~80 kHz required to produce 3 dB peak-to-sidelobe degradation.

This experimental method does not suffer from the practical difficulties encountered by Carr et al[46] who impulsed an AMF to generate the psk signal. Then, single-side band mixing plus appropriate bandpass filtering was employed to produce the desired frequency offsets. The main fault in this method lies in the reliance on maintaining fixed relative stability between two local oscillators. Inherent frequency jitter causes amplitude variation of the correlation peak and sidelobes due to degradations in coherence of the generated signal. The resulting decrease in peak-to-sidelobe ratio was reported as 3 dB.

(3) Periodic Input Signal:

The generation of the periodic signal is simply achieved by removing the mixer used as an rf switch from the set up shown in Figure 4.14.

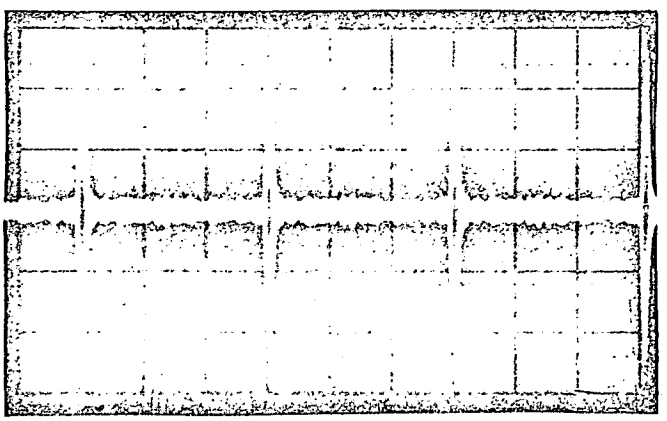

HORIZONTAL SCALE 2 μs/div

FIGURE 4.15 RESPONSE OF 31 CHIP PN CODED AMF TO THE MATCHED PERIODIC INPUT SIGNAL EXHIBITING 22 dB PEAK-TO-SIDELOBE

Figure 4.15 shows the response of the 31 tap AMF to a periodic input. Ideally a two-level ACF, Figure 2.3, should be obtained with a peak-to-sidelobe ratio of 20 $\log_{10}(L)$; which for L = 31 corresponds to ~30 dB. The response shown in Figure 4.15 exhibits a ~22 dB peak-to-sidelobe ratio. Further, the compression gain achieved with a periodic input corresponded to that observed with aperiodic signals.

Frequency-domain measurements

Several important device characteristics may be assessed conveniently through swept-frequency measurement of the scattering parameters with a network analyser[107]. Specifically, the following can be examined: input impedances; input IDT bandwidth; synchronous CW insertion loss; and frequency transfer function.

The display of the electrical reflection coefficient, S_{11}, on either the polar or phase and magnitude oscilloscope units enables accurate determination of input impedance. Return loss measurements using the phase and magnitude display enable rapid impedance matching and bandwidth tayloring.

Figure 4.16A shows a phase and magnitude plot of S_{11} for the 25 period input IDT tuned with a series inductor, and loaded with a series 50Ω resistor to lower the effective Q. This procedure introduced an extra ~7 dB conversion loss, but increased the measured 3 dB bandwidth by ~0.6 MHz. This technique was necessary because the initial design was based on a 4% B_{opt} whereas the actual value is ~4.5% requiring N_{opt} ~22. The amplitude plot (A) has a vertical sensitivity of 2.5 dB/div and the phase plot (B) has a vertical sensitivity of 10°/div. The horizontal axis calibration corresponds to a frequency sweep of ~20 MHz centred at ~127 MHz. The curves show:

- a reflection loss minima of ~10 dB which corresponds to an input impedance of ~100 + j0.Ω;
- a phase change close to the expected[105] 90° phase change through resonance;
- a 3 dB bandwidth of ~5.0 MHz;
- a slight asymmetry due to a marginally low inductance; and
- a small (~1 dB) peak at f_o due to a reflected wave from the tap array.

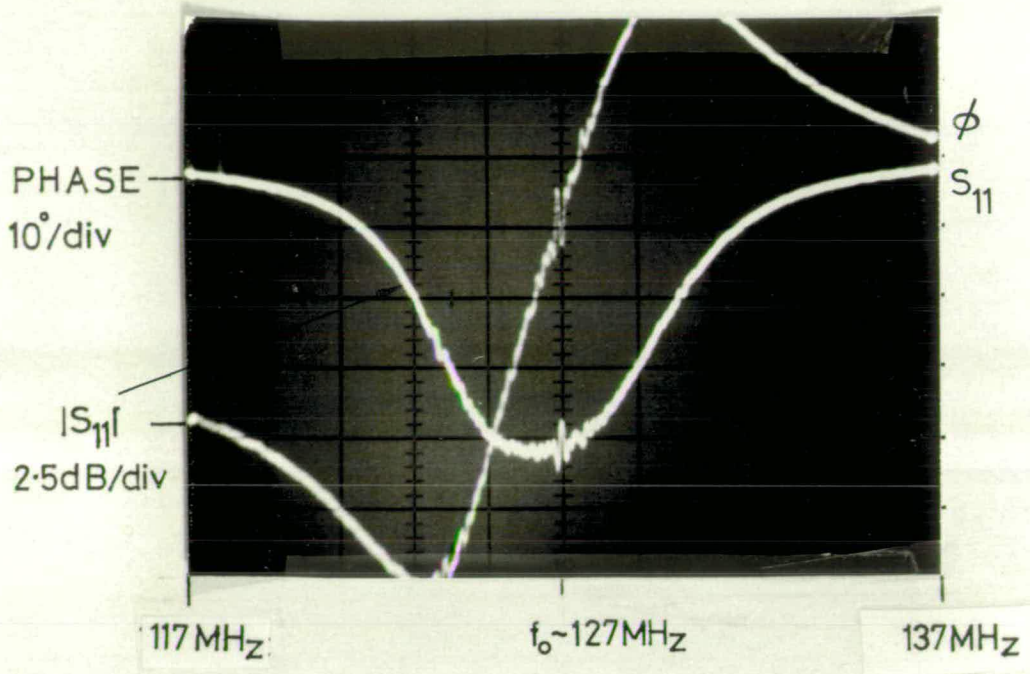

[A] AMPLITUDE AND PHASE PLOT OF TUNED IDT REFLECTION LOSS

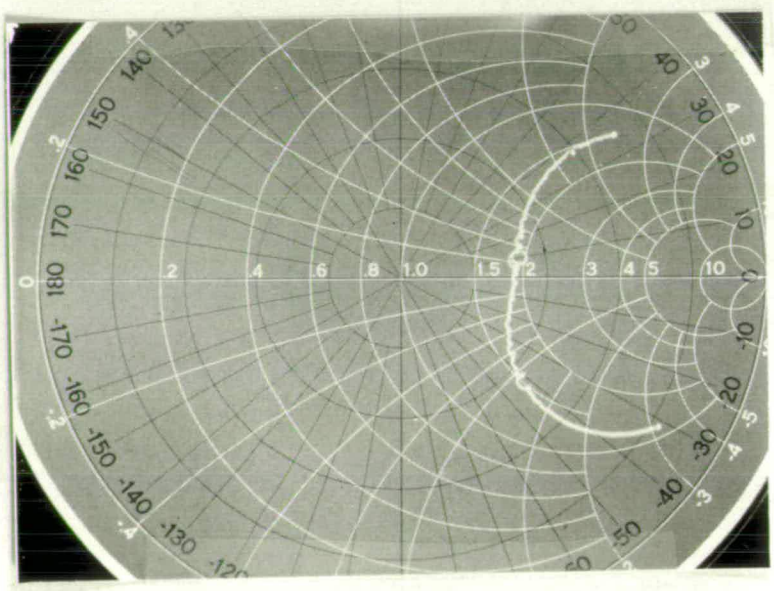

[B] POLAR DISPLAY OF REFLECTION LOSS WITH SMITH CHART OVERLAY

FIGURE 4.16 SWEPT FREQUENCY MEASUREMENT OF TUNED INPUT IDT

Figure 4.16B shows a polar display of S_{11} for the same arrangement with a Smith chart superimposed on the plot for direct measurement of normalised input impedance. The loop at ~2 + j 0.2 corresponds to the acoustic resonance at f_o.

Figure 4.17A shows the reflection loss characteristics of an input IDT designed specifically for use with the two stage input matching network shown in Figure 4.17B. The IDT, again acoustically synchronous at 127.3 MHz, consisted of 24 electrode pairs with acoustic aperture 80λ. ($\hat{R}_{as}$~25Ω). The network was designed to transform the generator impedance (50Ω) to $\hat{R}_{as}$, and give >5 MHz 3 dB bandwidth with <0.5 dB amplitude ripple. The response shown exhibits a 3 dB bandwidth of 8.0 MHz, with an amplitude ripple of <1 dB across 6 MHz centred at f_o, and a return loss at f_o of ~15 dB.

Distortions in the measured transfer function, $H(\omega)$, are difficult to interpret because the contributions from individual taps are not readily isolated. Figure 4.18 shows the results for the 13 chip Barker coded AMF and, for comparison, a theoretical curve computed, using equation 4.7, for the specific first order geometry employed. The vertical scale is logarithmic with a sensitivity of 10 dB/div and the horizontal scale is 4 MHz/div. The first two nulls in the response occur at f_o ±5 MHz which corresponds to the ~5 MHz chip rate for this AMF. The CW insertion loss at f_o was measured from the response curve as 40 dB which is in good agreement with the 41 dB value predicted from the pulse response measurement.

Figure 4.19 shows the transfer function of the 31 chip m-sequence coded AMF together with a theoretical response curve. Again, the experimental curve exhibits nulls at f_o ±5 MHz. The synchronous CW insertion loss was measured as 55 dB in good agreement with the pulse response measurement and theory.

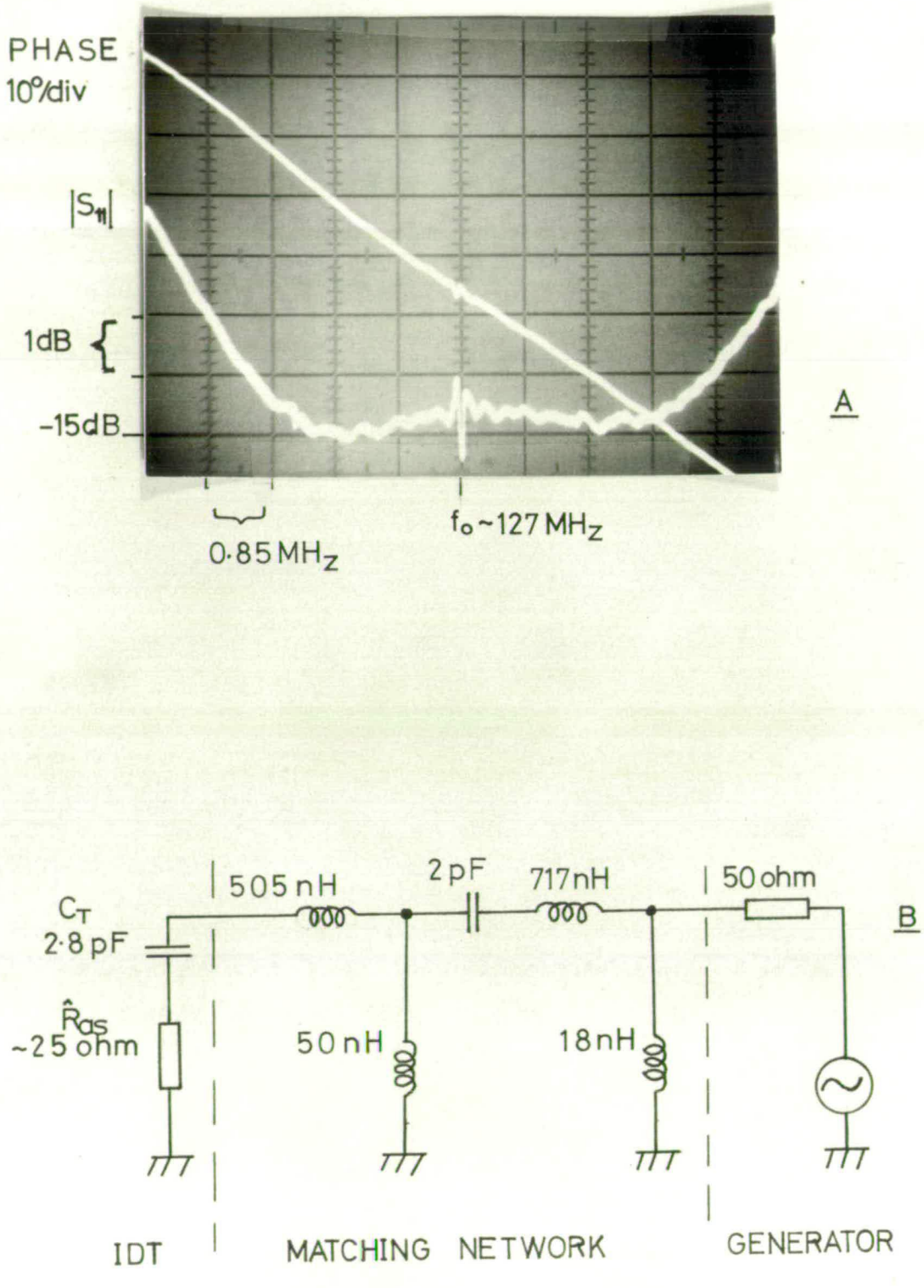

FIGURE 4.17 REFLECTION LOSS CHARACTERISTICS [A]; AND THE 2-STAGE MATCHING NETWORK EMPLOYED[B]

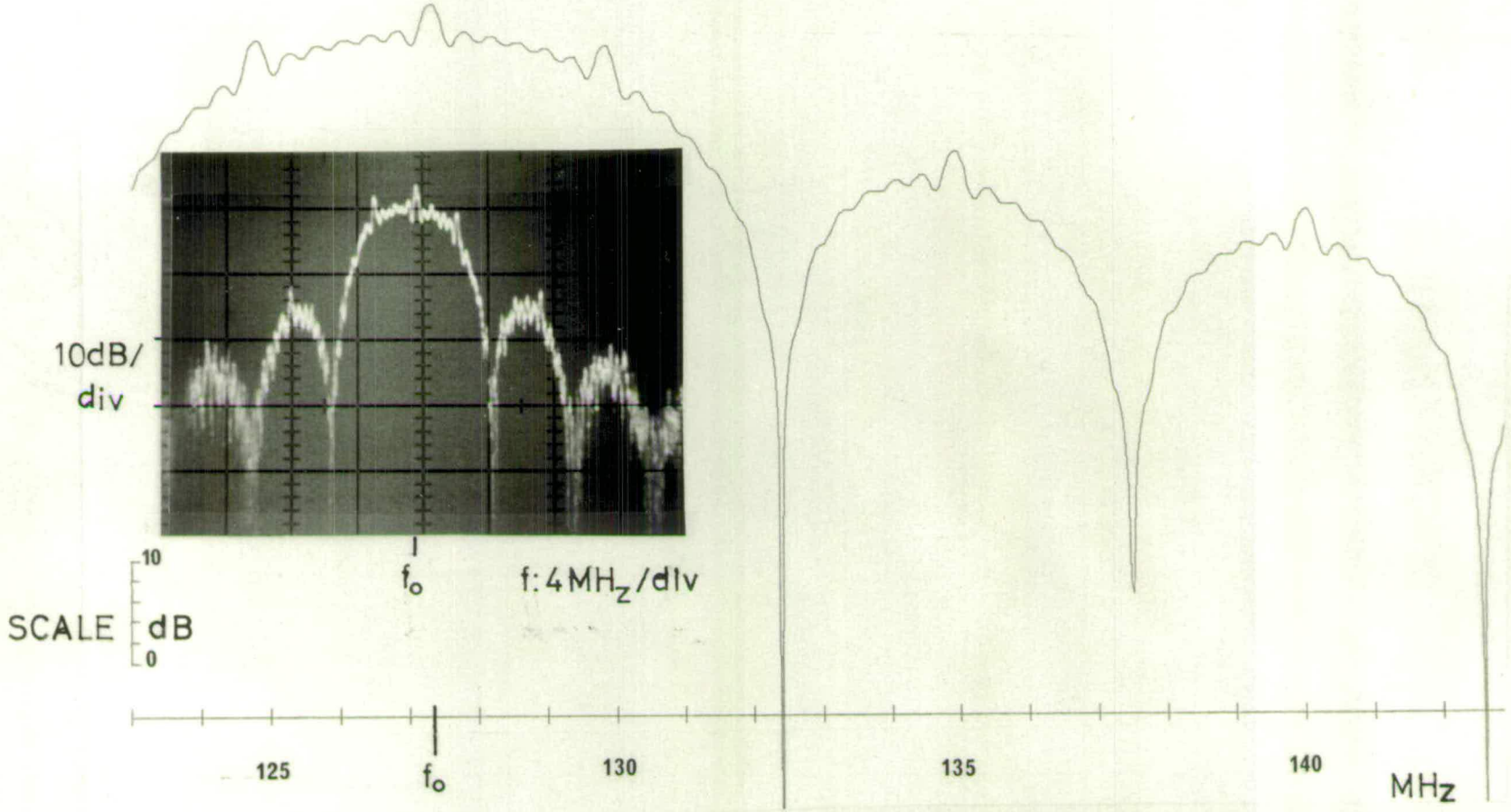

FIGURE 4.18 MEASURED AND THEORETICAL 13 CHIP BARKER CODED FIRST ORDER AMF FREQUENCY-TRANSFER FUNCTION

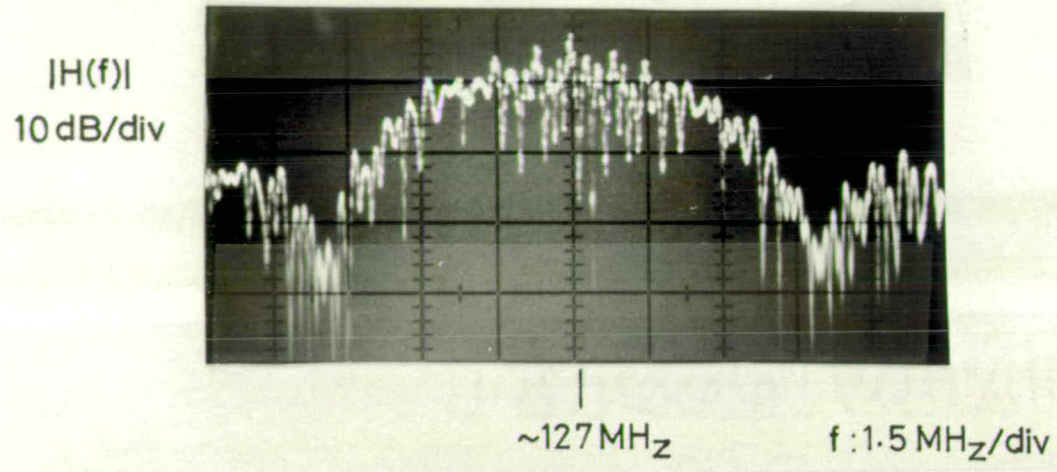

H(f) FIRST ORDER DESIGN

A

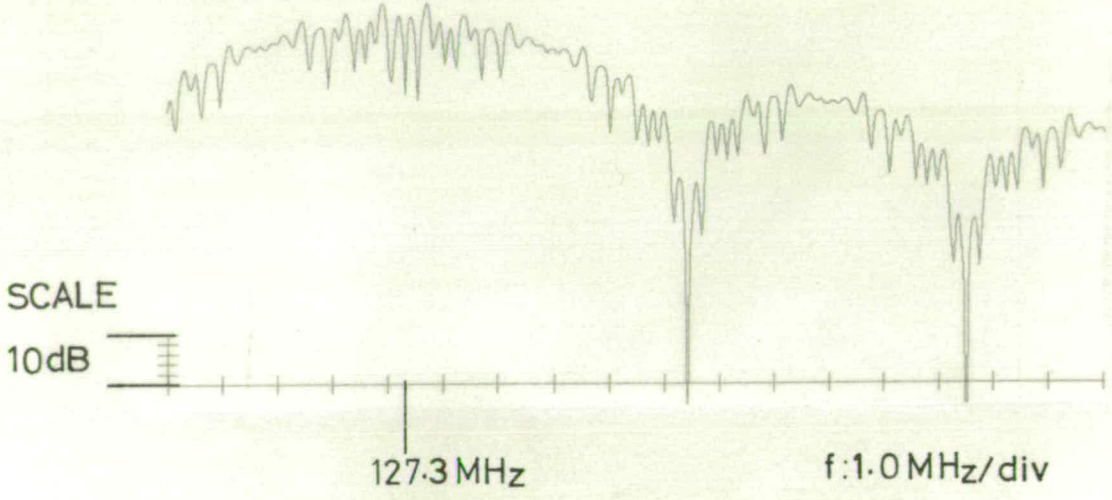

DELTA-FUNCTION THEORY

B

FIGURE 4.19 EXPERIMENTAL [A] AND THEORETICAL [B] 31 CHIP PN CODED AMF TRANSFER FUNCTION

Both response functions show the main features of the ideal theoretical curves but do not closely follow the predicted fine structure. Also, the transfer function is not symmetrical about f_o. For $f>f_o$, a slightly higher loss, ~1 dB, is observed. This is attributed to scattering to bulk modes from the widely spaced periodic discontinuities of the tap array this commences at $f \gtrsim f_o$ for the weakly coupled slow shear modes on (ST,X) quartz.

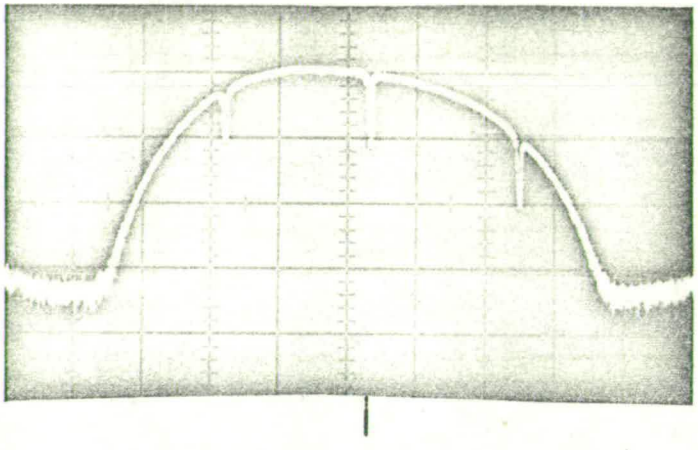

FIGURE 4.20 TRANSMISSION CHARACTERISTICS OF A 65 TAP ARRAY WITH 31 TAPS CODED. SHOWING PERIODIC STOPBANDS DUE TO ACOUSTIC WAVE IMPEDANCE MISMATCH

Figure 4.20 shows the main lobe of the transmission response of a delay line comprising two input IDT separated by a coded 31 tap array plus 34 uncoded taps, ie using the two input IDT of Figure 4.2. The vertical scale is logarithmic with 10 dB/div and the horizontal scale is 1.25 MHz/div

The delay line response not only exhibits nulls spaced approximately ±5 MHz from f_o as expected, but also narrow stop bands occuring at intervals of 2.5 MHz. These stopbands arise from a reflected SAW from each tap in the array; since the taps are periodically spaced at 0.2 μsecond delays the reflections reinforce every 2.5 MHz. The transmission characteristic was measured for loads on the array varying from R_L = 0 to 1 kΩ without measurable change in the response. A key indication that the most important source of distortion arises from wave-impedance discontinuity.

4.2.3 Analysis of Acoustic Wave Impedance Mismatch

The presence of IDT metal electrodes modifies the electrical and mechanical boundary conditions at the substrate surface. On high coupling materials, the principal effect is to reduce the wave velocity under the metal electrode due to shorting of the tangential electric field. Both the velocity slowing and mass loading produce discontinuities in acoustic wave impedance resulting in acoustic reflections. These primary reflections are also partially reflected at successive discontinuities. Although the reflected wave amplitude is small for a single electrode, the reflections can sum coherently to give a significant resultant wave in a large array; witness Figure 4.20.

The discontinuity in the medium may be represented by an *effective* change (ΔZ) in the characteristic wave impedance (Z_o) of the unloaded medium. The reflected wave amplitude is proportional to the parameter ($\Delta Z/Z_o$). It is not generally possible to define a scalar wave impedance in keeping with a transmission line model of wave propagation. However, the assumption made is consistent with extensions of the one dimensional crossed-field model which incorporate an impedance change proportional to the change in SAW velocity[27]. Thus, for each electrode edge, an

effective acoustic reflection coefficient (S_{11}) may be determined:

$$S_{11} = \left| \frac{Z_m - Z_o}{Z_m + Z_o} \right| \qquad \ldots 4.37$$

where Z_m is the impedance of the metallised region. For $\Delta Z = Z_m - Z_o \ll 1$:

$$S_{11} = \frac{\Delta Z}{2Z_o} \qquad \ldots 4.38$$

Now, from Smith et al[9] for *thin* metal films:

$$\left| \frac{\Delta Z}{Z_o} \right| \simeq \frac{1}{2} k^2 \qquad \ldots 4.39$$

where k^2 is the electromechanical coupling constant.
Thus, for (ST,X) quartz, S_{11} is approximately 0.00043 when including the shorting effect only. A simple approach enables the computation of the resultant reflected SAW signal as a function of array geometry. The assumptions made are as follows:

- each electrode in the tap array is regarded as an independent line scatterer with constant amplitude reflection coefficient $r(\omega) = r = 2S_{11}$
- the maximum reflected signal, $\hat{R} \ll 1$, allowing multiple internal reflections to be neglected, and
- depletion of power from the incident beam due to bulk mode generation and over coupling may be ignored.

A significant reduction in reflected SAW power over a wideband may be accomplished by deploying an electrode array spaced an odd number of quarter wavelengths from the active tap electrodes. This has been implemented in two different ways:

splitting each tap electrode[27,68] to form a doublet with electrodes spaced by $\lambda_o/4$, and arranging a dummy array[12] spatially interlaced with the receiving array, with members of the dummy array positioned an odd number of synchronous quarter-wavelengths from the corresponding members of the receiving array.

The tap geometries are illustrated in Figure 3.1, their effectiveness in spurious signal suppression may be judged by comparing the reflected power levels with the power reflected from an array of conventional taps.

For conventional taps the normalised complex amplitude of the resultant reflected wave is given by:

$$R(j\omega) = \sum_{\ell=1}^{L} \sum_{m=1}^{2M} r \cdot \exp j\omega[2(\ell-1)N\lambda_o/v_s + (m-1)\lambda_o/v_s] \quad \ldots 4.40$$

which may be expressed in closed form:

$$R(j\omega) = r. \frac{(1-\exp jL\psi)}{(1-\exp j\psi)} \cdot \frac{(1-\exp jM\phi)}{(1-\exp j\phi)} \quad \ldots 4.41$$

where $\psi = 2\ N\lambda_o/v_s$, and $\phi = \omega\lambda_o/v_s$ and the reflected wave amplitude from each electrode is given by

$$r \sim \Delta Z/Z_o$$

Hence, the normalised reflected power is given by

$$P_{11}(\omega) = r^2 \frac{\sin^2(L\psi/2)}{\sin^2(\psi/2)} \cdot \frac{\sin^2(M\phi)}{\sin^2(\phi/2)} \quad \ldots 4.42$$

maxima of $(2rLM)^2$ occur when

$$f = f_o \pm n\ f_o/2N \quad \ldots 4.43$$

where $n = 0, 1, 2 \ldots$

For a dual array, or split-electrodes the complex reflected wave amplitude is given by

$$R'(j\omega) = R(j\omega)\ [1 + \exp j(2\omega\, b\, \lambda_0/v_s)] \qquad \ldots 4.44$$

The corresponding normalised reflected power is

$$P'_{11}(\omega) = 4\ .\ P_{11}(\omega)\ .\ \cos^2(\theta/2) \qquad \ldots 4.45$$

where $\theta = 2\omega\, b\, \lambda_0/v$ and b is the spacing of electrode sets expressed in synchronous wavelengths. Thus, for zero reflected power at acoustic synchronism, $\theta = \pi$ which is achieved by selecting

$$b = (2p + 1)/4 \qquad \ldots 4.46$$

where p = 0, 1, 2 ...

With split-electrodes, $b = \frac{1}{4}$ and for dual taps

$$b_{min} = (2M + \tfrac{1}{4})$$

Figures 4.21 and 4.22 compare the normalised power reflected from conventional and split-electrode, and conventional and a dual array geometry respecitvely. The parameters chosen correspond to the first order design: f_0 = 127.3 MHz, N = 25, M = 3, d = 620 μm and L = 65.

With either geometry, reflection peaks still occur at $f_0 \pm n\, f_0/2N$, (n = 1, 2, ...) because the taps act as a periodic grating with acoustic stop bands occuring at one half the chip rate. These can be significantly reduced with split electrode geometries by filling in the inter-tap regions with $\lambda_0/8$ electrodes shorted together as described by Judd et al.[27,68] The effect of periodically loading the surface in this manner is to shift the acoustic stop bands and synchronous bulk mode frequencies to twice their original values, while not altering the periodicity for excitation of the surface wave. This array geometry does not solve the

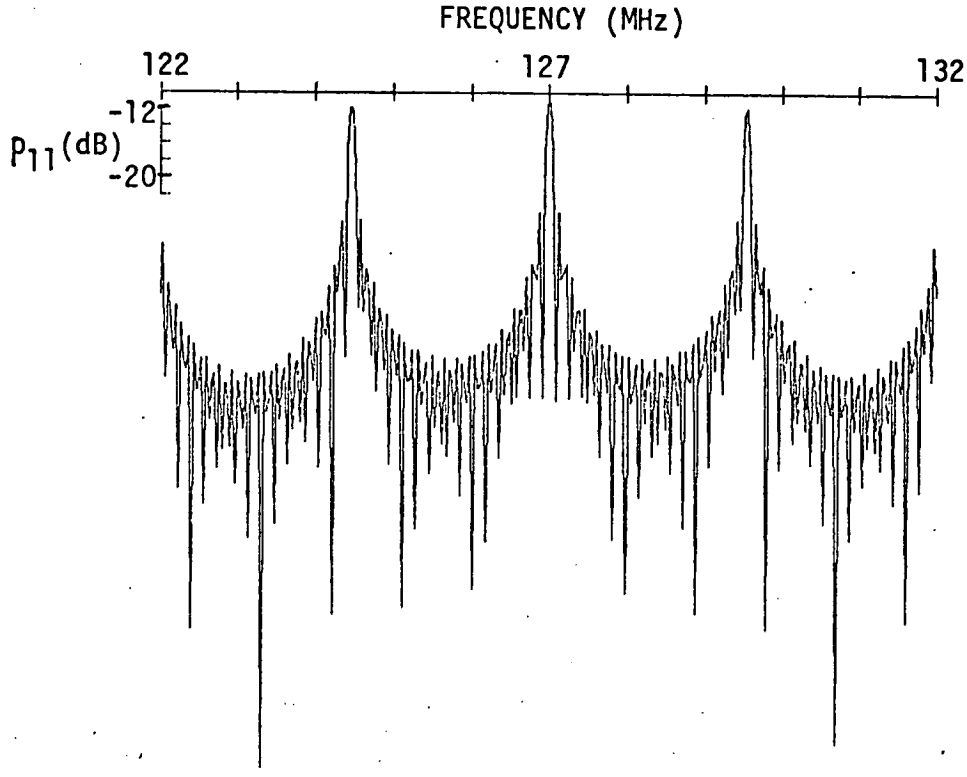

A CONVENTIONAL TAP ARRAY

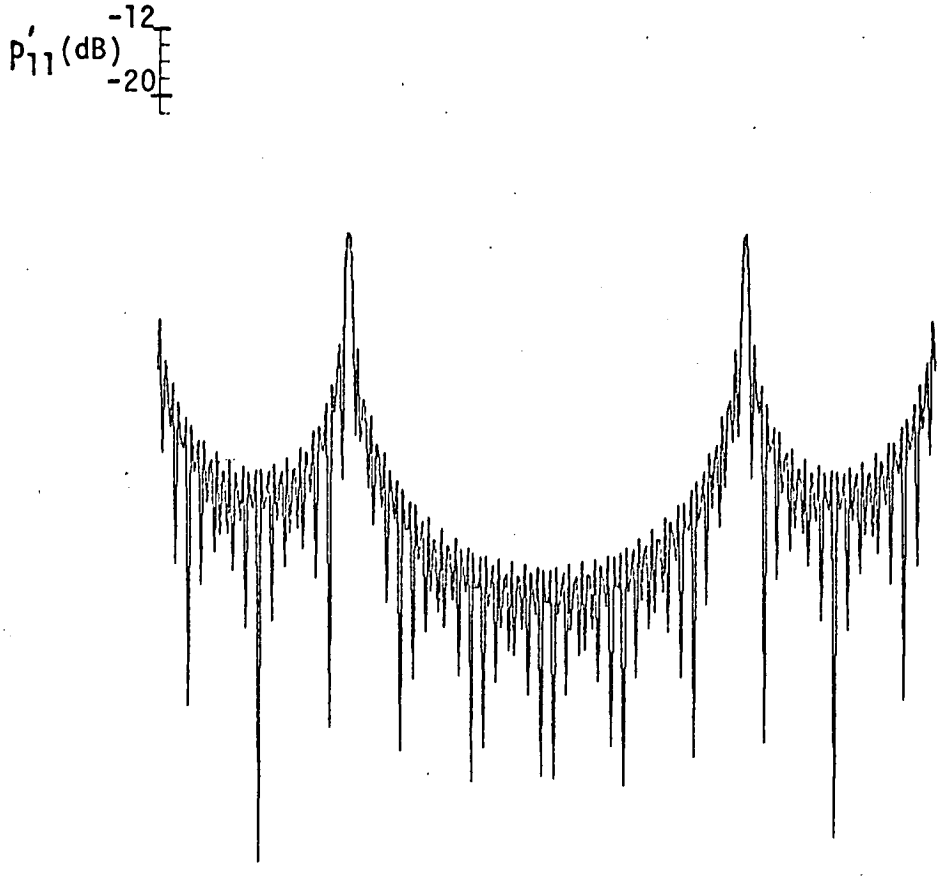

B SPLIT-ELECTRODE TAP ARRAY

FIGURE 4.21 COMPARISON OF REFLECTED ACOUSTIC POWER LEVELS (ρ_{11}) DUE TO IMPEDANCE MISMATCH FROM AN ARRAY OF 65 CONVENTIONAL TAPS (A) AND AN ARRAY SPLIT ELECTRODE TAPS (B), d = 620 μm, M = 2.

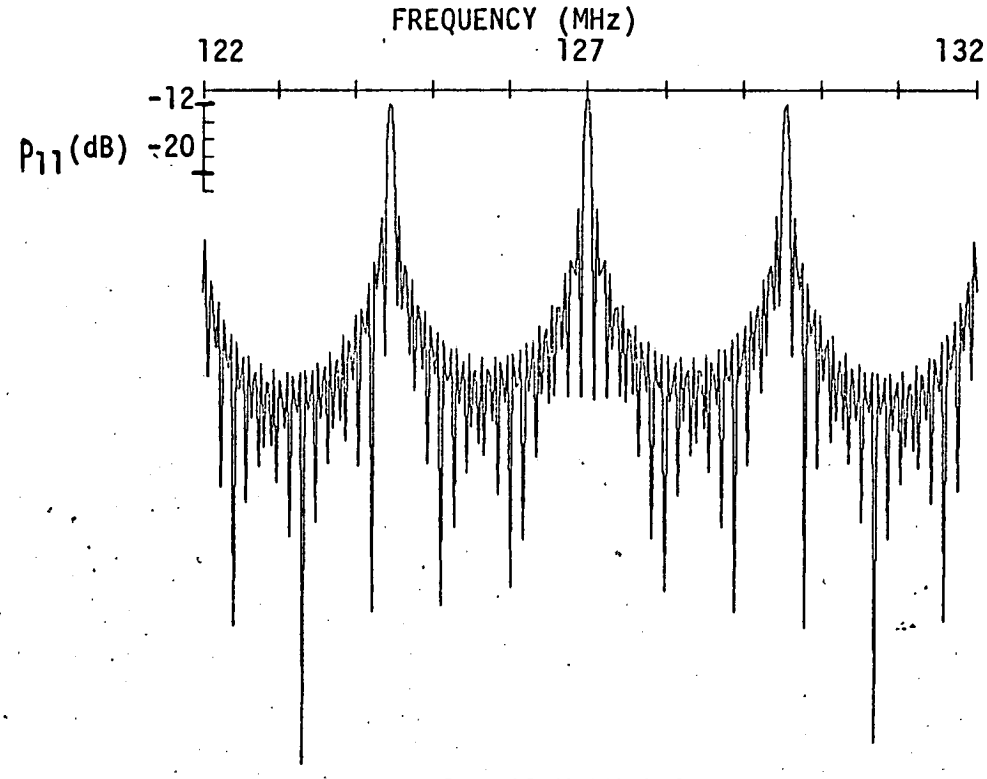

A CONVENTIONAL ARRAY

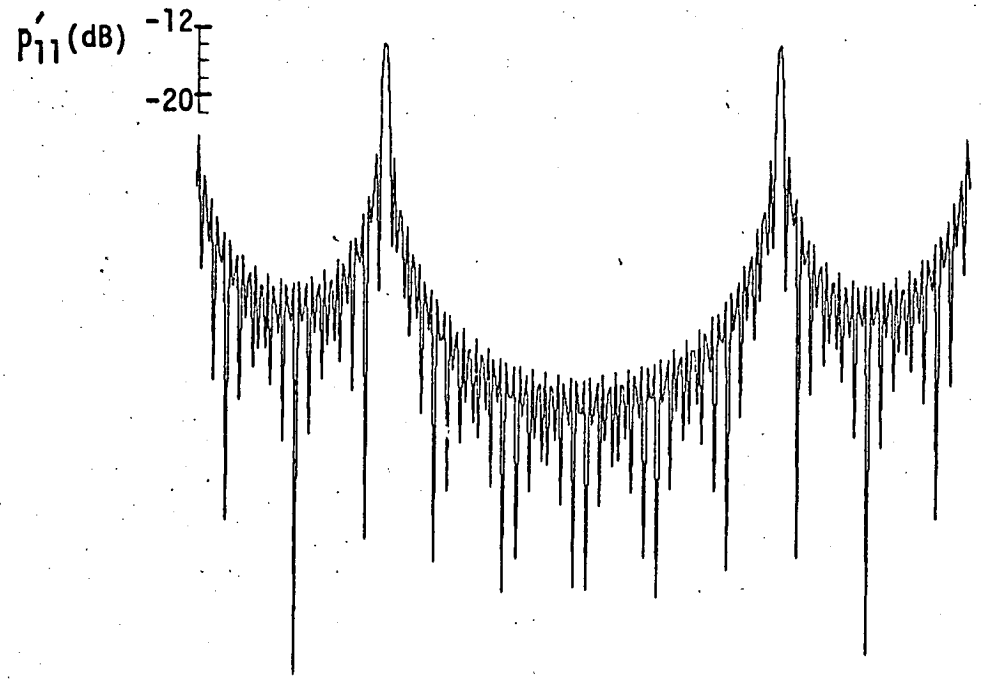

B DUAL-TAP ARRAY

FIGURE 4.22 COMPARISON OF REFLECTED ACOUSTIC POWER LEVELS (P_{11}) DUE TO IMPEDANCE MISMATCH FROM AN ARRAY OF 65 CONVENTIONAL TAPS (A) AND AN ARRAY OF DUAL TAPS (B). d = 620 μm, M = 2.

problem of regenerated spurious which is related to the external load, equations 4.21 and 4.31.

In contrast, the *dual-tap geometry will suppress regenerated signals* when both arrays are identically terminated, but will *increase the level of scattered bulk modes*. These may be reduced either by (1) using multi-layer metallisation, as reported by La Rosa[71] et al, in conjunction with the dual-tap configuration; or (2) splitting each dual-tap electrode and filling in the intervening space with a shorted dummy array as described above.

The major disadvantage with the split-electrode technique is the increased resolution required and, for the dual-tap geometry the major disadvantage lies in the additional interconnection complexity. The next section describes results with these improved geometries.

4.2.4 Performance of Second-Order AMF Designs

Three second-order AMF designs were evaluated, the design parameters are given in Table 4.1.

TABLE 4.1 DETAILS OF SECOND-ORDER AMF DESIGNS

	DESIGN		
	A[12]	B	C
Geometry	D	S	D
f_o (MHz)	127.3	81.5	118.3
N	24*	14*	10*
Chip rate (MHz)	5.09	5.09	9.85
d (μm)	620	620	320
M	2	2	2
W_I	$80\lambda_o$	$77\lambda_o$	$82\lambda_o$
W_T	$80\lambda_o$	$65\lambda_o$	$75\lambda_o$
Insertion loss (dB)	53 (31 taps)	50	60
L	65	63†	127†
Code	--	$x^6 + x^1 + 1$	$x^7 + x^3 + 1$
Initial vector	--	<111111>	<1111111>

Key: D, dual-tap; S, split electrode; * broad band matching; † precoded.

Design A, Figure 4.23, was initiated for comparison with the first order design with the difference that the input IDT aperture was doubled and N reduced by 1 to facilitate broad band matching, and to reduce loss, $\alpha \sim 0$ equation 4.35. Figure 4.24 shows the loop performance of a conjugate AMF pair matched to the 13 chip Barker code with the unused (dummy) array on both filters loaded with[12] 50Ω. In comparison with the conventional geometry, the sequence of spurious pulses following the phase coded waveform generated by the expansion filter are reduced[12] by ~7 dB to -24 dB (top of the narrow spikes) trace A. The narrow spikes are a consequence of the delay between receiving and dummy taps which results in incomplete overlap of the two spurious signals[12]. In the region of complete overlap the suppression is >20 dB. Trace B shows the compressed pulse with a peak-to-maximum sidelobe ratio of 21 dB±0.2 dB with a peak-to-spurious ratio of 30 dB±0.5 dB. The theoretical[44,45] peak-to-sidelobe ratio for this code is 22.3 dB, Figure 4.13A. The insertion loss to a synchronous CW signal was 41 dB and the insertion loss from the expanded pulse to correlation peak was 33 dB. Hence, the measured compression gain is 22 dB (22.3 dB theory).

Again, for comparison with the initial AMF, design A was coded with the 31 chip m-sequence with characteristic polynomial $x^5 + x^3 + 1$ commencing with the initial vector<11111>. Figure 4.25 shows the impulse response, trace A; response to actively generated aperiodic signals, trace B; trace C is expanded about the ACF peak; and the response to a periodic matched signal, trace D. The spurious levels, on the impulse response are <-25 dB down on the expanded pulse. The mean loss to one tap was measured as 54 dB in good agreement with the measured CW loss of 55 dB. A taper,~1 dB, is evident on the impulse response. The normalised power extracted from the ℓ^{th} tap is given by:

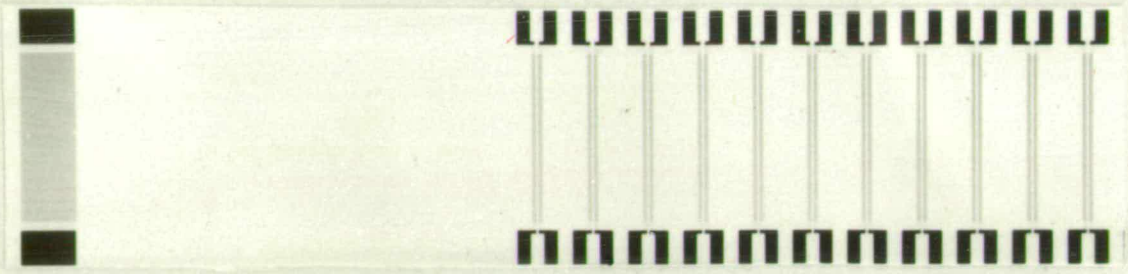

DUAL-TAP ARRAY

FIGURE 4.23 SECOND-ORDER AMF: DESIGN A

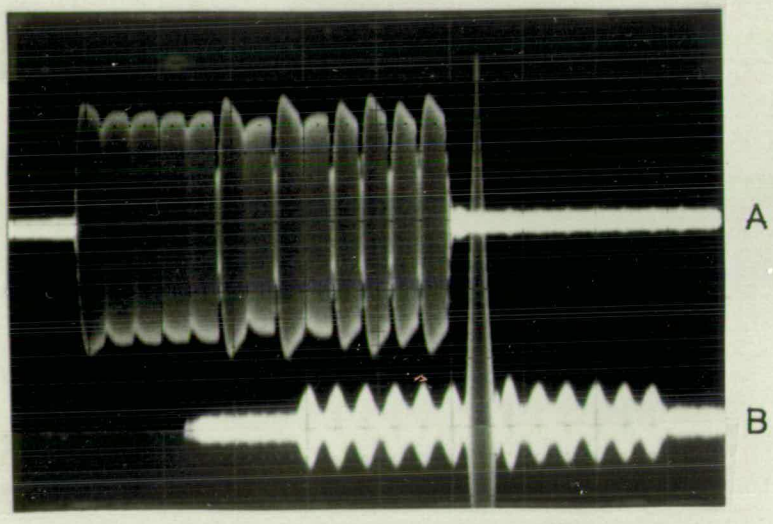

FIGURE 4.24 DESIGN A PERFORMANCE:

13 CHIP BARKER CODED TAPS

TRACE A: EXPANSION AMF IMPULSE RESPONSE 0·5μs/div

TRACE B: COMPRESSION AMF OUTPUT 1μs/div

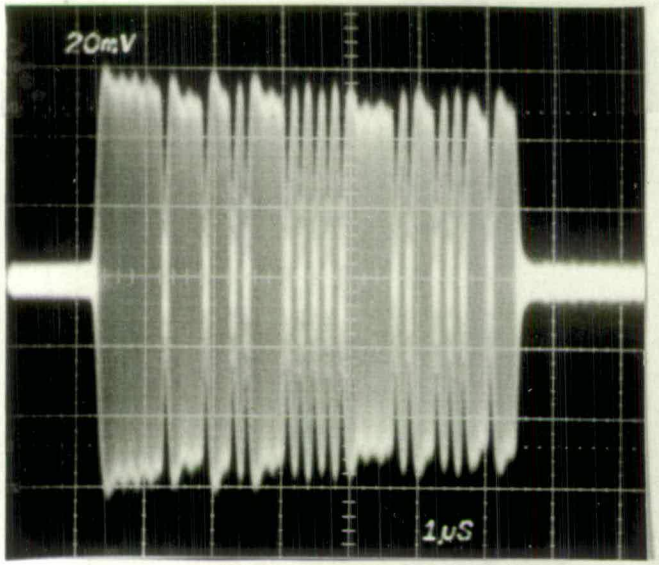

A IMPULSE RESPONSE

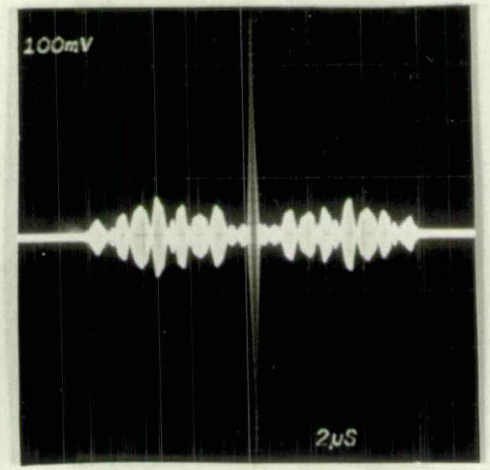

B RESPONSE TO APERIODIC I/P

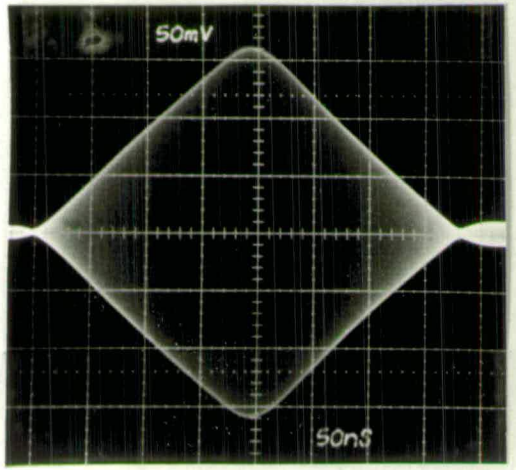

C EXPANDED PEAK

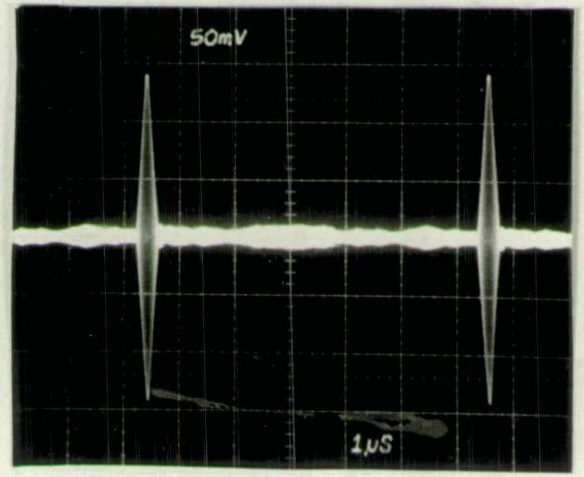

D RESPONSE TO PERIODIC I/P

FIGURE 4.25 DESIGN A PERFORMANCE: 31 CHIP M-SEQUENCE CODED TAPS

$$P_{\ell} = p_{31}\,[1 - p_{31} - p_{11}]^{(\ell-1)} \qquad \ldots 4.47$$

where the power scattering coefficients are assumed constant for each tap in the array. Scattering to bulk modes, propagation loss and diffraction and beam steering have been neglected. Now, $p_{31} \sim 10^{-4}$ and $p_{11} \sim 4r^2 \sim 7.4 \times 10^{-7}$ for each tap. Hence, the ratio of output powers for the first and 31st taps is:

$$\frac{P_1}{P_{31}} \simeq [1 - p_{31} - p_{11}]^{-30} \qquad \ldots 4.48$$

which, on substituting for p_{31} and p_{11} and converting to decibels, indicates a taper of ~0.015 dB on the impulse response. Thus, the mechanism producing the roll-off is not totally due to depletion of power by preceding taps. Propagation loss[21] over the 6.2 μsec pulse is ~0.42 dB, and hence provides a significant proportion of the loss. Beam steering and diffraction losses[21], equations 1.13, 1.14 are insignificant <0.05 dB which leaves ~0.5 dB loss unaccounted for, part of which is due to bulk mode generation as the SAW pulse propagates through the dual array.

The response to the aperiodic matched signal, trace B, accurately follows the theoretical response shown in Figure 4.13. A peak-to-sidelobe ratio degradation of 0.5 dB was obtained and spurious signals were -30 dB on the peak. Trace C shows the expanded peak having a basewidth of 380 nsec in good agreement with the theoretical value of 390 nsec. Trace D shows the performance for a periodic input signal having a peak-to-maximum sidelobe ratio of ~24.0 dB compared with the ~30 dB theoretical value and exhibiting an improvement of only ~2 dB over the first-order design. This is due, in part to the two stop bands occuring at ±2.5 MHz from f_0.

Figure 4.26 shows the measured transfer function for the m-sequence coded AMF where the fine structure closely follows the theoretical curve calculated from the Tancrell and Holland δ-function model. Trace A has a vertical sensitivity of 10 dB/div and a horizontal calibration of ~1.5 MHz/div, the corresponding figures for trace B are 2.5 dB/div and 0.5 MHz/div.

Design B, Figure 4.27 comprises a split-electrode tap array plus the dummy fill-in array to *suppress bulk mode scattering*. Figure 4.28 shows the impulse response, trace A; the response to actively generated periodic signals, trace B; and the loop performance, trace C. Spurious signal levels of <-25 dB on the expanded pulse, trace A, together with <0.5 dB taper were obtained. The measured CW insertion loss was 49 dB in good agreement with theory. The periodic ACF exhibited a degradation in peak-to-sidelobe ratio of ~10 dB from a theoretical value of 36 dB. The insertion loss to the peak was 14 dB indicating a close to theoretical compression gain. Trace C, shows the loop performance which accurately follows the theoretical performance given for comparison. A degradation of <0.5 dB was obtained in the peak-to-maximum sidelobe ratio. Spurious signals were measured at -40 dB with respect to the peak. Figure 4.29 shows the measured and theoretical transfer functions, which are in close agreement.

Figure 4.30A shows the dual-tap geometry of design C which is coded with a 127 chip m-sequence at the step and repeat stage. Figure 4.30B shows the implementation of the phase change. The performance is shown in Figure 4.31. Trace A shows the impulse response with a mean loss to each tap of ~62 dB and a roll-off ~2 dB. Trace B shows the response to the periodically generated matched signal exhibiting a peak-to-sidelobe ratio of 29 dB in comparison with the theoretical level of ~42 dB.

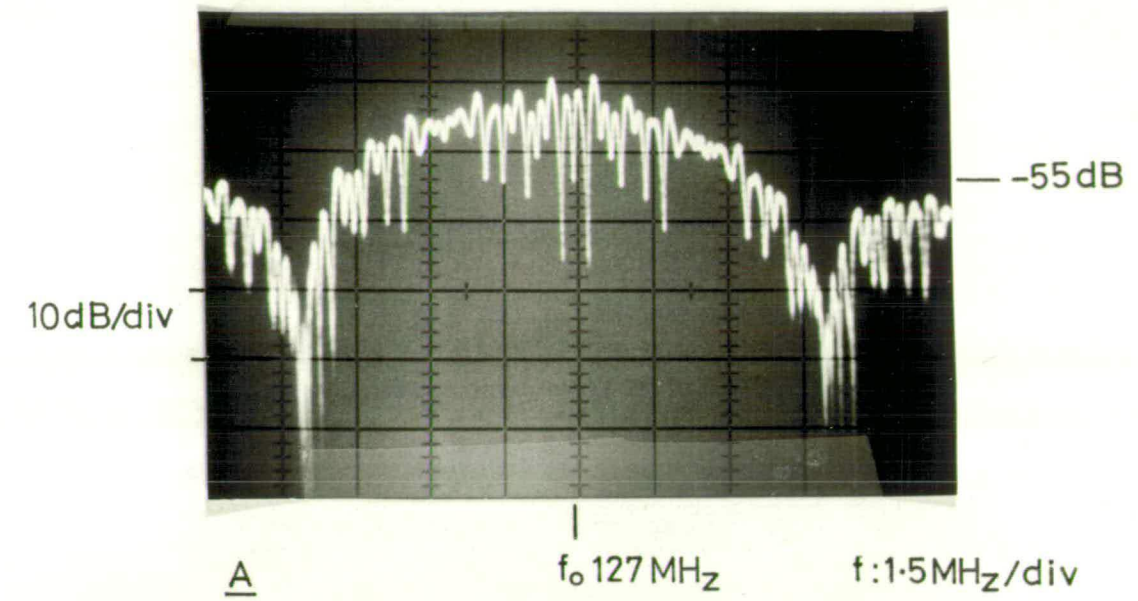

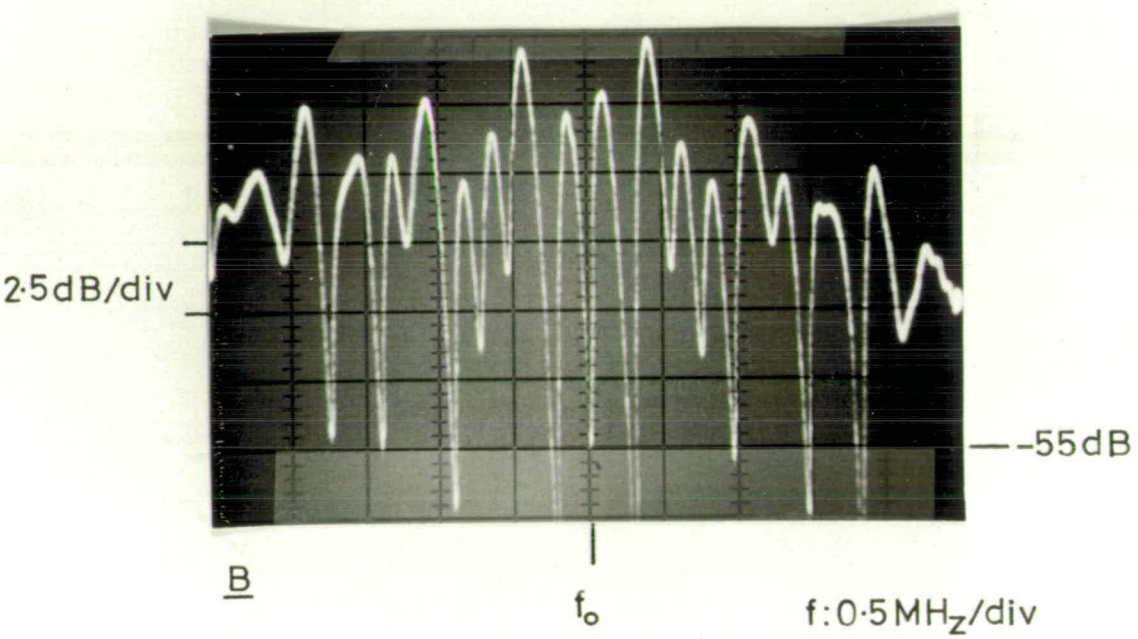

FIGURE 4.26 DESIGN A PERFORMANCE: H(f) 31 TAP AMF

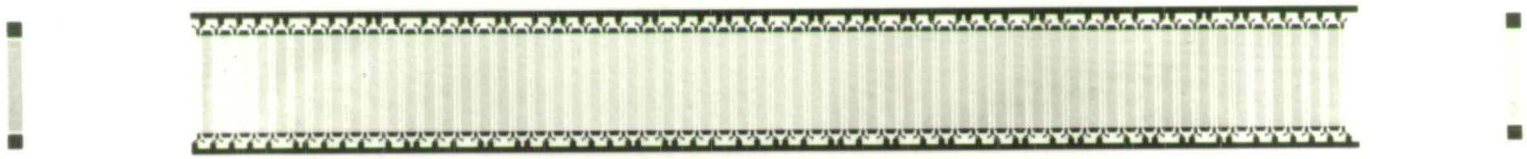

SPLIT-ELECTRODE + FILL-IN ARRAY

FIGURE 4.27 SECOND-ORDER AMF: DESIGN B

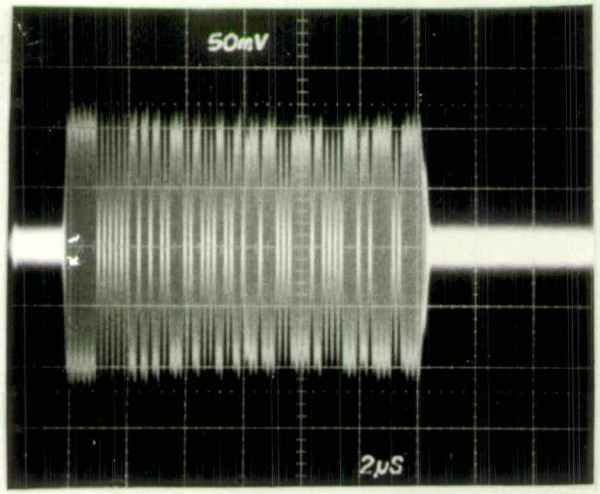

A IMPULSE RESPONSE

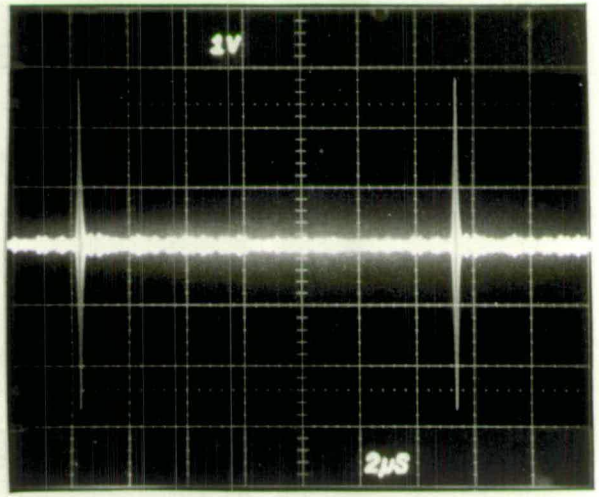

B RESPONSE TO PERIODIC I/P

FIGURE 4.28 DESIGN B PERFORMANCE

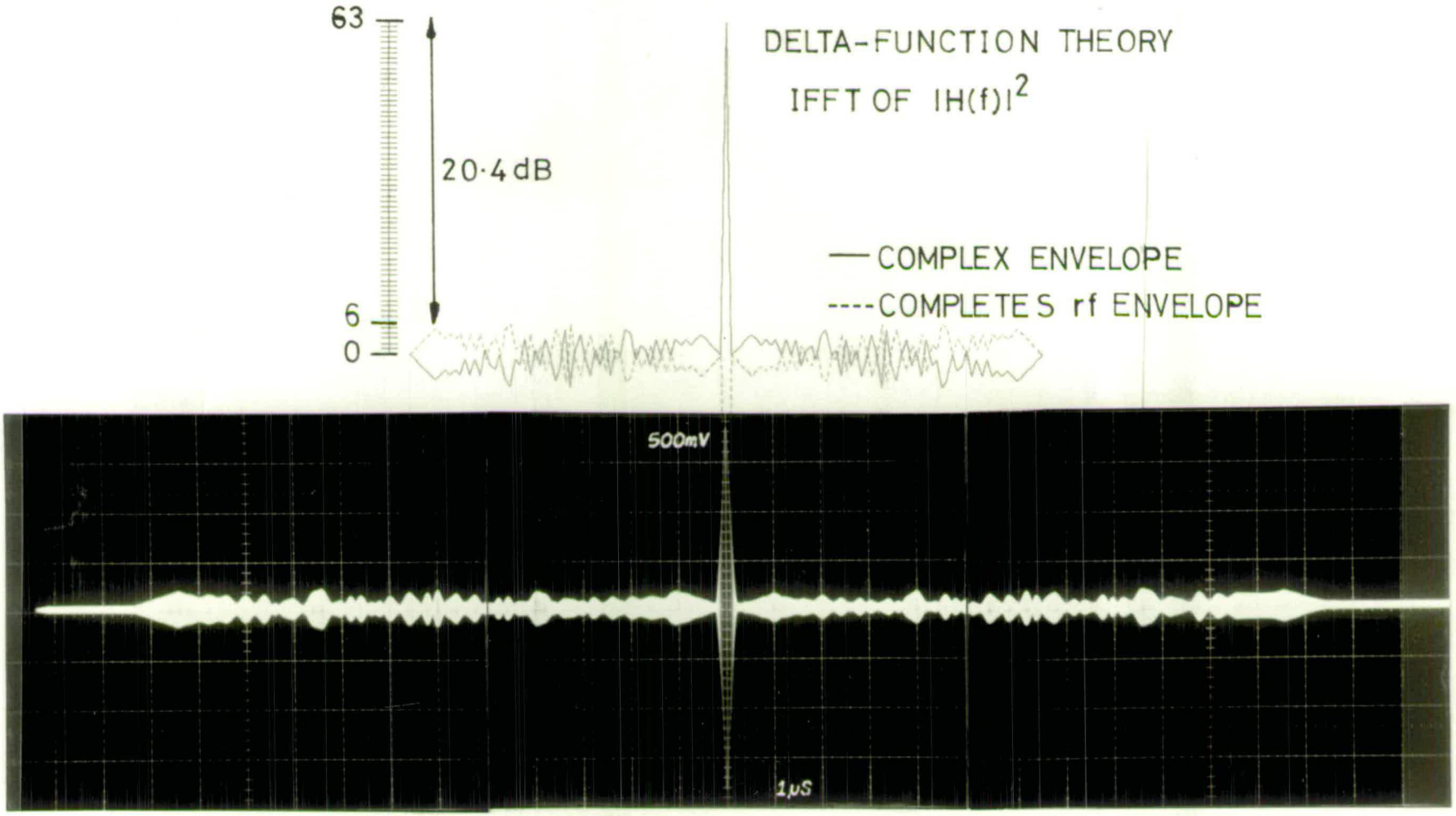

C

FIGURE 4.28 DESIGN B THEORETICAL AND EXPERIMENTAL LOOP PERFORMANCE

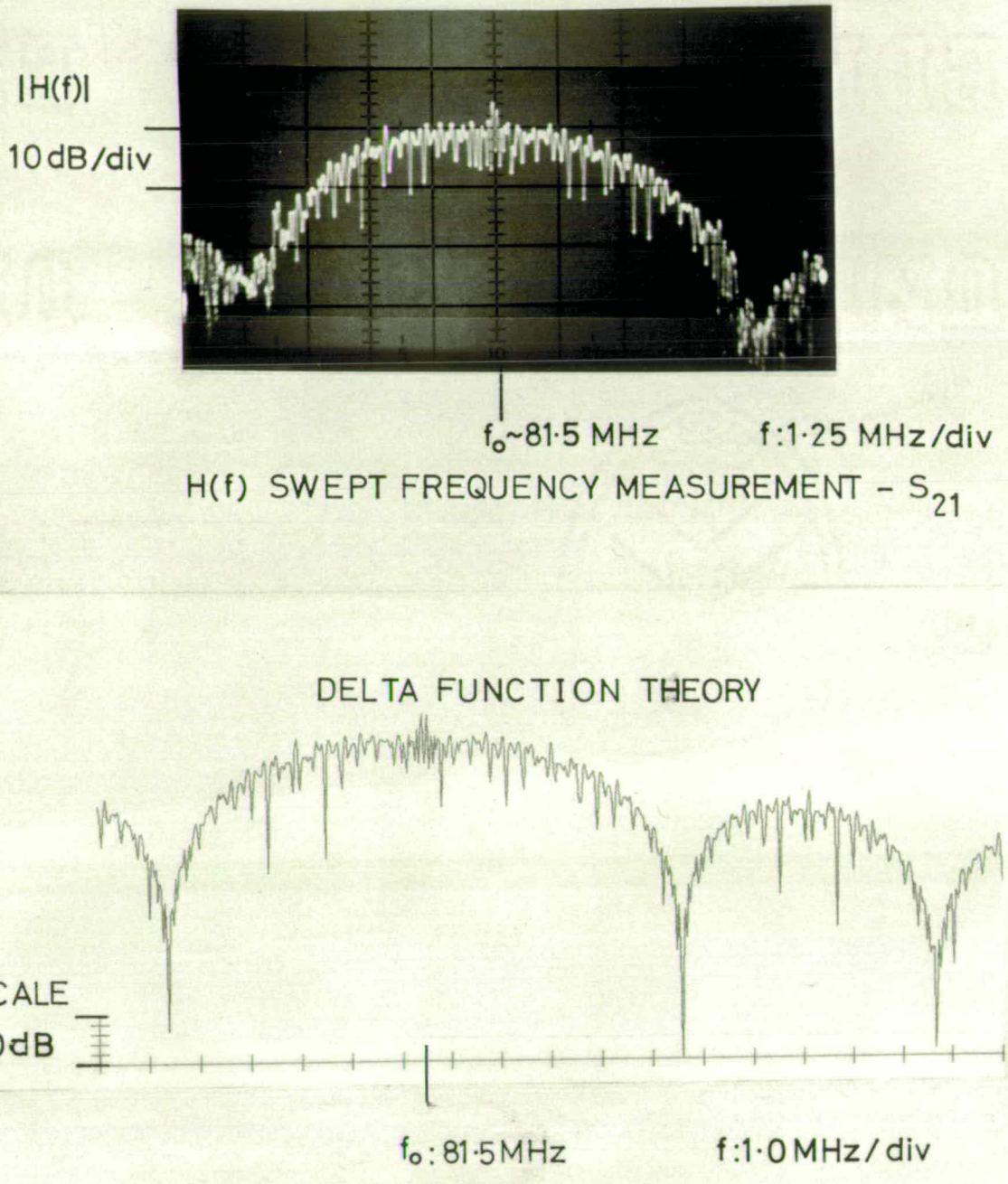

FIGURE 4.29 DESIGN B MEASURED AND THEORETICAL 63 CHIP PN CODED AMF TRANSFER FUNCTION

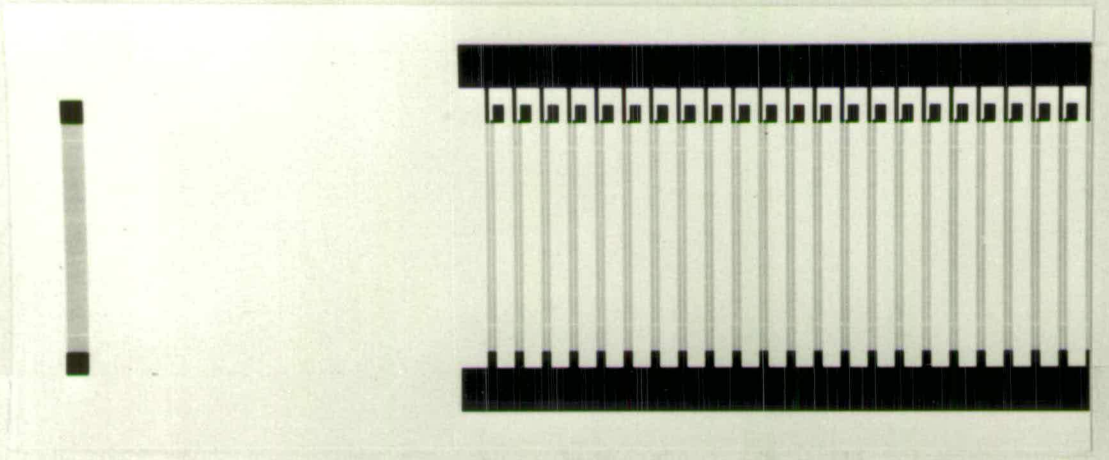

A DUAL-TAP ARRAY DETAIL

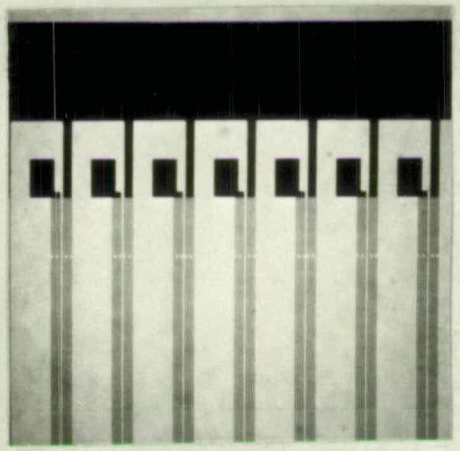

B 1 -1 -1 1 -1 1 1
TAP POLARITY REVERSALS

FIGURE 4·30 SECOND-ORDER AMF: DESIGN C

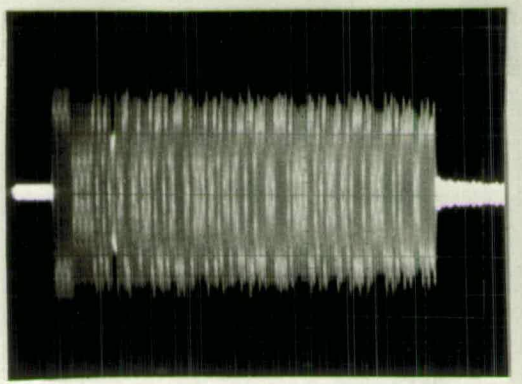

A IMPULSE RESPONSE 2μs/div

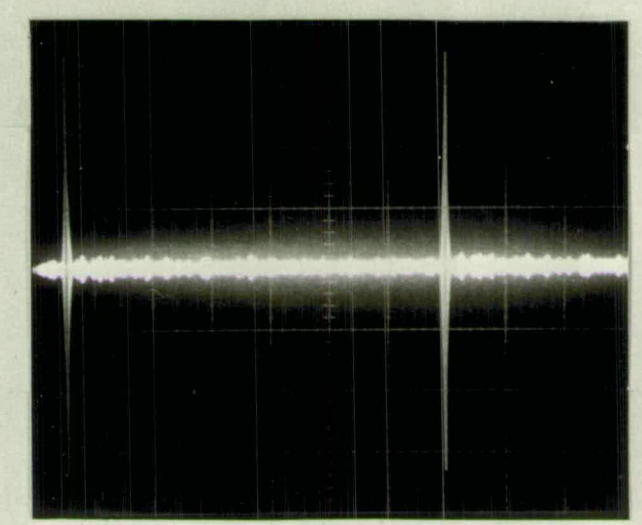

B RESPONSE TO PERIODIC I/P 2μs/div

FIGURE 4·31 DESIGN C PERFORMANCE

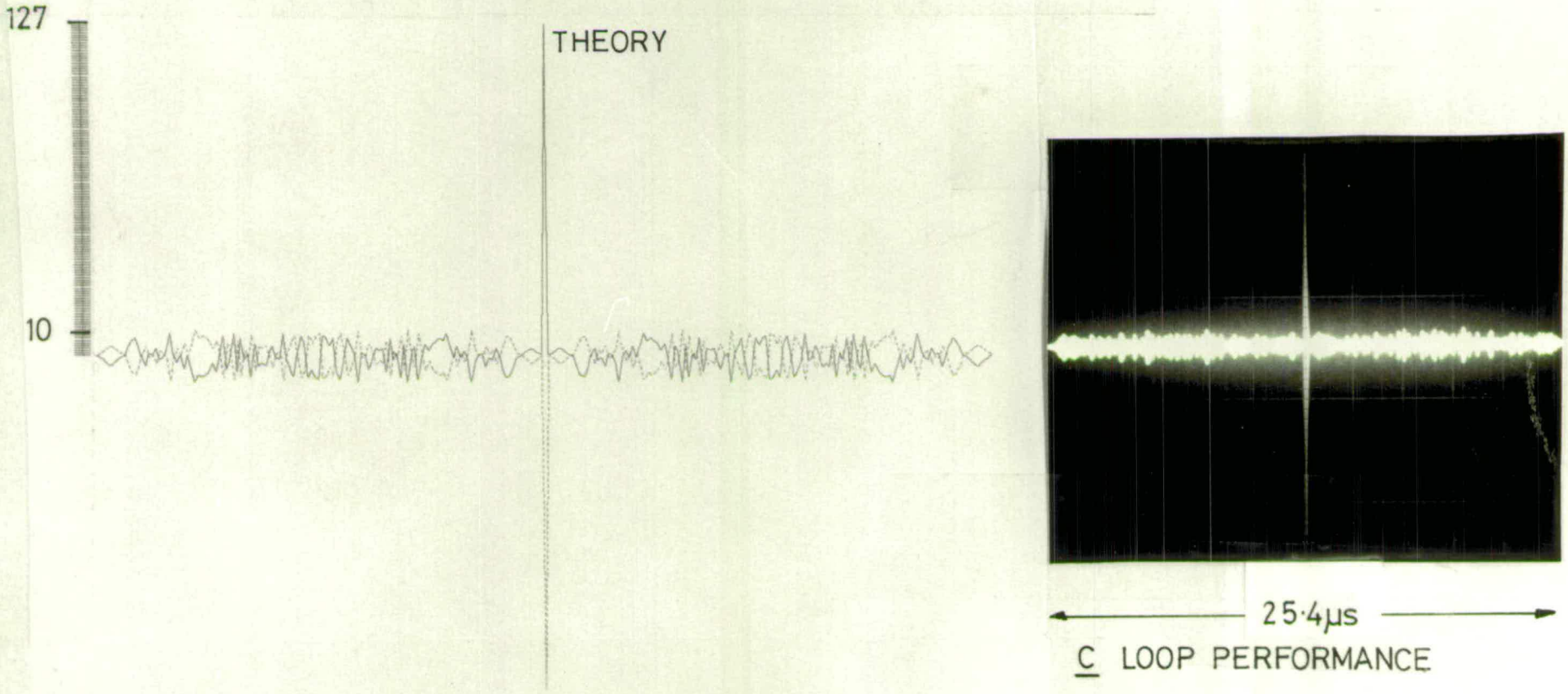

FIGURE 4·31 DESIGN C PERFORMANCE

Finally, trace C shows the response to an actively generated aperiodic signal. Although the peak-to-maximum sidelobe ratio is within 2 dB of theoretical the sidelobe pattern does not exhibit the expected symmetry about the peak. Spurious signal levels were measured at <-37 dB below the peak.

4.2.5 Summary on AMF Design

Firstly, two initial AMF were investigated and their performances characterised. Distortions in their responses were identified as arising mainly from acoustic wave impedance mismatch, witness Figure 4.20 and the insensitivity of spurious to load variations. *Significant improvements* in fidelity over low TB_S first order designs were obtained using the dual-tap geometry *without* increased insertion loss. Next, larger TB_S designs, exhibiting high performance incorporating, B, the split electrode geometry and, C, the dual-tap geometry were investigated. With these, two points of difference in performance emerge:

(1) The dual-tap geometry increases scattering to bulk modes, witness the different roll-off exhibited by trace A, Figure 4.25 and trace A, Figure 4.28 where the latter impulse response was obtained from a split-electrode configuration. Here the roll-off observed can be accounted for simply by propagation loss and compensated by apodisation.

(2) The split-electrode geometry does not reduce the level of regenerated spurious; this was not verified since the designs were intended to produce low regeneration (<80 dB) with a 50Ω load.

Possible solutions were given, namely: that the first difficulty can be partially circumvented by reducing the mismatch with multi-layer metal; alternatively, both problems are solved by employing a hybrid split-electrode-dual-tap plus fill-in geometry. This latter solution should be useful in achieving low-loss AMF with large TB_S products on high coupling substrates.

The use of a simple two-stage impedance matching network was demonstrated. This has important applications in reducing the fractional bandwidth for decreased temperature sensitivity, equation 4.17 especially for applications requiring lithium niobate, and for reduced photolithographic resolution when using split-electrodes. For the networks employed on the second-order designs only ~3 dB additional loss was incurred for fractional bandwidths of 4%, 6.1% and 8.5% for AMF designs A, B, C respectively.

4.3 SAW NON-LINEAR CONVOLVER EXPERIMENTS

4.3.1 Basic Phenomenological Convolver Theory

The simultaneous propagation of two contra-directed, colinear acoustic beams through a non-linear medium results in the generation by a parametric interaction, of a third acoustic signal at the sum frequency. Svaasand[108] demonstrated the detection of this sum frequency component with a uniform electrode deposited between SAW IDT's on quartz. Later, Quate and Thompson[109] demonstrated the convolution of rectangular pulses through the interaction of contra-directed bulk longitudinal waves at S-band. A similar experiment was then performed at VHF by Luukkala and Kino[80] using SAW propagating on $LiNbO_3$. This paper also introduced the non-degenerate configuration, illustrated in Figure 3.5, and reported time-reversal. The experiments outlined in this Chapter were directed toward the demonstration of correlation using a *degenerate* SAW convolver.

The exact nature of the parametric interaction is not known, however the constitutive relationship between electric displacement (D), electric field (E) and acoustic strain, (S) for a nonlinear piezoelectric can be written in the form:

$$D = \varepsilon E + eS + K_1E^2 + K_2 ES + K_3S^2 \qquad \ldots 4.49$$

(K_1E^2: electro-optic; $K_2 ES$: photo-elastic)

In the commonly adopted phenomenological description the second order terms are combined[109] to give:

$$D = \varepsilon E + eS + KS^2 \qquad \ldots 4.50$$

If the two input waveforms, $s(t)$ and $r(t)$ are both CW centred at ω_1 and ω_2 and the corresponding SAW strain amplitudes are S_{10} and S_{20}, the travelling waves are expressed by:

$$S_1 = S_{10} \exp j\omega_1(t-z/v_s)$$

$$S_2 = S_{20} \exp j\omega_2(t-T+z/v_s) \qquad \ldots 4.51$$

where T is the total delay between transducers.

Then, substituting $S = S_1 + S_2$ in equation 4.50, produces a polarisation P from the product term S_1S_2 such that:

$$P \propto \exp j(\omega_3 t - \kappa_3 z) \qquad \ldots 4.52$$

For non-dispersive media[109] the energy and wave-vector conservation relations are satisfied thus:

$$\omega_3 = \omega_1 + \omega_2$$

$$\kappa_3 = |\omega_1 - \omega_2| v_s^{-1} \qquad \ldots 4.53$$

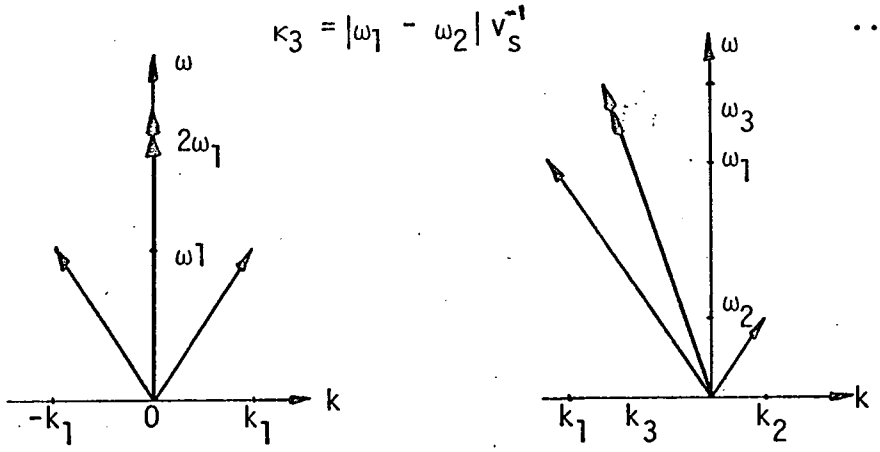

DEGENERATE ($\omega_1 = \omega_2$) NON DEGENERATE ($\omega_1 \neq \omega_2$)

FIGURE 4.32 TIEN (ω,k) DIAGRAMS FOR DEGENERATE AND NON DEGENERATE CONVOLVERS

Figure 4.32 gives the Tien diagrams for both degenerate and non-degenerate processing. For degenerate operation equation 4.52 describes a product term at $2\omega_0$ ($\omega_1=\omega_2=\omega_0$) with *no spatial variation*, ($\kappa_3=0$).

Other $2\omega_o$ terms are periodic in z and are integrated to zero by the uniform parametric electrode[80]. At the *ends* of this electrode, where discontinuity in electrical boundary conditions exists and weak transduction results. This gives rise to a spurious output as discussed in Chapter 3.

If s(t) and r(t) modulate the input carriers, at ω_o, then the resulting strain patterns are proportional to $s(t-z/v_s)$ and $r(t-T+z/v_s)$. Thus, the output signal, V_o, is given by

$$V_o(t) = B \exp j2\omega_o t \int_{-\ell/2}^{+\ell/2} s(t-z/v_s) \cdot r(t-T+z/v_s)dz \quad \ldots 4.54$$

where B is a constant and the output is integrated over the parametric port $-\ell/2 \leqslant z \leqslant \ell/2$. Now, assuming that $T_p = \ell/v_s > T_o$, the waveform duration and making the substitution $\tau = (t-z/v_s)$, the integral becomes:

$$V_o(t) = v_s B \exp j2\omega_o t \int_{-\infty}^{\infty} s(\tau) \cdot r(2t-T-\tau)d\tau \quad \ldots 4.55$$

Thus, the output waveform is the convolution of the two input waveforms compressed in time by a factor of 2 (compare with equation 2.5). The device operation therefore involves:

- translation of one function of time with respect to the other- achieved by generating colinear contra-directed SAW signals representing: s(t), r(t).
- forming the product of the translated functions - multiplication in the overlap region of both SAW signals results from the parametric interaction, equation 4.50, producing an electric polarisation.
- an integration of the product signal - performed by sensing the polarisation field with a capacitor electrode distributed over the desired interaction length.

The convolver acts as a linear filter with a characteristic impulse response determined by the input reference waveform, r(t). Since the reference waveform parameters are limited only by the input bandwidth and delay under the parametric port ($\frac{1}{2}T_p$ for asynchronous operation, Chapter 3 and reference 81) the convolver possesses a high degree of programmability. For matched filtering the device impulse response must be the time-reverse of the signal waveform; equation 2.3. Hence, by analogy with equation 2.6, the time-contracted, delayed autocorrelation function of s(t) is given by:

$$V_o(t) = v_s \; B \exp j2\omega_o t \int_{-\infty}^{\infty} s(\tau) \; . \; s(T-2t+\tau)d\tau \qquad \ldots 4.56$$

Maxima occur when T-2t = 0, thus for *periodic* inputs two correlation peaks of height L are obtained during each period of the input sequence. This has been verified experimentally and is discussed in the next section.

Lim et al[84] have shown recently from basic considerations, that the convolver parametric port can be represented by the series equivalent circuit shown in Figure 4.33.

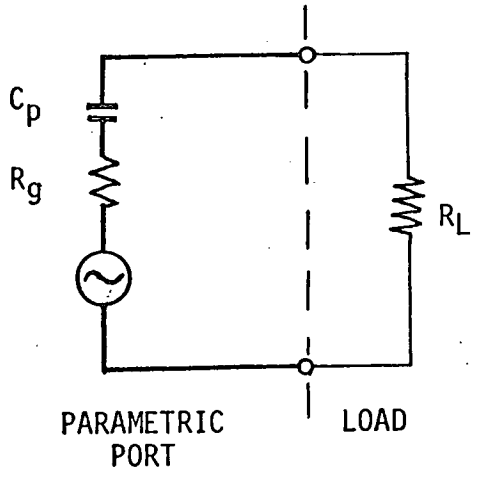

FIGURE 4.33 SERIES EQUIVALENT CIRCUIT OF THE DEGENERATE CONVOLVER PARAMETRIC PORT

The generator resistance (R_g) is very small (<1Ω) due to the weakness of the parametric coupling and its value has not been measured accurately (Kino et al[34] have estimated a value of ~0.6Ω for one particular experiment). For CW input signals, which interact throughout the length of the parametric port, the rms open circuit voltage generated, V_{oc}, is given by[34,38]:

$$V_{oc} = \frac{M}{W} \; (P_{as}.P_{ar})^{\frac{1}{2}} \qquad \ldots 4.57$$

where M is a constant depending on material parameters only - for $LiNbO_3$, $M \simeq 1.2 \times 10^{-4}$ volt-m/watt; W is the width of the SAW beams and also the output electrode; and P_{ar}, P_{ar} are the signal and reference acoustic wave powers. Thus, the power (P_o) delivered to the load (R_L) is given by:

$$P_o = \frac{M^2}{W^2} \; \frac{R_L \; P_{as} \; P_{ar}}{[(R_g+R_L)^2 + (1/\omega C_p)^2]} \qquad \ldots 4.58$$

where $\omega = 2\omega_o$.

With the assumption that R_g is negligible compared with R_L, maximum power transfer occurs for the untuned case, Figure 4.34 when

$$R_L = |1/\omega C_p| \qquad \ldots 4.59$$

This is the "modulus-match" condition which leads to a value for the internal bilinear coefficient C_I, defined by equation 3.1, given by:

$$C_I = \frac{M^2}{W^2.2.R_L} \qquad \ldots 4.60$$

Since, $R_L = \frac{1}{\omega C_p}$ and $C_p \propto \frac{W.\ell}{d}$ where d is the crystal thickness

$$C_I \propto \frac{\omega \ell}{Wd} \qquad \ldots 4.61$$

ω and ℓ are usually fixed by constraints on the external circuitry and waveform duration respectively. Thus, C_I can be increased by beam compression techniques through waveguiding[35] or multi-strip coupler[86] configurations. Decreasing the crystal thickness, d, is also a possibility but trouble may be experienced with excitation of spurious bulk modes and reduced mechanical strength.

4.3.2 Degenerate Convolver Experiment

The geometry of this initial degenerate convolver was not ideal because of limitations imposed by the available photomask. This consisted of two IDT patterns separated by 9 mm each comprising 4 finger pairs with 56 μm periodicity and acoustic aperture 1.5 mm. This mask was modified with tape to include a parametric electrode 7.5 mm long by 1.5 mm wide. The convolver structure was etched in a 2500 Å thick aluminium film on a small piece of Y,Z $LiNbO_3$ approximately 0.5 mm thick. Operating as a delay line an insertion loss of 37 dB was obtained at acoustic synchronism, ~61 MHz, without tuning the IDTs. This value is approximately 10 dB more than the figure calculated from the IDT parameters. The additional loss is attributed to propagation losses in the parametric port[14]. The isolation between input ports was ~75 dB and the isolation between inputs and parametric port was ~40 dB.

Figure 4.34 shows the experimental arrangement used to perform *convolution* between two rectangular pulses each having 2 μsec duration on a 64 MHz carrier. Due to the poor electromagnetic isolation obtained it was necessary to use low-pass filters at the inputs and a high-pass filter on the output. The low-pass filters were designed to attenuate second harmonic components produced by the mixers and power amplifiers

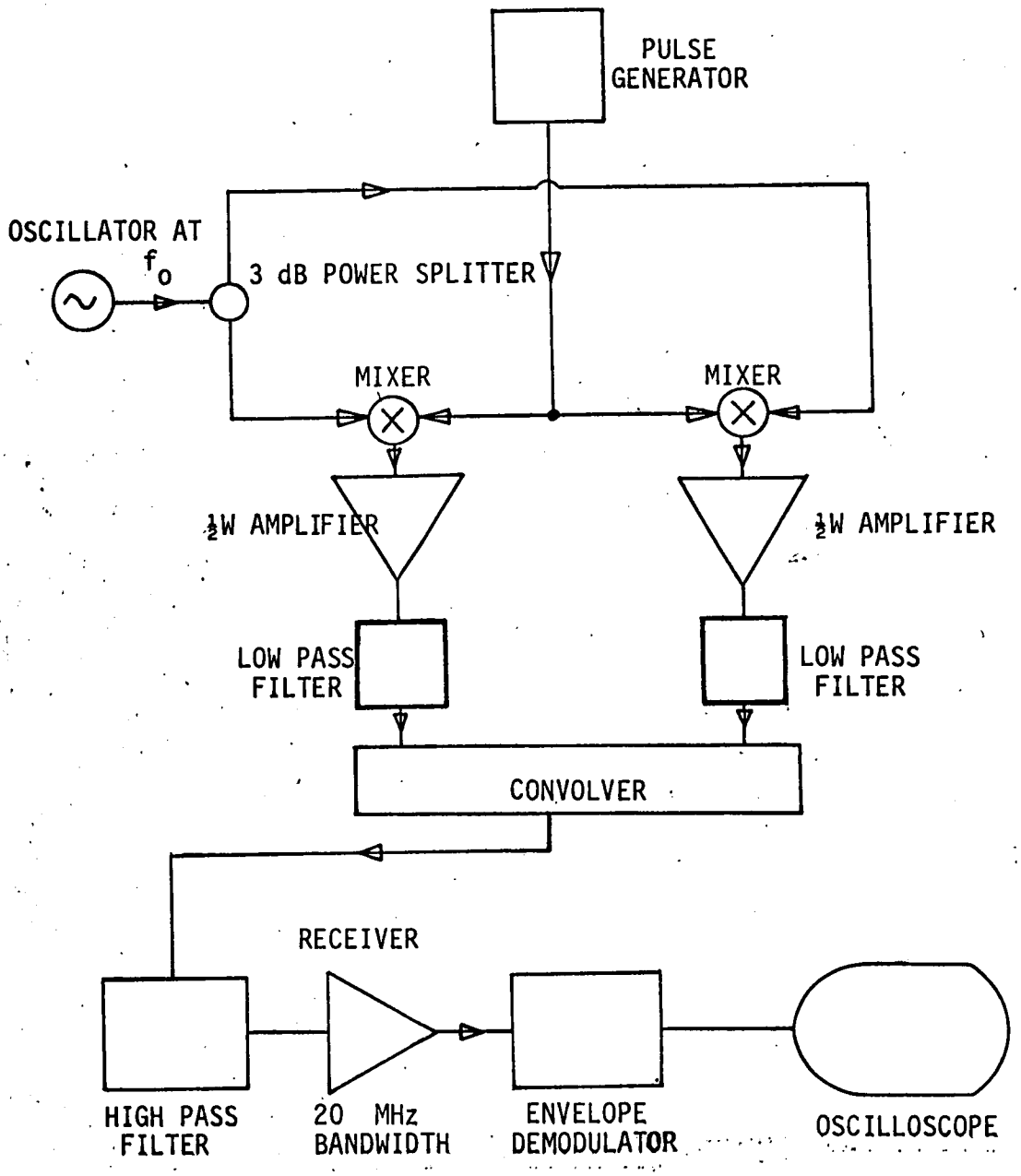

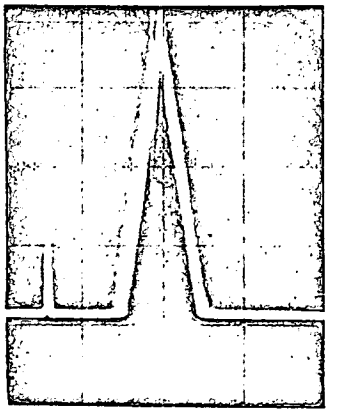

2 μs/div CONVOLUTION of 2 μs PULSES

FIGURE 4.34 EXPERIMENTAL ARRANGEMENT FOR DEMONSTRATION OF CONVOLUTION OF RF PULSES

and were based on 7 section Tchebychev, 0.5 dB ripple designs[106] and exhibited a cut-off at 90 MHz with 65 dB insertion loss at 128 MHz. Similarly, the high-pass filter was designed to suppress direct feedthrough signals at 64 MHz while passing the 128 MHz output signal. A cut-off at ~120 MHz with 50 dB insertion loss at 64 MHz was obtained from the same prototype design.

The output waveform shown in Figure 4.34 exhibits both the expected triangular shape and the time compression by a factor of 2; since the basewidth of the triangular output signal is 2 μsec.

This experiment was used to verify[14] (1) that the output amplitude is proportional to the product of the two input amplitudes, and (2) that the output amplitude is proportional to pulse length. Figure 4.37 illustrates the convolution of double pulses on a coherent 64 MHz carrier, again the expected output shape is approximately obtained; the centre pulse having twice the amplitude of the other two. The spurious signals are due to a direct leakage component and the other due to convolution of signals returning after reflection from opposing ports.

This convolver was used to demonstrate the correlation of periodic 31-chip m-sequences[14]. The signal code s(t) and its time reverse r(t) were produced by two free-running 5-stage shift-register sequence generators with characteristic polynomials $x^5 + x^3 + 1$ and $x^5 + x^2 + 1$. The unipolar pulses from each TTL shift register were level shifted using a single transistor to provide bipolar current pulses of 10 mA to switch the double-balanced mixers. This resulted in two 64 MHz carriers biphase modulated at 7.5 MHz by the 31 chip binary sequences s(t) and r(t). Figure 4.35 illustrates the experimental configuration. The convolver output is also shown in Fig 4.35. As predicted by equation 4.55 there are two correlation peaks for each PN period. As the input code

CHAPTER 5

POTENTIAL APPLICATIONS OF SAW AMF IN SPREAD SPECTRUM COMMUNICATIONS MODEMS

5.1 INTRODUCTION

A variety of proposed communications systems will transfer intermittently small amounts of data at high rate between a large number of subscribers. One challenging area lies in the design of future air traffic control (ATC) systems which, with current thinking[36], will employ short (≲600 bit) data blocks for exchange of flight information between ground control centres and a large number of aircraft. The system characteristics desired[36]: low equipment cost; asynchronous reception; low coordination of transmissions; a high data rate; and protection against multipath[110] and mutual interference for high reliability, predicate spread spectrum techniques (Chapter 2).

This Chapter describes some potential applications of SAW AMF in IF spread spectrum modems for multiple access[15] systems (Chapter 2); employing on-off keyed (OOK), Section 5.2, and multiple-alternative (M-ary), Section 5.3, signaling. Emphasis is given to applications where the AMF performs the *primary* signal processing for high data rate, *noncoherent* modems. Here, the unique features of the SAW AMF are exploited; namely: their passive, carrier and chip asynchronous operation (Chapter 3); and, their ability to generate and decode optimally, complex frequency and time encoded pulse patterns for hybrid spread spectrum modulations, (Chapter 2, Section 2.6). This latter facility was demonstrated experimentally with an OOK random access, discrete address (RADA) modem, the evaluation of which is described in Chapter 6.

[15,56,58,70]

5.2 BANDSPREAD OOK SIGNALING

Simple OOK signaling[57] has been virtually replaced by binary frequency shift keyed (FSK) and phase shift keyed (PSK) transmissions in coordinated high-traffic systems (FDMA, TDMA). However, several important bandspread links use OOK techniques to perform detection and synchronisation of PN and FH signals[56,58]; generation and detection in RADA links[15, 43]; and detection and accurate timing of received signals for navigation and ranging applications[38, 48]. In each case, the reliability of link operation is dictated by the ability to detect a burst of spreading code (PN, Chirp, Barker etc). Completely asynchronous operation with a small degradation in error rate is possible with high order signaling alphabets or by transmission of short (<~20 bits) data blocks[70], Sections 5.2.3, 5.3.2 respectively. However, the conditional error probabilities for noncoherent detection calculated in this Section assume precise bit synchronisation as is achievable with conventional phase locked sampling loops

The basic OOK receiver configuration is shown in Figure 5.1. In each signaling interval, the transmitter emits a spread spectrum coded pulse, s(t), for data '1' or no signal for data '0'. The attenuated signal is linearly superimposed with thermal noise and multiple access interference at the receiver input. The resulting 'noisey' signal is down-converted to IF and processed by a non-coherent matched filter, which comprises an SAW AMF followed by an envelope demodulator. Prior to envelope demodulation the noise statistics are assumed to follow a Gaussian distribution[42], see Section 2.4. Post demodulation noise then has a Rayleigh distribution[57]. A simplified error probability analysis further assumes that:

(1) sampling of the matched filter output envelope occurs at the instant t=T when the output signal to noise ratio is maximised, equations 2.7, 2.12;

(2) the signal sample is compared with a predetermined threshold and the decision rule applied: "If the output envelope exceeds the threshold level, accept 'signal transmitted'; otherwise accept the 'no signal' hypothesis".

Due to interference and noise, two types of decision error occur. The Type I error of false alarm when no signal was transmitted, and the Type II error of false rest (miss) when s(t) was sent but not detected. The probabilities of making these errors will be denoted by P_F and P_M respectively.

The selection of threshold level depends on the prior probabilities of transmitting binary '1' and '0' and the relative cost assigned to each error type. In communications the binary digits occur with equal probability ($\frac{1}{2}$) and the relative costs of each error type are usually equal. Then, the threshold is set to the *Ideal Observer* criterion which seeks to minimise the *total* error rate[59]; P_E given by:

$$P_E = \tfrac{1}{2} P_F + \tfrac{1}{2} P_M \qquad \ldots 5.1$$

The expressions for *conditional* decision error probabilities with OOK signaling are well known[42, 57]. Specifically, for the case of *noncoherent* processing of the AMF output; Mayher[42] gives:

$$P_F = Q[0, \gamma \sqrt{\rho_0}\,] \qquad \ldots 5.2$$

and

$$P_M = 1 - Q[\sqrt{\rho_0}, \quad \gamma\sqrt{\rho_0}] \qquad \ldots 5.3$$

where ρ_0 is the peak-output-to-average signal to noise ratio (SNR) at t=T given by equation 2.12. The Q-function, introduced by Marcum[111],

is defined by:

$$Q(\alpha,\beta) = \int_{\beta}^{\infty} x\, I_0(\alpha x) \exp -(x^2 + \alpha^2)/2\, dx \qquad \ldots 5.4$$

which is the probability that the envelope of a sine wave of peak α plus additive Gaussian noise exceeds a given level, β; $I_0(\alpha x)$ is the modified zero order Bessel function and γ is the ratio of threshold level to the AMF peak output[42, 59].

In the experimental evaluation of an OOK modem incorporating SAW AMF described in Chapter 6, the worst case situation of cochannel interference was simulated. From equations 2.14 and 2.15, this occurs when $B_S = B_I$ and, $x = 0$. Thus,[42]

$$P_F = \exp - \frac{\gamma^2 TB_S}{\left[\frac{I}{S} + \frac{N}{S}\right]} \qquad \ldots 5.5$$

and

$$P_M = 1 - Q\left[\left(\frac{2TB_S}{\frac{I}{S} + \frac{N}{S}}\right)^{\frac{1}{2}}, \gamma\left(\frac{2TB_S}{\frac{I}{S} + \frac{N}{S}}\right)^{\frac{1}{2}}\right] \qquad \ldots 5.6$$

where S/I and S/N are the input signal-to-interference ratio, assumed to be a *bandlimited*, white Gaussian noise process (see Section 2.4); and the input thermal SNR respectively. As the curves given by Raemer[59] and the tabulation of Di Donato and Jarnagin[112] were not sufficiently detailed, the Q-function was computed over the range of interest (see Chapter 6). This was achieved using IBM SSP routines[113] both to calculate $I_0(\alpha x)$ and to perform the integration with a Simpson's rule alogrithm. The values obtained were checked against the tabulated values[112] and were found to have reasonable accuracy (~3%). The curves are presented in Chapter 6, Section 2 together with the experimental data on the OOK modem performance.

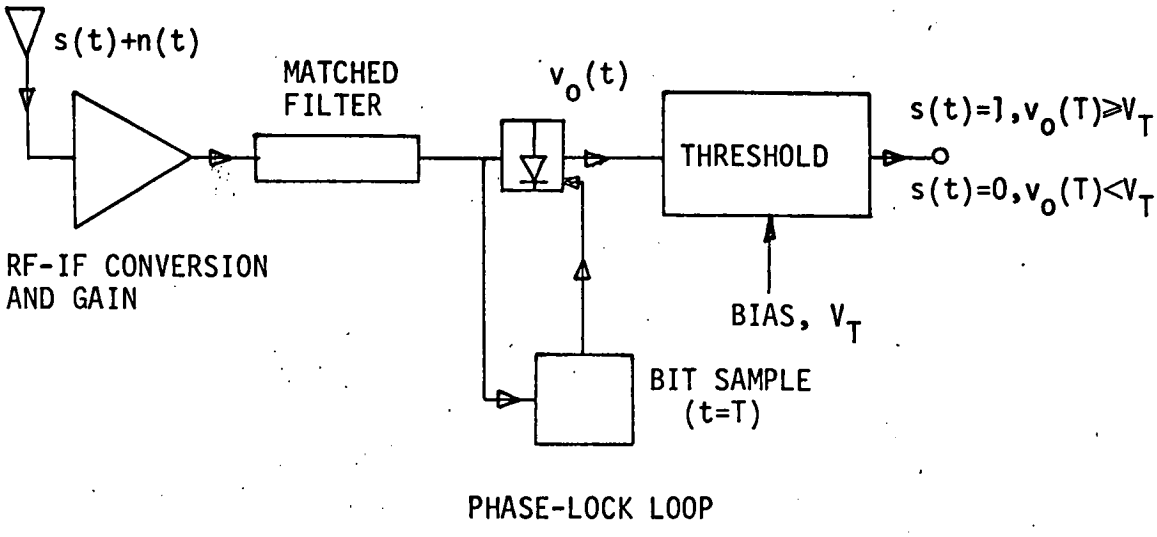

FIGURE 5.1 BASIC OOK RECEIVER CONFIGURATION

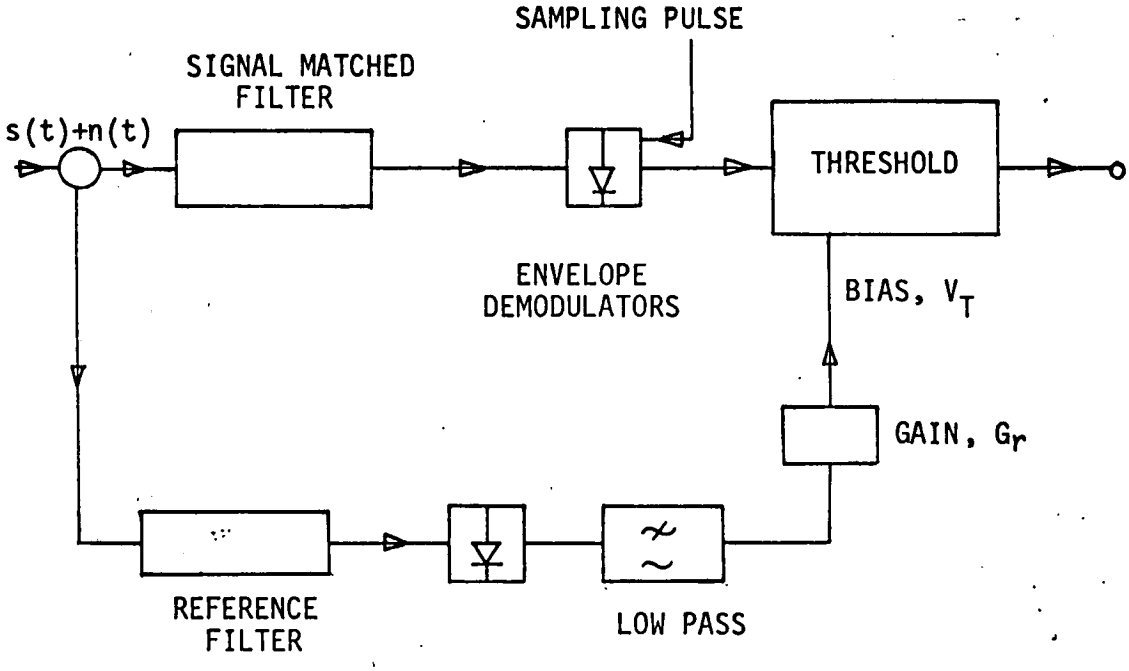

FIGURE 5.2 SELF-REFERENCING THRESHOLD ARRANGEMENT FOR OOK RECEPTION

From equations 5.1 , 5.2, 5.3 the total error probability, P_E is given by:

$$P_E = \tfrac{1}{2}\left[1 - Q(\sqrt{\rho_0},\ \gamma\sqrt{\rho_0}) + \exp -\gamma^2\rho_0/2\right] \qquad \ldots 5.7$$

With *fixed* thresholds the curves of P_E versus ρ_0 asymptotically approach a lower bound at large ρ_0. This arises because P_F dominates at large SNR and is termed the constant false-alarm rate (COFAR) situation. Hence, a fixed threshold is suboptimum for minimisation of *total* error rate. An optimum threshold (γ_0) exists for each value of signal-to-noise ratio. This occurs to close approximation for values of γ_0 satisfying:

$$\gamma_0 = \sqrt{\frac{1}{\rho_0} + \tfrac{1}{4}} \qquad \ldots 5.8$$

Thus, for high SNR $\gamma_0 \sim \frac{1}{2}$, which corresponds to the optimum threshold for coherent OOK reception, and the total error probability approximates to:

$$P_E \sim \tfrac{1}{2} \exp -\left(\rho_0/4\right) \qquad \ldots 5.9$$

where P_E is again determined predominantly by P_F.

5.2.1 Adaptive Threshold Receiver Concept Incorporating SAW AMF

The prime disadvantage of OOK signaling is due to the fact that acceptable performance depends on the maintenance of threshold level at the optimum value. This requirement makes OOK signal reception difficult in channels subject to fading. For narrow band signaling systems particularly, a fixed threshold cannot *reliably* discriminate signal (Mark) from noise (Space) over the range of signal levels commonly encountered in selective fading[59]. Deep fades result in the signal falling below threshold for significant periods compared with the data bit duration. Even with spread spectrum techniques large, rapid

signal variations could be expected when several multipath components interfer. Solutions to this extreme problem involve both large degrees of diversity[66,110] (see Section 2.5.3) and sufficiently large fade margins incorporated in the link power budget.

However, in less severe fading situations, for example as found in terminal area avionics line-of-sight communication, a relatively fast acting adaptive or self-referencing detection technique could be implemented. One possible simple arrangement illustrated in Figure 5.2 relies on obtaining a threshold reference from the *interference level*. Here, the interference is assumed to arise from *cochannel* users operating on a code division multiple access basis and therefore will suffer fades *approximately equal to* that experienced by *the desired signal*. To obtain the threshold reference, the outputs of two matched filters (MF) are compared. One MF responds maximally to the Mark signal while the reference MF ideally produces a zero crosscorrelation signal at time t=T. This second 'orthogonal' MF thus provides a reference level which depends mainly on the uncorrelated signal and 'noise' levels. The reference MF operates over the same bandwidth, at the same centre frequency and with the same TB_s product as the signal MF. Low-pass filtering is employed to average out the rapid fluctuations of the interfering signal crosscorrelations. The reference gain factor, G_r, provides control of threshold level relative to noise and thus determines P_F and P_M. Normally the link power budget will allow MF output SNR of >15 dB to ensure[57] $P_E<10^{-3}$ and thus under this condition Gr is adjusted to give $\gamma\sim0.5$. SAW AMF make this arrangement practicable since the hardware is simple and the adaptive operation is passive and asynchronous.

5.2.2 OOK Modems for Multiple Access Discrete Address Systems

Multiple access, discrete address (MADA) systems use quasi-orthogonal signals from a large alphabet both to identify transmissions (transmitter signatures, or receiver addresses, see Chapter 2) and carry information. Two basic categories exist:

(1) The signals are continuous in time and frequency and the total energy of each signal is accepted as interference by all other users.

(2) The signals are discontinuous in time or frequency, or both, and only a fraction of the signal energy is accepted as interference by other users.

The first category includes the direct PN spread spectrum system described in Chapter 2 Section 2.3. Reliable reception is possible with direct PN only after the receiver has achieved accurate synchronisation with the transmitted signal, (Chapter 2). Also, the multiple access capability of direct PN bandspreading is limited by the available processing gain and the distribution of desired and interference power levels. For this reason direct PN systems usually operate via a transponding relay (Chapter 2, Section 2.5). The danger is that if one signal is larger than the sum of the other signals at the repeater input, the limiter is "captured" by the strong signal and the limiter action effectively suppresses the other signals[60]. This is a consequence of "constant envelope" transmissions operating without coordinated power and is also a problem with FDMA systems.

The second category uses a characteristic *sequence* of pulses on one or several frequencies to *address* transmissions. The resulting pulse group is modulated as a unit: analogue signals being digitally encoded, for processing flexibility, into eg quantised pulse position modulation; delta modulation; or pulse code modulation and digital data transmitted either simply through OOK, or by allocating M addresses per receiver to allow M-ary signaling (Section 5.3.3).

High-order address alphabets prove to be the key to multiple access communication over a common wideband channel in the presence of a mixture of signal powers. These high-order alphabets can, for example, be constructed from *selected* time-frequency pulse patterns[43] which can be chosen with high degrees of orthogonality. Further, a spread spectrum modulation (eg PN or chirp) can be applied to each pulse in the address, extending the number of useful addresses by code-division techniques and increasing multipath resolution and processing gain.

Each address waveform can be specified by dividing the time-frequency plane into a contiguous matrix as shown in Figure 5.3. The address alphabet construction determines the address recognition technique employed. If the addresses are obtained by simply considering the combinations of time and frequency "slots" yielding *unique* addresses (ie addresses transposed in time are not unique since RADA transmissions are uncoordinated) as described by Magnuski[43], hard decisions must be made to recognise the address (N out of N logic). Assuming white Gaussian noise interference, the resulting bit error probability, assuming statistically independent noise samples, is given by:

$$P_E = \tfrac{1}{2} P_F^N + \tfrac{1}{2} N P_M \qquad \ldots 5.10$$

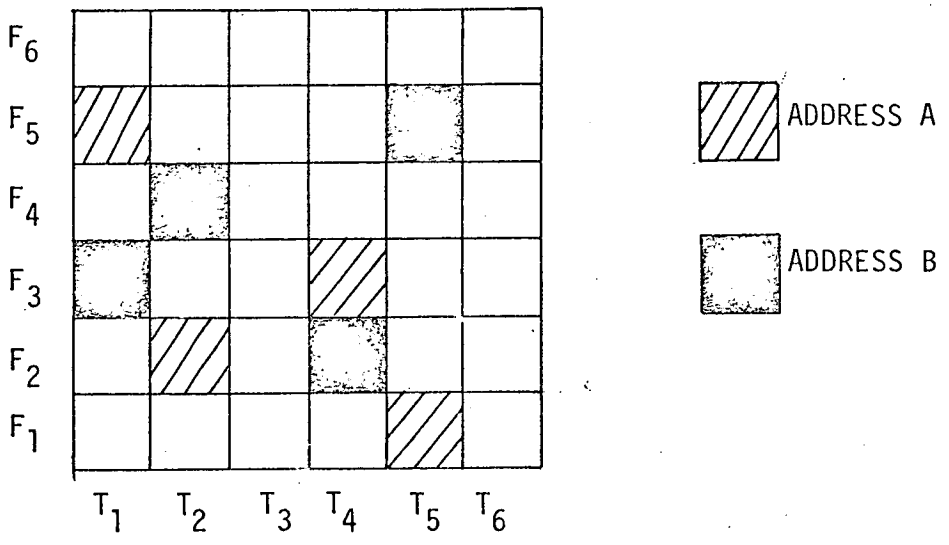

FIGURE 5.3 TIME-FREQUENCY ADDRESS MATRIX

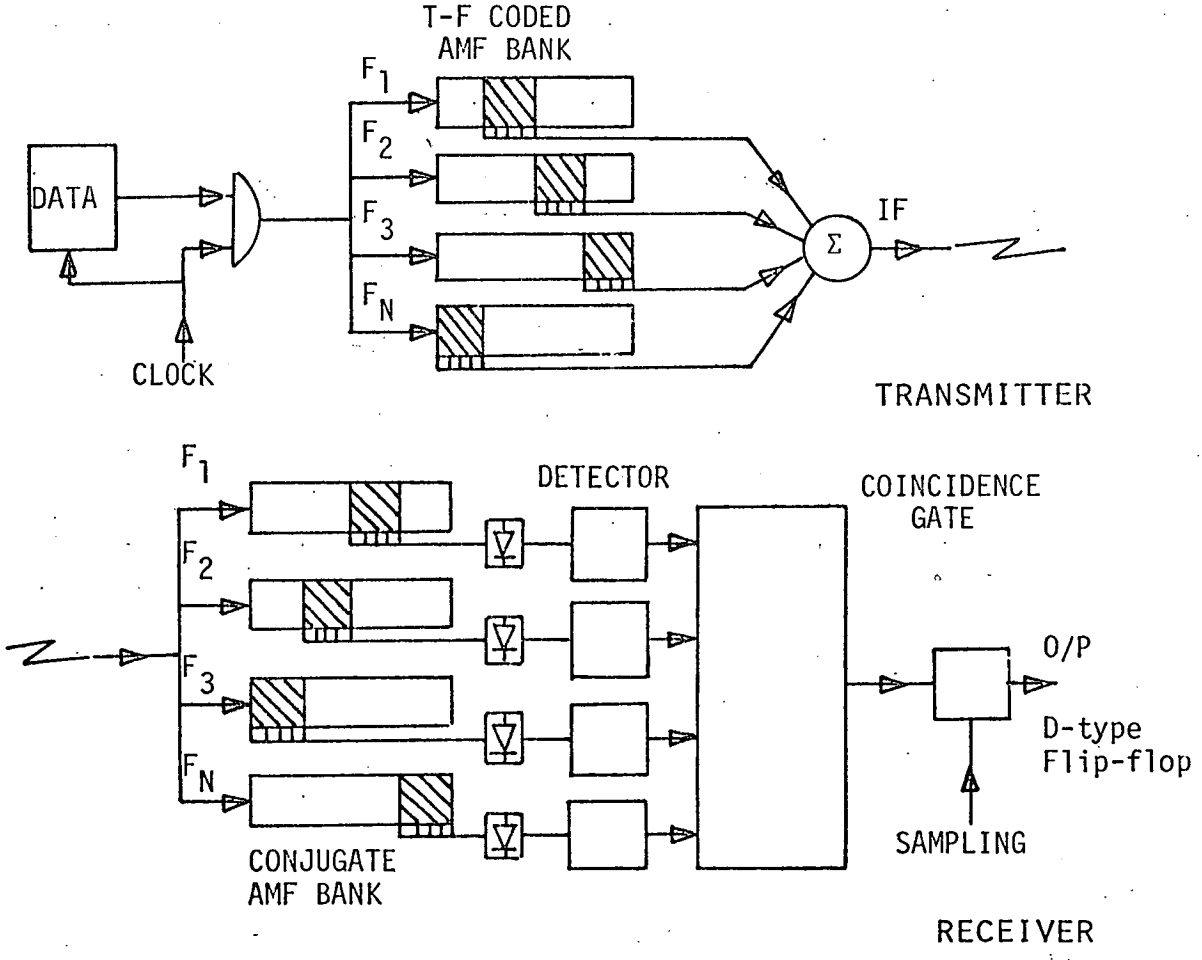

FIGURE 5.4 BASIC OOK RADA MODEM

where N is the number of pulses per address and P_M and P_F are the conditional error probabilities in detecting each pulse, for OOK signaling given by equations 5.1, 5.3. The factors of $\frac{1}{2}$ relate to the equal prior probabilities of ones and zeros. It is evident that the full processing gain (NTB_S) is not achieved. The effects of this logic are discussed further in Section 5.3.2, and Chapter 6, where the evaluation of a simple (N = 2) RADA modem is described.

Soft decisions are possible when the *addresses are orthogonal* and this leads to a reduction in bit cancellation errors (misses) due to the gain in SNR achieved. A suitable address alphabet can be constructed from the Reed-Solomon (R-S) codes[113]. As an example, the (7,2) octal R-S code used by Reed and Blasbalg[110,36] in a TDMA-M-ary system would be a useful basis and could be extended by code-division techniques.

An example of a possible OOK RADA modem configuration using SAW AMFs is shown in Figure 5.4. At the transmitter, the data generator triggers an impulse generator which feeds a bank of coded SAW AMFs. For short coded pulses ($\leqslant$15 μs) differential delays can be incorporated in the AMF bank as indicated. (Other addresses can be synthesised by switching on and off other coded sections as shown in Figure 5.5). At the receiver an array of conjugate matched filters plus appropriate compensating delays, Figure 5.4, recognises each coded pulse and brings all correlation peaks into coincidence. Each correlation peak is detected separately and a coincidence gate performs the necessary baseband decoding. This configuration implements the hard-decision receiver.

A soft-decision receiver can be implemented as shown in Figure 5.6; here, an R-S code alphabet is employed as a basis for address selection. In this example, each digit of the R-S code corresponds to a specific frequency slot. As above the frequency slots are contiguously spaced

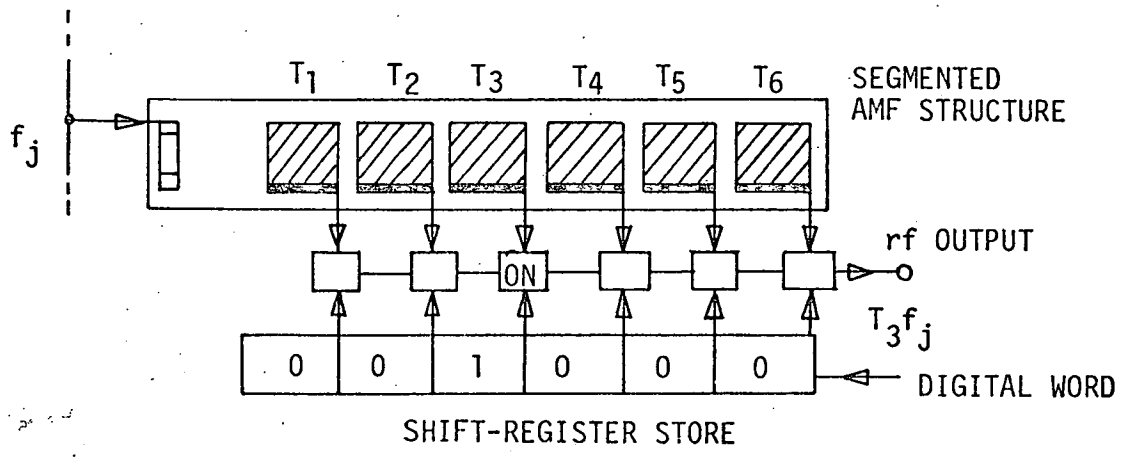

FIGURE 5.5 POSSIBLE METHOD FOR MULTIPLE-ADDRESS SELECTION

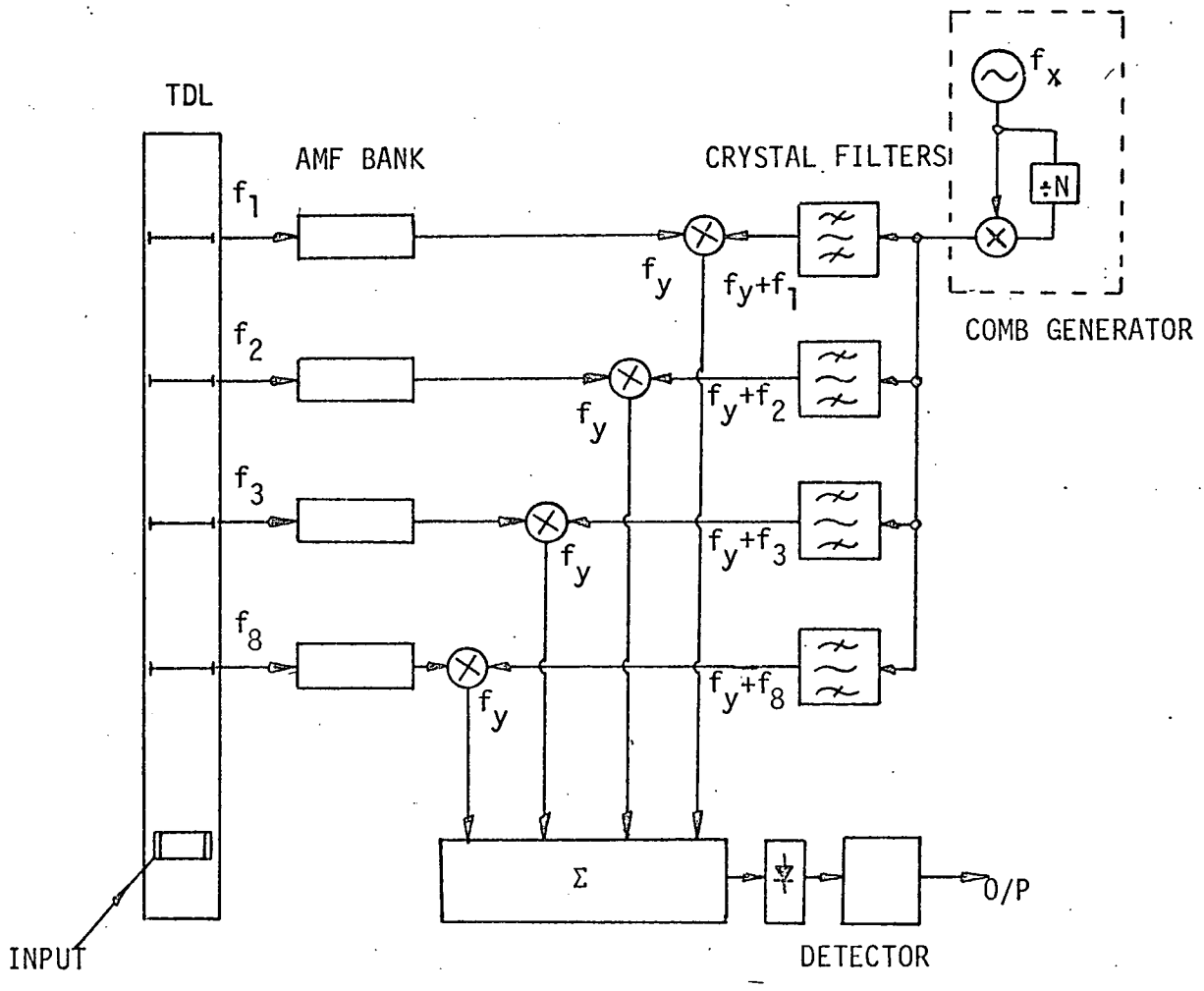

FIGURE 5.6 SOFT DECISION RADA RECEIVER

to achieve orthogonality. Consider the (7,2) R-S alphabet[113]. When *synchronised* the 64 time-frequency patterns produced agree, at most, in one position. However, since RADA transmissions are not synchronised, the 8 patterns consisting of identical subpulses (ie a run of seven digits, one of 0, 1, ..., 7) must be removed to allow synchronous link operation. Also, code division techniques must be employed to prevent false alarms arising through partially overlapping code words which are cyclic shifts of one another. In principle, 8 code words exhibiting low mutual crosscorrelations (see Chapter 2, Section 2.3) would suffice since there are 8 basic patterns, each undergoing 7 cyclic shifts to produce other code words. This combination therefore yields a total of 8 x 56 = 448 address patterns with low mutual crosscorrelations.

After bringing the correlation peaks into coincidence using a tapped delay line (TDL), as shown in Figure 5.6, the output of each AMF is down converted to a common IF. The configuration shown ensures that the *full processing gain is achievable* through coherent summation of the correlation peaks when the 7 AMF all exhibit identical propagation delays and the TDL produces exactly one bit delay. The summed output is envelope demodulated since bit pulse-to-bit-pulse coherence does not exist. A processing gain of ~30 dB is possible with AMF matched to a 127 chip code, allowing the link to operate with down to ~-10 dB input SNR with bit error rates $<10^{-6}$. Thus, illustrating that high processing gains can be achieved using combined characteristic waveforms.

5.3 SPREAD SPECTRUM MULTIPLE-ALTERNATIVE SIGNALING

It is well known[59,66,114] that high order *signaling alphabets* can be used either to effect an increase in information rate (R) or a decrease in error probability. The penalty is an exponential increase in required bandwidth for "orthogonal" signaling alphabets, and an exponential increase in required transmitter power for multiamplitude and multiphase alphabets where the signal bandwidth is essentially independent of the alphabet size[57]. Both multiamplitude and multiphase signaling techniques have been used for data transmission over telephone lines[115] but not extensively for radio links because good channel gain and phase stability, respectively, are mandatory for alphabet sizes in excess of 4. In this section, the advantages in performance gained by using "orthogonal" signaling alphabets are briefly examined. In multiple-alternative (M-ary) signaling k bit data subsequences, produced at a rate of R bit/sec, are accepted by the baseband encoder which performs a one-to-one mapping of each data subsequence onto an alphabet of M distinct signaling waveforms of duration $T(= k/R)$, Figure 5.7. Each signal produced by the modulator uniquely specifies one of the $2^k(=M)$ possible data subsequences. On reception, the waveform is processed in a parallel bank of matched filters, Figure 5.7. At the instant of decision maximum likelihood decoding[66] selects the largest signal plus noise envelope from the outputs of the MF bank and declares the hypothesis that the associated signal from $\{S_m\}$ was transmitted. The baseband decoder then produces the corresponding k bit data subsequence. The probability of error is determined essentially by M and the output SNR of the matched filter containing the signal. The relative output SNR of the bank of matched filters depends on the cross correlation coefficients of the signaling waveforms. With a number of assumptions,

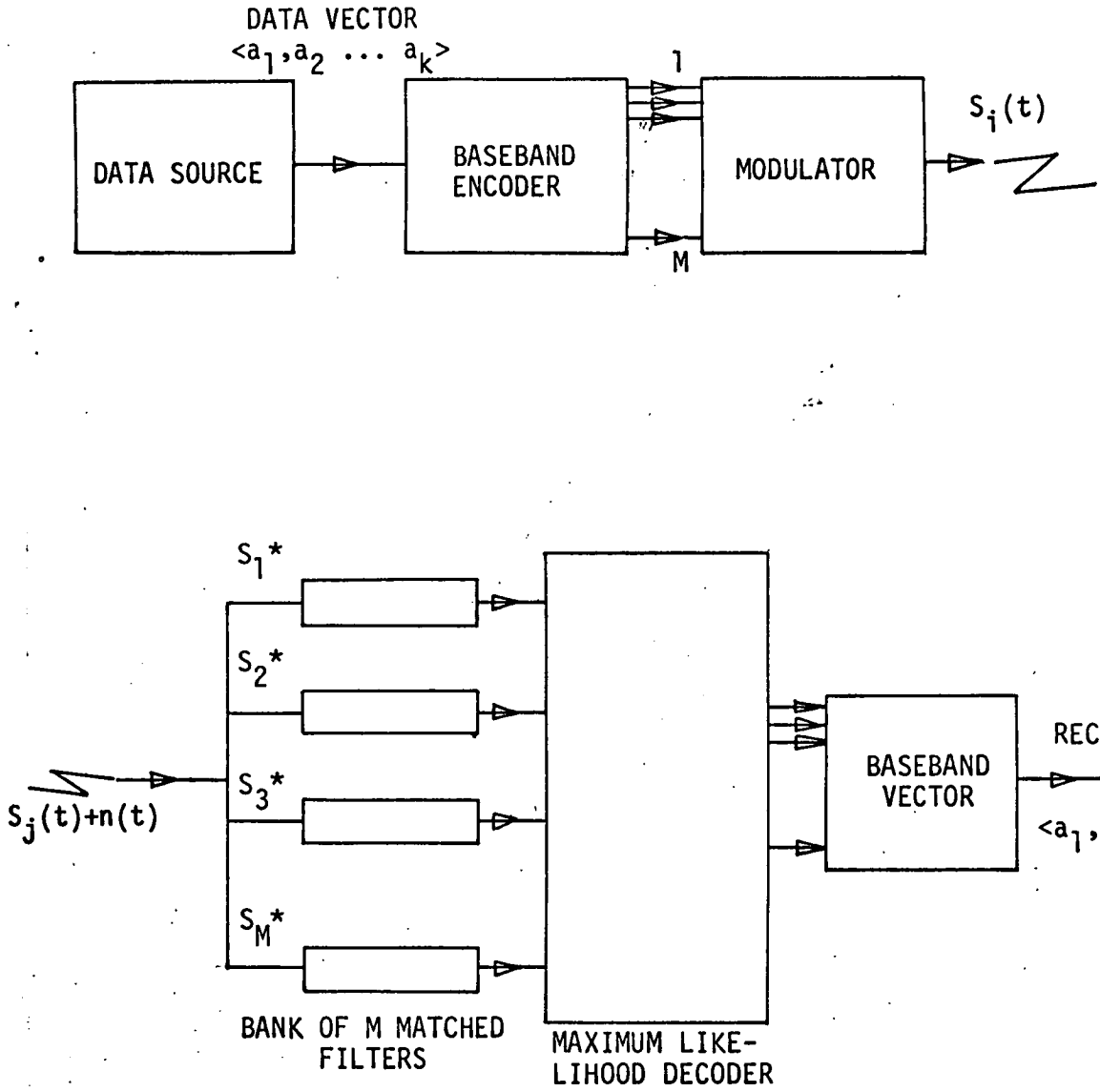

FIGURE 5.7 ESSENTIAL FEATURES OF MULTIPLE-ALTERNATIVE MODEM

the probability of error can be explicitly stated. These assumptions are:

(1) The source produces a random binary sequence which in turn makes each of the M signals equiprobable

(2) The signals have equal energies, this condition is linked with (1) - weighting on a differential prior probability basis is not required (Wozencraft and Jacobs[66], p234)

(3) The signals are equicorrelated[114] with a cross correlation coefficient, χ given by:

$$\chi = \chi_{ij} = \frac{1}{E} \int_0^T S_i(t)\, S_j(t) \cdot dt \qquad \ldots 5.11$$

where E is the received signal energy. The matched filter output signal-to-noise ratio, is scaled[114] by the factor $(1-\chi)$.

(4) Reception is assumed to be noncoherent which dictates that minimum error probability is obtained with waveforms which are *orthogonal* $(\chi=0)$ *at the sampling instant* $(t=T)$. This assumption greatly simplifies the receiver construction and does not significantly degrade error rate performance for large M compared with coherent reception[57].

(5) Finally, bandlimited, white Gaussian noise is assumed to corrupt the received signals and the channel is assumed free from multiplicative disturbances.

The exact expression for symbol error probability is well known[66] and can be written as:

$$P_E = \sum_{j=1}^{M-1} (-1)^{j-1} \binom{M-1}{j} \frac{1}{(j+1)} \exp - \frac{\rho_o}{2} \cdot \frac{j}{j+1} \qquad \ldots 5.12$$

where ρ_o is the output SNR of the MF containing the signal. An upper bound on P_E exists, given by[57,66]:

$$P_E \leq \frac{M-1}{2} \exp - \rho_o/4 \qquad \ldots 5.13$$

With equation 5.13, the significant advantages of orthogonal M-ary signaling can be derived. The first advantage noted is the *absence of any quantity dependent on a threshold* and therefore automatic gain control is no longer required with bit synchronous operation. If the information rate, R is fixed then an increase in M results in an increase in the duration of the transmitted signal, T so that:

$$T = \frac{1}{R} \log_2 M \qquad \ldots 5.14$$

Hence, from equation 2.12 the symbol SNR changes with respect to the SNR per information bit, ρ_b:

$$\rho_o = k\rho_b \qquad \ldots 5.15$$

From equation 5.13, a weaker bound[40] can be established:

$$P_E < \exp \left[-\log_2 M \left(\frac{\rho_b}{2} - \ell n\ 2\right)\right] \qquad \ldots 5.16$$

Equation 5.16 gives the important result that if the SNR per bit exceeds $2\ell n\ 2$ (~1.4 dB) P_E *decreases exponentially* with increased k. The bandwidth expansion ratio (B/R) is determined by the dimensionality theorem[66] which relates the *total bandwidth* (B) and M:

$$BT = M \qquad \ldots 5.17$$

Hence,

$$\frac{B}{R} = \frac{M}{\log_2 M} = \frac{2^k}{k} \qquad \ldots 5.18$$

If each signaling waveform $\{S_m\}$ consists of L chips each of duration τ equation 5.17 gives:

$$B = \frac{MB_s}{L} \qquad \ldots 5.19$$

Where, if L = 1, $B = MB_s$. Thus "multitone" or FSK signaling is employed with tones spaced contiguously [-3 dB points overlap] in the frequency domain to achieve orthogonality. If, however, L = M, $B = B_s$ the system operates with orthogonal codewords each conveying k bits of information. With M-ary signaling, bandspreading improves communication efficiency, equation 5.16, but does not necessarily provide multiple-access capability. This can be achieved with TDMA or, by *further bandspreading*, with spread spectrum techniques. For example by code division multiple access where the dimensionality of the signal set is M x A, where A is the number of potential subscriber addresses, or by frequency hopping [38,55,58] (Chapter 2).

It is also apparent from equations 5.16, that the error probability can be held at a fixed level as M increases for values of $\rho_b > 1.4$ dB. This is accomplished through increasing the symbol signal-to-noise ratio ρ_o as $\ell n(M)$ or decreasing the energy per bit ρ_b as $1/\log_2(M)$. The required bandwidth increasing as M/k.

Finally, the other parameter in the "trade-off": information rate, can be increased by keeping T constant and increasing k and hence M. The error rate bound, equation 5.16, indicates that the signal power for fixed error rate must increase linearly with $k(\log_2 M)$ and the required signal-to-noise per bit ρ_b is independent of k. As before, the total bandwidth increases exponentially with k.

5.3.1 Binary Modems Incorporating Coded SAW AMF

The primary disadvantage of OOK signaling results from the necessity to maintain the threshold at the optimum level, Section 5.2. As this level is a function os SNR fixed thresholds cannot reliably discriminate between signal and noise in channels subject to deep fade. In contrast binary signaling employs two distinguishable waveforms with a comparison of the receiver AMF output envelopes at the sampling instant as shown in Figure 5.8. Minimum error probability for equally energetic and equiprobable Mark and Space signals is achieved with zero threshold level. An experimental evaluation of a simple binary FSK modem is described in Chapter 6.

Setrin et al[70] have recently described a high performance binary modem for aperiodic transmission of data blocks comprising 8 bits to be used in military ATC. Each T second bit is encoded with a different 127-chip PN sequence at a 50 M chip rate on a common carrier. The 8 bit spread spectrum coded waveform is conveniently generated by sequentially impulsing 8 orthogonally coded AMF pairs.
In the receiver, Figure 5.9, the spread spectrum demodulator comprises a parallel bank of 16 conjugate AMF fed in pairs from an 8 tap delay line. At time t = 8T, the received data block registers with the 16 AMF to produce 8 coincident correlation peaks occuring at either the Mark or Space outputs of each AMF pair. With accurate design of delay and centre frequency the 8 correlation peaks are in phase coherence. This was used by Setrin et al[70] to produce a combined peak (compare with Figure 5.6) 18 dB greater than each AMF output with potentially 9 dB SNR improvement for orthogonal codes. In practice a loss of 3 dB was reported because of incomplete orthogonality resulting in a SNR of 19 dB for the combined[70] peak. The resulting peak was envelope demodulated and a threshold set. For optimum threshold $P_E \sim 10^{-7}$, equation 5.9,

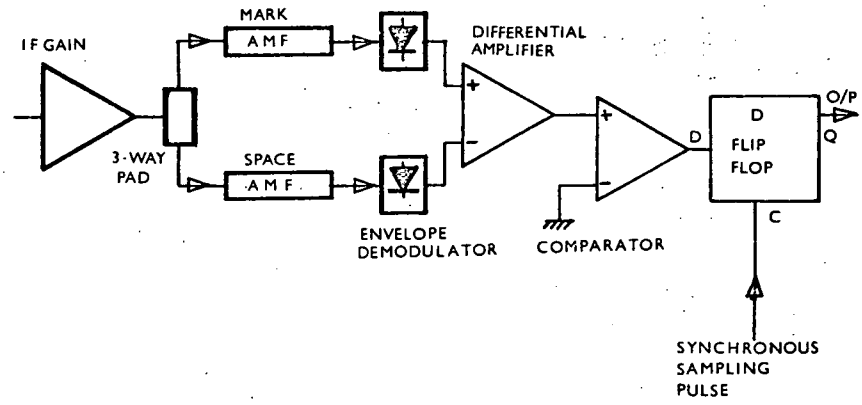

FIGURE 5.8 SIMPLE BINARY FSK RECEIVER

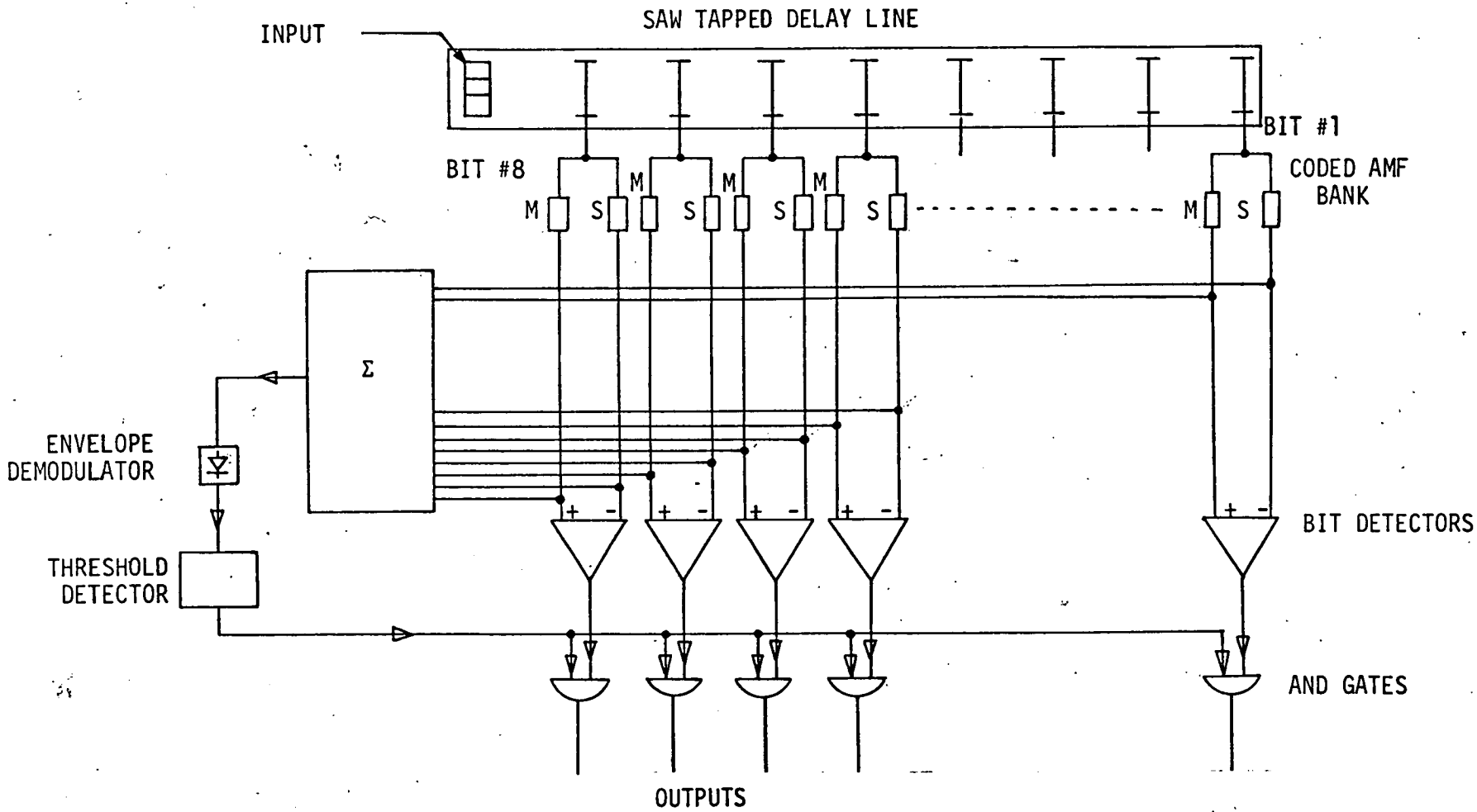

FIGURE 5.9 ESSENTIAL DETAILS OF THE BLOCK PROGRAMMABLE BINARY ORTHOGONAL-SIGNAL RECEIVER

at this level of SNR at the detector. The detected baseband signal was then employed as a sampling pulse having a timing accuracy with a standard[70] deviation of $(0.08/B_s)$. The receiver thus functions completely asynchronously with a bit error rate of $\sim 10^{-5}$ determined essentially by binary orthogonal signaling[57] with output SNR of 13 dB.

At the transmitter, different address waveforms are generated by changing the order of the 8 bit code. Thus, a total of 8! = 40,320 code permutations are available for discrete addresses. However, not all permutations will be *strictly unique* since some codeword combinations will comprise cyclic shifts of others. Partial overlap of one of these addresses would cause a spurious detection at an unintended receiver. This problem was solved by logical AND gating of the sampling pulse and 8 baseband pulses obtained from each Mark-Space AMF pair by threshold detecting the video sum signal. The output of the AND gate enables the baseband decoder only when 9 *simultaneous* pulses are produced. Thus a *hard decision address* logic was implemented as described for the simple OOK RADA modem[15,36] with an address false alarm rate for noise given by equation 5.10.

5.4 SUMMARY

This Chapter has highlighted some SAW AMF applications in spread spectrum modems for low activity factor transmissions. Emphasis has rested on OOK and M-ary signaling with multiple access capability being achieved with time-frequency and time-code address patterns. The examples given illustrate the new dimension of signal complexity achieved with SAW *without* the prohibitive hardware complexity and power consumption, associated with the competing DMF and synchronisation aquisition problems associated with active correlators.

CHAPTER 6

EXPERIMENTAL SPREAD SPECTRUM MODEMS INCORPORATING BINARY PHASE CODED SAW AMF

6.1 INTRODUCTION

Experimental evaluations of the error rate performance of basic modem configurations using SAW AMFs interfaced with linear integrated circuits are reported in this Chapter. Specifically, simple prototype on-off keyed (OOK), binary frequency-shift keyed FSK and OOK random access, discrete address (RADA) modems[15] were tested to illustrate and evaluate the use of SAW AMFs in the more complex arrangements discussed in Chapter 5.

The next section deals specifically with error rate measurements for an OOK signaling modem with received signals corrupted by band-limited noise. Near theoretical error rate performance was obtained over a threshold range of -4 dB to -7 dB and a range of error rates from 10^{-1} to 10^{-6}, in a comparison of conjugate AMF pairs processing equal bandwidth signals with time-bandwidth products of 1, 13, 15 and 31.

The third section briefly considers the problems of cross-talk in M-ary FSK signaling. Measurements are described which indicate the relative cross-talk levels, obtained for $t \neq T$ with carriers spaced at multiples of B_s. A method, which is simply achieved with SAW AMFs, is described for eliminating cross-talk signals *at the sampling instant* and is applied to a bit synchronous binary FSK spread spectrum modem. Measurements of error rate in an experimental link corrupted by bandlimited noise show close to theoretical modem performance.

Then, modifications made to the detector for *fully asynchronous* operation are described and the modem operation demonstrated.

In Section 6.4, a novel prototype modem configuration employing 2 AMFs, with TB_s = 15, for address generation and decoding in RADA communications is described and an experimental evaluation reported.

6.2 SPREAD SPECTRUM OOK MODEM EVALUATION

The simple arrangement shown in bold outline, Figure 6.1, models a noncoherent spread spectrum modem for OOK signaling in a gain stable channel. The peripheral equipment, shown in thin outline, allows direct measurement of both conditional error rates (P_F and P_M) under controlled signal-to-noise conditions and decision threshold, for comparison with the theory given in Chapter 5.

All AMFs employed in this and subsequent modems described in this Chapter were *not* of dual-tap array[12] geometry. The practical consequence, indicated by the close agreement with theory achieved[15], is that coded AMFs exhibiting imperfect time domain responses to the matched signal (Chapter 4) are usable in prototype spread spectrum modems. This fact further enhances the attractiveness of SAW matched filter implementation over other technologies (see Figure 3.13) when viewed from the manufacturing standpoints of development cost, device yield and bond integrity and tap switching component reliability in programmable devices.

The AMF conjugate pairs (A,A*) used in the arrangement of Figure 6.1 were designed to process the biphase modulated signals detailed in Table 6.1. As an indication of device performance, the table also compares measured and theoretical peak-to-sidelobe ratios for the corresponding aperiodic waveform.

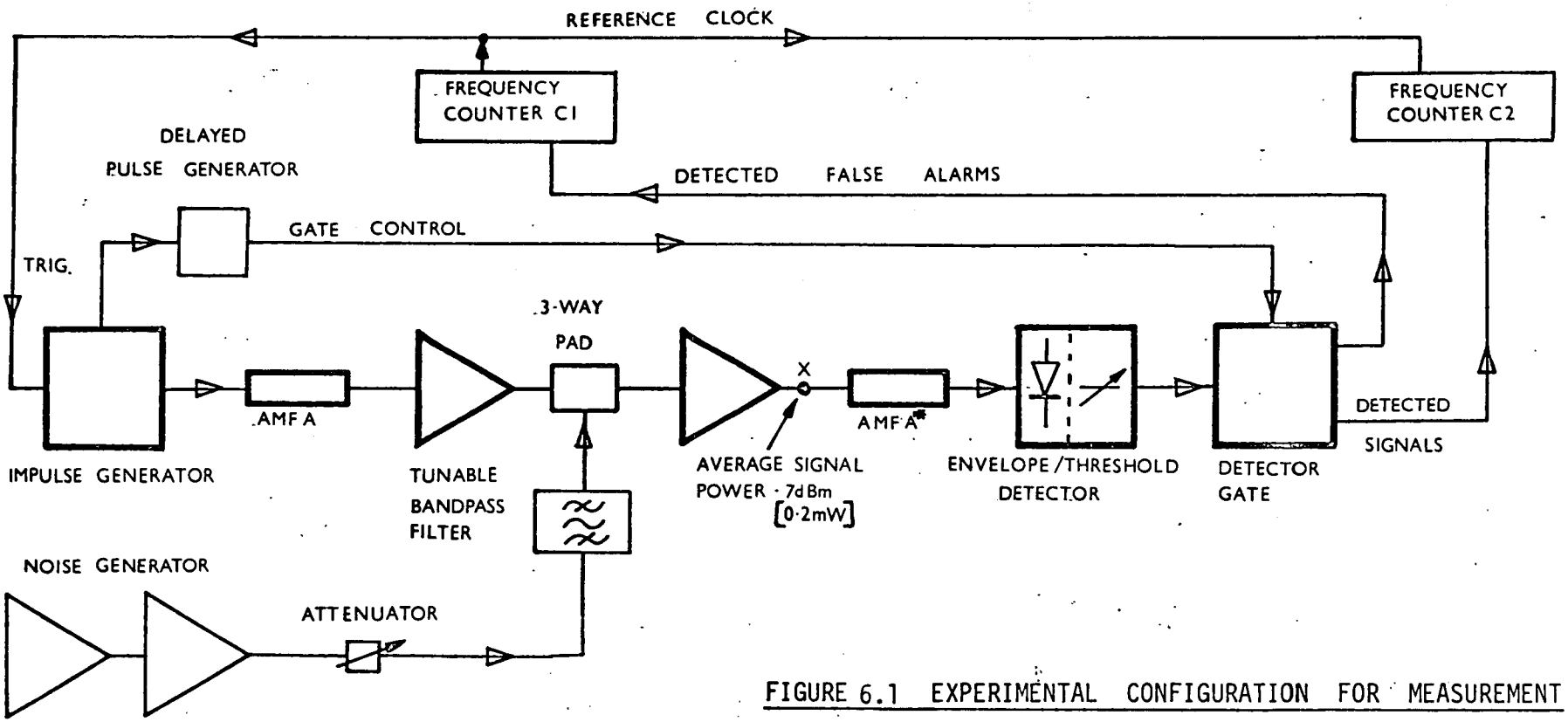

FIGURE 6.1 EXPERIMENTAL CONFIGURATION FOR MEASUREMENT FOR P_F AND P_M OOK SIGNALS

TABLE 6.1 DETAILS OF SPREAD SPECTRUM SIGNALS AND RESPONSES OF THE CORRESPONDING AMF USED IN THE OOK MODEM EVALUATIONS

BANDSPREAD SIGNALS EMPLOYED			*AMF RESPONSE*	
f_o (MHz)	B_s (MHz)	L	Aperiodic Peak/Sidelobe (dB)	
			Measured	Theoretical
100	5	13 (B)	18 0.5	22.3
100	5	31 (m)	16 0.5	16
127.3	5	15 (m)	11 0.5	11.5
90	5	1	--	--

Key: f_o: carrier frequency; B_s: signal bandwidth (chip rate); L: code length; m: maximal-length sequence; B: Barker sequence.

For direct comparison with the coded AMF pairs, sequences of IF pulses were generated and matched by replacing both expansion (A) and compression (A*) AMF with unity time-bandwidth product filters centred at 90 MHz with *5 MHz bandwidth*.

Aperiodic mode signals, s(t), were generated by impulsing AMF A (see Chapter 4, Section 4.2.2) at a data rate determined by an accurate (100 kHz) clock taken from frequency counter C_1. This clock was used both as a trigger signal for the impulse generator and timing reference for counter C_2. In this manner clock rate variations were automatically compensated for.

After amplification the signal was processed by the corresponding conjugate AMF (A*) whose output was envelope demodulated and monitored by a simple variable integrated circuit threshold detector. To facilitate error rate measurement, a pair of synchronous sampling pulses were generated and gated with the threshold detector output. Figure 6.2 shows the relationship between sampling pulses used to separate the noise induced outputs and detected correlation (strictly cross-correlation) peaks and therefore enable independant measurement of

both false alarm and miss rates respectively. Strictly, the sampling pulse relationship shown allows measurement of *only one conditional* error rate, namely the miss rate (P_M), since each sampling pulse coincides with a correlation peak. The false alarm rate measured is *unconditional* and represents the false alarm rate obtained with *fully asynchronous* reception as occurs, for example, when searching for synchronisation. A second point concerning the sampling pulses relates to the individual pulse widths:

(1) SP_1 has a width equal to the basewidth of the correlation peak (400 nS) and hence $\overline{SP}_1$ effectively excludes the baseband pulses corresponding to the peak from the false alarm counter (C_2);

(2) the width of SP_2 (200 nS) was determined experimentally by adjusting its width at a fixed threshold level (-6 dB) for three (-3 dB, 0 dB, and +3 dB) input signal-to-noise ratios and observing the alterations in the number of detected peaks. The largest sampling pulse width (200 nS) consistent with an arbitrarily chosen increase (<5%) in the number of indicated peaks over that obtained with a 50 nS pulse width was selected.

Wideband Noise was first generated by cascading high gain wideband amplifiers and then bandlimited with a variable filter to 10% of f_0; the AMF centre frequency. This simulated the worst-case situation of equation 2.14 where $\Delta\omega = 0$, corresponding to cochannel interference. The noise was introduced to the link via the 3-way pads and controlled with the variable attenuator.

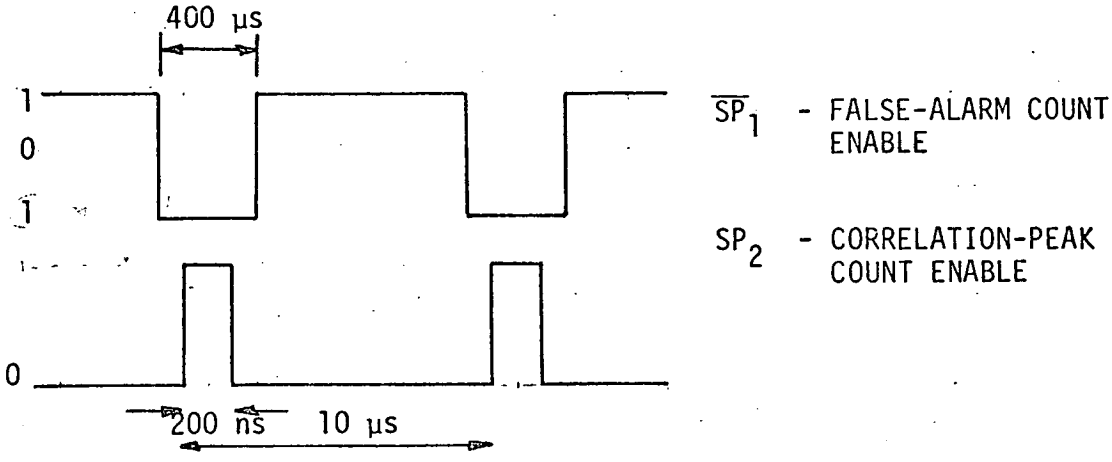

FIGURE 6.2 SAMPLING PULSE RELATIONSHIPS

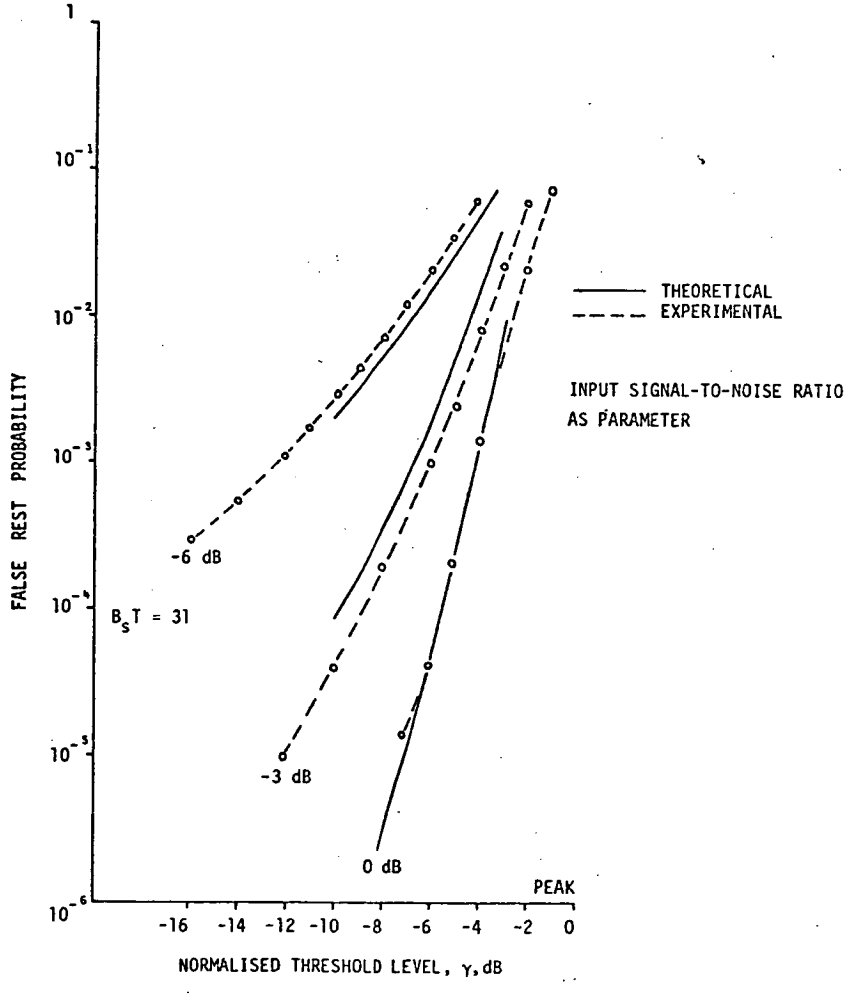

FIGURE 6.3 OOK MODEM - P_M VERSUS γ AT FIXED SIGNAL-TO-NOISE RATIO

To calibrate the attenuator, the circuit was broken at "X" and the mean power level of the noise adjusted to equal the average power (-7 dBm) of the coded IF pulse. Linearity was ensured between attenuator settings and power level measured at "X" for the range of noise powers used. This verifies that the amplifiers employed were operating below saturation which is a necessary condition for making reliable variations of the signal-to-noise ratio.

For comparison between the three bandspread OOK modems modelled, measurements were made with the same normallised threshold settings, and with the same peak signal levels at the detector.

False alarm probabilities (P_F) were determined by taking the average frequency of pulses, over a one second counter gate interval, at counter C_1 (f_1) and dividing by the frequency of the impulses used to generate the signals (f_R).

$$P_F = {}^{f_1}/_{f_R} \qquad \ldots 6.1$$

Similarly, false rest probability (P_M) was obtained by subtracting the averaged reading on counter C_2 (f_2) from the clock frequency (f_R) and dividing by the latter.

$$P_M = (f_R - f_2)/f_R \qquad \ldots 6.2$$

Low error rates were achieved in high signal-to-'noise' conditions witnessed by a count of 10^5 pulses per second in counter C_2 and zero pulses per second in counter C_1.

Figure 6.3 shows the measured variation of false rest probability (P_M) with normalised threshold level (γ) for a range of fixed input signal-to-bandlimited-noise namely 0 dB, -3 dB and -6 dB, using as the characteristic waveform the 31 chip m-sequence. The threshold scale is calibrated in dB with 0 dB corresponding to the correlation peak and -16 dB to the largest sidelobe. Values of P_M calculated directly

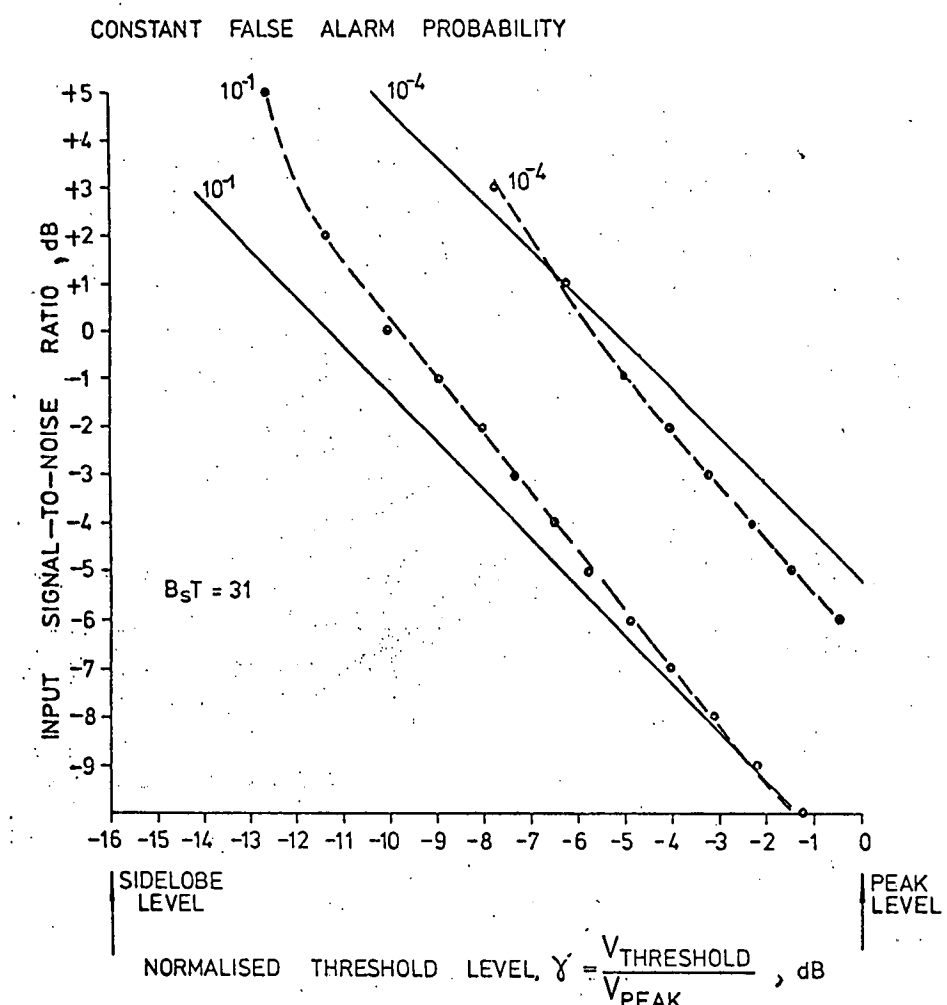

FIGURE 6.4 OOK MODEM - SIGNAL TO-NOISE-RATIO VERSUS γ AT FIXED P_F

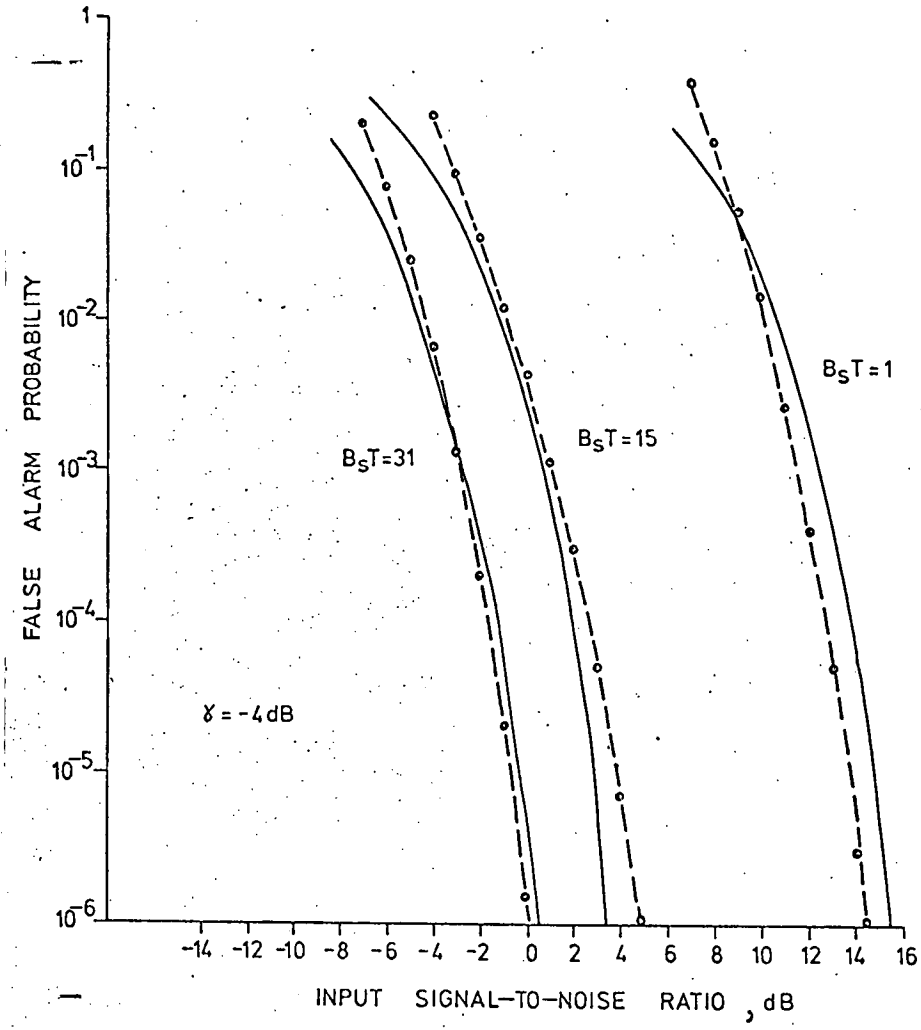

FIGURE 6.5 OOK MODEM - P_F VERSUS SIGNAL-TO-NOISE RATIO

from the Q-function (Chapter 5) and from the limited tabulation of DiDonato and Jarnagin[12] are included.

Figure 6.4 shows experimentally obtained curves of input signal-to-noise ratio versus normalised threshold level for *constant* values of false alarm probability, P_F, obtained with the 31 chip coded AMFs. For comparison, the corresponding theoretical plots of fixed P_F are given. With envelope detection, equation 5.5 may be rearranged to give:

$$10 \log_{10} (\rho_i) + 10 \log_{10} (2B_sT) = 10 \log_{10} [\ell n(P_F)^{-1}] = 20 \log_{10}\gamma \quad \ldots 6.3$$

where ρ_i is the input signal-to-noise plus interference ratio, and B_sT (=31) and P_F are constant in this experiment. This equation (6.3) is linear in $\log_{10}\gamma$ and in the form given indicates clearly the effect of using differing values of time-bandwidth product, since the left hand side equals the output peak signal-to-noise ratio.

The following observations can be made on the results of Figures 6.3 and 6.4:

(1) Agreement between the theoretical and measured error probabilities is within ±1 dB in input signal-to-noise ratio (SNR) over the threshold range, γ = -2 dB to γ = -7 dB for the P_F curves and similarly, with ±0.5 dB in input SNR over the threshold range, γ = -2 dB to γ = -10 dB. This range of close agreement encompasses the range of optimum thresholds for OOK signal reception discussed in Chapter 5.

(2) These two characteristics illustrate the different error probability weightings achievable in any specific application.

The effect of *increasing time-bandwidth product* is demonstrated in Figure 6.5 which shows the theoretical and measured false alarm probabilities, obtained with a fixed normalised threshold of -4 dB, versus input SNR for three expansion-compression loops of 1, 15 and 31 time-bandwidth product. The close agreement between theoretical and practical results for the coded 15 and 31 chip loops is noted. The uncoded IF pulse loop exhibits some divergence from theory partly due to the difficulty found in accurate calibration of the input SNR for this case. These characteristics clearly illustrate the processing gain achievable for a fixed false alarm probability when using coded signals of increasing B_sT at a *fixed signal bandwidth* (increasing signal energy). For clarity, the 13 chip Barker coded characteristic was omitted because it coincided (within 0.5 dB) with that of the 15 chip m-sequence.

The final characteristic obtained for signals corrupted by bandlimited noise is shown in Figure 6.6 where false rest probability (P_M) is plotted as a function of γ, versus input signal-to-noise ratio for the 31 chip m-sequence coded IF pulse. Again, close to theoretical performance was achieved for the range of thresholds and input signal-to-noise ratios employed in the evaluation. Similar curves were also obtained, with fixed threshold, for the 15 chip m-sequence coded AMFs incorporated in an OOK RADA modem the results of this evaluation are discussed in Section 6.4.

6.3 EXPERIMENTAL BINARY FSK SPREAD SPECTRUM MODEM

In this section two simple implementations of binary spread spectrum modems are described. The discussion in Chapter 5 of M-ary signaling considered the important special case of zero cross-talk at the sampling instant. Here, cross-talk levels are quantified for two

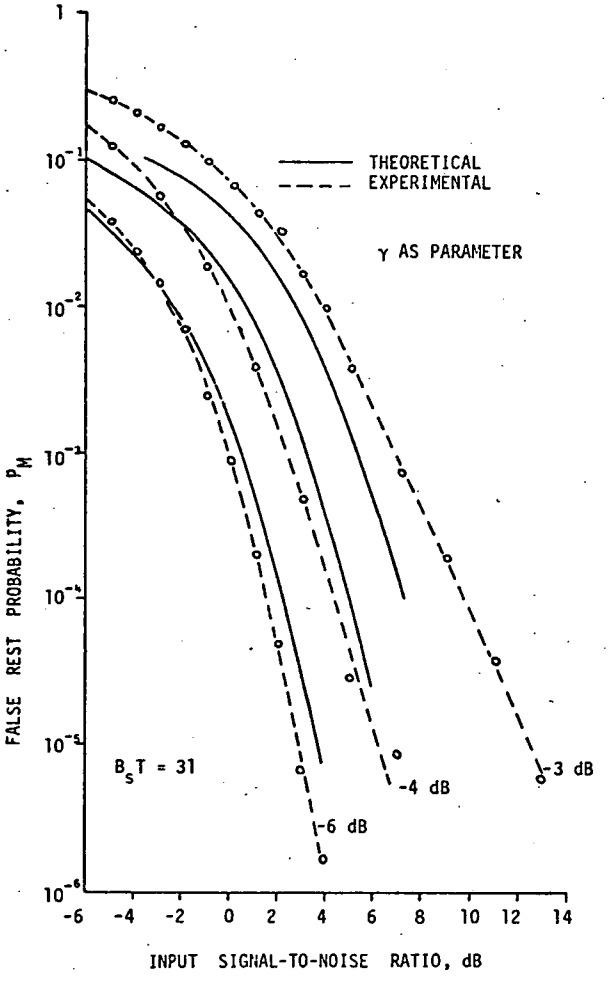

FIGURE 6.6 OOK MODEM - P_M VERSUS SIGNAL-TO-NOISE RATIO AT FIXED γ

specific AMFs processing 15 and 31 chip signals with carriers shifted by multiples of B_s and a practical arrangement for eliminating cross-talk is suggested for a receiver operating with bit synchronisation.

For the reception of binary transmissions employing a pair of distinguishable waveforms to denote the two message states, the error probability depends only on the signal-to-noise ratio and the degree of mutual crosscorrelation. In a binary modem designed to receive equally energetic, *orthogonal* Mark and Space signals, the difference between the envelopes of the matched filter outputs is compared against zero threshold *at the sampling instant*, simply to determine the sign of this difference voltage.

In achieving orthogonality it is first instructive to examine the response of a matched filter for rectangular pulses of length T, on a carrier at f_o, to a pulse signal of equal duration with a carrier at $f_o + \Delta f$, where $\Delta f \ll f_o$. At the sampling instant ($t = T$) the envelope can be written in the form:

$$v_o(T) = kT \operatorname{sinc}(\pi \Delta f T) \qquad \ldots 6.4$$

where k is constant. It can be shown from the property of the sinc function that the *effective* frequency domain transfer function *at the sampling instant* has nulls at frequencies spaced by integer multiples of $^1/T$ from f_o. In FSK signaling with matched filtering of rectangular pulses, the tone spacing would be $^1/T$ for no cross-talk between the filter outputs at the sampling instants and, also efficient spectral utilization would be obtained.

A similar analysis holds for spread-spectrum signals comprised of coded sequence of L bi-phase modulated chips of duration τ, here the spectral bandwidth of the whole signal equals the chip bandwidth

($^1/\tau$) and at time t = T the output is the sum of L identical terms hence,

$$v_o(T) = k\tau L \text{ sinc } (\pi \Delta f \tau) \qquad \ldots 6.5$$

Similarly, orthogonality is achieved for carrier spacings of integral multiples of B_s (= $^1/\tau$).

For experimental verification, a modified version of the arrangement of Figure 4.14 was employed.

Here, the modification consisted of removing the divide by N clock generator in order to maintain the clock frequency at 5 MHz while varying the carrier frequency. The response of an AMF acoustically synchronous at 127.3 MHz with 5 MHz bandwidth and matched to a 15 chip m-sequence, with characteristic polynomial $x^4 + x^2 + 1$, was examined. Figure 6.8 shows the time domain responses for carrier frequencies of (1) 117.3 MHz, (2) 122.3 MHz and (3) 127.3 MHz. Traces (A) and (B) show the zero-level cross correlation coefficient (χ_{12}= 0) at the sampling instant. Also, it is worth noting in the context of uncoordinated multiple access systems that cross-talk levels for *adjacent* bands are similar in magnitude to the code's autocorrelation time sidelobes ($\sim \sqrt{L}$). Lower cross-talk signals are obtainable by time reversing codes for adjacent channel transmission as illustrated in Figure 6.8b. Given *synchronous transmissions* (eg TDMA) other methods of achieving *instantaneous* orthogonality between letters of a common signaling alphabet include the use of selected PN codes, Walsh functions, or other distinctive, eg simplex codes, for alphabet construction. An alternative practical approach would arrange differential delays in the receiver's filters so that temporal separation is achieved between

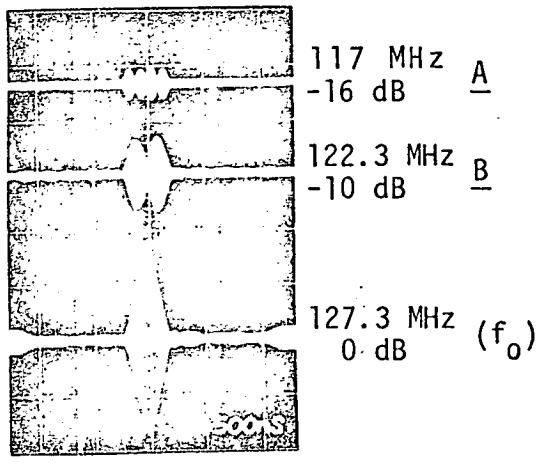

(a)

FIGURE 6.8a RESPONSE OF AMF TO ADJACENT CHANNEL SIGNALS and,

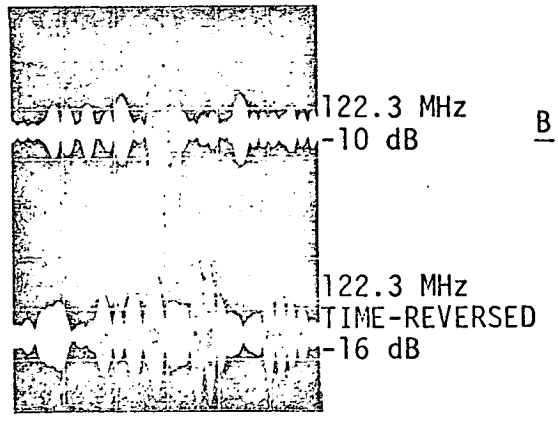

(b)

FIGURE 6.8b EFFECT OF TIME-REVERSING ADJACENT CHANNEL CODE

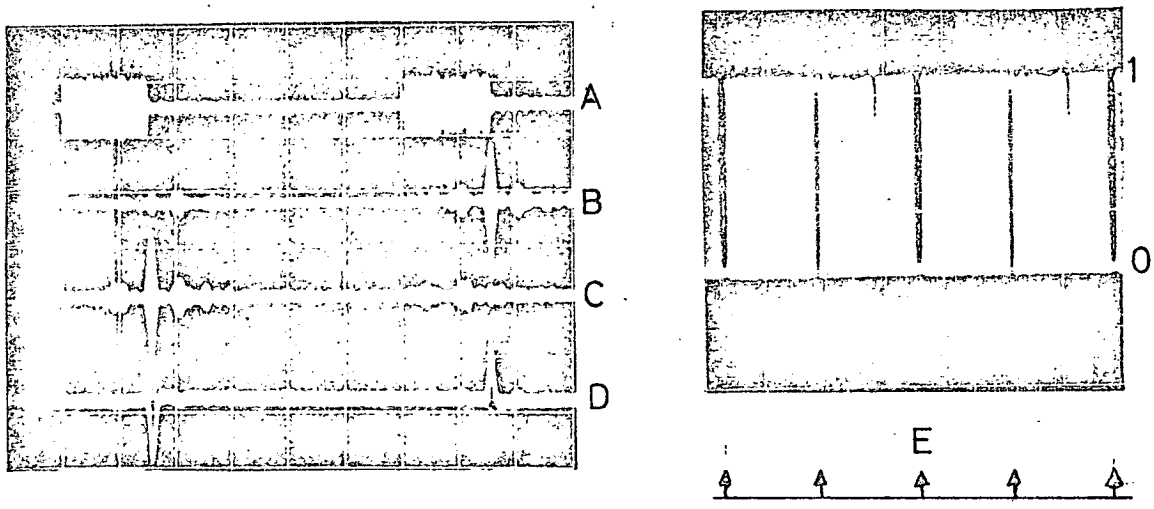

FIGURE 6.9 EXPERIMENTAL BINARY FSK RECEIVER WAVEFORMS (A) INPUT SIGNALS; (B), (C) AMF OUTPUTS; (D) OUTPUT OF DIFFERENTIAL AMPLIFIER; (E) OUTPUT OF ZERO-THRESHOLD COMPARATOR

the cross-talk and matched outputs. Then, to retain equal Mark-Space ratios, or equivalently equal sampling intervals to simplify the receiver logic, the conjugate filters in the transmitter must compensate for the differential delay in the receiver. This requirement also imposes the restriction that for a peak power limited transmitter (typified by satellite networks) the Mark-Space signals must not overlap. Otherwise a loss in signal energy and an increase in intermodulation products occurs.

A bit synchronous experimental spread spectrum binary modem was constructed using AMFs matched to the 15 chip m-sequence modulating carriers at 127.3 MHz Mark and 132.3 Space at a 5 MHz chip rate, Figure 6.9, Trace A. Thus invoking the condition for orthogonality described above. The initial circuit used in the receiver is shown in Figure 5.8, the AMF outputs, Figure 6.9, traces B, C were envelope demodulated and combined in a differential amplifier which performed the necessary envelope subtraction (Mark-Space). The output of the differential amplifier consists of bi-polar signals; positive excursions being due to Mark signal presence and negative due to Space signals, Figure 6.9, trace D. Positive and negative swings result in defined output levels from the comparator at the sampling instants, Figure 6.9, trace E. Random decisions on noise and corresponding rapid fluctuation of the output occur in the 'no signal' interval. A D-type flip flop, clocked by the sampling pulse, reconstitutes the data stream.

The transmitter schematic and an alternative decision configuration for the receiver is shown in Figure 6.10. The encoder at the transmitter is simply implemented, with a data source synchronised to a clock, by the logical AND gate arrangement shown. When the clock goes high, binary ones are routed through the upper AND gate and trigger the impulse generator connected to AMF A resulting in a Mark transmission. Similarly, binary zeros are routed through the lower AND gate and a Space

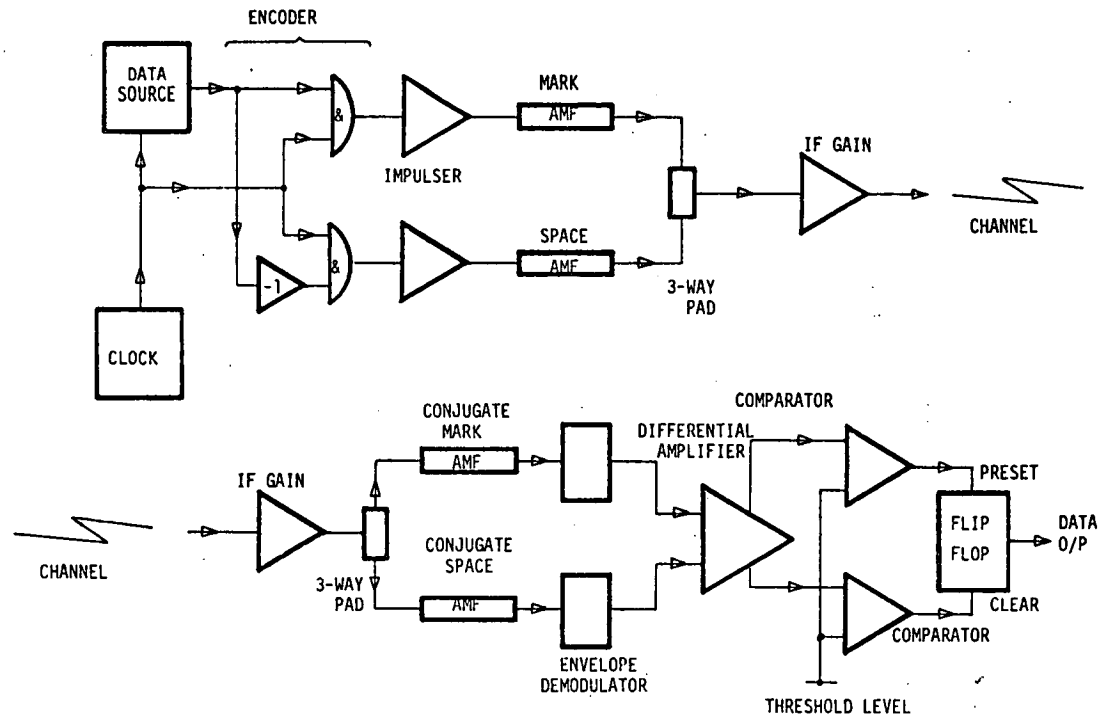

FIGURE 6.10 EXPERIMENTAL BINARY FSK MODEM

signal is transmitted. Fully asynchronous operation of the receiver is achieved by using the complementary bipolar signals provided by the differential output circuit of the IC video amplifier employed (Texas Instruments 2N72733). Reliable asynchronous operation is achieved at high output SNR by raising the threshold level (V_T) and detecting *both* Mark and Space video signals. The data is *unambiguously* regenerated by using the separate decisions to preset and clear a flip flop. However, without a sampling pulse and with raised threshold (to avoid detection of AMF cross-talk outputs), the link is subject to the same operational drawbacks (limited dynamic range, maintenance of optimum threshold level) as for OOK transmissions.

However, a compromise scheme may be envisaged whereby a locally generated sampling pulse may be synchronised to the bit period by raising the threshold and using the detected Mark and Space peaks to lock a phase-locked sampler. Once synchronisation had been established, the threshold would then be returned to zero level for maximum signal dynamic range until the synchronisation command was reinitiated, for example by exceeding an error count bound on an error detection monitor.

The modem performance was evaluated at zero decision threshold with the same basic peripheral equipment described in Section 6.2. Error rate measurements with the addition of bandlimited noise only to the channel were made by independently monitoring the rate of Mark and Space signals emerging from the flip flop. Again, synchronous 200 nS wide sampling pulses were employed. The average error rate is the average of the individual Mark and Space error rates determined by subtracting the appropriate counter readings from the clock rate (100 kHz). For equally energetic signals and equal thresholds (V_T = 0 in this experiment) the Mark and Space miss rates are equal, this fact was verified in the course of the evaluation. The resulting error

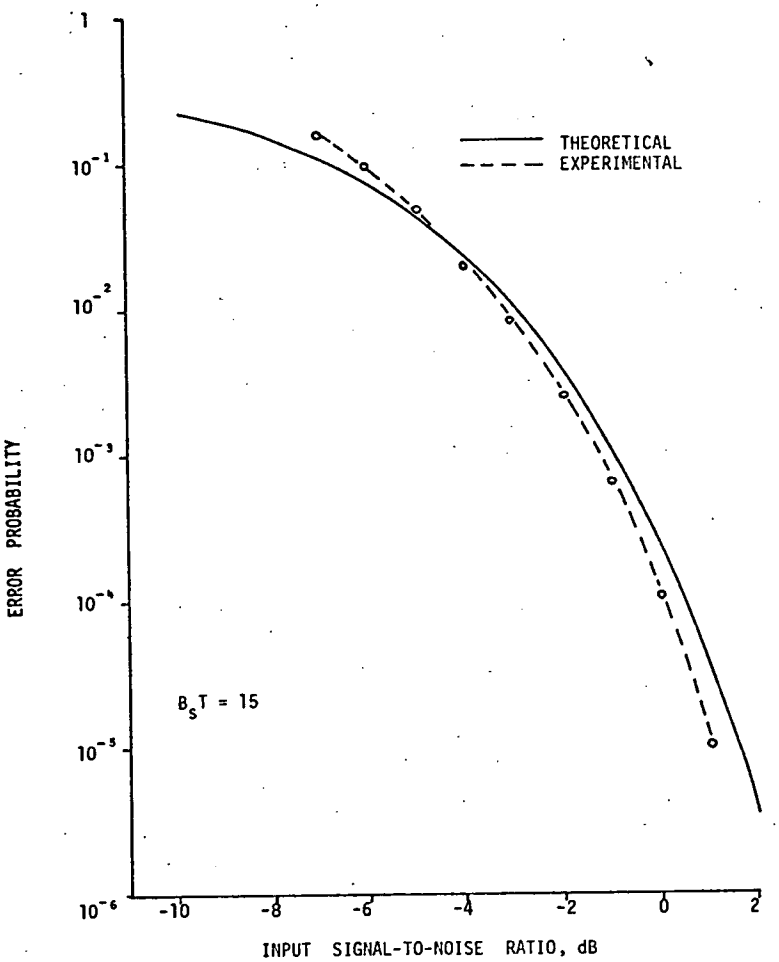

FIGURE 6.11 BINARY FSK MODEM PERFORMANCE

probability is shown together with the theoretical curve in Figure 6.11. Again, the close agreement between measured and theoretical performances realisable with simple modem configurations has been demonstrated.

6.4 OOK MODEM FOR RANDOM ACCESS, DISCRETE ADDRESS COMMUNICATIONS

In RADA communications (see Chapter 5) the transmitted signal conveys both the unique address of the receiver and the data. An attractive address structure for providing large address directories is comprised of a sequence of N bandspread pulses further encoded in both time and frequency domains (see Chapters 2 and 5). The significant practical features offered by SAW AMFs are twofold; firstly the ease with which matched filtering of a variety of complex signals can be implemented (ie for each of the N coded pulses) and secondly, for short waveform durations (<15 μs), the decoding of the relative temporal pulse positions can be achieved through appropriate characteristic delays incorporated in the AMF geometry[15].

Experiments were conducted on a simple OOK, RADA communications modem (Figure 5.4) employing two characteristic waveforms in the address. A set of 4 frequency contiguous AMFs were designed for frequency-hopped communications described in Chapter 4. Two 15 chip conjugate AMFs were fabricated on ST-cut quartz using designs centred at 127.3 and 132.3 MHz. A waveform diagram is given in Figure 6.12 showing details of relative pulse delay, frequencies and coding employed. Again, cross-talk signals were minimised by using the time-reversed modulation on one adjacent channel and virtually eliminated by the delay mechanism inherent in implementing a RADA receiver.

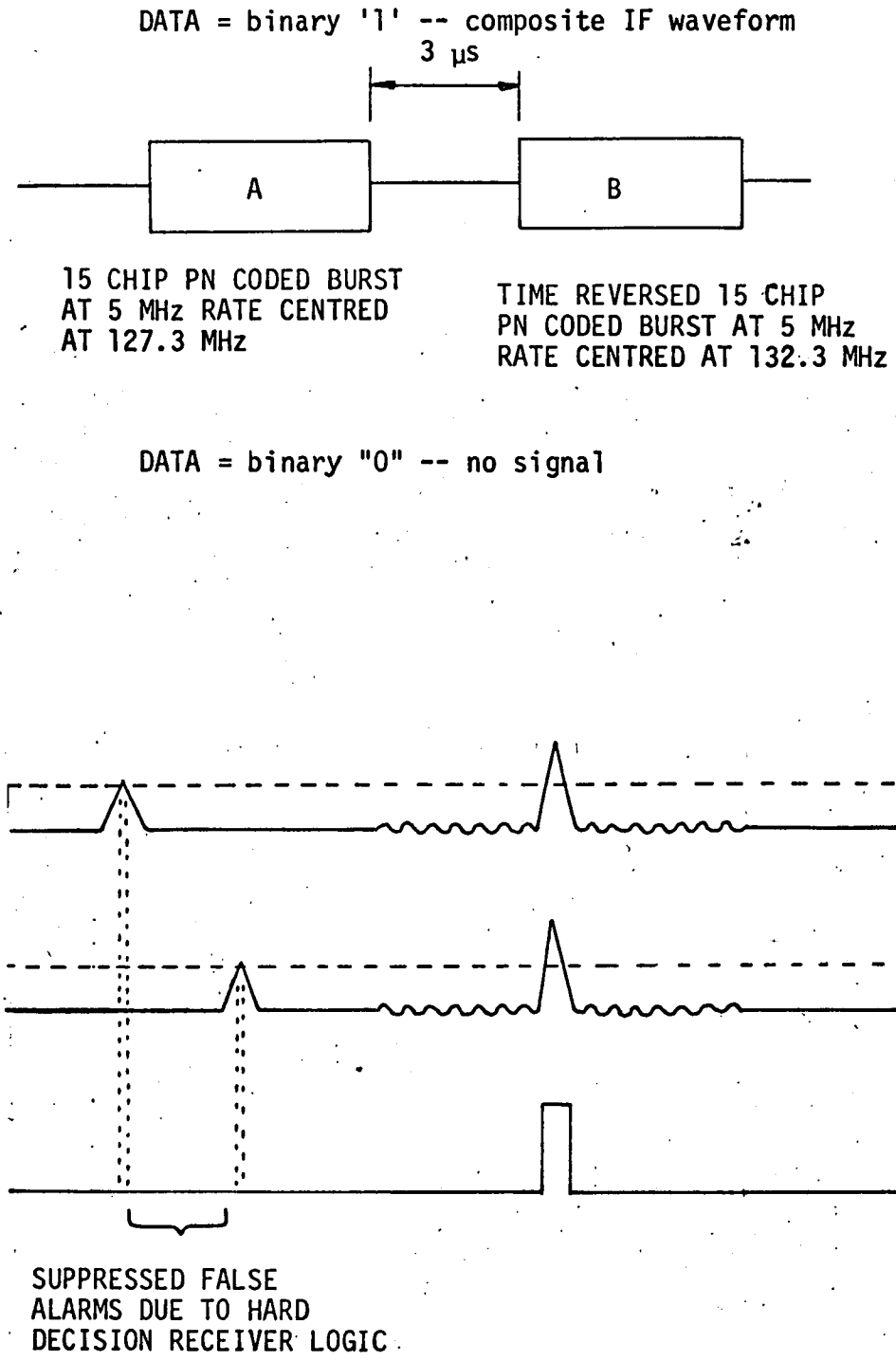

FIGURE 6.12 SIMPLIFIED RADA MODEM WAVEFORM DIAGRAM

In the transmitter a single 5 nsec duration, 10 volt peak impulse from an avalanche mode circuit was used to generate the IF address waveform illustrating the convenience of SAW in enabling the rapid, passive generation of complex waveforms. The hardware used should be compared with that described in other reports (eg Blasbalg et al[98] and Corr et al[99]) which comprised either frequency agile oscillators or a system of gated oscillators plus a balanced modulator and microelectronic code generator.

After matched filter processing and envelope demodulation the correlation peaks were individually detected and the resulting baseband pulses combined logically in a coincidence gate to generate a sequence of return-to-zero (RTZ) pulses. These RTZ pulses may be directly processed by the appropriate decoder if QPPM or a varient of delta modulation[43] is being used. In the case of PCM, the digital waveform may be reconstructed by a D-type flip-flop and synchronous clock.

The performance of this two-signature address modem was evaluated using the OOK synchronous measurement procedure previously described, with the addition of bandlimited noise (15 MHz bandwidth filter) to the link. A full experimental evaluation of the interference immunity of the RADA receiver would involve the synthesis of many RADA system signals. The purpose of this evaluation was to investigate the operation of the hard decision receiver logic employed. Similarly computer simulations involves extensive programming[116] and is only meaningful for a given set of system requirements.

However, plots of both conditional error probabilities (P_F and P_M) for thresholds of -5 dB on both filter outputs versus input signal-to-*noise* ratio are reproduced in Figure 6.13. The conditional error probabilities measured are plotted separately to illustrate the action of the hard decision address recognition logic. These curves are compared with theoretical curves for P_F obtained with signals having time-bandwidth products (B_sT) of 15 and 31, and P_M for $B_sT = 15$.

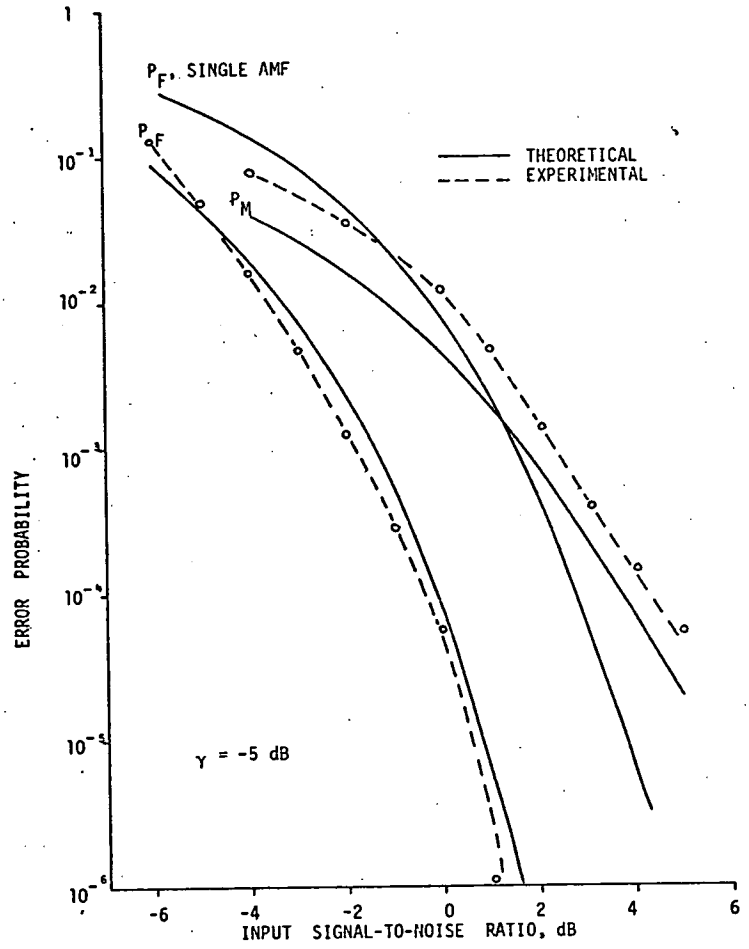

FIGURE 6.13 RADA MODEM PERFORMANCE

For the experimental modem described, equation 5.10 becomes:

$$P_E = \tfrac{1}{2}P_F^2 + \tfrac{1}{2}(2P_M) \qquad \ldots 6.6$$

where N = 2.

The measured false alarm rate lies close to the theoretical curve for BT = 31, as predicted by equation 6.6 where the effective false alarm rate P_F^1 is given from equation 5.5 by

$$P_F^1 = \exp - \gamma^2\ 2TB_s\rho: \qquad \ldots 6.7$$

Thus, the hard decision receiver effectively multiplies the processing gain (BT) by N in terms of false alarm rejection. Close agreement exists between measured false rest probability and the effective probability (P_M^1) indicated by theory.

For the normalised threshold setting used in the experiment the combined error rate P_E, is predominantly due to P_M^1. This indicates that the threshold used was too high and could be reduced to increase the detection probability while maintaining acceptably low P_F^1. The optimum threshold for the detection of OOK signals minimises the total average probability of error and is a function of signal-to-noise ratio. In practice it may be more meaningful to adopt the Neyman-Pearson[59] strategy which awards different costs to each error type. The decision boundary chosen guarantees that the expected frequency of occurrence of the most costly error does not exceed some given upper bound.

The simple configuration described is the building block for the more complex arrangements suggested in Chapter 5.

6.5 SUMMARY

This chapter has examined the performance under laboratory conditions of moderate TB_s product SAW AMF incorporated in prototype IF spread spectrum digital communication modems employing OOK and binary FSK signaling techniques. Close to theoretical error rate performance has been achieved.

Experiments on a simple OOK RADA modem demonstrated the unique advantages of SAW AMF in the rapid synthesis and detection of complex frequency and time encoded pulse patterns with minimal hardware. This RADA modem exhibited predictable error rate performance in the presence of bandlimited noise at the receiver input.

RADA techniques offer uncoordinated[43] multiple access capability. Achievement of this in practical systems requires larger address alphabets and larger TB_s product SAW AMF than were utilised in the above experiments. Deployment of binary FSK signaling[70] would remove the OOK requirement to maintain accurate receiver thresholds. This would be advantageous for practical channels subject to deep fade.

FOOTNOTE

The departure from theory exhibited by the experimentally derived error rate curves arose partially through measurement inaccuracies and through the deployment of first-order AMF's. In order to achieve good error rate performance with large address signal TBs products it will probably be necessary to incorporate second-order AMF's with additional compensation for propagation losses.

CHAPTER 7

FINAL REMARKS

This Thesis has examined the advantages and limitations of SAW technology in realising binary phase coded AMF, and has identified potential applications in digital spread spectrum communications modems. Using the techniques described high performance AMF can be realised and used in novel configurations allowing processing of complex time and frequency domain encoded signals for uncoordinated multiple-access systems.

Specifically, a novel dual-tap geometry was devised to reduce distortion arising from SAW impedance mismatch and regeneration. Significant improvements in the fidelity of the AMF response were demonstrated for 13 chip Barker and 31 chip m-sequence coded devices. Encouraging results were also obtained with a 127 tap AMF although scattering to bulk modes produced a 2 dB taper on the impulse response. Negligible bulk mode production was obtained with a 63-tap split-electrode design which gave close-to-theoretical performance. Hence, a hybrid geometry incorporating dual-taps with split-electrodes was suggested for reduction of *all three* major causes of degradation.

It was recognised that an increasing volume of communications traffic is comprised of short, intermittently transmitted, data blocks. Typical networks being those of terminal area and en-route air traffic control; the security systems which interrogate remote sensors; and emergency services systems. In each example the system characteristics desired: immediate uncoordinated multiple access; low cost equipment; protection against interference and multipath; and high reliability, predicate spread spectrum techniques. However, current equipments,

ie direct PN and PN-FH modems, do not provide the essential features of: asynchronous operation, since significant fractions of a minute are encountered for synchronisation acquisition; and, for direct PN, protection against a mix of signal powers - the near far problem. Attention was thus focussed on the attainment of the necessary processing gains through complex time-frequency encoded address pulse patterns and serial-parallel processing techniques with modest (~100) TB_s product AMF. Simple configurations for OOK and M-ary signaling were described. Prototype modems were constructed and near theoretical performance demonstrated for signals corrupted by white noise.

The basic arrangements outlined form the basis of sophisticated modems employing hybrid spread spectrum RADA techniques which do not require inclusion of special synchronisation signals in the date sequence. The developments deemed necessary in SAW AMF design include: the achievement of TB_s products of >1000 and bandwidths approaching 100 MHz, made possible with improved fabrication and a thorough understanding of errors due to bulk mode production and diffraction. This will allow design of multi-function equipments for supersonic transport where accurate navigation and altitude measurement and high message rate communications are becoming increasingly important.

Strong competition can be expected from low TB_s AMF employing magnetostatic waves on epitaxial YIG substrates at UHF where the wider signal bandwidths ($\gtrsim$100 MHz) can be used. Also, competition will arise from LSI semiconductor technology certainly at the lower bandwidths ($\lesssim$20 MHz) where both charge coupled devices and conventional logic families can achieve comparable TB_s products. However, the significant advantages in hardware reduction offered by SAW places the technology in a strong position.

REFERENCES

1. Lord Rayleigh, "On waves propagated along the plane surface of an elastic solid," Proc London Math Soc, vol 17, pp 4-11, November 1885.
2. E A H Love, Some Problems in Geodynamics. New York: Cambridge University Press, 1911.
3. R Stoneley, "Elastic waves at the surface of separation of two solids", Proc Roy Soc (London), ser A, vol 106, pp 416-428, 1964.
4. K A Ingebrigtsen, "Elastic surface waves in piezoelectrics and their coupling to carriers in an adjoining semiconductor," Norwegian Institute of Technology, Trondheim, Norway, Elab Rept TE-94, November 1967.
5. W Strauss, "Magnetoelastic waves in yttrium iron garnet," J Appl Phys, vol 36, pp 118-123, January 1965.
   J H Collins and F A Pizzarello, "Propagating magnetic waves in thick films. A complementary technology to surface wave acoustics", Int J Electronics, vol 34, No 3, pp 319-351, 1973.
6. B J Darby and P M Grant, "Key applications of SAW devices in communications links", Microwave Systems News, vol 3, No 6, pp 73-77, Jan 1974.
7. G S Kino and H Matthews, "Signal processing in acoustic surface-wave devices", IEEE Spectrum, pp 22-35, August 1971.
8. R M White and F W Voltmer, "Direct piezoelectric coupling to surface elastic waves", Appl Phys Lett, vol 7, pp 314-316, Dec 15, 1965.
9. W R Smith, H M Gerard, J H Collins, T M Reeder and H J Shaw, "Analysis of Interdigital surface wave transducers by use of an equivalent circuit model", IEEE Trans on Microwave Theory and Techniques, vol MTT-17, No 11, pp 856-864, November 1969.

10. W S Jones, R A Kempf and C S Hartmann, "Practical surface wave chirp filters for modern radar systems", Microwave J, vol 15, pp 43-86, May 1972.

11. R F Mitchell, "Acoustic surface wave transversal filters: their use and limitations", IEE Conf Publ, No 109, pp 130-140, September 1973.

12. B J Darby, "Suppression of spurious acoustic signals in phase coded surface acoustic wave analogue matched filters using a dual-tap geometry", IEEE Trans on Sonics and Ultrasonics, vol SU-20, No 4, pp 382-384, October 1973.

13. J H Collins, B J Darby, R D Pringle, "Correlation of pseudo-random sequences using parametric interactions between surface acoustic waves", Proc 1971 European Microwave Conference, Stockholm, paper C7/1.

14. D P Morgan, B J Darby, J H Collins, "Programmable correlation using parametric interactions in acoustic surface waves", Electron Lett, vol 8, No 2, pp 40-42, January 27, 1972.

15. B J Darby, P M Grant, J H Collins and I M Crosby, "Performance of aperiodic spread spectrum modems incorporating surface acoustic wave analogue matched filters", IEE Conf Publ, No 109, pp 319-328, 1973.

16. R M White, "Surface elastic waves", Proc IEEE, vol 58, No 8, pp 1238-1276, August 1970.

17. D P Morgan, "Surface acoustic wave devices and applications, 1. Introductory review," Ultrasonics, vol 11, No 3, pp 121-131, May 1973.

18. J H Collins and P J Hagon, "Applying surface wave acoustics," Electronics, vol 42, pp 97-103, November 10, 1969.
J H Collins and P J Hagon, "Amplifying acoustic surface waves," Electronics, vol 42, pp 102-111, December 8, 1969.

18. J H Collins and P J Hagon, "Surface wave delay lines promise filters for radar, flat tubes for television, and faster computers," Electronics, vol 43, pp 110-122, January 19, 1970.

19. R M White, "Surface elastic-wave propagation and amplification," IEEE Trans on Electron Devices, vol ED-14, No 4, pp 181-189, April 1967.

20. W D Squire, H J Whitehouse, and J M Alsup, "Linear signal processing and ultrasonic transversal filters", IEEE Trans on Microwave Theory and Techniques, MTT-17, No 11, pp 1020-1040, November 1969.

21. A J Slobodnik Jr, "A review of material tradeoffs in the design of acoustic surface wave devices at VHF and microwave frequencies", IEEE Trans on Sonics and Ultrasonics, vol SU-20, No 4, pp 315-323, October 1973.

22. J H Collins, P J Hagon and G R Pulliam, "Evaluation of new single crystal piezoelectric materials for surface acoustic-wave applications", Ultrasonics, pp 218-226, October 1970.

23. C S Hartmann, D T Bell and R C Rosenfeld, "Impulse model design of acoustic surface-wave filters", IEEE Trans on Microwave Theory Tech, vol MTT-21, No 4, pp 162-175, April 1973.

24. L P Solie, "Surface acoustic wave velocities for two metal layers on lithium niobate and bismuth germanium oxide substrates", IEEE Trans on Sonics Ultrasonics, vol SU-20, No 4, pp 379-382, October 1973.

25. H Skeie, "Electrical and mechanical loading of a piezoelectric surface supporting surface waves," J Acoust Soc Am, vol 48 (No 5 Part 2), p 1098.

26. T M Reeder and W R Sperry, "Broad-band coupling to high-Q resonant loads," IEEE Trans on Microwave Theory Tech, vol MTT-20, pp 453-458, July 1972.

27. T W Bristol, "Analysis and design of surface acoustic wave transducers," IEE Conf Publ, No 109, pp 115-129, 1973.

28. W R Smith, H M Gerard, J H Collins, T M Reeder, and H J Shaw, "Design of surface wave delay lines with interdigital transducers", IEEE Trans on Microwave Theory Tech, vol MTT-17, No 11, pp 865-873, November 1969.

29. F G Marshall, C O Newton, and E G S Paige, "Surface acoustic wave multistrip components and their applications," IEEE Trans on Microwave Theory Tech, vol MTT-21, No 4, pp 216-225, April 1973.

30. R D Weglein, M E Pedinoff, H V Winston, "Diffraction spreading of surface waves on $LiNbO_3$," Electronics Letters, vol 6, pp 654-655, October 15, 1970.

31. T L Szabo and A J Slobodnik, "The effect of diffraction on the design of acoustic surface wave devices," IEEE Trans Sonics Ultrason, vol SU-20, No 3, pp 240-251, July 1973.

32. E G H Lean, C C Tseng, and C G Powell, "Optical probing of acoustic surface-wave harmonic generation," Appl Phys Lett, vol 16, pp 32-35, January 1, 1970.

33. P O Lopen, "Second-harmonic generation in an elastic surface wave in alpha-quartz", J Appl Phys, vol 39, pp 5400-5404, November 1968.

34. G S Kino et al, "Signal processing by parametric interactions in delay-line devices," IEEE Trans Microwave Theory Tech, vol MTT-21, No 4, pp 244-255, April 1973.

35. P E Lagasse, I M Mason, and E A Ash, "Acoustic surface wave guides - Analysis and assessment," IEEE Trans Microwave Theory Tech, vol MTT-21, No 4, pp 225-236, April 1973.

36. P M Grant, J H Collins, B J Darby, and D P Morgan, "Potential applications of acoustic matched filters to air-traffic control systems", (Invited Paper) IEEE Trans on Microwave Theory Tech, vol MTT-21, No 4, pp 288-300, April 1973.

37. R L Harris, "Introduction to spread spectrum techniques", Proc AGARD Lecture Series No 58, Ref 3, 1973.

38. C R Cahn, "Spread spectrum applications and state-of-the-art equipments", Proc AGARD Lecture Series No 58, Ref 5, 1973.

39. R Gold, "Optimal binary sequences for spread spectrum multiplexing", IEEE Trans on Information Theory, vol IT-13, No4, pp 619-621, October 1967.

40. J C Hancock and P A Wintz, "Signal Detection Theory", p 66 ff, McGraw-Hill, 1966.

41. G L Turin, "An introduction to matched filters", IRE Trans on Information Theory, vol IT-6, pp 311-329, June 1960.

42. R J Mayher, IEEE EMC Symp Rec, pp 230-237, 1967.

43. M Magnuski, "Address communication systems", in "Communication Systems Engineering Handbook", D Hamsher, Ed. New York: McGraw-Hill 1967, Ch 18.

44. R H Barker, "Group synchronisation of binary digital systems", in "Communications Theory", W Jackson, Ed. New York: Academic Press, pp 273-287, 1953.

45. C E Cook and M Bernfeld, "Radar Signals", New York: Academic Press, 1967.

46. P H Carr, A de Vito and T L Szabo, "The effects of temperature and doppler shift on the performance of elastic surface wave encoders and decoders", IEEE Trans Sonics Ultrasonics, vol SU-19, No 3, pp 357-369, July 1972.

47. G F Gott, J P Newsome, "H.F. data transmission using chirp signals", Proc IEE, vol 118, No 9, pp 1162-1166, Sept 1971.

48. J Burnsweig and J Woodridge, "Ranging and data transmission using digital encoded FM - 'chirp' surface acoustic wave filters", IEEE Trans on Microwave Theory Tech, vol MTT-21, No 4., pp 272-279, April 1973.

49. L D Baumert, "Generation of specified sequences", in "Digital Communications", S W Golomb, Ed: Prentice Hall, 1964, Ch 2.

50. W W Peterson, "Error Correcting Codes", MIT Press and John Wiley, 1961.

51. F H Lange, "Correlation Techniques", Iliffe and Van Nostrand, 1967, Ch 4.

52. A Boehmer, "Binary pulse compression codes", IEEE Trans Information Theory, vol IT-13, No 2, pp 156-167, April 1967.

53. D E Findley, "Satellite considerations in future ATC systems", in AGARD Conf Proc, No 105, ATC Systems, paper 30, 1972.

54. A M McCalmont, "Multiple-access, discrete-address communication systems", IEEE Spectrum, vol 4, No 8, pp 87-94, Aug 1967.

55. B J Hunsinger, "Surface wave devices in spread spectrum processors", Ultrasonics, pp 254-262, November 1973.
B J Hunsinger, "Application of SAW devices to wideband communication links", IEE Conf Publ No 109, pp 309-318, 1973.

56. N G Davies,"Performance and synchronisation considerations", Proc AGARD Lecture Series No 58, ref 4, 1973.

57. S Stein and J J Jones, "Modern Communication Principles", New York: McGraw-Hill, 1967, Ch 9-14.

58. A G Burke, "A frequency hopped pseudo-noise modem using surface wave techniques", 1973 IEEE Intercon, March 26-30, 1973.

59. H R Raemer, "Statistical Communication Theory and Applications", Information theory series, Prentice Hall, 1969, Ch 3, 6, 7.

60. J W Schwartz, J M Aein and J Kaiser, "Modulation techniques for multiple access to a hard-limiting satellite repeater", Proc IEEE, vol 54, No 5, pp 763-777, May 1966.

61. J H Bagley, "Specification of the communications system", IEE Conf Publ No 63, SKYNET, pp 12-17, 20 April 1970.

62. J P Costas, "Poisson, Shannon and the radio amateur", Proc IRE, No 47, pp 2058-2068, Dec 1959.

63. J J Kepcke, "Maximum spectrum utilization by wide bandwidth transmission", IEEE Trans Vehicular Comm, No 1, pp 81-87, 1963

64. J H Collins and P M Grant, "The role of surface acoustic wave technology in communication systems", Ultrasonics, vol 10, No 2, pp 59-71, March 1972.

65. D Chesler, "Performance of a multiple address RADA system", IEEE Trans Commun Technol, vol COM-14, pp 369-372, Aug 1966.

66. J M Wozencraft and I M Jacobs, "Principles of Communication Engineering", New York: John Wiley, 1965, Ch 7.

67. W Stanley-Jones, C S Hartmann, and T D Sturdivant, "Second-order effects in surface wave devices", IEEE Trans on Sonics and Ultrasonics, SU-19, No 3, pp 368-377, July 1972.

68. G W Judd, W R Jones, and T W Bristol, "An improved tapping transducer geometry for surface wave phase coded delay lines", IEEE Ultrasonics Symposium, Boston 1972, Proceedings 72CH0708-8SU, pp 373-376.

69. T S Fisher, E Patterson and D G Scotter, "Surface-wave correlator with inclined transducer", Electron Lett, vol 9, No 3, p 55, 8 February, 1973.

70. M. Setrin, D T Bell, M B Schulz and M G Unkauf, "An IFF system using block programmable surface wave signal expander and compressor", IEEE Ultrasonics Symposium, Monterey 1973, Proceedings 73 CHO 807-8 SU, pp 316-323.

71. R LaRosa, C F Vasile and D V Zagardo, "Comparison of surface-wave reflection coefficients for different metals on quartz", Electron Lett, vol 9, No 21, pp 495-496, 18 October 1973.

72. M J Butler and J N Johnston, Private Communication.

73. G A Keig, "The economics of producing SAW materials for volume production", IEE Conf Publ No 109, pp 33-39, September 1973.

74. C F Vasile and R LaRosa, "1000 bit surface-wave matched filter", Electron Lett, vol 8, No 19, pp 479-480, 21 September 1972.

75. A J Bahr, "Fabrication techniques for surface-acoustic-wave devices", IEE Conf Publ No 109, pp 22-32, September 1973.

76. E J Staples and L T Claiborne, "A review of device technology for programmable surface-wave filters", IEEE Trans on Microwave Theory Tech, vol MTT-21, No 4, pp 279-287, April 1973.

77. P J Hagon, F B Micheletti, R N Seymour, and C Y Wrigley, "A programmable surface acoustic wave matched filter for phase-coded spread spectrum waveforms", IEEE Trans on Microwave Theory Tech, vol MTT-21, No 4, pp 303-306, April 1973.

78. P J Hagon, "Programmable analogue matched filters", IEE Conf Publ, No 109, pp 92-101, September 1973.

79. R D Lambert, P M Grant, D P Morgan, and J H Collins, "Programmable surface acoustic wave devices utilising hybrid microelectronic techniques", IERE Conf Proc No 27, pp 161-172, September 1973.

P M Grant, Private Communication.

80. M V Luukkala and G S Kino, "Convolution and time-inversion using parametric interactions of acoustic surface waves", App Phys Lett, vol 18, pp 393-394, May 1971.

81. D P Morgan, J H Collins, and J G Sutherland, "Asynchronous operation of a surface acoustic wave convolver", IEEE Ultrasonics Symposium, Boston 1972, Proc 72 CHO 708-8 SU, pp 296-299.

82. T M Reeder and M Gilden, "Convolution and correlation by nonlinear interaction in a diode-coupled tapped delay line", App Phys Lett vol 22, pp 8-10, January 1973.

83. E A Kraut, T C Lim and B R Tittman, "Application of non-linear interactions in ferroelectric ceramics to microwave signal processing", IEEE Trans Sonics and Ultrasonics, vol SU-19, pp 247-255, April 1972.

84. T C Lim, E A Kraut and R B Thomson, "Nonlinear materials for the acoustic-surface-wave convolver", App Phys Lett, vol 20, pp 127-129, 1972.

85. D P Morgan, Private Communication.

86. F G Marshall, C O Newton, and E G S Paige, "Surface acoustic wave multistrip components and their applications", IEEE Trans Microwave Theory Tech, vol MTT-21, No 4, pp 216-225, April 1973.

87. E Stern, "Current status of silicon-lithium niobate convolvers", IEE Conf Publ No 109, p 85, September 1973.

88. T M Reeder, "Electronically programmable convolution and correlation using nonlinear delay line filters", IEE Conf Publ No 109, p 73-84, September 1973.

89. D P Morgan and J G Sutherland, "System aspects of the utilisation of SAW convolvers", IEE Conf Publ No 109, pp 86-91, September 1973.

90. F L J Sangster, "The bucket-brigade delay line, A shift register for analogue signals", Philips Tech Rev, vol 31, pp 92-110, 1970.

W J Butler, C M Puckette, M B Barron and B Kurz, "Analogue operating characteristics of bucket-brigade delay lines", 1972 IEEE Solid-State Circuits Conf Dig Tech Papers, pp 138-139, 226-227.

91. W S Boyle, and G E Smith, "Charge coupled semiconductor devices", Bell Syst Tech J, vol 49, pp 587-593, April 1970.

G F Amelio, M F Tompsett, and G E Smith, "Experimental verification of the charge coupled device concept", ibid, pp 598-600.

92. D D Buss, W H Bailey, and D R Collins, "Matched filtering using tapped bucket-brigade delay lines", Electron Lett, vol 8, pp 106-107, February 1972.

93. D R Collins, W H Bailey, W M Gosney, and D D Buss, "Charge-coupled-device analogue matched filters", Electon Lett, vol 8, pp 328-329, June 1972.

94. C S Hartmann, L T Claiborne, D D Buss, and E J Staples, "Programmable transversal filters using surface waves, charge transfer devices, and conventional digital approaches", IEE Conf Publ No 109, pp 102-114, September 1973.

95. D D Buss, D R Collins, W H Bailey, and C R Reeves, "Transversal filtering using charge-transfer devices", IEEE J Solid-State Circuits, vol SC-8, pp 138-146, April 1973.

96. M F Tompsett, W J Bertram, D A Sealer, and C H Sequin, "Charge coupling improves its image, challenging video camera tubes", Electronics, pp 162-169, January 18, 1973.

97. G C Bagley, "Radar pulse-compression by random phase coding", Radio and Electronic Eng, vol 36, pp 5-15, July 1968.

98. H Blasbalg, D Freeman, and R Keeler, "Random-access communications using frequency shifted pseudo-noise signals", IEEE Int Convention Rec, vol 12, pt 6, pp 192-216, 1964.

99. F P Corr, R Crutchfield and J Marchese, "A pulses pseudo noise VHF radio set", IBM J, vol 9, pp 256-263, 1965.

100. R H Tancrell and M G Holland, "Acoustic surface wave filters", Proc IEEE, vol 59, No 3, pp 393-409, March 1971.

101. M B Schulz and M G Holland, "Materials for surface acoustic wave components", IEE Conf Publ No 109, pp 1-10, September 1973.

102. H J Carlin and A B Giordano, "Network Theory", Prentice-Hall, 1964, Ch 4.

103. H M Gerard, "Acoustic scattering parameters of the electrically loaded interdigital surface wave transducer", IEEE Trans on Microwave Theory Tech, vol MTT-17, No 11, pp 1045-1046, Nov 1969.

104. R A Waldron, "Power transfer factors for nonuniformly irradiated interdigital piezoelectric transducers", IEEE Trans on Sonics and Ultrasonics, vol SU-19, No 4, pp 448-453, October 1972.

105. W S Jones, C S Hartmann and J L Harris, "Matching optimisation to interdigital surface-wave devices", Electron Letters, vol 6, No 11, pp 333-335, 28 May 1970.

106. G L Matthai, L Young and E M T Jones, "Microwave filters, impedance-matching networks and coupling structures", McGraw-Hill, 1964, Ch 8, 11.

107. H P Application note number AN117.

108. L O Svaasand, "Interaction between elastic surface waves in piezoelectric materials", Appl Phys Lett, vol 15, pp 300-302, 1969.

109. C F Quate and R B Thompson, "Convolution and correlation in real time with nonlinear acoustics", Appl Phys Lett, vol 16, pp 494-496, June 15, 1970.

110. I S Reed and H Blasbalg, "Multipath tolerant ranging and data transfer techniques for air-to-ground and ground-to-air links", Proc IEEE, vol 58, p 422-429, Mar 1970.

111. J I Marcum, "A statistical theory of target detection by pulsed radar", IRE Trans PGIT, IT-6, p 145, ff, April 1960.

112. A R DiDonato and M P Jarnagin, "A method for computing the circular coverage function", Mathematics of Computation, vol 16, pp 347-355, 1962.

113. I S Reed and G Solomon, "Polynomial codes over certain finite fields", J Soc Ind Appl Path, vol 8, pp 300-314, 1960.

114. A H Nuttall, "Error probabilities for equicorrelated M-ary signals under phase coherent and phase incoherent reception", IRE Trans Information Theory, vol IT-8, No 4, pp 305-314, July 1962.

115. W R Bennett and J R Davey, "Data Transmission", McGraw-Hill, New York, 1965.

116. B W Beals and F R Zitzmann, "Simulation for RADAS", IEEE Trans on Communication Tech, vol COM-14, No 5, pp 553-561, October 1966.

APPENDIX

The following four published papers are included:

I D P Morgan, B J Darby and J H Collins, "Programmable correlation using parametric interactions in acoustic surface waves", Electron Lett, vol 8, No 2, pp 40-42, January 27, 1972.

II B J Darby, P M Grant, J H Collins and I M Crosby, "Performance of aperiodic spread spectrum modems incorporating surface acoustic wave analogue matched filters", IEE Conf Publ, No 109, pp 319-328, 1973.

III B J Darby, "Suppression of spurious acoustic signals in phase coded surface acoustic wave analogue matched filters using a dual-tap geometry", IEEE Trans on Sonics and Ultrasonics, vol SU-20, No 4, pp 382-384, October 1973.

IV P M Grant, J H Collins, B J Darby and D P Morgan, "Potential applications of acoustic matched filters to air-traffic control systems", (Invited Paper) IEEE Trans on Microwave Theory Tech, vol MTT-21, No 4, pp 288-300, April 1973.

PROGRAMMABLE CORRELATION USING PARAMETRIC INTERACTIONS IN ACOUSTIC SURFACE WAVES

Indexing terms: Correlation detectors, Parametric devices, Acoustic microwave devices, Signal processing

Real-time correlation of 31 chip binary p.s.k. waveforms has been obtained using nonlinear interactions of acoustic surface waves, with a signal bandwidth of 8 MHz. A dynamic range of 20 dB was obtained. Calculations indicate that a dynamic range of 50 dB should be obtainable quite readily, making the device attractive for adaptive signal processing.

Recent experiments carried out by Luukkala and Kino[1] have shown that the nonlinear interaction of acoustic surface waves in Y cut Z propagating $LiNbO_3$ can be used to perform real-time convolution of two r.f. waveforms. If one of these waveforms, designated as the reference, is a time-reversed replica of the other, the autocorrelation function is produced. Since the reference waveform can be varied at will, the device has the attractive feature of a high degree of programmability. This is emphasised by the results of Bongianni,[2] who auto-correlated a linear f.m. pulse, thus using the device as a programmable pulse-compression filter. In this letter, we describe results obtained using binary-coded phase-shift-keying (p.s.k.) waveforms, and consider the practical applicability of the device as determined by its dynamic-range capability. Preliminary results of this work have been reported elsewhere.[3]

The device is shown schematically in Fig. 1. Modulated surface waves of frequency f_0 are launched towards the centre of the crystal by interdigital transducers. The nonlinear

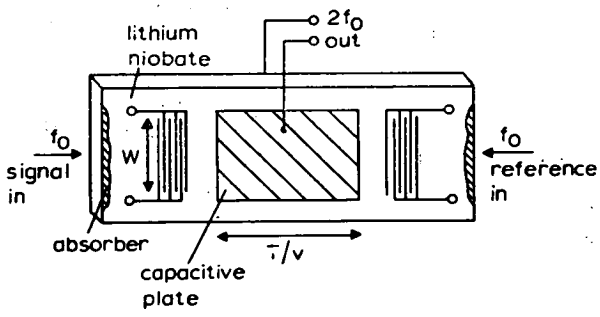

Fig. 1 *Configuration of an acoustic-surface-wave convolver*

interaction causes mixing of these waves to produce a spatially uniform electric field at frequency $2f_0$, which is detected by means of a capacitive plate. As shown by Quate and Thompson,[4] the envelope of the $2f_0$ signal is the convolution of the envelopes of the two inputs. Thus, if the inputs are both rectangular r.f. pulses, the output will be a triangular pulse whose amplitude is proportional to the input pulse-length. We have verified this experimentally, and have also shown experimentally that

(*a*) if the amplitude of the signal is varied, keeping the reference amplitude constant, the output amplitude is proportional to the signal amplitude

(*b*) if the two input amplitudes are kept the same and varied together, the output amplitude is proportional to the square of one input amplitude.

These relationships are expressed by a bilinearity factor C, defined as

$$C = \frac{P_0}{P_{ar} P_{as}} \qquad (1)$$

where P_0 is the output power delivered into 50 Ω, and P_{ar} and P_{as} are the acoustic powers for reference and signal.

Larson[5] derived eqn. 1 in studying convolution using bulk acoustic waves. It should be noted that C is proportional to the square of the input pulselength.

Our experiments with coded waveforms utilised pseudo-random binary codes, impressed on the carrier by p.s.k. modulation. The signal code and its time-reverse (which is used for the reference) are generated using shift registers, as described by Golomb *et al.*,[6] who also describe the correlation properties and usage of these codes.

Fig. 2 shows the experimental circuitry. The code generators are clocked at 7·5 MHz and give 31 chip codes of length 4·0 μs. The 62 MHz carrier is phase modulated by the codes using balanced mixers. The code generators are free running (i.e. repetitive). Synchronisation of the two codes is not necessary, since a time displacement of one code relative to the other has no effect except for time displacement of the correlation output. The two interdigital transducers in the convolver have eight electrodes each and are separated by 9 mm, with a 7·5 mm plate situated in between. The transducer width W (Fig. 1) is 1·5 mm. The output (at 124 MHz) is passed through a receiver with 20 MHz bandwidth prior to detection. The output obtained, for input levels of 20 dBm, is shown in Fig. 3. This shows two correlation peaks for each cycle of the input code, as expected. The signal/noise level is 20 dB if we ignore the smaller spikes, which are due to leakage.

Insertion loss and dynamic range: The insertion loss is defined in terms of the ratio of output power delivered into 50 Ω to the available power from a 50 Ω source supplying the signal waveform. It should be noted that the insertion loss, defined in this way, is a function of the reference level. The insertion loss is found by two separate measurements of the input and output levels at the convolver relative to the level at the

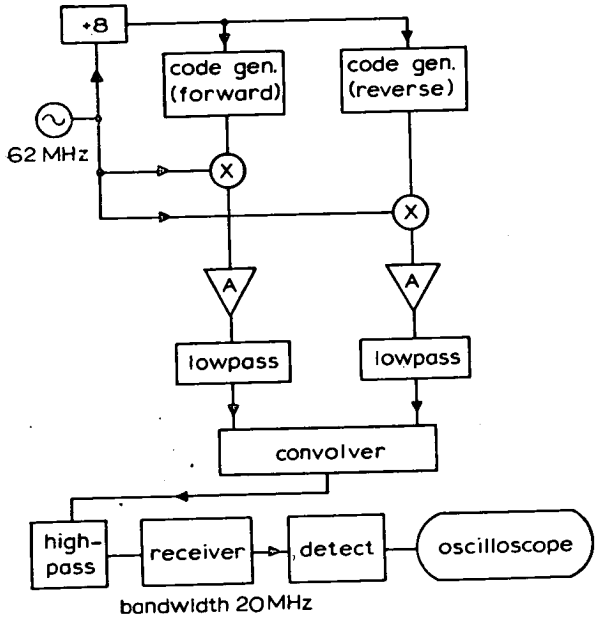

Fig. 2 *Experimental circuitry for correlation of biphase p.s.k. waveforms*

oscilloscope. Using coded waveforms, with input levels (available electrical power) of 20 dBm, we obtained a figure of 88 dB. The insertion loss for r.f. pulses was found to be the same to within 1 dB, provided that the pulses are long enough to give an acoustic wavetrain as long as the output plate. The insertion loss is thus independent of the nature of the waveform, a result which is intuitively obvious but of great importance practically.

The interdigital transducers have a conversion loss of 15·5 dB, so that $P_{ar} = P_{as} = 4{\cdot}5$ dBm. Using this in conjunction with the insertion loss, eqn. 1 gives the bilinearity factor $C = 2 \times 10^{-8}\ (\text{mW})^{-1}$. This figure refers to a plate length of 7·5 mm (= 2·5 μs) and a signal of duration 2·5 μs or more. This value of C is similar to the value obtained by Larson[5] for convolution of bulk waves in lithium niobate, although Larson used high-Q factor coupling on the output.

The dynamic range of the device is defined as the maximum range of signal level which can be used, with the reference level held constant. The minimum acoustic input power P_{min} is the level at which the output signal power becomes equal to the output noise power P_{on}. The maximum acoustic input power P_{max} is determined by breakdown of the inter-

digital transducers. The reference waveform is assumed to be at its maximum level. From eqn. 1, P_{min} is given by $P_{min} = P_{on}/CP_{max}$ so that

$$\text{dynamic range} = 10 \log_{10} (CP^2_{max}/P_{on}) \quad . \quad . \quad . \quad (2)$$

Using eqn. 1, we find that this is equal to the signal/noise ration at the output when the input levels are maximised.

Our experiments were done with 20 dBm input levels, giving an output of −68 dBm. The output noise level, including the receiver noise figure, is calculated to be $P_{on} = -90$ dBm. Thus the output signal/noise ratio should be 22 dB, in good agreement with the observed value of 20 dB. As a check, it was found that a reduction of one input level by 20 dB caused the output signal to be reduced to the noise level. The dynamic range is therefore 20 dB if input powers of 20 dBm cannot be exceeded. However, the transducers should withstand a peak voltage of 1 V/μm of gap width,[7] giving input powers of 27 dBm and a dynamic range of 34 dB. We note that still greater input voltages can be used if the interdigital transducers are covered with an SiO_2 overlay, as done by Reeder *et al.*[9]

Dynamic range as a function of systems parameters: The dynamic range obtainable with this device depends on parameters of the signal which it is used to process.

A significant factor is the maximum power which can be launched by the interdigital transducers. If V_0 is the maximum transducer r.m.s. voltage, the maximum power radiated in one direction is given by

$$P_{max} = \tfrac{1}{2} V_0^2 \hat{G}_a = 4 V_0^2 f_0 C_s k^2 N^2 \quad . \quad . \quad . \quad . \quad (3)$$

where $\hat{G}_a$ is the parallel conductance of the transducer at the resonance frequency f_0, as given by Smith *et al.*[8] The section capacity C_s is proportional to the aperture W (Fig. 1), and is independent of f_0. The number of sections N is roughly equal to f_0/B, where B is the transducer bandwidth. Using $V_0 \propto f_0^{-1}$, eqn. 3 becomes

$$P_{max} \propto \frac{W f_0}{B^2} \quad . \quad . \quad . \quad . \quad . \quad . \quad . \quad . \quad . \quad . \quad (4)$$

This is related to the output power by eqn. 1, in which C is proportional to T^2, where T is the length of the output plate (assuming that the input waveforms have lengths of at least T). We assume that C is independent of f_0, a result which was found by Larson[5] for convolution of bulk waves. Using eqn. 4, we then have

$$P_0 \propto \frac{f_0^2 W^2 T^2}{B^4} \quad . \quad . \quad . \quad . \quad . \quad . \quad . \quad . \quad . \quad (5)$$

Here we assume, in analogy with Larson's results, that C is independent of W. Assuming that the output amplifier has a bandwidth equal to the device bandwidth, the noise level P_{on} will be proportional to B, so that

$$\text{dynamic range} = 10 \log_{10} \left(\frac{f_0^2 W^2 T^2}{B^5} \right) + \text{constant} \quad (6)$$

Thus the dynamic range can be improved substantially, particularly by reducing the bandwidth. Our experiments have been conducted under conditions which are almost optimal with respect to the signals used, in the sense that the device bandwidth (15 MHz) and output-amplifier bandwidth (20 MHz) are not far in excess of the signal bandwidth (8 MHz). The results can therefore be used in conjunction with eqn. 6 to give a guide to the dynamic range expected in a given situation. For example, a dynamic range of 50 dB should be obtained if the bandwidth is reduced from 15 to 7·0 MHz, or if the convolver plate length is increased from 2·5 to 16 μs.

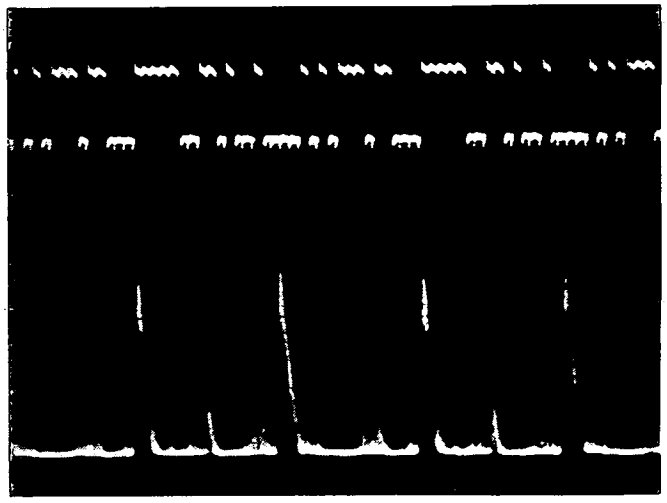

Fig. 3 *Upper trace: pseudorandom code; lower trace: correlation output*

We conclude that very acceptable figures for the dynamic range can be obtained using lithium niobate given proper design, especially if the bandwidth required is not too large. We have here ignored the possibility of tuning the convolver output. This will, of course, increase the dynamic range, particularly if the fractional bandwidth is small so that a high-Q factor can be used.

Acknowledgment: This letter incorporates work carried out under a CVD contract and is published by permission of the UK Ministry of Defence (Procurement Executive).

D. P. MORGAN
B. J. DARBY
J. H. COLLINS

Department of Electrical Engineering
University of Edinburgh
Mayfield Road
Edinburgh EH9 3JL, Scotland

1st December 1971

References

1 LUUKKALA, M., and KINO, G. S.: 'Convolution and time inversion using parametric interactions of acoustic surface waves', *Appl. Phys. Lett.*, 1971, **18**, pp. 393–394
2 BONGIANNI, W. L.: 'Pulse compression using nonlinear interaction in a surface acoustic wave convolver', *Proc. Inst. Elec. Electron. Eng.*, 1971, **59**, pp. 713–714
3 COLLINS, J. H., DARBY, B. J., and PRINGLE, R. D.: 'Correlation of pseudo-random sequences using parametric interactions between surface acoustic waves'. European microwave conference, Stockholm, 1971, paper C7/1
4 QUATE, C. F., and THOMPSON, R. B.: 'Convolution and correlation in real time with non-linear acoustics', *Appl. Phys. Lett.*, 1970, **16**, pp. 494–496
5 LARSON, J. D.: Ph.D. thesis, Stanford University, 1971
6 GOLOMB, S. W. (Ed.): 'Digital communications' (Prentice-Hall, 1964)
7 WHITE, R. M.: 'Surface elastic wave propagation and amplification', *IEEE Trans.*, 1967, **ED-14**, pp. 181–189
8 SMITH, W. R., GERARD, H. M., COLLINS, J. H., REEDER, T. M., and SHAW, H. J.: 'Analysis of interdigital surface wave transducers by use of an equivalent circuit model', *ibid.*, 1969, **MTT-17**, pp. 856–864
9 REEDER, T. M., KINO, G. S., and ADAMS, P. L.: Stanford University Microwave Laboratory report ML-1982

PERFORMANCE OF APERIODIC SPREAD SPECTRUM MODEMS INCORPORATING SURFACE ACOUSTIC WAVE ANALOGUE MATCHED FILTERS

B J Darby, P M Grant, J H Collins and I M Crosby

1. Introduction

This paper assesses the error-rate performance, under noise and interference conditions, of several distinct IF modulator-demodulator (modems) utilising surface acoustic wave (SAW) analogue matched filter[1] (AMF) arrays, designed with bandspreading and time domain encoding[2] to give digital data transfer with cochannel multiple access capability. The unique advantages of SAW devices which emerge are carrier and chip asynchronous operation combined with rapid generation of, and switching between, complex frequency and time encoded pulse patterns.

The main theme of the paper is the application of SAW AMF's to two basic signaling techniques, namely on-off keyed (OOK) and binary frequency-shift keyed (FSK). Sections 5 and 6 respectively are dedicated to these topics. These sections are fundamental to the discussion in Section 7 of a specific multiple access concept, namely random access discrete address (RADA). The OOK RADA modem demonstrates both the inherent hardware reduction and the ability to significantly increase the complexity of coding formats with SAW devices.

Before discussing these SAW modems basic spread spectrum techniques (Section 2); multiple access requirements (Section 3); and error rate considerations (Section 4) are reviewed briefly.

This paper does not address the application of SAW devices to the reduction of lock-up time in high processing gain spread spectrum links. A complementary paper by Hunsinger[3] examines this topic.

2. Basic Spread Spectrum Techniques

Spread spectrum modulation is achieved through the multiplication of a narrow bandwidth, B_d, data bit modulated IF carrier by a distinct wideband signal which spreads the intelligence over a large chip bandwidth, $B_s \geqslant B_d$. The generalised spread spectrum transceiver is illustrated in Figure 1. The wideband modulation can be classified under three headings[2]:

(1) direct pseudo-noise (PN); (2) frequency-hopping (FH); and
(3) time-hopping (TH).

Specific combinations of the properties of these permit the optimum trade for any desired system between:

Cochannel multiple access; channel utilisation; low detectability by unauthorised users; jamming immunity; multipath resolution; and range and velocity measurement.

B J Darby, P M Grant, J H Collins and I M Crosby are with the University of Edinburgh, Scotland.

4. Error Rate Considerations for OOK and Binary FSK Signaling

Simple OOK signaling, reference 9 chapter 10, has been virtually replaced by binary FSK and PSK transmission in coordinated high-traffic systems (FDMA, TDMA). However, several important bandspread links use OOK techniques to perform detection and synchronisation of PN and FH signals[2]; generation and detection in RADA[8] (Section 7); and detection and accurate timing of received signals for navigation and ranging[10] applications.

In each case, link operation necessitates the asynchronous detection of a burst of bandspread signal. This involves noncoherent (envelope) demodulation. The analysis of error probabilities for such OOK reception assumes that:

(1) sampling of the matched filter output envelope occurs at the instant t=T when the output SNR is maximised;
(2) the signal sample is compared with a predetermined threshold and the decision rule applied, "If the output envelope exceeds the threshold level, accept 'signal transmitted'; otherwise accept the 'no signal' hypothesis".

Due to interference and noise, two types of decision error occur. A false alarm when detection results and nothing was transmitted. A false rest when a signal was sent but not detected. The probabilities of making these errors will be denoted by P_F and P_M respectively. Mayher[4] has derived expressions for conditional decision error probabilities with large B_sT, OOK signals. This paper applies Mayher's equations to the worst case situation of cochannel interference; when

$$P_F = \exp - \frac{\gamma^2 \quad B_sT}{\left(\frac{I}{S} + \frac{N}{S}\right)} \qquad \ldots (1)$$

and,

$$P_M = 1 - Q\left[\left[\frac{2B_sT}{\frac{I}{S} + \frac{N}{S}}\right]^{\frac{1}{2}}, \gamma \quad \left[\frac{2B_sT}{\frac{I}{S} + \frac{N}{S}}\right]^{\frac{1}{2}}\right] \qquad \ldots (2)$$

where the Q-function[11] is defined by:

$$Q(\alpha,\beta) = \int_{\beta}^{\infty} x \exp\left| \frac{-1}{2} (x^2 + \alpha^2) \right| \; I_0(\alpha x).\, dx \qquad \ldots (3)$$

and γ is the ratio of threshold level to AMF peak output, N the noise power, I the interference power, S the signal power and I_0 the modified zero order Besel function.

The primary disadvantage of OOK signaling results from the necessity to maintain the threshold at the optimum level, reference 9 chapter 10. As this level is a function of SNR fixed thresholds cannot reliably discriminate between signal and noise in channels subject to deep fade.

In contrast binary FSK signaling, reference 9, chapter 11 employs two distinguishable waveforms with a comparison of the receiver AMF output envelopes at the sampling instant. Minimum error probability for equally energetic and equiprobable Mark and Space signals is achieved with zero

threshold level. Total error probability (P_e) for a noncoherent orthogonal binary FSK modem is given by[12]:

$$P_e = \tfrac{1}{2} \exp\left[-\tfrac{1}{2}\rho_o\right] \quad \ldots (4)$$

where $\rho_o = B_S T(\frac{S}{N})$ is the AMF output SNR at the sampling instant in the filter which receives the signal.

It is important to review the condition for orthogonality between FSK rf pulses of equal duration (T). This is obtained by examining the response of a matched filter, centred at f_o to an rf pulse with a carrier at $f_o+\Delta f$, where $\Delta f \ll f_o$. At the sampling instant (t = T) the output envelope ($v_o(t)$) is given by:[9]

$$v_o(T) = kT \text{ sinc } (\pi \Delta f T) \quad \ldots (5)$$

where k is constant. Thus, the effective frequency domain transfer function at the sampling instant has nulls (zero cross talk) at frequencies spaced by integer multiples of $1/T$ from f_o. A similar analysis holds for spread-spectrum signals comprised of a sequence of (L) biphase PN modulated chips each of duration τ, where $L\tau = T$. Here the signal bandwidth (B_S) is $1/\tau$ and at time t = T, the AMF output is the sum of L identical terms, hence

$$v_o(T) = k\tau L \text{ sinc } (\pi \Delta f \tau) \quad \ldots (6)$$

Again, instantaneous orthogonality is achieved for carrier spacings of integral multiples of B_S ($=1/\tau$).

5. Spread Spectrum OOK Modem Evaluation

Figure 2 details the experimental configuration adopted to evaluate a noncoherent spread spectrum OOK modem in a gain stable channel. The bold outline shows the modem hardware connected for a back-to-back test. The modulator-demodulator functions of Figure 1 are accomplished by a conjugate pair arrangement of SAW AMF's (A,A*). The peripheral equipment, shown in thin outline, allows direct measurement of the error rates P_F and P_M, see Section 4. These evaluations are executed under controlled signal-to-noise plus co-channel interference conditions for specific decision thresholds. This permits comparison with Mayher's theory[4].

Passive spread spectrum modulation of the base-band OOK signal is achieved by impulsing the expansion AMF, A to generate its characteristic 5 MHz bandwidth PSK waveform. The reference clock (100 kHz) of counter C_1 is used both to trigger the impulse generator and to reference the counter C_2. This automatically compensates for any variations in C_1 clock rate. The expanded signal is amplified prior to spread spectrum demodulation in the conjugate AMF, (A*).

Bandlimited noise was generated by cascading amplifiers and filtering[13]. Interference consisted of an incoherent carrier at f_o biphase modulated by a pseudo random binary sequence (PRBS) asynchronously clocked at 5 MHz. The independent measurement of both P_F and P_M necessitates the generation of two sampling pulses from the dual gate control signal to separate the noise induced outputs and detected correlation peaks. Strictly, since each sampling pulse coincides with a correlation peak only one conditional error rate, P_M, is measured. The P_F measured is unconditional as occurs in synchronisation search conditions, P_F was determined by taking the average frequency of the pulses measured by counter $C_1(f_1)$ and dividing by the reference frequency. Similarly, P_M was obtained by subtracting the averaged reading on counter $C_2(f_2)$ from f_R, and dividing by f_R. Low error rates were achieved in high signal-to-noise conditions; witnessed by a count of 10^5 per second in counter C_2 and zero pulses per sec in counter C_1.

BANDSPREAD SIGNALS EMPLOYED			AMF RESPONSE	
			Aperiodic Peak/Sidelobe (dB)	
f_o(MHz)	B_s(MHz)	L (chips)	Measured	Theoretical
100	5	13 (B)	18 ± 0.5	22.3
100	5	31 (m)	16 ± 0.5	16
127.3	5	15 (m)	11 ± 0.5	11.5
90	5	1	--	--

key: f_o: carrier frequency, B_s : signal bandwidth (chip rate)
L : code length, m : maximal-length sequence.
B : Barker sequence.

TABLE 1 SPREAD SPECTRUM SIGNALS AND RESPONSES OF THE OOK MODEMS CORRESPONDING AMF'S

This modem was evaluated with several AMF's whose characteristic signals, measured and theoretical autocorrelation responses, are detailed in Table 1. Figure 3 shows curves of input SNR, ρ_i, versus γ for constant values of P_F, obtained with the 31 chip coded AMF's. The corresponding theoretical plots are given. With envelope detection, eqn 1 may be rearranged to give:

$$10 \log_{10} (\rho_i) + 10 \log_{10} (B_s T) = 10 \log_{10} [\ln(1/P_F)] - 20 \log_{10} \gamma \quad .. \quad (7)$$

where $B_s T$ and P_F were constant in this experiment. Eqn 7 is linear in $\log_{10}\gamma$, and shows how Figure 3 is modified for different time-bandwidth product signals. Figure 4 shows the variation of P_M, with γ for fixed SNR, ρ_i. For comparison, theoretical values of P_M calculated from the Q-function (ref 11) and from the limited tabulation of DiDonato et al[14] are included. These Figs show close agreement over the range of γ values encompassing the optimum threshold for OOK reception. Figure 5 highlights the improvement in processing gain when the time duration of the coded waveform is increased at constant signal bandwidth. Figure 6 shows P_M as a function of γ, versus input SNR with $B_s T = 31$. In Section 7 similar curves are presented for 15 chip m-sequence coded AMF's and their evaluation discussed in the context of an OOK RADA modem. Comparisons of large $B_s T$ (>10) device performances in both noise and interference limited channels illustrates that similar processing gains are obtainable.

6. Experimental Binary FSK Spread Spectrum Modem

Binary FSK signaling employs a pair of distinguishable waveforms (Mark, Space) to denote the two message states (1,0). Receiver performance is dependent on both the SNR and mutual correlation of the two waveforms, as discussed in Section 4.

Experimental verification of Eqn 6 has been achieved with an AMF receiving a microelectronically generated 15 chip m-sequence coded pulse modulating an rf carrier at f_o, $f_o + B_s$ and $f_o + 2B_s$. The time domain response of the AMF exhibits orthogonality for the offset carriers. Maximum cross-talk, when $t \neq T$ is -10 dB for an adjacent band. In comparison the autocorrelation time-sidelobe levels were -12 dB. Cross-talk signals were reduced to -14 dB by time reversing the adjacent channel code, or to -16 dB by separating Mark and Space carriers by $2B_s$. Low cross-talk levels are desirable in synchronisation search since false alarms increase acquisition times.

An experimental bit synchronous binary modem, Figure 7, was constructed using AMF's matched to the 15 chip m-sequence. Carriers of 127.3 MHz (Mark) and 132.3 MHz (Space) were modulated at a 5 MHz chip rate to [illegible] orthogonality. The baseband encoder is implemented with a clock synchronised data stream by the logic circuit shown. On positive clock transitions binary ones are routed through the upper AND gate and trigger [illegible] impulse resulting in a Mark transmission. Similarly, binary zeros are routed through the lower AND gate to transmit Space signals. Signal

conjugate AMF outputs, traces B and C, are envelope demodulated prior to subtraction in the differential video amplifier. Complementary bipolar outputs, traces D and E, demonstrate reception of the Mark and Space signals respectively. With zero threshold level, the dual comparators make random decisions except at the sampling instant when Mark and Space signals are easily identified, trace F. Reliable asynchronous operation is achieved at high output SNR, by raising the threshold level, which removes the random fluctuations of the comparator output. Separate Mark and Space decisions are obtained and used to preset and clear the flip flop to regenerate the data unambiguously. This mode of operation would be utilised for synchronisation search procedures[3] when a limited dynamic range can be tolerated[12].

Modem performance has been evaluated at zero decision threshold with the same basic peripheral equipment described in Section 5. Error rate measurements were made only with the addition of bandlimited noise to the channel, by summing the independently monitored equal error rates of Mark and Space signals emerging from the flip flop. The resulting P_E is shown together with the theoretical curve, eqn 4, in Figure 9.

7. Application of SAW in RADA Systems

RADA systems, contrary to some other multiplexing techniques which employ address preambles, impress on the data a unique spread spectrum modulation exclusively to address transmissions to the intended receiver. Specifically quantised pulse position modulation (QPPM), pulse code modulation (PCM), or other digital traffic is further modulated bit by bit by one of an alphabet of frequency-time coded pulse patterns. This permits uncoordinated access of many subscribers to the same wideband channel. OOK and binary FSK signaling techniques are both applicable to RADA systems.

Experiments were conducted on a simple OOK RADA communications modem employing two characteristic waveforms in the address, Figure 10. Two similar AMF's to those utilised in the binary FSK modem were employed. Suitable design of AMF geometry[15] permitted compensating delays as shown in Figure 10. Cross talk signals were further minimised by time-reversed coding AMF's A and B. In addition crosstalk at the sampling instant was eliminated by the temporal separation of the RADA waveforms.

In the transmitter a single 5 nsec duration, 10 volt peak impulse from an avalanche mode circuit was used to generate the complete IF address waveform, illustrating the simplicity of SAW device and peripheral hardware when compared with that described by Blasbalg[16] and Corr[17]. After matched filter processing in the receiver and envelope demodulation the correlation peaks were detected individually. The resulting baseband pulses were combined logically in a coincidence gate (hard decision) to regenerate the transmitted data.

The performance of the modem was determined when bandlimited noise was applied to the receiver input using the OOK synchronous measurement procedure, Section 5. This experiment demonstrated the operation of the hard decision receiver logic. Comprehensive evaluation of the interference immunity of the RADA receiver was not carried out as this involves the synthesis of many RADA system signals.

The total error rate for this RADA modem can be derived as:

$$P_E = \tfrac{1}{2}P_F^{\,2} + \tfrac{1}{2}(2P_M) \qquad \ldots (8)$$

where P_F and P_M are given by equations 1, 2. Thus, in terms of P_F, the hard decision logic effectively doubles the processing gain. This is illustrated by the curves of Figure 11. Included are theoretical P_F

characteristics for a single AMF with B_ST = 15, and effective B_ST = 30 for the modem. The effective false rest probability, $2P_M$, is twice that obtained from a single AMF. Note that the experimental and theoretical P_M curves for the modem are closely aligned. For all SNR the combined error rate P_E is predominantly due to false rests, indicating that the γ = -5 dB level was too high. A reduction in γ will decrease P_M while still maintaining an acceptably low P_F, improving overall error rate, P_E.

8. Conclusions

This paper has examined the performance under laboratory conditions of moderate time-bandwidth product SAW AMF's to prototype IF spread spectrum digital communication modems employing OOK and binary FSK signaling techniques. Close to theoretical error rate performance has been achieved. Laboratory experiments on a simple OOK RADA modem demonstrated the unique advantages of SAW AMF's in the rapid synthesis, switching between and detection of frequency and time encoded pulse patterns with minimal hardware. This RADA modem exhibited predictable error rate performance in the presence of bandlimited noise at the receiver input.

RADA techniques offer uncoordinated multiple access capability. They are particularly significant for mobile communications over geographical areas where low activity factors of subscribers exist, for example terminal area air-traffic control[15]. Achievement and detailed error rate assessment requires larger address alphabets (>2) and larger time-bandwidth product (>15) SAW AMF's than were utilised in the above experiments. Deployment of binary FSK signaling would remove the OOK requirement to maintain accurate receiver thresholds. This is advantageous for practical channels subject to deep fade.

Acknowledgements

The authors would like to thank D Lambert and R Halstead for device fabrication and acknowledge the British Science Research Council who supported this work.

References

1. S T Costanza et al, MTT-17, pp 1042-1043, Nov 1969.
2. C R Cahn, AGARD No 58, Reference 5, 1973.
3. B J Hunsinger, IEE Proc. This Conference.
4. R J Mayher, IEEE EMC Symp Rec, pp 230-237, 1967.
5. C.F Vasile et al, Electron Lett, vol 8, pp 479-480, 1972.
6. J.H Bagley, IEE Conf Publ No 63, pp 12-17.
7. J J Kepcke, IEEE Trans VC-1, pp 81-87, 1963
8. M Magnuski, "Communications Systems Engineering Handbook", Ch 18,1953.
9. S Stein et al, "Modern Communication Principles", 1967
10. J Burnsweig et al, IEEE Trans MTT-21, pp 272-279, 1973.
11. C W Helstrom, "Statistical Theory of Signal Detection", p 153, 1960.
12. A H Nuttall, IRE Trans IT-8, pp 305-314, 1962.
13. B J Darby et al, Proc Ultrasonics International, April 1973.
14. A R DiDonato et al, Mathematics of Computation, 16, pp 347-355, 1962.
15. P M Grant et al, IEEE Trans MTT-21, pp 288-300, 1973.
16. H Blasbalg et al, IEEE International Conv Rec, pp 192-216, 1964.
17. F Corr et al, IBM Journal, vol 9, pp 256-263, 1965.

Glossary: B_S Signal Bandwidth; T data bit time; OOK on off keyed; FSK frequency shift keyed; PSK phase shift keyed; RADA random access discrete address; FDMA frequency division multiple access; TDMA time division multiple access; PN pseudo noise; FH frequency hopping; TH time hopping; γ normalised threshold level; SNR signal-to-noise ratio; ρ_i input SNR; ρ_o output SNR; P_F false alarm probability; P_M false rest probability; P_E total error probability.

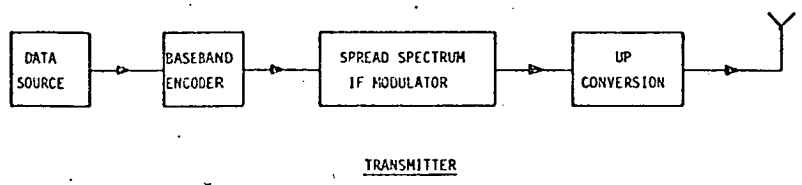

FIGURE 1 GENERALISED SPREAD SPECTRUM TRANSCEIVER

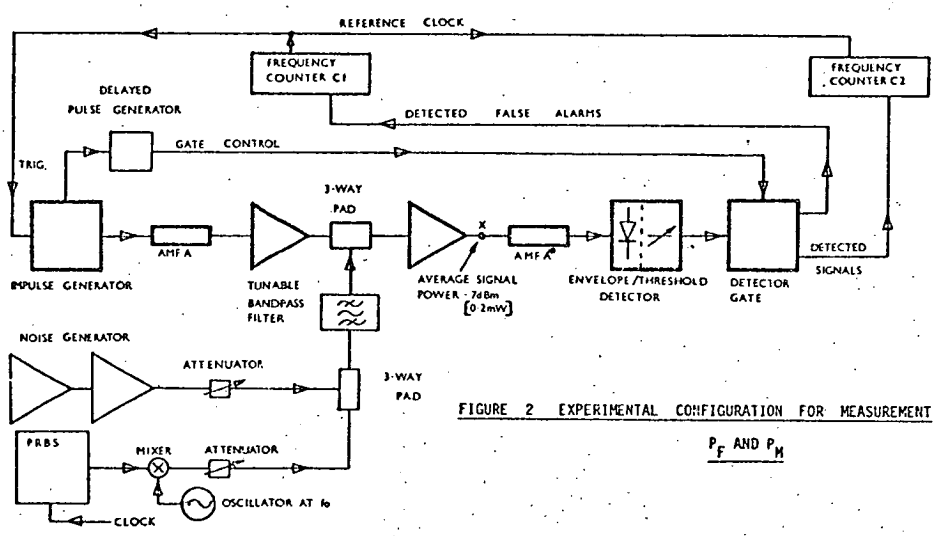

FIGURE 2 EXPERIMENTAL CONFIGURATION FOR MEASUREMENT P_F AND P_M

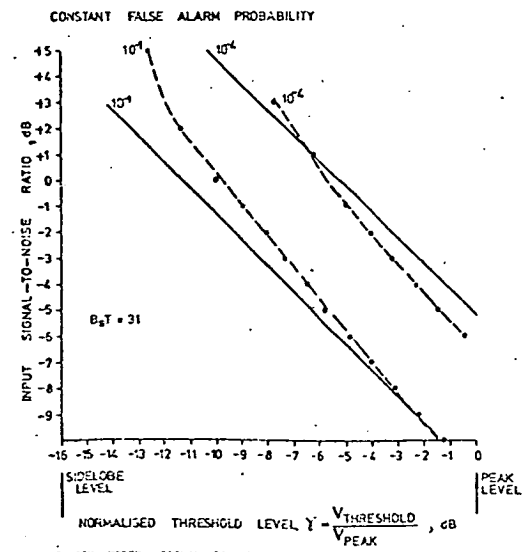

FIGURE 3 OOK NONCOH - SIGNAL TO-NOISE - RATIO VERSUS γ AT FIXED P_F

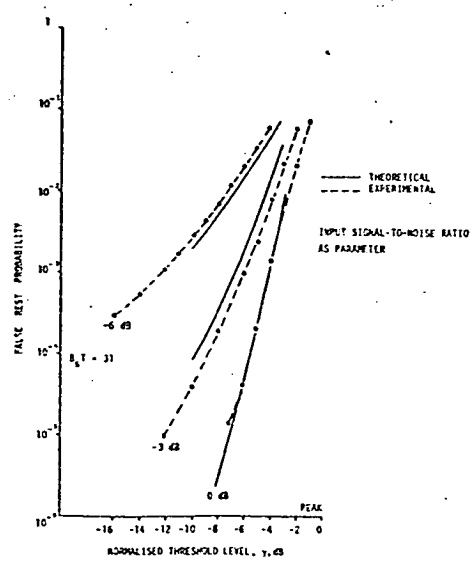

FIGURE 4 OOK NONCOH - P_M VERSUS γ AT FIXED SIGNAL-TO-NOISE RATIO

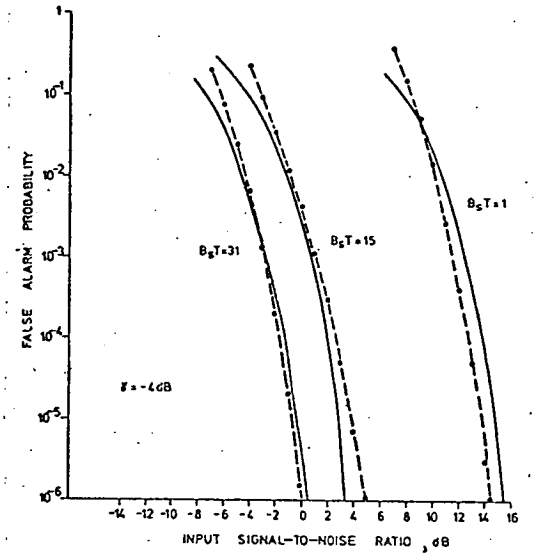

FIGURE 5 OOK MODEM - P_F VERSUS SIGNAL-TO-NOISE RATIO

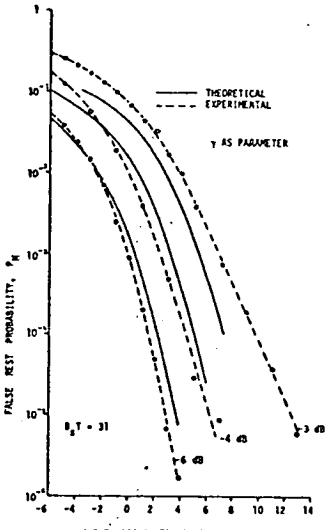

FIGURE 6 OOK MODEM - P_M VERSUS SIGNAL-TO-NOISE RATIO AT FIXED γ

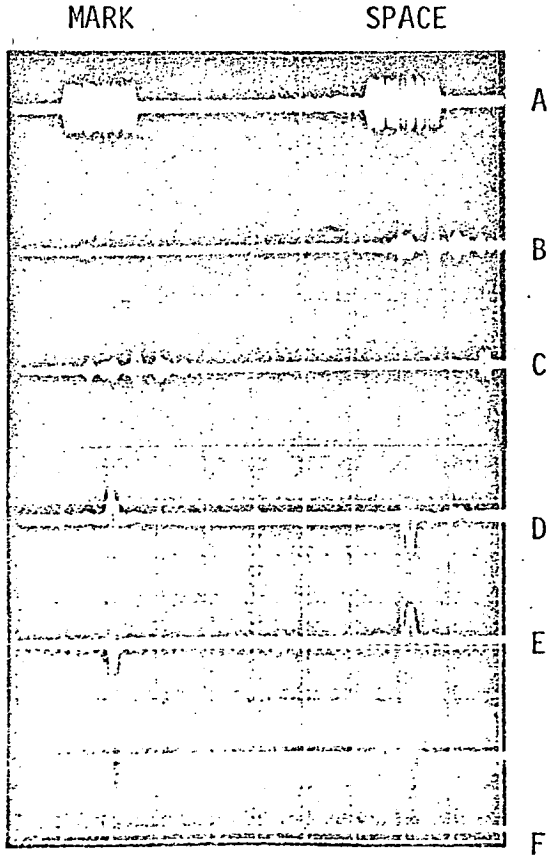

FIG 8 BINARY FSK MODEM WAVEFORMS

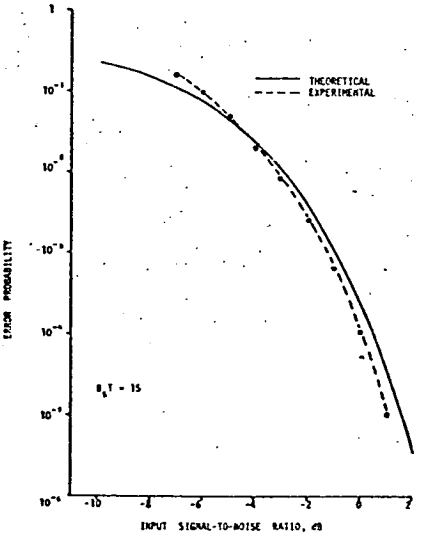

FIGURE 9 BINARY FSK MODEM PERFORMANCE

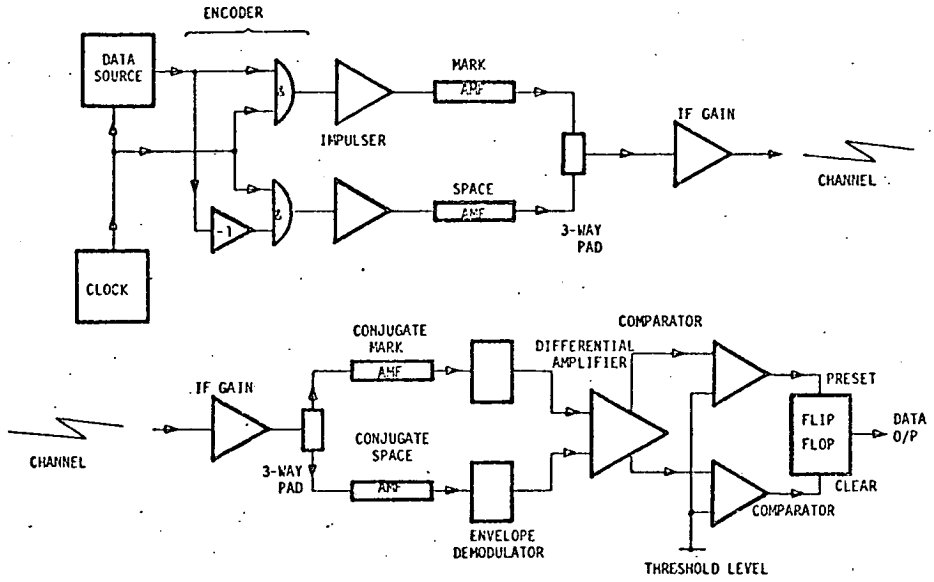

FIGURE 7 BINARY FSK MODEM

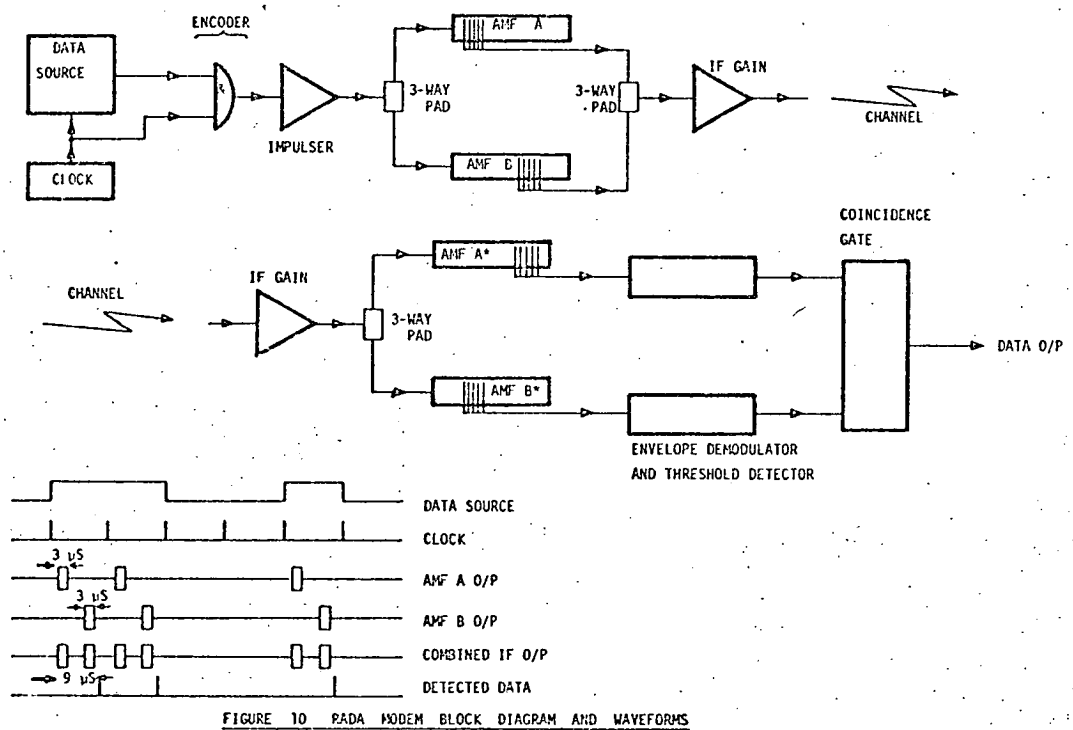

FIGURE 10 RADA MODEM BLOCK DIAGRAM AND WAVEFORMS

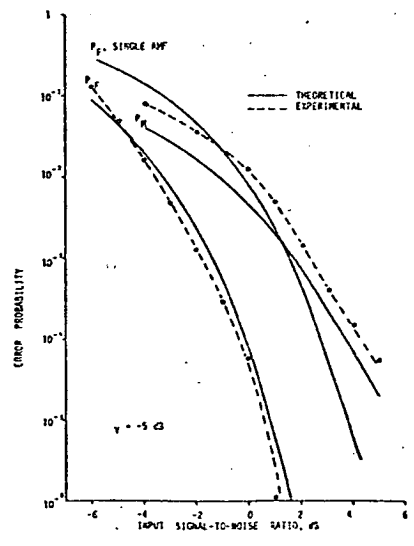

FIGURE 11 RADA MODEM PERFORMANCE

Reprinted by permission from IEEE TRANSACTIONS ON SONICS AND ULTRASONICS
Vol. SU-20, No. 4, October 1973, pp. 382-384
Copyright 1973, by the Institute of Electrical and Electronics Engineers, Inc.
PRINTED IN THE U.S.A.

Suppression of Spurious Acoustic Signals in Phase Coded Surface Acoustic Wave Analog Matched Filters Using a Dual-Tap Geometry

BARRY J. DARBY

Abstract—A dual-tap geometry which significantly reduces purious acoustic signals in phase coded surface acoustic-wave nalog matched filters is reported. The dual array exhibits ear (within 1.4 dB) theoretical expansion-compression loop erformance, for 13-chip Barker coded devices, while retaining /4 electrode widths. Experimental results compare conven- onal and dual-tap array 13-chip Barker coded AMF.

Manuscript received March 29, 1973; revised May 7, 1973. This work as supported by the British Science Research Council.
The author is with the Department of Electrical Engineering, Uni- rsity of Edinburgh, Scotland.

The surface acoustic wave (SAW) technology promises convenient realization of analog matched filters (AMF) for a variety of IF signal waveforms. To match binary phase-coded waveforms the device consists of an input transducer and an array of wideband taps [1] having constant spatial periodicity. For simple-tap designs, Fig. 1(a), this device is subject to a number of 'second-order' effects [2], which give rise to the following multiple coherent spurious acoustic signals:

1) reflected SAW signals due to acoustic wave impedance mismatch between metallized and unmetallized sections of the propagating path;

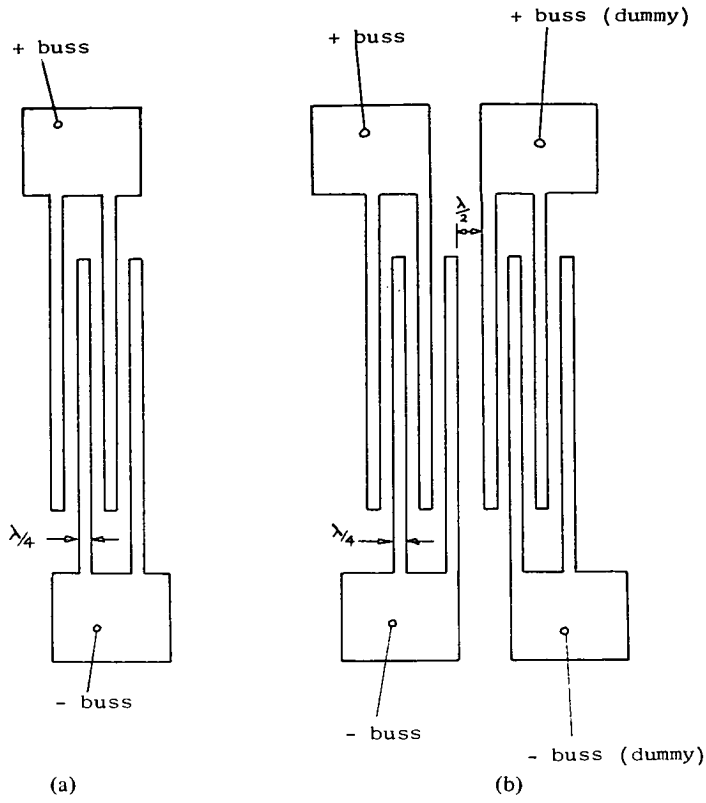

Fig. 1. Comparison of conventional (a) and dual-tap (b) geometries.

2) reradiated bidirectional SAW signals due to electroacoustic regeneration, a function of material coupling constand and tap loading; and

3) bulk waves produced by synchronous scattering, at frequencies above SAW synchronism.

The recently developed split electrode transducer [3] reduces mechanisms 1 and 3. However, these transducers require electrode widths of $\lambda/8$ instead of $\lambda/4$, thus reducing the bandwidth available for a given standard of photolithography. Furthermore, these split electrode geometries do not cancel spurious signals due to electroacoustic regeneration. The usual technique used to decrease mechanism 2 on high coupling materials like $LiNbO_3$ is to reduce the number of electrodes on the tap and to decrease the load resistance. The penalty incurred is an increased insertion loss.

A colinear dual-tap array approach is reported which provides significant cancellation of spurious signals while retaining conventional $\lambda/4$ linewidths and offering no extra insertion loss. The dual-array consists of a receiving tap array spatially interlaced with a dummy tap array. Members of the dummy array are positioned an odd number of synchronous quarter-wavelengths from the corresponding members of the receiving array, Fig. 1(b), and are connected to an independent summing bus and an identical load. This provides the required equal amplitude and opposite phase conditions for destructive interference to occur where the generated spurious signals due to mechanisms 1, 2 overlap.

The loop performances of two sets of conjugate AMF fabricated on *X*-propagating, *ST*-cut quartz have been compared. The compression filter of each loop is matched to a 127 MHz carrier, biphase modulated at 5 MHz by the 13-chip Barker

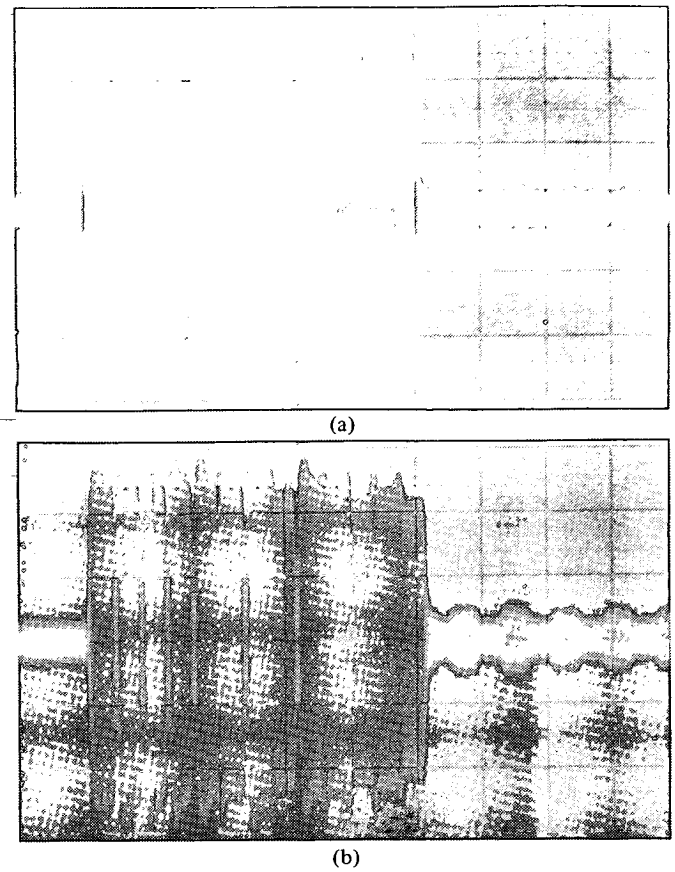

Fig. 2. Code generation comparison of expanded pulse. (a) From AMF incorporating dummy array. (b) From AMF with conventional taps.

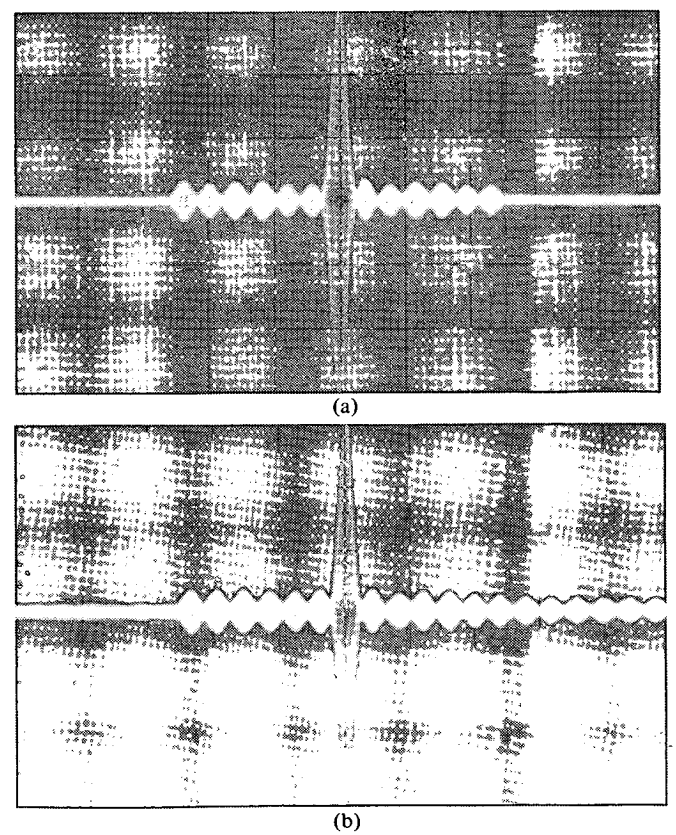

Fig. 3. Aperiodic correlation of expanded pulse in conjugate AMF. (a) AMF incorporating dummy array. (b) AMF with conventional taps.

code. One loop incorporates a phase coded dummy array loaded with 50 Ω on both expansion and compression filters, while the other loop comprises filters of conventional tap design, all devices having λ/4 electrode widths and identical tap apertures.

Fig. 2 compares the expanded pulse from the device (a) incorporating the dummy array with the expanded pulse from the 'conventional' device (b). The sequence of spurious pulses following the phase coded waveform are reduced from a maximum relative height of -17 dB for the single array (b) to -24 dB (to the top of the narrow 'spikes') for the dual array (a). The narrow spikes are a consequence of the delay between receiving and dummy taps which results in incomplete overlap of the two spurious signals. In the region of complete overlap the suppression is >20 dB.

The average insertion loss from a 25 cycle RF pulse centered at 127 MHz to the expanded (phase-coded) pulse was measured as 55 dB, for both conventional and dummy array devices.

On compression, Fig. 3, the conventional array (b) produces a peak-to-maximum sidelobe ratio of 20 dB ±0.2 dB with a peak-to-spurious ratio of 22 dB ±0.2 dB. The corresponding figures for the dual array (a) are 21 dB ±0.2 dB and 30 dB ±0.5 dB, respectively. The theoretical peak-to-sidelobe ratio for this code is 22.3 dB. The insertion loss from expanded (phase-coded) pulse to correlation peak was 33 dB for both conventional and dummy array devices. Hence, the measured compression gain is 22 dB compared with the theoretical 22.3 dB for this Barker code.

Apart from the improvement in performance offered by the dual array, a 90° phase shifted signal is obtainable from the dummy taps; this has potential applications in generating signals for single side-band transmission [4], and providing both 'in phase' and 'quadrature' signal components for synchronous demodulation [5].

ACKNOWLEDGMENT

The author wishes to thank R. D. Lambert for device fabrication.

REFERENCES

[1] W. D. Squire, H. J. Whitehouse, and J. M. Alsum, "Linear Signal Processing and Ultrasonic Transversal Filters," IEEE Trans on Microwave Theory and Techniques, *MIT-17*, No 11, pp 1020-1040, Nov 1969.
[2] W. Stanley-Jones, C. S. Hartmann, and T. D. Sturdivant, "Second-Order Effects in Surface Wave Devices," IEEE Trans on Sonics and Ultrasonics, *SU-19*, No 3, pp 368-377, July 1972.
[3] G. W. Judd, W. R. Jones, and T. W. Bristol, "An Improved Tapping Transducer Geometry for Surface Wave Phase Coded Delay Lines," IEEE Ultrasonics Symposium, Boston 1972, Proceedings 72CH0708-8SU, pp 373-376.
[4] E. Q. Papenfus, W. B. Bruene, and E. O. Schoenike, "Single Sideband Principles and Circuits," McGraw-Hill, 1964, p. 34.
[5] P. F. Panter, "Modulation, Noise and Spectral Analysis," McGraw-Hill (1965), p 722.

IV

POTENTIAL APPLICATIONS OF ACOUSTIC MATCHED FILTERS TO AIR-TRAFFIC CONTROL SYSTEMS (*INVITED PAPER*)

BY

P. M. GRANT, J. H. COLLINS, B. J. DARBY, AND D. P. MORGAN

Reprinted from IEEE TRANSACTIONS
ON *MICROWAVE THEORY AND TECHNIQUES*
Volume MTT-21, Number 4, April, 1973
pp. 288-300
COPYRIGHT © 1973—THE INSTITUTE OF ELECTRICAL AND ELECTRONICS ENGINEERS, INC.
PRINTED IN THE U.S.A.

Potential Applications of Acoustic Matched Filters to Air-Traffic Control Systems

PETER M. GRANT, JEFFREY H. COLLINS, BARRY J. DARBY, AND DAVID P. MORGAN

Invited Paper

Abstract—**The potential role of acoustic matched filters in the demanding field of civil and military air-traffic control (ATC) systems is examined. Highlighted are the problems of current ATC systems and the significant aspects of acoustic matched filters and their expeditious usage in modems employing band spreading for a multisubscriber environment and certain envisaged ATC systems deemed necessary for future traffic growth that could benefit materially from acoustic technology.**

I. Introduction

THE long-term applications of acoustic matched filters to the demanding field of civil and military air-traffic control (ATC) systems are examined. Highlighted is the fact that at current levels of air traffic, existing systems possess a capability just in excess of that required to handle the peak load of today, and further that although projected growth is to be handled in the short term by upgrading and supplementing present systems, particularly with computer complexes, such an approach does not represent a viable long-term solution. In logical sequence this paper contains three parts: current ATC systems in the United States, Great Britain, and Europe, and their basic deficiencies and lessons for future designs (Sections II through V); the significant and unique features of acoustic matched filters and their performance status as devices and in modem usage (Section VI); and envisaged ATC systems which are necessary to meet forecast traffic requirements emphasizing these systems that acoustic technology impacts (Sections VII and VIII). Liberal deployment of references for existing ATC systems serves to minimize the length of the paper, and the Appendix contains a glossary of commonly used ATC abbreviations.

II. Current ATC Procedures

Following the first powered flight of the Wright brothers on December 17, 1903, air traffic soon reached a congested state necessitating the imposition of procedural rules [1]. The control of air traffic requires the use of a multitude of equipment hardware encompassing ground-based surveillance and identification equipment to enable the controller to know the position and identity of aircraft, accurate onboard navigation equipment for pilot position determination, and voice communication equipment to handle message transfers between pilot and traffic control. The procedures adopted for civil ATC have evolved over many years through international cooperation [2] of government control bodies (e.g., the FAA and CAA) aided by the intrinsic global nature of air traffic. For example, European air-traffic handling systems have evolved by consultation between the major European organizations resulting in the Eurocontrol authority with exclusive responsibility for the upper airspace.

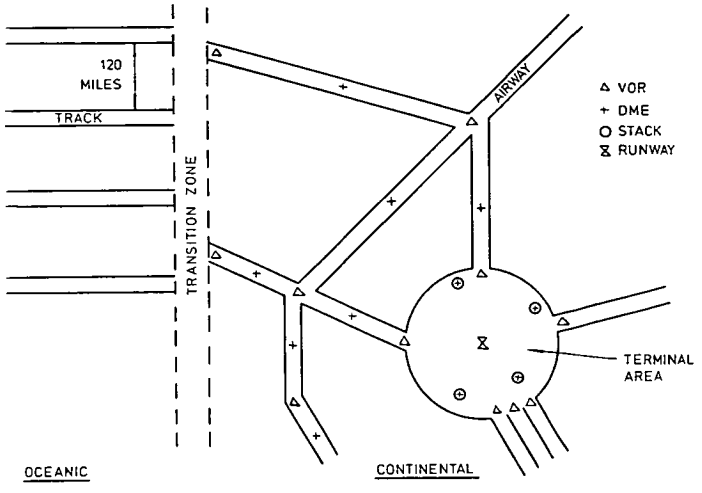

Fig. 1. Typical example of present airways system.

Current civil ATC can be subdivided into terminal, continental (overland), and oceanic areas (Fig. 1), all of which have a ground-based controller. Before entering an ATC system the airline must file a flight plan to enable the routing of each aircraft through the control network. Accepted flight plans are then entered as flight progress strips to enable controller monitoring of progress against schedule. Terminal area procedures [3] involve the scheduling of takeoffs and landings of aircraft to meet the available capacity. En route control [4] overland is accomplished by constraining the aircraft to fly along agreed airways. Transoceanic control involves a two-way structure of tracks or air corridors that are exclusively allocated across the North Atlantic by the oceanic planners [5]. Separation standards for all three areas are maintained by the ground-based controllers who possess exclusive ATC authority.

Military ATC [6] involves a more comprehensive surveillance facility requiring tracking of both friendly and enemy aircraft. With large areas of airspace reserved for military use there are fewer constraints on the pilot who exercises exclusive control requiring the incorporation of navigation, surveillance, and communication equipment of increased accuracy to meet the demanding requirements of intercept and strike maneuvers.

III. Classification, Functional Capability, and Operating Limitations of Existing ATC Systems

A. Classification and Functional Capability

Tables I and II detail current ATC equipments and frequency allocations in the three main areas of communications, navigation, and surveillance.

Manuscript received October 27, 1972; revised November 27, 1972. This work was supported by the British Science Research Council and the DCVD (United Kingdom Ministry of Defence PE).

The authors are with the Department of Electrical Engineering, University of Edinburgh, Edinburgh, Scotland.

TABLE I
CLASSIFICATION OF EXISTING ATC EQUIPMENT

	Communications	Navigation		Surveillance
		Radio	Other Techniques	
Line of Sight Short range (continental)	VHF radio	TACAN ILS DME VOR DECCA ADF console	compass sextant altimeter area navigation inertial	radar IFF/SSR ARTS/MEDIATOR MADAP
Long range (oceanic)	HF radio	LORAN OMEGA Doppler	inertial	onboard radio position reporting

TABLE II
FREQUENCY ALLOCATIONS FOR ATC EQUIPMENTS

Equipment	Frequency Allocation	Reference
OMEGA	10–14 kHz	[8], [9]
LORAN C/DECCA	90–110 kHz	[7]–[9]
ADF/CONSOL	200–1800 kHz	[9]
LORAN A	1.7–2.0 MHz	[7], [8]
HF communications	3–30 MHz	[7]
VHF FM communications	30–70 MHz	[7]
ILS (localizer)	108–112 MHz	[7]
VOR	108–118 MHz	[9]
VHF (civil)	118–136 MHz	[7]
UHF (military)	225–400 MHz	[7]
ILS (glide)	330–335 MHz	[7]
TACAN/DME	960–1210 MHz	[10]
IFF/SSR	1030–1090 MHz	[16]
SATCOM/radio navigation	1535–1660 MHz	[28]
Collision avoidance	1592–1622 MHz	[32]
Radar	2.75–3.60 GHz	[15]
Radio altimeter	4.2–4.4 GHz	[9]
MLS	5.0–5.25 GHz	[14]
Radar	9.07–9.50 GHz	[15]
Doppler navigation	8.75–9.50 GHz	[12]
MLS	15.4–15.7 GHz	[14]

Communications are handled by voice procedures on either a VHF or HF net [7] depending on the range to the ground-based antenna. DECCA, LORAN, and OMEGA are all examples of external reference hyperbolic navigation systems [7], [8] that utilize one-way ground-derived signal transmissions. The civil DME [9] and military TACAN [10] overland equipments operate by two-way interrogation of a ground-sited transponding beacon. Inertial [11] and Doppler [12] are examples of self-contained navigation equipments, although more expensive, inertial navigation systems are currently fitted as standard in the 747 [13] and are superseding Doppler equipment in 707 and DC8 aircraft. Primary [15] and secondary radar [16] (SSR for civil and IFF for military applications) are the fundamental equipments used for continental, en route, and terminal surveillance (Fig. 2).

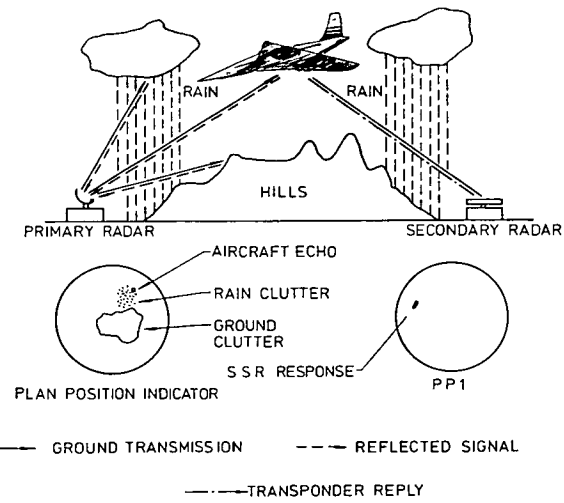

Fig. 2. Principles of primary and secondary radar.

Both civil computer-aided congested area (terminal control) systems, i.e., ARTS and MEDIATOR [17], and military systems, SAGE (United States) and LINESMAN (Great Britain) make extensive use of secondary radar to obtain accurate identification and authentication of primary radar returns.

B. Operational Limitations

Primary radar, whose coverage cannot extend to oceanic crossings like the Atlantic, is particularly subject to rain and ground clutter. Rain clutter can be reduced either by using an MTI system or with a wider bandwidth chirp waveform and pulse compression [18], thus reducing the range cell. Modest compression ratios, e.g., 25, are adequate, and surface acoustic wave (SAW) technology is readily applicable, particularly in airborne radar where size and weight are more significant.

Secondary radar [16] is not affected by clutter. Here an airborne transponder replies to the transmitted signal at a different frequency (Fig. 3). Confusion due to "fruit" and "garble," i.e., unwanted replies, is presently reduced by plot extraction on a PPI, although an alternative method using selective address (ADSEL or DABS) is also under development [19].

HF radio communication links over the North Atlantic are presently marginally reliable, provided a suitable "family" of channels is available to overcome propagation effects. The requirement for improved voice and data link facilities is apparent [20] due to the increase in subsonic air traffic and the introduction of supersonic aircraft. This necessitates consideration of new systems employing satellite repeaters [21].

Due to the requirement for high reliability in airborne equipment there is a built-in redundancy both of equipments

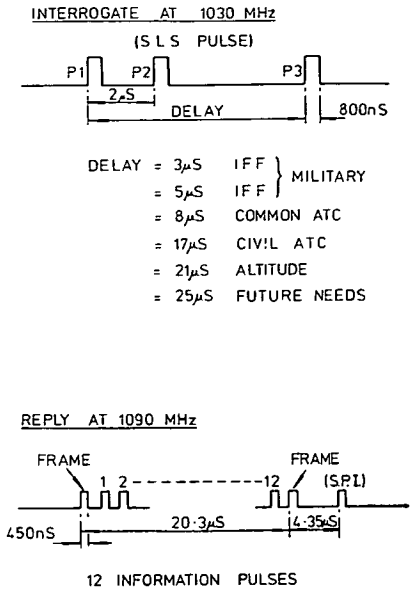

Fig. 3. Present SSR signal format.

and systems hardware, placing heavy pressure on both controllers and aircrew who must perform constant display monitoring. Several alternative schemes are under consideration to perform a level of integration of these equipments and displays in both military and civil environments.

IV. Projected Growth of Civil Air Traffic Indicating Further Deficiencies in Existing Systems

In the United States the projected aircraft fleet for the year 2000 is approximately 1 million, with the peak airborne count exceeding 50 000 [22]. Here there is a preponderance of private fliers which results in a mix of VFR and IFR, as the private aircraft are not all equipped with SSR. Problems of congestion can be overcome either by installing onboard collision avoidance equipment or by imposing a discipline to restrict private aircraft from using congested areas.

The main problem in Europe, where air traffic is double the estimates of 5 years ago, covers the preponderance of protected areas resulting in congestion of the upper airspace, where route crossings now exceed 20 per hour. The MADAP system [23] situated near Brussels is a data processing system to handle the flight plans and SSR returns from aircraft in the upper airspace over Belgium, Luxemburg, The Netherlands, and West Germany. Although just commissioned, it is already inadequate to handle existing traffic.

The North Atlantic ATC system with its large peak summer load (524 crossings in one day in 1971) is becoming severely congested. A quarter million annual flights are forecast by 1980 [24] with 160 aircraft simultaneously outside line-of-sight communications. The high accuracy of inertial navigation equipment, which is currently fitted on most aircraft (Section III-A) that use the North Atlantic track system, can permit the use of composite tracks with reduced separations.

V. Design Considerations Relevant to Future ATC Systems

A. Procedures

It is helpful to comment on possible modifications to ATC procedures and to review design considerations for ATC systems before discussing the relevance of acoustic matched filters. Existing control procedures rely on a ground-based controller with total responsibility for the aircraft in his sector. Systems, such as the McDonnel Douglas EROS, Bendix IMAGE, and RCA SECANT [25], [26] provide the pilot directly with air-derived collision avoidance information placing the onus on him to make an avoiding maneuver without consulting any ground controller. The advent of area navigation on overland routes involves consideration of systems such as intermittent positive control (IPC) [19] that sends positive commands from the ground to selected low priority aircraft to avoid potential collisions.

B. Satellite Hardware Considerations

Microwave satellite repeaters with their demonstrated capability and reliability for communications [27] are under active consideration for the functions of communication, navigation, and surveillance [28] in ATC systems. A synchronous satellite provides an area of coverage well in excess of that obtained from a single ground station. This enables a single repeater to operate, for example, over the majority of the United States without the mutual interference currently experienced from the many ground stations deploying SSR systems [16]. In RF link design the usual prime consideration is bandwidth conservation for optimum utilization of the available spectrum. Fixed ground-to-ground and satellite-to-ground microwave communications are essentially directional links employing high-gain narrow-beamwidth antennas. Here, bandwidth conservancy is not of prime importance as spuriously radiated spectral products are acceptably small. Links between aircraft and satellites are generally omnidirectional, which often results in critical power budgeting requirements because of the low antenna gains. One solution for optimizing the signal-to-noise ratio is to allocate many distinct exclusively assigned frequency channels in the satellite repeater. This complication of expensive satellite hardware is unnecessary when a single wide-band channel is utilized into which all subscribers are accessed on a code selection basis [28]. This is a natural application for matched filter reception techniques based on acoustic technology.

Consideration must be given also to interrelating the oscillator stability requirements with the Doppler shift expected on signals transmitted between a supersonic aircraft and ground terminal or synchronous satellite. The Doppler shift encountered on a 1.6-GHz L-band link with an aircraft flying at Mach 3.5 is typically 5 kHz [29], demanding an oscillator frequency stability better than 3×10^{-6}. This is a formidable requirement for microwave solid-state sources. These observations predicate the use of wide channel allocations (>100 kHz) with simultaneous access of several subscribers for optimal channel utilization.

C. Propagation Effects

Propagation effects such as atmospheric distortion, attenuation, and ducting are broad-band phenomena. Further, a severe problem in communicating with an aircraft over sea on a satellite link is the sea-reflected multipath return [29]. The separation of the direct and multipath return can be accomplished with antenna directivity, suitable antenna polarization, or spread spectrum coding of the transmitted signal [29], which again predicates acoustic matched filter techniques. However, practical measurements to establish the magnitude of the multipath return [30] are inconclusive.

D. Examples of Integration of ATC Equipments or Signals

An important consideration in the implementation of new systems involves the proposed level of equipment integration, particularly in military environments. Table II shows that aircraft currently contain a multitude of equipments. Equipment simplification starts with a progressive integration of the outputs of the existing equipments onto a common data processing system with a single sophisticated display, and progresses through integration of equipment operating in the same frequency band to the combination of the functions of communication, navigation, and identification into a single signal format. The totally integrated ICNI system [31], detailed in Section VII-C, is envisaged primarily for military applications where high security is mandatory. Its inherently high accuracy (typical positional errors less than 10 ft) solves the problem of providing a single navigation equipment for both terminal and en route control, a factor also of considerable interest to civil operators. Such equipment redesign will enable a vast reduction in the onboard power consumption, number of antennas required, spectral occupation, operation and maintenance costs, and will give increased accuracy, reliability, security, and interference protection. These latter features again point towards acoustic matched filter techniques. The collision avoidance surveillance (CAS) [25], [26] systems that involve the processing of air-derived signals to compute position of all aircraft within the system are intended primarily for the private pilot and thus price of usage is his key consideration. These systems position the expensive hardware in satellite-sited repeaters and ground processors to avoid avionics equipment costs.

E. Voice and Data Link Considerations

ATC reporting based on short messages (<600 bit) does not justify the use of the voice link, which is already becoming overloaded. Instead all these could be accommodated on a single data channel [20] with a message format containing aircraft identity (30 bit), flight level (12 bit), and present position (44 bit). ATC messages necessitate a very high integrity data link as a single bit error can potentially result in a collision, particularly in a congested terminal area. The allocation of exclusive time slots (TDMA) for each aircraft represents a complicated and expensive solution to this problem, due to the necessity for accurate onboard clocks. The design of a novel completely asynchronous system which includes a message addressing capability [33] is described in Section VIII.

New techniques to provide a multiple access capability for voice traffic over, for example, the North Atlantic are also under consideration [21], [34]. Short messages with low channel occupancy preclude the use of uneconomic FDMA and TDMA systems which use a large bandwidth when the system accommodates a large number of aircraft. A random access discrete address (RADA) system [35] might represent a better technique where multiple access of a large number of subscribers is required. To realize a RADA system the baseband (vocoded) transmissions from each aircraft are bandspread by encoding each digit with a distinctive IF signature. The IF signature is used for both address and modulation. The design of the system, discussed in Section VI, results in interference which is proportional to the number of active subscribers. A given optimum usage can be designed into the system.

F. Summary

It is preferable to finalize ATC procedures prior to concluding the final design of new ATC systems such as those detailed in Sections VII and VIII. Future deployment of satellites is predicted to obtain the maximum possible area coverage with a single system further accentuating the movement of ATC functions from VHF into microwave communications [14]. Band spreading, in preference to conventional FDMA, techniques are becoming attractive with the advent of acoustic matched filters and the need to cope with multipath environments. The areas of partial replacement of voice by data links and the integration of both ATC signal formats and equipments are justifying increased emphasis in the light of predicted overloading for existing ATC systems.

The necessary complexity in both signal formats and equipment hardware can be partially offset by the application of novel flexible signal processing techniques, especially by those realizable in SAW devices. Thus, it is considered relevant to examine briefly the significant and unique features of SAW technology.

VI. Performance and Modem Design with Acoustic Matched Filters

A. Introduction

Communication with low error rate in the presence of noise and interference is achieved efficiently by signal processing [36] prior to transmission and the corresponding inverse process at the receiver. This encoding and decoding involves the assignment of a particular code word (signature) to each message. The code word is selected from an appropriate "alphabet" of signal waveforms chosen such that their transmission makes the *best* use of the given noisy channel. Coded waveforms have also proved attractive for radar systems [18] where the definitions of noise and interference must be extended to include clutter. The signal waveforms after transmission through the channel arrive at the receiver in a corrupted form where an estimate (decoding) must be made in optimum fashion as to which message was sent. This involves the taking of a decision on the presence or absence of the received RF signals. These results are governed by the setting of a decision threshold that must be designed for a minimum probability of error. For any required maximum error rate with a specified signature and signal-to-noise ratio there exists an upper and lower threshold bound. Lower thresholds result in a higher probability of *false alarms* (noise voltages exceeding the threshold), and higher thresholds result in a greater probability of *missing* a received signature. Therefore, an acceptable compromise must balance the *false-alarm* rate and the *miss* rate. Now, if the signal-to-noise ratio at the threshold stage input is increased, the threshold can be raised for a given *false-alarm* probability. On the basis of maximizing both output signal-to-noise ratio and probability of detection for a linear filter, when the additive part of the channel disturbance is stationary, white, and Gaussian, the matched filter is the optimum primary signal processor [37].

B. Performance of Acoustic Matched Filters

Impulsing a matched filter generates the time-reversed replica of the matched signal. Hence, the encoding and decoding operations can be accomplished, within certain technology bounds, with conjugate matched filter pairs. Fig. 4(a) (upper trace) shows a phase-shift keyed (PSK) IF signature gen-

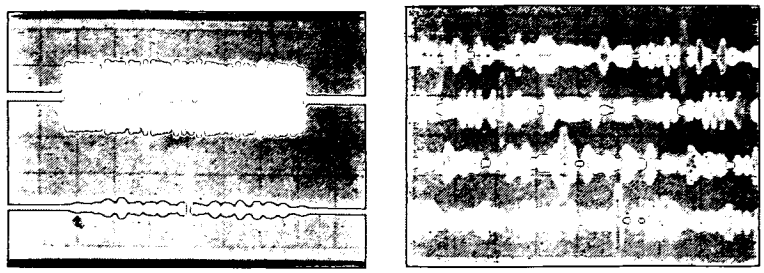

(a) (b)

Fig. 4. (a) Top trace: Impulse response of AMF binary phase coded with 31-chip m sequence at 5-MHz chip rate on 90-MHz carrier (1 μs/large-scale div.). Lower trace: Aperiodic autocorrelation with same device (2 μs/large-scale div.). (b) Demonstration of synchronization acquisition for periodic autocorrelation functions of parent 31-chip m sequence with 4 distinct 7-chip subsequences.

TABLE III

SUMMARY OF KEY ADVANTAGES OF ACOUSTIC MATCHED FILTERS

Feature	Radar	Communications
Processing gain (provided prior to detection in devices)	reduced peak power for same range power: can be compatible with communications	increased signal to noise in band-spreading system
Band spreading	increased resolution increased jamming immunity	multipath resolution interference rejection increased jamming immunity less LO stability required
Waveform flexibility[a]	optimize for best clutter rejection	multiple addresses and signatures
Passive generation[a]	simple realizations of complex waveform	easy frequency hopping
Passive detection	permits truly asynchronous operation	permits truly asynchronous systems
Programmability[a]	electromagnetic compatibility, reduce crosstalk	random access by variable address (RADA) improved security

Note: Asynchronous tailor-made passive devices performing linear filtering.
[a] Features possessed particularly by surface acoustic wave devices.

TABLE IV

OPERATING RANGES AND PRACTICAL DATA FOR MATCHED FILTERS

		Operating Ranges			Practical Data			
	Device	f_0 (MHz)	T (μs)	B (MHz)	TB	Sidelobe[b] Level (dB)	Insertion[c] Loss (dB)	Reference
Electromagnetic	lumped circuit	0.2– 30	1000–10	0.02– 5	50	−28		[39]
	tapped RF cable[a]	100 – 500	<1	50 – 300	100	−30	50	[40]
	folded tape waveguide	500 –2500	<1	200 –1000	720		24	[41]
Acoustic	magnetostrictive wire (tapped)	0.5– 2	1000–10	0.1 – 2	500		90	[42]
	strip	1 – 30	1000–30	0.1 – 5	64	−23		[43]
	diffraction grating	30 – 500	40– 1	10 – 250	160	−40	29	[44]
	love wave	1 – 100	200–10	0.5 – 100	60	−20	50	[45]
	SAW IDT[a]	20 – 300	50– 2	1 – 50	1000	−25		[46]–[48]
	SAW grooved grating	20 – 300	100– 2	1 – 100	1500		37	[49]
	convolver[a]	20 –1000	40– 2	1 – 100	31	theoretical	90	[50]
Microelectronic	digital[c]	baseband	5000–10	0.1 – 20	127	theoretical	N/A	[51]
	analog[a]	baseband	1000	0.01– 15	13	theoretical	N/A	[52]

[a] Programmable devices.
[b] Sidelobe levels are quoted relative to the correlation peak.
[c] For CW at center frequency.

erated by impulsing surface acoustic wave analog matched filter (SAW AMF) and its detection in the conjugate AMF (lower trace). Coded time-domain signatures, such as PSK and chirp, with flat frequency spectra offer operational advantages when hard limiters are incorporated in receivers enabling subscribers at widely differing ranges to be accommodated.

Table III summarizes the key advantages that can be obtained with suitable waveform design and acoustic matched filter detection. A comparison of the operating ranges and known practical data of various acoustic devices with electromagnetic and microelectronic techniques is given in Table IV. New operating ranges ideal for many important radar and communications systems are reported in this issue of this

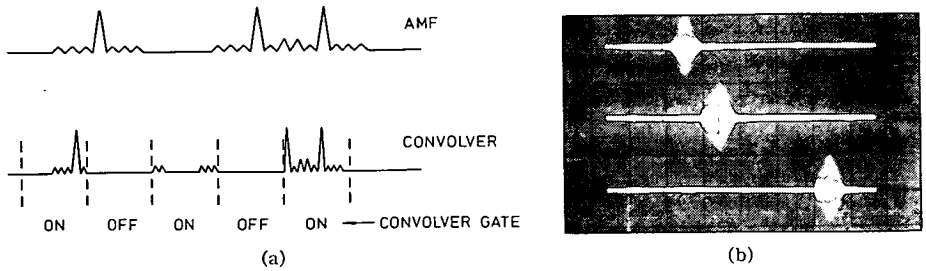

Fig. 5. (a) Schematic showing a received radar signal after processing in a matched filter, and the same signal after processing in convolver operating asynchronously (see Section VI-B). For simplicity, the transmitter pulse is taken as a 7-chip Barker coded waveform, and the three target returns are shown with the same amplitude. (b) Experimental result for an asynchronous convolver using rectangular RF pulses for the signal and reference. The three traces correspond to three values of signal delay, covering a range greater than the propagation delay in the device.

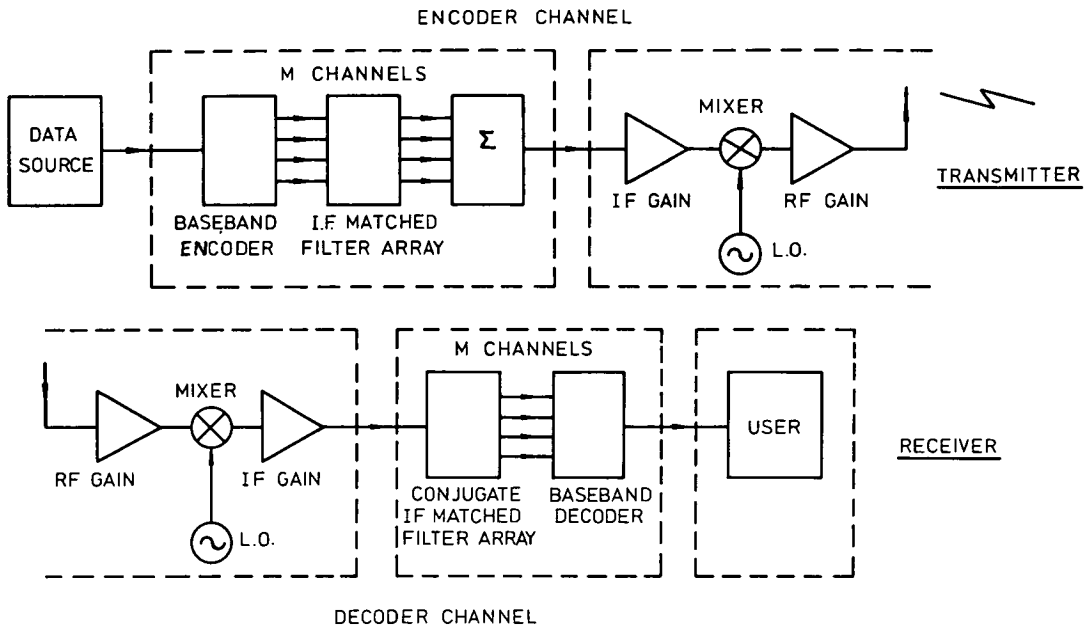

Fig. 6. *M*-ary modem using SAW matched filters for efficient encoding and decoding operations.

TRANSACTIONS. Further, development is necessary to realize devices for long delays (∽1 ms) with processing gain ∽100 for narrow-band (∽100-kHz) systems; time–bandwidth products in excess of 1000 to reduce search times in synchronization; fast reprogramming (<100-ns) PSK filters processing 10-Mchip/s signals for ICNI; very high chip rate (>100-Mchip/s) devices for secure coded radio altimeter applications.

One crucial advantage of the acoustic filters (especially SAW) is their inherently asynchronous operation at RF, giving rise to fully asynchronous systems (see Sections VI-C and VIII-D) and powerful techniques for synchronization acquisition [53] in secure communications. For, secure spread spectrum applications, programmability is necessary and acoustic devices with the most promising features are the SAW programmable AMF and the nonlinear convolver. Fig. 4(b) illustrates the principle of synchronization acquisition [47] with a 7-tap SAW programmable AMF which is used to correlate four distinct 7-chip subsequences of a 31-chip waveform. Convolvers are not inherently asynchronous owing to the requirement for an accurately timed reference to ensure complete overlap of signal and reference in the region where their interaction is sensed. However, by using a repetitive reference signal and appropriate gating [54], asynchronous operation may be achieved. The output produced is shown schematically in Fig. 5(a). For visual display [Fig. 5(b)] the time segmentation effect is removed by arresting the time base when the output is gated off.

One further problem concerns the timing of the autocorrelation peak that is not directly related to the input signal timing due to the time segmentation effect. True timing is obtained in a *real-time recovery* unit using the reference timing information. Additional hardware is therefore required for applications that require asynchronous operation and true timing output. For comparison, a programmable PSK filter, although having limited programmability compared with the convolver, requires only tap switching circuitry and a read-only memory for code vector selection.

C. Definition and Characteristics of Band-Spread Communications Modems

It is now possible to indicate how matched filters might fit into communication systems by investigation of a simple modem (Fig. 6). Consider the encoder and decoder processors split into baseband and IF sections. At the transmitter, digital data from a source (e.g., computer terminal or vocoder) is fed into a baseband encoder. Each message is assigned one or more of *M* code words generated first at IF, by impulsing

TABLE V
EFFECT OF TIME-BANDWIDTH PRODUCT ON MINIMUM SIGNAL-TO-(NOISE PLUS INTERFERENCE) RATIO

B_ST	min $(S/I+N)_{i/p}$ dB	Relative Improvement (dB)
1	11.5	0
13	0.4	11.1
31	−3.4	14.9
127	−9.5	21.0
511	−15.5	27.0

Note: P upper bound $= 10^{-6}$ for $\gamma = 1$.

the appropriate matched filter, and then translated to RF by mixing with a local oscillator. Each matched filter has a distinct *signature*, or code word, characterized by 1) waveform, e.g., phase-shift-modulated sequences such as the pseudonoise [55] and Barker [56] sequences, or frequency-modulated signals such as the linear chirp [18]; 2) center, or carrier frequency and modulation bandwidth; 3) relative delay (the delay is of importance in some frequency hopping schemes).

The choice of signature *alphabet* depends on the system requirements, e.g., number of users, mode of operation, i.e., coordinated or uncoordinated, propagation characteristics of the channel, desired level of message integrity, etc. At the receiver, the incoming signal is down-converted to IF and recognized in a conjugate matched filter array. Following demodulation of the matched filter output, a threshold detector stage makes the required decisions and sends pulses into the baseband decoder, whose output is a reconstruction of the source data stream.

The type of demodulator used can effect the error rate, which is dependent on the received signal-to-noise plus interference and the time–bandwidth product of the transmitted code waveform. In practice, the use of envelope demodulation instead of the preferred [36] phase or synchronous demodulation, which results in an effective 3-dB increase in error rate, is commonly necessary due to the difficulty of extracting phase information. Large time–bandwidth product codes are therefore required to ensure sufficient signal-to-noise ratios for a given false-alarm rate.

In [57], the equation relating false-alarm probability, P to Gaussian disturbances and waveform time–bandwidth product for an envelope detector in the worst case situation, where the bandwidths of signal B_S and interference B_I are equal, is

$$P = \exp - \left[\gamma^2 B_S T \left(\frac{S}{I+N}\right)\right] \quad (1)$$

where γ is a normalizing threshold constant and S, N, and I are the signal, noise, and interference powers, respectively. Table V shows the minimum input signal-to-(noise plus interference) ratio which can be tolerated to obtain a false-alarm probability not exceeding 10^{-5} for various values of time–bandwidth product, taking $\gamma = 1$.

D. Experiments on a Simple M-ary SAW AMF Modem

We have shown experimentally [58] that a matched filter expansion–compression loop offers a useful improvement in detection probability for a signal in noise and strong interference. However, in practice a simple loop does not make best use of the given channel. The M-ary system (Fig. 6) increases the efficiency of the communications channel. To illustrate the

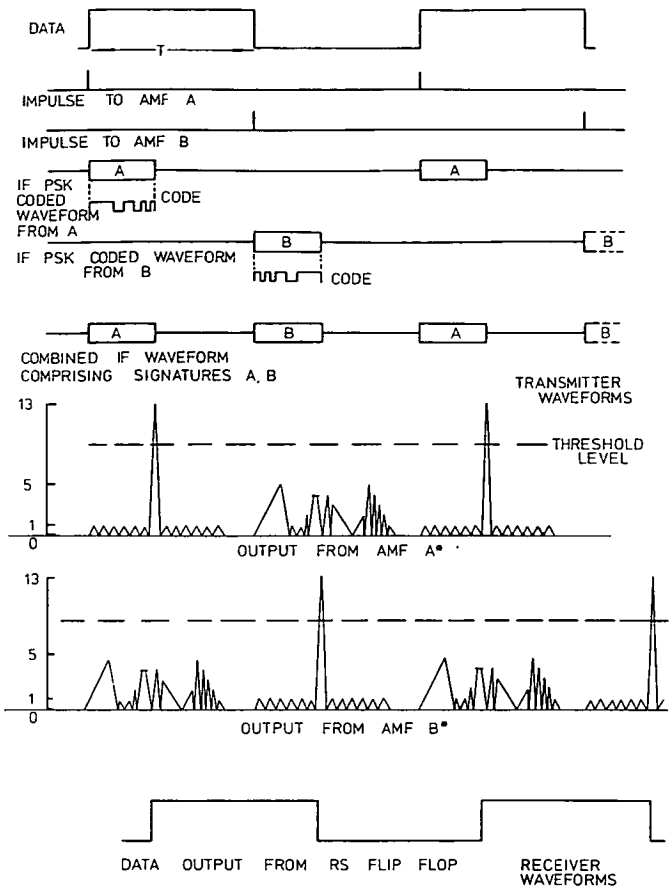

Fig. 7. Waveform diagram for simple two-signature M-ary SAW AMF modem.

M-ary principle, experiments were conducted for the simple case where $M = 2$. Thus, in each T s one binary digit is transmitted and the corresponding data rate, $1/T$ bit/s, is subject to the maximum rate, $2B_S$, given by the sampling theorem.

The waveforms corresponding to the modem experiment are indicated in Fig. 7. For convenience four identical 13-chip Barker coded devices are used. Thus the two signatures generated (A and B) were simply the Barker Code (1111100110101) and its time reverse (1010110011111). The cross correlation with the time-reverse sequence has peaks of relative height (5:13). These cross-correlation peaks arise from the imbalance of "1" and "0" states in the sequence and are not representative of the best autocorrelation and cross-correlation functions obtainable with selected binary PSK sequences [59]. In the receiver, the conjugate matched filters A^* and B^* have maximum response to codes A and B, respectively. However, unlike the simple loop experiment, the threshold must be set halfway between the top of the autocorrelation peak and the top of the cross-correlation peak. This causes a degradation in performance because of the reduction in usable threshold range. The outputs of the threshold detectors are connected to set and reset a flip-flop which regenerates the data stream. Thus it is noted that a significant feature of SAW matched filters is their ability to retrieve data without synchronization preambles, enabling the construction of a truely asynchronous data detection system (as detailed in Section VIII).

The transfer of data (a 7-bit pseudonoise sequence) has been demonstrated at a clock rate of 25 kHz with low error rate ($<10^{-7}$) in a noise and interference free coaxial wire link.

Error rates of less than 10^{-4} have been measured for simultaneous signal-to-noise and signal-to-"in-band" interference ratios of +8 dB. Selected signatures would enable the threshold to be lowered to the optimum [58] level and hence the error rate could be minimized.

The number of usable signatures and frequency slots is usually not sufficient in a simple M-ary system to provide random and simultaneous multiple access to a large number of subscribers. In Section VII the problems of selecting a sufficient number of codes with bounded cross correlations is highlighted in range differencing surveillance systems. The following two subsections indicate briefly certain possible implementations of SAW matched filters to previously published multiple access systems.

E. Time-Domain Multiple Access

Reed and Blasbalg [60] described a time-domain multiple access (TDMA) M-ary system using the (7, 2) octal Reed–Solomon [61] code to generate a time–frequency pattern for each signal waveform. These codes exhibit orthogonality with an almost flat power spectrum, in addition, pseudorandom frequency hopping into eight channels is employed to combat multipath. The seven subpulses of each signature are *uncoded* 1.8-μs bursts of RF selected from eight possible frequency slots, the total message bandwidth being 5 MHz and the total RF bandwidth 40 MHz. A synchronized receiver first removes the pseudorandom frequency hop, then each subpulse is detected by its appropriate matched filter and maximum likelihood decoding extracts the data. This multiple frequency-shift keyed (FSK) system accommodates 4000 users at a data rate of 100 bit/s per user.

SAW matched filters can be used both to generate and detect the uncoded subpulses for the time–frequency pattern. Further, programmable AMF's duplicated in each of the eight pseudorandomly selected frequency slots would remove the synthesized local oscillator and only involve synchronous baseband gating of the matched filter outputs.

F. Random Access Discrete Address (RADA) Modem Implementation

In address communication systems (Section V-E) a number of individual signatures constitute an address resulting in many different combinations providing a large address alphabet. Many subscribers can send arbitrary messages over a common wide-band channel at the same time and in the same geographical area by addressing each communication. The transmitted waveform has to carry both address and modulation. The most promising addressing technique is the exclusive allocation of a time–frequency pattern to each receiver, and possible modulation techniques are the digital delta modulation, quantized pulse position modulation (PPM), pulse code modulation, and analog PPM or pulse frequency modulation.

The number of addresses is determined inherently by the size of the time–frequency matrix. The selection of addresses depends on the system details. Certain solutions are outlined in the paper by Blasbalg *et al.* [62]. They propose a multiple FSK pseudonoise addressing modem, into which SAW matched filters could be fitted. A guide to the number of *unique* addresses A, obtained from a time–frequency matrix, is given by Magnuski [35]

$$A = \frac{F!}{(F-N)!N!} \times \frac{(T-1)!}{(T-N)!} \qquad (2)$$

where F denotes the number of frequency slots, T the number of time slots, and N the number of coded sequences transmitted in the address. As a simple example, consider four frequency slots ($F=4$), five time slots ($T=5$), and three identical code sequences per address ($N=3$), yielding 48 unique addresses. These addresses are *quasi-orthogonal* in that two addresses may coincide in more than one time–frequency box. Their resolution becomes increasingly difficult as the mutual cochannel interference increases. A solution has been proposed by Chesler [63] combining M-ary and RADA techniques. A number of addresses M are assigned to each receiver providing an optimum value of M for which a minimum probability of error is obtained for each matrix size and channel utilization.

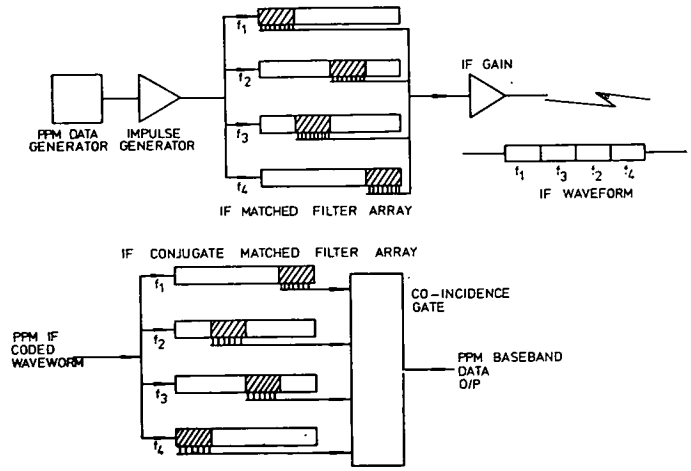

Fig. 8. Random access discrete address using SAW AMF's and SAW delay lines for encoding and decoding addressed PPM data.

TABLE VI
FUTURE ATC SYSTEMS

Simple ←			→ Comprehensive
Ground-based and onboard equipment	radar (primary and secondary)	air-derived collision avoidance (SECANT)	ICNI
Satellite transponder systems	inertial navigation reporting	AEROSAT	collision avoidance range differencing system

A simple realization of a RADA modem for transferring PPM data is shown in Fig. 8. The recognition of both coded IF waveforms and the time–frequency pattern is necessary as this represents the receiver's address. For short coded waveforms, recognition of the time–frequency pattern may be accomplished through expeditious use of SAW delay lines to ensure that correct correlation in each frequency slot occurs in the same time slot. A coincidence gate performs the baseband decoding necessary to regenerate the PPM signal.

VII. POSSIBLE FUTURE ATC SYSTEMS

A. Classification

Following the review of properties, obtainable parameters, and advantages of utilizing acoustic matched filters in ATC, this section discusses certain representative new ATC systems under development for possible implementation in the late 1970's and beyond. These systems are classified in Table VI via a matrix scheme comprising simple though comprehensive

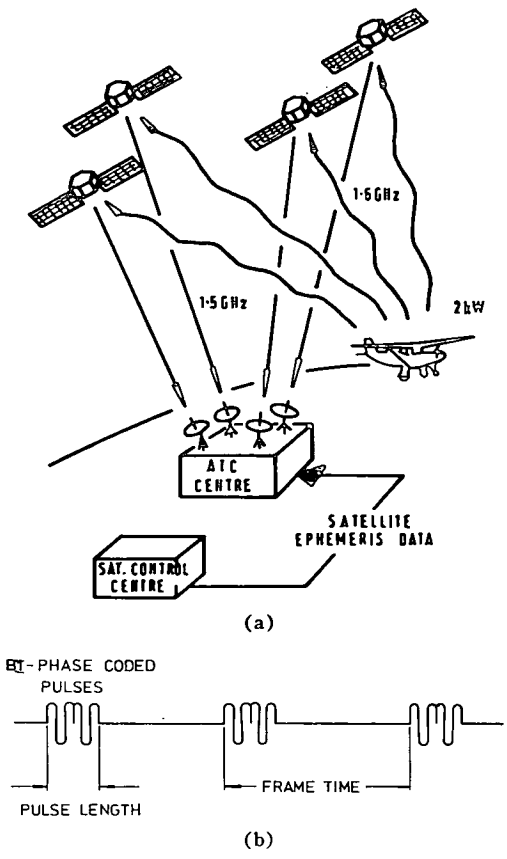

Fig. 9. Satellite range differencing systems. (a) Inclined eccentric orbiting satellites with ATC transponders. (b) Signal format.

systems. Space limitations preclude discussions of the important military IFF area where widespread interest in SAW matched filter techniques is currently being shown.

B. Range Differencing Surveillance Systems

These systems [28] which are primarily intended for use in the continental United States (CONUS) have as an essential requirement the inclusion of all aircraft. The proposed method of operation involves a one-way ranging system, for bandwidth conservancy, where each aircraft is equipped with a beacon transponder which generates a unique coded ranging signal [32]. The use of an upper hemispherical coverage antenna enables routing of the transmitted signal through several widely spaced satellites back to a ground-based control center (Fig. 9). As no synchronization exists between the aircraft and the ground station, the use of four or more satellites enables calculation of absolute user position. For accurate receiver timing and separation of the returns from the many aircraft in the system, it is proposed to biphase modulate the transmissions with a coded sequence. This enables usage of a matched filter in the receiver to extract the required signal from among the multiple retransmitted satellite signals and to provide a timing accuracy equal to 1 chip of modulating code. The system ranging accuracy is therefore governed by the bandwidth of the transmitted signal. However, it is impossible to obtain the required 100 000 codes [59] for unique identification of each aircraft. Proposals have been submitted by TRW, Boeing, and Autonetics [28] to generate these identities using unique combinations of codes, pulse repetition rates, pulse placements, and transmission frequencies (Table VII).

The TRW LIT system [32] utilizes a single transmission

TABLE VII
RANGE DIFFERENCING CAS SYSTEMS

Parameters of System	TRW	Boeing	Autonetics
Pulse length (μ/s)	51.1	255	20 (for 1 pulse)
Modulation rate (MHz)	10	2	10
Code length (chips)	511	511	200
Number of codes	25	16	10
Number of frequencies	1	1	10
Frame time (s)	1.0–1.1	1.0–1.3	N/A
Frame spacings (μs)	10	50	N/A
Number of frame addresses	10 K	6 K	100×100
Number of identifications	¼ million	100 K	1 million
Accuracy of position (ft)	250	300	260
Transmitter peak power (kW)	3.5	2	1

frequency of 1.6 GHz with a modulation rate of 10 MHz and a quarter of a million addresses as detailed in Table VII. The received signals, after recognition and timing, are fed into a PRP analyzing and tracking computer which predicts any likely conflicts. SAW AMF have been fabricated for generation and detection of the coded sequences used in this system. The Boeing proposals feature a similar LIT system of reduced accuracy due to the use of a signal of only 2-MHz bandwidth.

The Autonetics [28] proposal that covers not only simple surveillance but also en route navigation and communication, employs a pulse triplet containing the unique address. Air-to-ground communication messages can be sent 3 bit at a time by using the pulse triplet in a PPM format enabling the accomplishment of ranging and communications on the same signal format. This system represents a more comprehensive update version of the TRW and Boeing systems.

It should be noted that these surveillance systems transmit an identity pulse enabling the calculation of absolute position. However, the installation of accurate inertial navigation equipment offers an alternative surveillance system (discussed in Section VII) which transfers onboard navaid data to a ground controller over an asynchronous data link.

C. Integration of Communications, Navigation, and Identification Equipments

ICNI [31], which was initially discussed in Section V-D, is a military concept requiring a signal format of high security and information fidelity when subjected to multipath returns, interference, jamming, and spoofing signals.

The proposed system utilizes a single communications channel that is common to all users with subscriber allocations organized on a TDMA system [31]. One-way transmission provides bandwidth conservation and removes the self-interference experiences in two-way transmission systems (SSR [16], SECANT [26], etc.). A typical subscriber would utilize one 10-ms slot per 10-s time frame to transmit position, identity, mission, fuel, and ordinance status, etc., with ample provision for error detection and correction, utilizing an onboard clock to time the start of transmission. The single time slot allocation may be used in several modes, accommodating simple time ordered signaling as previously described or discrete address interrogation and reply including data exchange with another subscriber [31].

To combat the problems of jamming and interference, it is intended to utilize a moderate bandwidth (10 MHz) with both pseudorandom band spreading and frequency agile techniques. Band-spread coding with matched filter detection also enables minimization of the transmitter profile reducing the visibility of the transmitted signal and the effectiveness of any

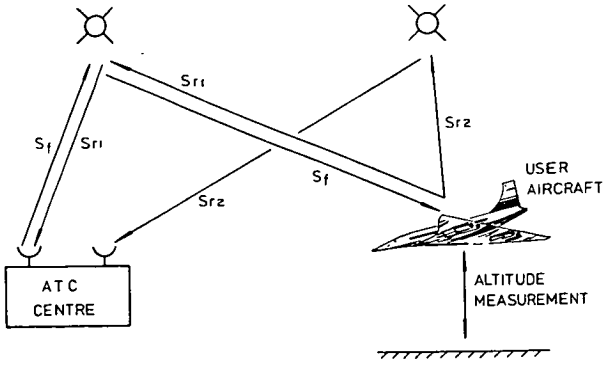

Fig. 10. Active tone ranging system.

hostile monitoring. These coding techniques which exhibit a reasonably flat spectral power density could permit utilization of the previously allocated TACAN band (960–1210 MHz) [10] for coexistence of both signals without any severe mutual interference. The bandwidths proposed for this system are between 10 and 25 MHz, which are easily accommodated by SAW AMF's. These AMF's, which perform rapid synchronization acquisition (Fig. 4), have been constructed to detect the 127-chip synchronization preambles [31]. It is anticipated that distinctly coded preambles will exceed the total currently achievable device delay, requiring a programmable AMF with the capability of changing code within a chip period. SAW matched filters are also expected to find many application in the detection of message data. This system highlights the advantages of a single signal format incorporating the functions of communication and ranging at the same transmitted power level without mutual interference.

D. AEROSAT

The North Atlantic aeronautical satellite system AEROSAT comprises a joint verture by FAA and ESRO to provide an extension of positive ATC surveillance [21], voice, and high data rate functions [64] over the busiest oceanic air-traffic route in the world. In establishing a communications link over the North Atlantic a synchronous satellite represents the optimum choice of signal routing repeater. The specification of *L*-band transmission for ATC is expedient following the reservation of a substantial band from 1535 to 1660 MHz for aeronautical radio navigation and communication (Table II). The system is to be controlled and accessed through two oceanic control centers, one situated on each side of the Atlantic, with communication facilities to the existing ATC centers at Gander and Shanwick.

The AEROSAT system proposes initially to utilize two satellites, each one placed in synchronous orbit over the ends of the present track system. Surveillance is to be performed with a ranging system of 1-nmi (1σ) accuracy based on chirp [65], multiple tones, or digital ranging techniques [66]. Active ranging (Fig. 10) is accomplished by selectively interrogating the aircraft through one satellite (*Sf*) prior to detection and timing on the reply (*Sr*), containing onboard altitude information, that has been routed through the two satellites. To meet the traffic forecasts it is proposed to design six communications channels, three in each satellite, using simplex operation with narrow-band FM modulation. Systems planning includes one 1.2-kBd DPSK data link to cover the entire area which uses one of the satellite voice channels.

The requirements for each satellite therefore include the capability of simultaneously relaying two surveillance signals, providing three communication channels, accepting and acting on telemetry tracking and command signals, and performing necessary frequency conversions on all signals. Power budgets have been derived for both uplinks and downlinks that highlight the requirement to evaluate the tradeoffs in aircraft installation costs (e.g., antenna phased array designs), spacecraft weight, and transponder reliability.

It is intended to evaluate a preoperational system using the ATS-F satellite in 1974 to ascertain both the optimum voice modem and ranging techniques and also to evaluate fully the problem of multipath returns from sea reflections. The AEROSAT system, which is likely to be the first operational satellite ATC system, as envisaged uses signals with time–bandwidth products that exceed the capabilities of currently existing SAW devices. However, the use of acoustic strip delay lines could present significant technological advantages when performing the signal processing functions. Should the design and construction of onboard electronically steered phase arrays be impossible, then band-spreading techniques with SAW matched filter detectors could represent a significant technique for achieving the required aircraft to satellite power budgets.

VIII. Novel High-Integrity *L*-Band Data Link for ATC

A. Introduction

Pending the deployment of AEROSAT, no ground-based surveillance exists for the North Atlantic crossing. It was previously stated in Section III-A that all large aircraft will shortly be equipped with sophisticated and accurate inertial navigational equipments. This section describes a simple high-integrity *L*-band data link to output onboard navaid data which contains SAW matched filters, and the features of fully asynchronous operation with built-in error checking procedures for verification of message authenticity.

B. Accessing Procedures

It is intended to confine reporting of position information to a single communications channel utilizing one-way signal transmissions combined with a selective address system. This differs from the ICNI concept by arranging subscriber accessing on an unsynchronized poled basis to accommodate individual aircraft interrogation rates suitable for both subsonic and SST. Navigation information which is always a message of known length (Section V-E) can therefore be accommodated within a fixed length message format (e.g., 120 bit), which includes address information. High integrity, the probability that a message will be received and outputed correctly, is vital in ATC data links. Throughput, which is a measure of the number of outputed messages for a given number of transmitted messages, is of lesser importance as it can be overcome by further interrogation. High integrity can be achieved for fixed length messages by the application of suitable baseband encoding techniques [33], [67].

C. High-Integrity Encoding–Decoding Procedure

Matched filters giving improved detection probabilities by processing at IF do not provide high integrity without baseband error detection techniques. In a system using binary registers, this is achieved through a high level of message redundancy to avoid the absence of a "1" being interpreted as a "0" in the receiver. The application of tristate receiver logic, described by Parker [67], where reception of either a "1" or "0" data bit always constitutes a change of state, offers a

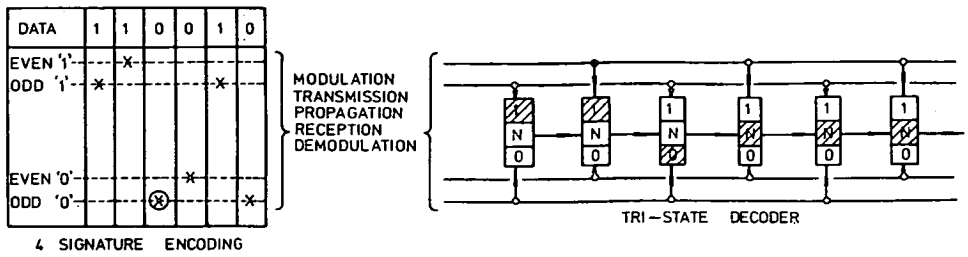

Fig. 11. Four-signature encoding and high-integrity decoding utilizing a tristate logic shift register.

significant improvement. A four-signature data encoding system allows encoding both for data level and for position in the message sequence. Fig. 11 shows the encoding in the transmitter of each data bit into one of four signatures. In the receiver, the detected baseband pulses are present on four wires feeding the decoding register. After clearing the register to the nondeterminate state, the first bit of message, which appears as an odd "0" clocks the first stage only to a "0" (because all other odd stages are inhibited) and removes the inhibit from the second stage. The receiving logic therefore ensures that even bits cannot be entered into odd states and vice versa. If one bit of the message is missing at the receiver the next bit, which possesses the incorrect positional information, is rejected. Then all the following bits are entered two stages in advance of their correct position resulting in a nondeterminate state in the last two stages. The occurrence of an odd and even bit overlap results in a register overflow. A single check bistable is employed to ascertain that no errors have been received before outputing the message onto the display. This illustrates a cheap and efficient method of realizing a self-checking high-integrity data detection system. It is fully asynchronous since the previous data bit provides the decoder shift pulses.

D. Modulation Format

The choice of waveforms for the four distinctive signatures will be governed by ease of generation and detection and by other factors influencing the system performance. The four signatures can be readily obtained by using four audio tones within the allocated frequency channel. However, for an *L*-band channel this involves problems of oscillator stability (Section V-C). Band-spreading techniques using SAW AMF's, which are asynchronous devices, have potential advantages in that discrimination between signatures can be achieved, multipath returns can be resolved, and the system will be less sensitive to interference and jamming (Table IV). Two signatures can be realized with two chirp pulses, one positive slope and the other negative slope. A further pair of chirp waveforms with a different center frequency make up the four signatures. PSK waveforms could also be employed but large time–bandwidth products are necessary to reduce the cross-correlation products to acceptable levels [59].

The overall system operation, which is represented in Fig. 6 with $M=4$, encompasses the feeding of incoming data stream in the transmitter into a four-signature encoder which routes the data on to four busses to impulse the associated filter and generate the required signature [68]. The filter outputs, at IF, are then summed, amplified, and up-converted to *L* band. In the receiver the down-converted IF signal is fed into the four conjugate chirp filters, each of which gives an output on one of four lines which lead to the tristate decoder.

E. Conclusions

The system as described is fully asynchronous and provides significant advantages, in privacy of transmitted signal and high message integrity, over existing and proposed data links. In addition, each of the individual facets of the system (Section VIII-A) uses proven techniques which if married should produce an easily engineered and operated system incorporating additional data link facilities to further reduce the communication channels load. It is concluded that the transmission of real-time navaid data represents a powerful technique for cost-effective surveillance system on oceanic crossings. However, the system as described has many wider areas of application to aircraft and battlefield IFF (high-integrity ADSEL/DABS concept), air-to-air computer dumping, and air-to-ground sonar buoy surveillance.

IX. Conclusions

Implementation of new ATC systems involves cooperation between a large number of parties, implying a long time scale prior to implementation. It is therefore important that device designers and system planners should immediately coordinate their efforts to evaluate the performance of acoustic wave technology in a real-world situation. Highlighted are system philosophies for new microwave ATC systems incorporating matched filters which offer attractive band-spread coding in place of more conventional multiple access techniques. Acoustic matched filters, particularly surface-wave filters, have many advantages, e.g., economics and performance reliability, although strong competition can be expected from LSI semiconductor technology, despite the additional complexity necessary to achieve large dynamic range and asynchronous operation. In the interest of brevity we have excluded discussion of other acoustic devices, such as frequency filters, delay lines, and UHF oscillators for applications such as FDMA data transmission, radio altimeter, and selective address SSR. It can be concluded that ATC systems development has reached a critical phase due to the congestion of air traffic, and that signal processing in acoustic devices can offer significant advantages in the next generation of ATC systems.

Appendix

Glossary of ATC Terminology

ADF	Automatic direction finding.
ADSEL	Address selective SSR.
AEROSAT	Aeronautical satellite system (North Atlantic).
AGARD	Advisory Group for Aerospace Research and Development.
ATC	Air-traffic control.
ARINC	Aeronautical Radio Incorporated.
ARTS	Automated radar terminal system.

ATS	Advanced technology satellite.
CAA	Civil aviation authority (United Kingdom).
CAS	Collision avoidance surveillance.
CONUS	Continental United States.
DABS	Discrete address beacon SSR.
DME	Distance measuring equipment.
EROS	Eliminate range zero system.
ESRO	European Space Research Organization.
FAA	Federal Aviation Administration (United States).
ICAO	International Civil Aviation Organization.
ICNI	Integrated communications navigation and identification.
IFF	Identification friend or foe.
IFR	Instrument flight rules.
ILS	Instrument landing systems.
IMAGE	Intruder monitoring ground equipment.
IPC	Intermittent positive control.
LIT	Location identification transponder.
MADAP	Maastrich automatic data processing equipment.
MLS	Microwave landing systems.
PPI	Plan position indicator.
SAGE	Semiautomatic ground environment.
SECANT	Separation and control of aircraft by nonsynchronous techniques.
SSR	Secondary surveillance radar.
SST	Supersonic transport.
TACAN	Tactical air navigation system.
VFR	Visible flight rules.
VOR	VHF omniranging.

Acknowledgment

The authors wish to thank Dollman Electronics and Microwave and Electronic Systems Ltd. for permission to describe their high-integrity *L*-band data link patent which originated in discussions between B. D. Parker, M. J. Moran, and J. N. Johnston; J. O. Clark, E. H. Boyenval, T. G. Thorne, C. Ullyatt, C. Ellingson, and D. Hitchings for positive contributions on ATC systems and philosophies; R. D. Lambert for SAW device fabrication; and J. G. Sutherland for experimental work.

References

[1] *Instrument Flying Handbook*, Dep. Transportation FAA, Washington, D. C., AC 61-27A, 1968.
[2] *International Standards and Recommended Practices, Annex 11: Aeronautical Communications*, Int. Civil Aviation Organization (ICAO) publ.
[3] "Terminal air traffic control," DOT/FAA Air Traffic Services, Washington, D.C., no. 7110.8A, Apr. 1971.
[4] "En route ATC," FAA Air Traffic Services, Washington, D. C., no. 7110.9, Oct. 1967.
[5] C. C. Jackson, "The separation of air traffic over the North Atlantic," *Flight Int.*, vol. 89, pp. 967–970, June 1966.
[6] D. L. Stevenson, "UK Military and Civil ATC in harmony," *Interavia*, 1971.
[7] R. F. Hansford, *Radio Aids to Civil Aviation*. London, England: Heywood and Company, 1960.
[8] F. S. Stringer, "Hyperbolic radio navigation systems," *Wireless World*, vol. 75, pp. 355–365, 1969.
[9] G. E. Beck, *Navigation Systems*. London, England: Van Nostrand-Reinhold, 1971.
[10] S. H. Dodington, "Recent developments of the TACAN navigation system," *Elec. Commun.*, vol. 44, pp. 316–321, 1969.
[11] C. F. O'Donnell, *Inertial Navigation: Analysis and Design*. New York: McGraw-Hill.
[12] J. E. Clegg and T. G. Thorne, "Doppler navigation," *Proc. Inst. Elec. Eng.*, paper 2568R, Mar. 1958.
[13] A Carousel IV inertial navigation system manufactured by AC Electronics in conformity with ARINC specification 561.
[14] "Microwave landing systems," *Microwave J.*, vol. 15, Jan. 1972.
[15] M. I. Skolnik, *Introduction to Radar Systems*. New York: McGraw-Hill, 1962.
[16] K. N. Shaw and A. A. Simolunas, "System capability of ATC radar beacon system," *Proc. IEEE*, vol. 58, pp. 430–437, Mar. 1970.
[17] "Mediator ATC system comes into operation," *Radio Electron. Eng.*, vol. 41, p. 181, Apr. 1971.
[18] J. R. Klauder, A. C. Price, S. Darlington, and W. J. Albersheim, "Theory and design of chirp radars," *Bell Syst. Tech. J.*, vol. 39, pp. 745–808, July 1960.
[19] G. E. Lundquist, "Status and trends in civil ATC control systems," in *AGARD Conf. Proc.*, no. 105, *ATC Systems*, paper 7, 1972.
[20] N. A. Blake and J. C. Nelson, "A projection of future ATC data processing requirements," *Proc. IEEE*, vol. 58, pp. 391–396, Mar. 1970.
[21] R. W. Meier, "North Atlantic aeronautical satellite system development," *Proc. IEEE*, vol. 53, pp. 448–455, Mar. 1970.
[22] "Report of the DOT air traffic control advisory committee 1969," U. S. Government Publ.
[23] G. H. Trow, "ATC in the Eurocontrol area," in *AGARD Conf. Proc.*, no. 105, *ATC Systems*, paper 2, 1972.
[24] "North Atlantic air traffic forecasts," NATCS, paper CP-11, Mar. 1971.
[25] W. F. Arnold, "CAS causes conflict," *Electronics*, p. 69, Dec. 20, 1971.
[26] J. L. Parsons, "SECANT—A solution to the problems of mid-air collisions," in *AGARD Conf. Proc.*, no. 105, *ATC Systems*, paper 23, 1972.
[27] J. G. Peunte, W. G. Schmidt, and A. M. Werth, "Multiple-access techniques for commercial satellites," *Proc. IEEE*, vol. 59, pp. 218–229, Feb. 1971.
[28] D. E. Findley, "Satellite considerations in future ATC systems," in *AGARD Conf. Proc.*, no. 105, *ATC Systems*, paper 30, 1972.
[29] G. W. Barnes, D. Hirst, and D. J. James, "Chirp modulation system in aeronautical satellites," in *AGARD Conf. Proc.*, no. 87, *Avionics in Spacecraft*, 1971.
[30] "ESRO ATC balloon-aircraft satellite simulation experiment," European Space Research Organization, June 1971.
[31] C. E. Ellingson, "A practical design of an ICNI system," in *AGARD Conf. Proc.*, no. 105, *ATC Systems*, paper 32, 1972.
[32] D. D. Otten, J. H. Craigie, A. Garabedian, and D. D. Morrison, "Satellite for domestic air traffic control," presented at the AIAA 3rd Communication Satellite Systems Conf., Los Angeles, Calif., Apr. 1970.
[33] B. D. Parker, "Design of an air to ground asynchronous digital communication system for ATC," in *Air Traffic Control Engineering and Design*, Inst. Elec. Eng. Conf. Publ. no. 28.
[34] "System definition and design study of a pre-operational aeronautical satellite system," British Aircraft Corp., phase 1, Final Rep., July 1971.
[35] M. Magnuski, "Address communication systems," in *Communication Systems Engineering Handbook*, D. Hamsher, Ed. New York: McGraw-Hill, 1953, ch. 18.
[36] R. M. Fano, *Transmission of Information*. New York: Wiley, 1961.
[37] G. L. Turin, "An introduction to matched filters," *IRE Trans. Information Theory*, vol. IT-6, pp. 311–329, June 1960.
[38] *IEEE Trans. Microwave Theory Tech.* (*Special Issue on Microwave Acoustic Signal Processing*), this issue.
[39] K. W. F. Steward, "A practical dispersive network system," *Marconi Rev.*, vol. 28, pp. 254–272, 1965.
[40] B. Loesch, E. M. Hofstetter, and J. P. Perry, "A technique for synthesising signals and their matched filters," M.I.T. Lincoln Lab., Cambridge, Mass., Tech. Rep. 475, Dec. 1969.
[41] H. S. Hewitt, "A computer designed 720 to 1 microwave compression filter," *IEEE Trans. Microwave Theory Tech.*, vol. MTT-15, pp. 687–694, Dec. 1967.
[42] T. Martin, private communication.
[43] J. H. Eveleth, "A survey of ultrasonic delay lines operating below 100 Mc/s," *Proc. IEEE*, vol. 53, pp. 1406–1428, Oct. 1965.
[44] Anderson Laboratories, Inc., IMCON series.
[45] C. Lardat, C. Maerfeld, and P. Tournois, "Theory and performance of acoustical dispersive surface wave delay lines," *Proc. IEEE*, vol. 59, pp. 355–368, Mar. 1971.
[46] J. Burnsweig and E. H. Gregory, "High performance surface wave signal processing filters," presented at the Int. Filter Symp., Los Angeles, Calif., Apr. 15, 1972.
[47] P. M. Grant and J. H. Collins, "Synchronisation acquisition and data transfer utilising a programmable surface-acoustic-wave analogue matched filter," *Electron. Lett.*, vol. 8, pp. 299–301, 1972.
[48] C. F. Vasile and R. LaRosa, "1000 bit surface wave matched filter," *Electron. Lett.*, vol. 8, pp. 479–480, 1972.
[49] R. C. Williamson and H. I. Smith, "Large time bandwidth product surface wave pulse compressor employing reflective gratings," *Electron. Lett.*, vol. 8, pp. 401–402, 1972.
[50] D. P. Morgan, B. J. Darby, and J. H. Collins, "Programmable cor-

relator using parametric interactions in acoustic surface waves," *Electron. Lett.*, vol. 8, pp. 40–42, 1972.
[51] G. C. Bagley, "Radar pulse-compression by random phase-coding," *Radio Electron. Eng.*, vol. 36, pp. 5–15, July 1968.
[52] D. R. Collins, W. H. Bailey, W. M. Gosney, and D. D. Buss, "Charge coupled device analogue matched filters," *Electron. Lett.*, vol. 8, pp. 328–329, 1972.
[53] J. H. Collins and P. M. Grant, "The role of surface acoustic wave technology in communications systems," *Ultrasonics*, vol. 10, pp. 59–71, Mar. 1972.
[54] D. P. Morgan, J. H. Collins, and J. G. Sutherland, "Asynchronous operation of a surface acoustic wave convolver," in *Proc. 1972 IEEE Ultrasonics Symp.*, 72 CMO 708-8 SU, pp. 296–299.
[55] *Digital Communications with Space Applications*, S. W. Golamb, ed. Englewood Cliffs, N. J.: Prentice-Hall, 1964.
[56] R. H. Barker, "Group synchronisation of binary digital systems," in *Communications Theory*, W. Jackson, Ed. New York: Academic Press, pp. 273–287, 1953.
[57] R. J. Mayher and R. O. Meyers, "Utilization of matched filters in cochannel interference suppression," *IEEE Trans. Electromagn. Compat.*, vol. EMC-10, pp. 285–292, June 1968.
[58] B. J. Darby, P. M. Grant, and J. H. Collins, "Performance of surface acoustic wave matched filter modems in noise and interference limited environments," to be presented at the 1973 Int. Ultrasonics Conf., London, England, Mar. 27–29, 1973.
[59] R. Gold, "Study of correlation properties of binary sequences," U. S. Air Force Avionics Lab., Wright-Patterson AFB, Ohio, Tech. Rep. AFAL-TR-67-311, 1967.
[60] I. S. Reed and H. Blasbalg, "Multipath tolerant ranging and data transfer techniques for air-to-ground and ground-to-air links," *Proc. IEEE*, vol. 58, p. 422–429, Mar. 1970.
[61] I. S. Reed and G. Solomon, "Polynomial codes over certain finite fields," *J. Soc. Ind. Appl. Math.*, vol. 8, pp. 300–314, 1960.
[62] H. Blasbalg, D. Freeman, and R. Keeler, "Random-access communications using frequency shifted pseudo-noise signals," in *IEEE Int. Convention Rec.*, vol. 12, pt. 6, pp. 192–216, 1964.
[63] D. Chesler, "Performance of a multiple address RADA system," *IEEE Trans. Commun. Technol.*, vol. COM-14, pp. 369–372, Aug. 1966.
[64] D. Leverington, "An appraisal of an aeronautical satellite system," *J. British Interplanatory Soc.*, vol. 24, pp. 263–272, 1971.
[65] J. Burnsweig and J. Wooldridge, "Ranging and data transmission using digital encoded FM-chirp surface acoustic wave filters," this issue, pp. 272–279.
[66] H. Wunnenberg, "Tone ranging versus digital ranging," European Space Research Organization, Tech. Note ATCS/368/HW/EG.
[67] B. D. Parker, "Improvements in or relating to data transmission systems," U.K. Patent Spec. 1246218.
[68] J. N. Johnston and B. D. Parker, provisional patent application filed.